

Sensing in Biological Systems

A thesis submitted in the total fulfilment of the requirements for the degree of

Doctor of Philosophy in Chemistry

by

Georgina Maree Sylvia



School of Physical Sciences/Discipline of Chemistry

University of Adelaide

4th May 2018

Table of Contents

Abstract	iv
Declaration of published works	viii
Publications	ix
Abbreviations	xi
Acknowledgements	xiii
CHAPTER 1 Introduction	1
1.1 Fluorescent Metal Ion Sensors	2
1.2 Photoswitchable Sensors	4
1.2.1 Spiropyran-based Metal Ion Sensors	6
1.3 Outline of Thesis	19
1.4 References	20
CHAPTER 2 A spiropyran with enhanced fluorescence: A bright, photostable and red-emitting calcium sensor	27
Statements of Authorship	28
2.1 Abstract	30
2.2 Introduction	30
2.3 Results and Discussion	32
2.3.1 Design	32
2.3.2 Synthesis	33
2.3.3 Absorbance Characterisation	34
2.3.4 Fluorescence Characterisation	35
2.3.5 Photostability Characterisation	39
2.4 Conclusion	40
2.5 Acknowledgements	40
2.6 References	41

CHAPTER 3 A rationally designed, spiropyran-based chemosensor for magnesium.....	44
Statements of Authorship.....	45
3.1 Abstract.....	47
3.2 Introduction.....	47
3.3 Results and Discussion.....	50
3.3.1 DFT Modelling.....	50
3.3.2 Synthesis.....	51
3.3.3 Sensor Characterisation.....	52
3.3.4 Photoswitching in an Optical Fibre.....	54
3.4 Conclusions.....	56
3.5 Acknowledgements.....	56
3.6 References.....	57
CHAPTER 4 Investigating the effect of <i>N</i>-indole functionalisation on metal ion selectivity in crowned spiropyran sensors.....	61
Statements of Authorship.....	62
4.1 Abstract.....	63
4.2 Introduction.....	63
4.3 Results and Discussion.....	65
4.3.1 Synthesis.....	65
4.3.2 Sensor Characterisation.....	66
4.4 Conclusions and Future Work.....	70
4.5 Acknowledgements.....	70
4.6 References.....	71
CHAPTER 5 Supporting Information.....	74
5.1 Experimental Techniques described in CHAPTERS 2-4.....	75
5.1.1 General Synthesis.....	75
5.1.2 Absorbance and Fluorescence Selectivity.....	75

5.1.3	Quantum Yield of Fluorescence (Φ).....	76
5.1.4	Job's Plot Analysis.....	76
5.1.5	Dissociation Constants (K_d).....	77
5.2	Supporting Information to CHAPTER 2.....	78
5.2.1	Chemical Syntheses	78
5.2.2	NMR and HRMS Characterisation Spectra	79
5.2.3	Absorbance and Fluorescence Spectra	80
5.2.4	Photoswitching in Optical Fibre	82
5.3	Supporting Information to CHAPTER 3.....	83
5.3.1	Chemical Syntheses	83
5.3.2	NMR and HRMS Characterisation Spectra	87
5.3.3	DFT Calculations	95
5.3.4	Absorbance and Fluorescence Spectra	102
5.3.1	Photoswitching in Optical Fibre	105
5.4	Supporting Information to CHAPTER 4.....	106
5.4.1	Chemical Syntheses	106
5.4.2	NMR and HRMS Characterisation Spectra	109
5.4.3	Absorbance and Fluorescence Spectra	116
5.5	References	120
CHAPTER 6 Conclusion and Further Studies		121
6.1	References	126
APPENDIX A Lithium 'Hot-spots': Real-time Analysis of Ion Conductance in Aquaporin-1		128
APPENDIX B Engineering of Surface Chemistry for Enhanced Sensitivity in Nanoporous Interferometric Sensing Platforms		151

Abstract

Metal ions are critical to a range of mammalian cell functions, including cell signalling, proliferation, differentiation and death. As such, changes in metal ion homeostasis can have a significant effect on cell health. Fluorescent chemosensors, in combination with specialised imaging technologies, provide a useful tool to study the role of metal ions in cellular processes as they enable detection in and around cells with spatial and temporal resolution. Commercially available and literature fluorescent probes, with core structures based on traditional fluorophores (e.g. fluorescein, coumarin and rhodamine) have been used extensively to study the relationship between cellular metal ion dynamics and disease. However, one drawback of current sensors is the lack of reusability.

Photoswitchable molecules present as an alternative core unit for the development of fluorescent metal ion sensors, with the potential for reversible analyte binding. The photochromic spiropyran molecule is of particular interest in our research group, as the core structure can be readily functionalised for analyte selectivity, surface attachment, and tuning of the photochromic properties. Photo-controlled switching between the weakly fluorescent spiropyran (SP) and highly fluorescent merocyanine (MC) isomers occurs on irradiation with UV light or in the presence of the target metal ion, while visible light reverses the isomerisation (see Figure 1).

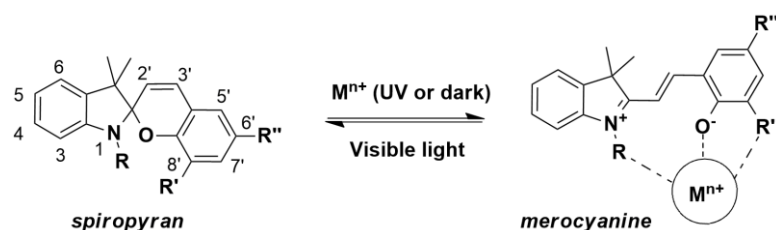


Figure 1. Structures of the ring-closed, weakly fluorescent spiropyran isomer (left) and the ring-opened, highly fluorescent merocyanine-metal bound complex (right). R, R' and R'' denote points of functionalisation explored in this thesis.

This thesis describes the functionalisation of the spiropyran molecule in order to improve fluorescence intensity (**Chapter 2**), develop selective metal ion sensors for Mg^{2+} (**Chapter 3**) and investigate structure-metal ion selectivity relationships (**Chapter 4**).

Chapter 1

Chapter 1 gives a broad introduction to fluorescent sensors and presents a literature review highlighting the use of photoswitchable spiropyrans as effective sensors for biologically relevant metal ions relevant such as calcium (Ca^{2+}) and zinc (Zn^{2+}), as well as the alkali metals sodium (Na^+), potassium (K^+) and lithium (Li^+).

Chapter 2

In **Chapter 2**, we took a unique approach to Ca^{2+} sensing with a rationally designed sensor which possess all the desirable characteristics (brightness, photostability and red fluorescence emission) of both the traditional and spiropyran-type sensor. This was accomplished by combining a traditional fluorophore (pyrene) with a photoswitch (spiropyran) with a Ca^{2+} -selective ionophore. The rationally designed, pyrene-spiropyran hybrid Ca^{2+} sensor (**Py-1**) displays enhanced fluorescence intensity compared to a standalone spiropyran analogue. Importantly, **Py-1** retains the characteristic red emission profile of the spiropyran, while fibre-based photostability studies show the sensor is stable after multiple cycles of photoswitching, without any sign of photodegradation. Such properties are of real advantage for cell-based sensing applications. An interesting observation is that, **Py-1** presents with two excitation options; direct green excitation (532 nm) of the photoswitch for a red emission, and UV excitation (344 nm) of the component pyrene, which gives rise to distinct blue and red emissions. This proof-of-concept hybrid sensing system presents as a general approach to brighter spiropyran-based sensors.

Chapter 3

Magnesium ions (Mg^{2+}) play an important role in mammalian cell function; however, relatively little is known about the mechanisms of Mg^{2+} regulation in disease states. An advance in this field would come from the development of selective, reversible fluorescent sensors, capable of repeated measurements. To this end, **Chapter 3** details the development of the first rationally designed, spiropyran-based fluorescent Mg^{2+} sensors. The most promising analogue, sensor **1**, exhibits 2-fold fluorescence enhancement factor and 3-fold higher binding affinity for Mg^{2+} (K_d 6.0 μM) over Ca^{2+} (K_d 18.7 μM). Incorporation of spiropyran-based sensors into optical fibre sensing platforms has been shown to yield significant signal-to-background changes with minimal sample volumes, a real advance in biological sensing that enables measurement on

subcellular-scale samples. In order to demonstrate sensor compatibility within the light intense microenvironment of an optical fibre, photoswitching and photostability of **1** within a suspended core optical fibre (SCF) was subsequently explored, revealing reversible Mg^{2+} binding with improved photostability compared to the non-photoswitchable Rhodamine B fluorophore. The spiropyran-based sensors reported here highlight untapped opportunities for a new class of photoswitchable Mg^{2+} probe and present a first step in the development of a light-controlled, reversible dip-sensor for Mg^{2+} .

Chapter 4

In **Chapter 4**, the influence of multiple chelating groups on calcium ion (Ca^{2+}) selectivity are explored with a series of spiropyran-based sensors incorporating both C8' and N1-indole metal ion binding domains. The sensors possess N1-indole functionalisation in the form of hydroxyethyl (**SP-1**), ethoxycarbonylbutyl (**SP-2**) and carboxybutyl (**SP-3**) groups, while all three sensors incorporate a 1-aza-15-crown-5 ionophore at the C8' position. Absorbance and fluorescence characterisation of metal ion binding revealed that in particular, sensor **SP-3** gave excellent Ca^{2+} -selectivity, improved dissociation constant ($K_d \text{ MC}(\text{SP-3})\text{-Ca}^{2+} = 22 \mu\text{M}$) and quantum yield of fluorescence ($\Phi \text{ MC}(\text{SP-3})\text{-Ca}^{2+} = 0.37$), compared to the other sensors. These results suggest the carboxybutyl N1-indole functionality of **SP-3** may play a role in stabilizing Ca^{2+} in the 1-aza-15-crown-5 ionophore, promoting metal-induced isomerisation to the $\text{MC}(\text{SP-3})\text{-Ca}^{2+}$ complex and thus a bright, Ca^{2+} -selective, red fluorescence signal.

Appendix A

One sensor from the selectivity study in Chapter 4 (labelled '**SHL**') was subsequently utilized with collaborators in a biological application, to study lithium 'hot-spots' in living colon cancer cells. The results show ion binding to the sensor intracellularly is dependent on exogenous Li^+ transport into the cell, and repeated cycles of photoswitching gave reproducible changes in fluorescence, demonstrating the ability of the sensor to reversibly photoswitch in living cells. Furthermore, 'hot-spots' of Li^+ -**SHL** binding induced fluorescence were observed at the leading edges of migrating cells, which correlates with ion movement through aquaporin transmembrane channels. These results

suggest that the aquaporin-1 (AQP1) ion channel could be a novel candidate for therapeutic interventions to manage metastasis in AQP1-dependent cancers.

Appendix B

The themes of tailored selectivity and signal enhancement developed in this thesis are further explored in **Appendix B**, where we report on improved sensitivity in a nanoporous anodic alumina (NAA) sensing platform, targeted towards the detection of analytes in biological media. Sensing on an NAA platform utilises reflectometric interference spectroscopy (RIFS), where the amount of light-based signal is proportional to the degree of conformational change of the surface. This work describes a range of Au³⁺ selective binding molecules, in a series of combined surface attachment strategies in order to improve fundamental knowledge of surface-engineering in these nanoporous materials. The most sensitive functional molecules from sensing approaches (i) and (ii) were combined into a third sensing strategy whereby the nanoporous platforms are functionalised on both the top and inner surfaces concurrently. Engineering of the surface according to this approach resulted in an additive enhancement in sensitivity of up to 5-fold compared to previously reported systems.

Declaration of published works

I certify that this work contains no material which has been accepted for the award of any other degree or diploma in my name, in any university or other tertiary institution and, to the best of my knowledge and belief, contains no material previously published or written by another person, except where due reference has been made in the text. In addition, I certify that no part of this work will, in the future, be used in a submission in my name, for any other degree or diploma in any university or other tertiary institution without the prior approval of the University of Adelaide and where applicable, any partner institution responsible for the joint-award of this degree.

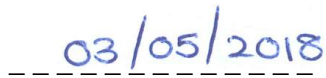
I acknowledge that copyright of published works contained within this thesis resides with the copyright holder(s) of those works.

I also give permission for the digital version of my thesis to be made available on the web, via the University's digital research repository, the Library Search and also through web search engines, unless permission has been granted by the University to restrict access for a period of time.

I acknowledge the support I have received for my research through the provision of an Australian Government Research Training Program Scholarship.



Georgina M. Sylvia



Date

Publications

Journal Papers

These publications comprise full chapters in this thesis:

Chapter 2: Sylvia, G. M.; Heng, S.; Bachhuka, A.; Ebendorff-Heidepriem, H.; Abell, A. D. A spiropyran with enhanced fluorescence: a bright, photostable and red-emitting calcium sensor. *Tetrahedron*, **2017**, 74(12), 1240-1244; doi:10.1016/j.tet.2017.11.020. Impact Factor 2016: 2.645, Ranking in Chemistry, Organic: Q2.

Chapter 3: Sylvia, G. M.; Mak, A. M.; Heng, S.; Bachhuka, A.; Ebendorff-Heidepriem, H.; Abell, A. D. A rationally designed, spiropyran-based chemosensor for magnesium. *Chemosensors*, **2018**, 6(2), 17; doi:10.3390/chemosensors6020017.

A significant contribution was made to two further publications presented as appendices in this thesis. I am not the principle author of these papers:

Appendix A: Pei, J. V. and Heng, S.; De Ieso, M.; **Sylvia, G. M.**; Kourghi, M.; Nourmohammadi, S.; Abell, A. D.; Yool, A. Lithium ‘Hot-spots’: Real-time Analysis of Ion Conductance in Aquaporin-1. *Manuscript in preparation*.

Appendix B: Law, C. S.; **Sylvia, G.**; Nemati, M.; Yu, J.; Abell, A. D.; Losic, D.; Santos, A. Engineering of Surface Chemistry for Enhanced Sensitivity in Nanoporous Interferometric Sensing Platforms. *ACS Appl. Mater. Interfaces*, **2017**, 9(10), 8929-8940; doi:10.1021/acsami.7b01116. Impact Factor 2016: 7.501, Ranking in Materials Science, Multidisciplinary: Q1.

Conference presentations

Conference paper:

Sylvia, G.; Heng, S.; Abell, A. D. Fluorescence enhancement of photoswitchable metal ion sensors. *Proc. SPIE 10013, SPIE BioPhotonics Australasia*, 100131X (December 9, 2016); doi:10.1117/12.2244656.

Oral Presentation:

Fluorescent enhancement of photoswitchable metal ion sensors, “Chemical Aspects of Sensing”, SPIE BioPhotonics, 16-19 October 2016, Adelaide SA 5000, Australia.

Posters:

2014 RACI National Congress, “Synthetic Chemistry”, 7-12 December 2014, Adelaide, Australia.

Nanopeptide 2015, “Peptide Nanostructures in Opto/Electronic Applications”, 2-4 March 2015, Glasgow, UK.

2015 International Chemical Congress of Pacific Basin Societies, Pacificchem, “Advances in Peptide and Peptide Chemistry”, 15-20 December 2015, Honolulu, Hawaii, USA. (Student Poster Competition Award).

Abbreviations

Abbreviation	Full Name
^1H NMR	proton nuclear magnetic resonance
^{13}C NMR	carbon nuclear magnetic resonance
ACN	acetonitrile
br	broad (spectroscopic)
calcd	calculated
CDCl_3	deuterated chloroform
CD_3CN	deuterated acetonitrile
conc	concentrated
DCM	dichloromethane
DIPEA	diisopropylethylamine
DMF	dimethylformamide
$\text{DMSO-}d_6$	deuterated dimethylsulfoxide
EDTA	ethylenediaminetetraacetic acid
ESI	electrospray ionisation
EtOH	ethanol
equiv	equivalents
h	hour
HPLC	high performance liquid chromatography
HRMS	high resolution mass spectrometry
<i>in vacuo</i>	in a vacuum
k_D	dissociation constant
MC	ring-opened merocyanine isomer of spiropyran
MeOH	methanol
min	minute
mL	millilitre
mM	millimolar
nm	nanometre
μm	micrometre
quant	quantitative
rt	room temperature

SCF	suspended-core optical fibre
SP	ring-closed isomer of spiropyran
TFA	trifluoroacetic acid
THF	tetrahydrofuran
TMS	tetramethylsilane
TOF MS	time-of-flight mass spectrometry
TLC	thin layer chromatography
UV	ultraviolet
UV-Vis	ultraviolet to visible absorption spectroscopy
v/v	volume per unit volume
w/w	weight per unit weight
λ_{em}	peak emission wavelength
λ_{ex}	excitation wavelength
λ_{max}	peak absorption wavelength
μL	microlitre
μM	micromolar
η	refractive index
Φ	quantum yield of fluorescence

Acknowledgements

Throughout my PhD I have been working at the University of Adelaide as a part of the ARC Centre for Nanoscale BioPhotonics (CNBP). The CNBP is a multidisciplinary organisation with collaborators from biology, chemistry, physics and engineering working across three major nodes in Australia, and in many affiliated institutions worldwide. The Abell research group works within the “Sensing” Impact Area of the CNBP, with the goal of using optically controlled surfaces to recognise analytes in living systems. This is achieved by developing novel reporter molecules, strategies for surface attachment and pursuing systems for continuous sensing with light-driven regeneration and control. The research presented in this thesis was primarily funded by the CNBP, and so the work presented reflects these core aims.

Firstly, I would like to acknowledge my supervisors, Professor Andrew Abell and Dr. Sabrina Heng. Thank-you to Andrew for your wisdom, patience and enthusiasm for a good NMR spectrum. In particular, your relentless encouragement to always ‘back myself’ has made me a more confident scientist. I would also like to express my endless gratitude to Sabrina, whose guidance and mentoring has taught me to grow and learn from my mistakes, both professionally and in life outside of research. I don’t think there are enough words to express how much you’ve helped me in this PhD, but I hope one day I can pay it forward. I am forever your ‘loyal minion’.

Thanks must also go to members of the Abell research group, past and present, for their continued support, valuable feedback and ideas. In particular, thank-you to Dr. Xiaozhou (Michelle) Zhang for your guidance in experiment design, machinery and all things spiropyran. Thank-you to the Institute for Photonics and Advanced Sensing (IPAS), where in the Braggs building I have happily been a member for the last two years and enjoyed a supportive environment of collaboration, discourse and Thursday morning teas.

Thank-you to my collaborators from Physics (Dr. Akash Bachhuka, Prof. Heike Eberndorff-Heidepriem), Chemical Engineering (Dr. Abel Santos, Ms Cheryl Suwen Law), Biology (Dr. Sanam Mustafa, Dr. Jinxin Pei, Prof. Andrea Yool) and Computational Chemistry (Dr. Adrian Mak). This research would not have been possible without your enthusiasm and expertise.

On a personal note, I am incredibly lucky to be supported by many wonderful people who I count as friends and family. Nathalie, Adrian, Rebekah, Jamie-Lee and Desiree your love and support all these years has been invaluable to my sanity. To my long-suffering House Friends, Felicity and Alana, your surprise acts of kindness and friendship have been the highlight of some very bleak days. Thank-you to my Dad, who through a mix of love, encouragement, incessant nagging and open threats has always strived to show me that ‘I can’. To my not-so-little brothers, Mervin and Bronn, I hope this encourages you to challenge yourself in life and know that you will always be supported. Thank-you to my Grandmother, for teaching me the importance of education and the joy of a good book – you inspire me to always keep learning. Finally, I would like to thank my Mum, the cleverest person I know, whose enthusiasm for solving a problem has given me an unending curiosity for life and inspired me to undertake this PhD.

CHAPTER 1

Introduction

1.1 Fluorescent Metal Ion Sensors

Metal ions play an important role in cellular function, and abnormal regulation of metal ions has been associated with conditions such as neurodegenerative diseases,¹⁻² diabetes³⁻⁵ and cancer.⁶⁻⁸ Fluorescent sensors, in combination with specialised imaging technologies, provide a useful tool to study the role of metal ions in cellular processes as they enable detection in and around cells with spatial and temporal resolution. Such fluorescent sensors usually comprise a small molecule organic fluorophore, synthetically modified to bear a metal ion-recognition domain (see Figure 1).⁹⁻¹¹ Typically in these systems, photo-induced electron transfer (PET) between the chelating moiety and the fluorophore gives a fluorescence quenching effect in the unbound state. Upon metal ion binding, there is a decreased charge transfer from the chelating moiety to the fluorophore, and improved fluorescence quantum yield (**1b**, Figure 1). Hence, chelation of the metal ion induces an intensity-based output of fluorescence signal for the sensor.¹²

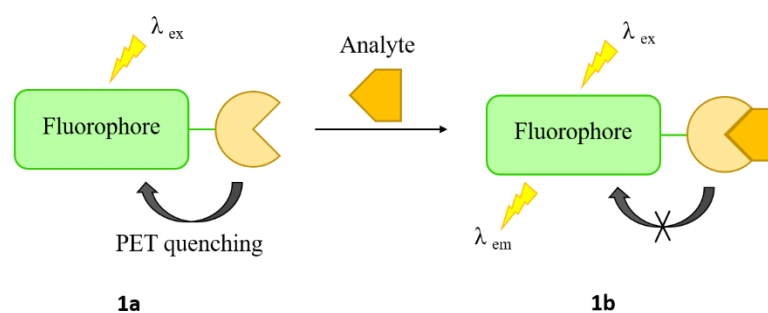


Figure 1. General schematic of a fluorescent metal ion sensor, with modular fluorophore and metal-chelating components. When there is no metal bound (**1a**), the fluorophore's fluorescence is quenched by photoinduced electron transfer (PET) from the chelating moiety. Analyte binding to the chelating moiety (**1b**) decreases this charge transfer, resulting in a fluorescence emission from the fluorophore.

This modular design strategy, of interchangeable fluorophore and metal ion chelating group, allows for tailored fluorescence properties and sensor selectivity to different metal ions. There are many commercial metal ion sensors available from distributors such as Molecular ProbesTM,¹³ and these are almost exclusively built upon traditional fluorophores with conjugated, polyaromatic scaffolds such as fluorescein, coumarin, rhodamine and boron-dipyrromethane (BODIPY) (Figure 2a).¹⁴⁻¹⁵ Commercially-available metal ion sensors based on these core fluorophores are often bright, well-characterised and readily adaptable to binding and detection of a diverse range of metal ions. For example, the fluorescein-based CoroNaTM indicator has been shown to detect sodium (Na⁺) in cells with spatial and temporal

resolution in the presence of physiological concentrations of other monovalent cations.^{13, 16-19} The rhodamine-based RhodZinTM-3 indicator exhibits a K_d for zinc (Zn^{2+}) of ~ 65 nM²⁰ and has been shown to localize into mitochondria (Figure 2b).^{13, 21-22} A comprehensive review of fluorescent sensors for binding metal ions has been published previously by Carter *et al.*⁹

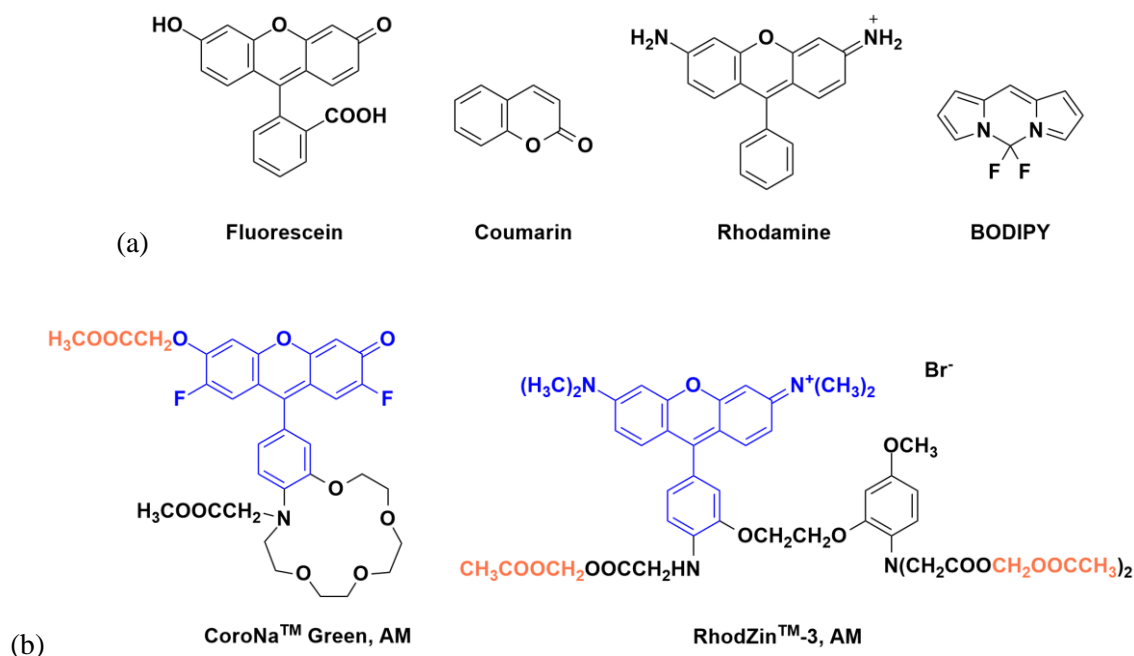


Figure 2. (a) Traditional fluorophore scaffolds fluorescein, coumarin, rhodamine and BODIPY. (b) Commercially available sensors: fluorescein-based CoroNaTM Green Na⁺ indicator and the rhodamine-based RhodZinTM -3 Zn²⁺ indicator. The fluorophore core is highlighted in blue, while the esterase-cleavable AM-ester group is highlighted in orange.

However, many sensors based on the core fluorophores in Figure 2 suffer from high background fluorescence in the absence of the ion, and signal overlap with native molecules in the cell such as NADH, a phenomenon known as cellular autofluorescence ($\lambda_{em} \sim 300-560$ nm).²³⁻²⁵ Additionally, sensors such as those described above require an appended esterase-cleavable AM ester protecting group (highlighted in orange, Figure 2b) to mask charged functional groups, in order for the sensor to permeate a cell membrane.²⁶

1.2 Photoswitchable Sensors

Ion concentrations in a cell often vary within a typical cell cycle, as ions are exchanged between protein-bound form, free in the cytoplasm, stored in cellular organelles and transferred in and out of the cell by active and passive transport mechanisms.^{15,27} Cell-based fluorescence sensors should therefore be reusable, to allow for multiple measurements to be taken in the cellular environment over time. An ability to switch between a metal-bound ‘active’ state and an ‘inactive’ state where metal ions are released would allow for reversible analyte detection. To this end, photoswitchable fluorophores present an alternative to traditional fluorophores for the development of fluorescent metal ion sensors. Photoswitches exhibit reversible changes in geometry, polarity, charge and/or fluorescence emission intensity in response to analyte binding, and light of different wavelengths (see **2b**, Figure 3a). Common photoswitches that can provide a basis of a photoswitchable sensor include an azobenzene, fulgide, dithienylethene and spiropyran (Figure 3b).²⁸

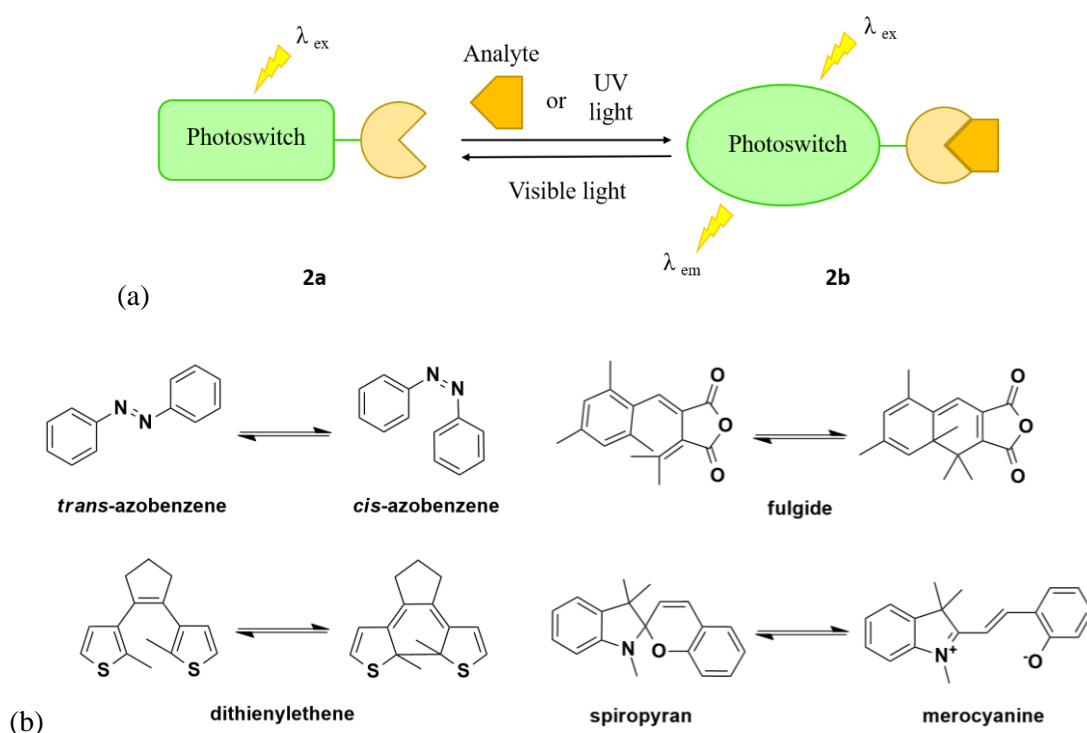


Figure 3. General schematic of a photoswitchable metal ion sensor, with modular photoswitchable fluorophore and metal ion chelating components. When there is no metal ion bound (**2a**), the sensor may be non-fluorescent or weakly fluorescent. Binding of analyte or irradiation with UV light induces photoisomerisation to the more fluorescent isomer (**2b**). This transition is reversible, by irradiation with visible light. (b) Photoswitchable fluorophore scaffolds azobenzene, fulgide, dithienylethene and spiropyran/merocyanine.

Among these, the photochromic spiropyran is a promising molecular scaffold for the development of photoswitchable metal ion sensors, with properties which address many of the challenges (specifically high background, signal overlap with autofluorescence and cell membrane impermeability) presented by other fluorophores for biological sensing. Firstly, spiropyran is excited by green light ($\lambda_{\text{ex}} \sim 500 - 550 \text{ nm}$), with an orange/red fluorescence emission profile ($\lambda_{\text{em}} \sim 600 - 700 \text{ nm}$),²⁹ thus minimizing the effects of signal overlap with autofluorescence in cell based applications. Secondly, it has the advantage of low background fluorescence as compared to non-photochromic sensors such as those based on rhodamine.³⁰ Finally, recent studies by our group and others have shown that spiropyran is generally cell-permeable, without the need for enzyme-cleavable protecting groups.³¹⁻³⁴ A spiropyran is reversibly photoswitched between a ring-closed, weakly fluorescent spiropyran (SP) isomer, and a charge-delocalized, highly fluorescent merocyanine (MC) isomer when exposed to stimuli such as light or interaction with a charged metal ion (Figure 4).

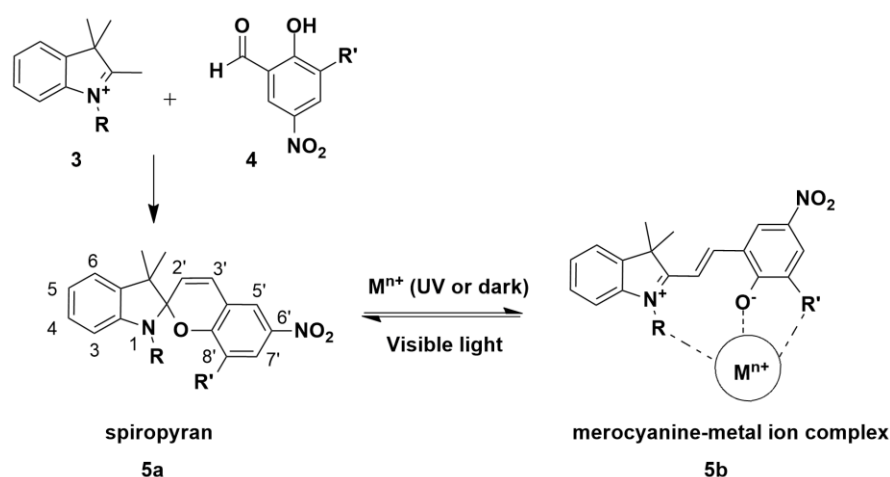


Figure 4. General spiropyran synthesis, with structures of the ring-closed, weakly fluorescent spiropyran isomer, **5a**, and the ring-opened, highly fluorescent merocyanine-metal bound complex, **5b**. R and R' denote common positions for the incorporation of a metal ion binding domain.

Importantly, a spiropyran scaffold can be functionalised at multiple positions with metal chelating groups in order to promote specific binding of metal ions.³⁵⁻³⁸ These groups can be incorporated into the indoline and aldehyde synthetic precursors (**3** and **4**, Figure 4), which allows the sensor to be constructed from a library of functionalised building blocks. Incorporation of an electron withdrawing substituent such as $-\text{NO}_2$ at the C6' position is known to stabilize the ring-opened merocyanine isomer which then promotes metal ion binding.³⁹ Additionally, the phenolic oxygen of the ring-opened merocyanine isomer

provides an additional chelation site for metal ion binding (**5b**, Figure 4).⁴⁰ This enables the spiropyran sensor to bind metal ions with a higher affinity while in the ring-opened form (resulting in high fluorescence), and release metal ion when photoswitched back to the ring-closed, spiropyran form (resulting in weak fluorescence).

1.2.1 Spiropyran-based Metal Ion Sensors

Sensors for Alkali Metals (Na⁺, K⁺, Li⁺)

Alkali metal ions, such as sodium (Na⁺), potassium (K⁺) and lithium (Li⁺), play an important role in physiological and pathological processes of living cells, and as such have been the subject of extensive sensor development.⁴¹ Na⁺ and K⁺ are highly abundant extracellular and intracellular cations, respectively, which function as charge carriers, maintaining osmotic balance and transmembrane potential across the cell wall, enabling energy production and electron transfer reactions. The ability of cells to generate this transmembrane potential is critical to a range of functions such as neurotransmission, muscle contraction and heart function.⁴²⁻⁴³ In contrast, lithium ions (Li⁺) are a trace metal of unknown biological function, with significant but not well understood therapeutic application in the treatment of bipolar disorder.⁴⁴⁻⁴⁵ Lithium as a clinical treatment is only effective within a narrow therapeutic window (0.6 – 1.2mM), where a higher dose can be lethal and a low dose has no effect.⁴⁶⁻⁴⁷

Some of the earliest spiropyran-based sensors for alkali metal ions were developed by Inouye *et al.*⁴⁸⁻⁴⁹ Complexation of Li⁺, Na⁺ and K⁺ was achieved with an azacrown moiety at the N1-position of the indolic nitrogen (Figure 5a, labelled as **6-9**). Sensors **6** and **7** display absorbance selectivity for Li⁺, while **8** preferred Na⁺ and **9** showed no absorbance changes in the presence of alkali metal ions. Analogously, spiropyran-based sensors developed by Kimura *et al* possess the azacrown moiety at the C8'-position of the benzopyran ring (**10-12**, Figure 5b). Chelation of Li⁺, Na⁺ and K⁺ to the ionophore in this position induced remarkable isomerisation to the merocyanine isomer, even under dark conditions.⁵⁰ Sensors **10** and **11** exhibit absorbance selectivity for Li⁺, while **12** was selective for Na⁺. ⁷Li and ²³Na NMR spectroscopy sensor-binding experiments suggested that the metal ions, in particular Li⁺, are stabilized in the crown ionophore by binding to the merocyanine phenolate anion and are thus more strongly bound in the ring-opened merocyanine than in the ring-closed spiropyran form.

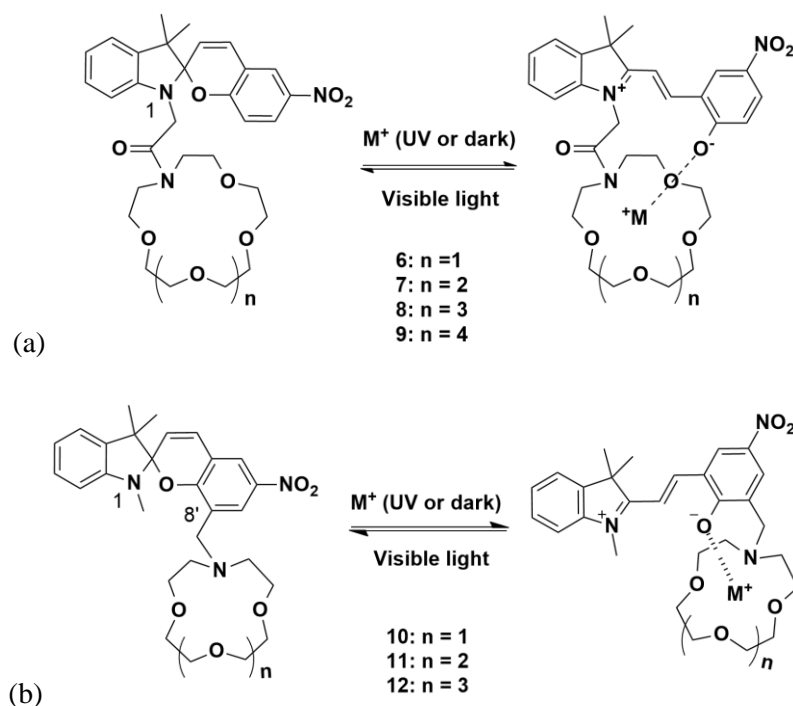


Figure 5. (a) Spiropyran-based sensor with azacrown N1-indole functionalisation, **6-9**, reported by Inouye *et al.*⁴⁸⁻⁴⁹ (b) C8' azacrown functionalised spiropyrans **10-12**, reported by Kimura *et al.*⁵⁰

We have recently reported a further advance in the development of spiropyran-based alkali metal ion sensors, by incorporating the C5 carboxy-functionalised sensor **13** (see Figure 6a, an analogue of **11**) into a microstructured optical fibre (MOF) platform.⁵¹ Air holes are incorporated within the cross section of MOFs, and these holes can be used to control the interactions between guided light and matter located within the holes while simultaneously acting as tiny sample chambers (Figure 6b).⁵²⁻⁵³ The overall size of the fibre is less than 300 μm , allowing measurements of nanoscale volumes. Additionally, optical fibres provide a platform for sensing metal ions in confined spaces such as the medium surrounding cell clusters, oocytes and embryos, and in the *in vivo* environment.⁵⁴⁻⁵⁵

A silica-based optical fibre was fabricated in-house according to methods described previously.⁵⁶⁻⁵⁷ Silica is an ideal material for optical sensing as it has a high transmission in the UV-Vis-NIR spectral range.⁵⁸⁻⁵⁹ Functionalisation of **13** to the interior optical fibre surface was achieved by reaction with *N*-hydroxysuccinimide (NHS) to give **13**-NHS, which was then covalently attached to the silica surface via APTES (Figure 6a). Fluorescence experiments were performed by exciting the sensor-filled MOF (**13**-MOF) with a 532 nm green laser and recording the resulting fluorescence signal according to the schematic in Figure 6c.

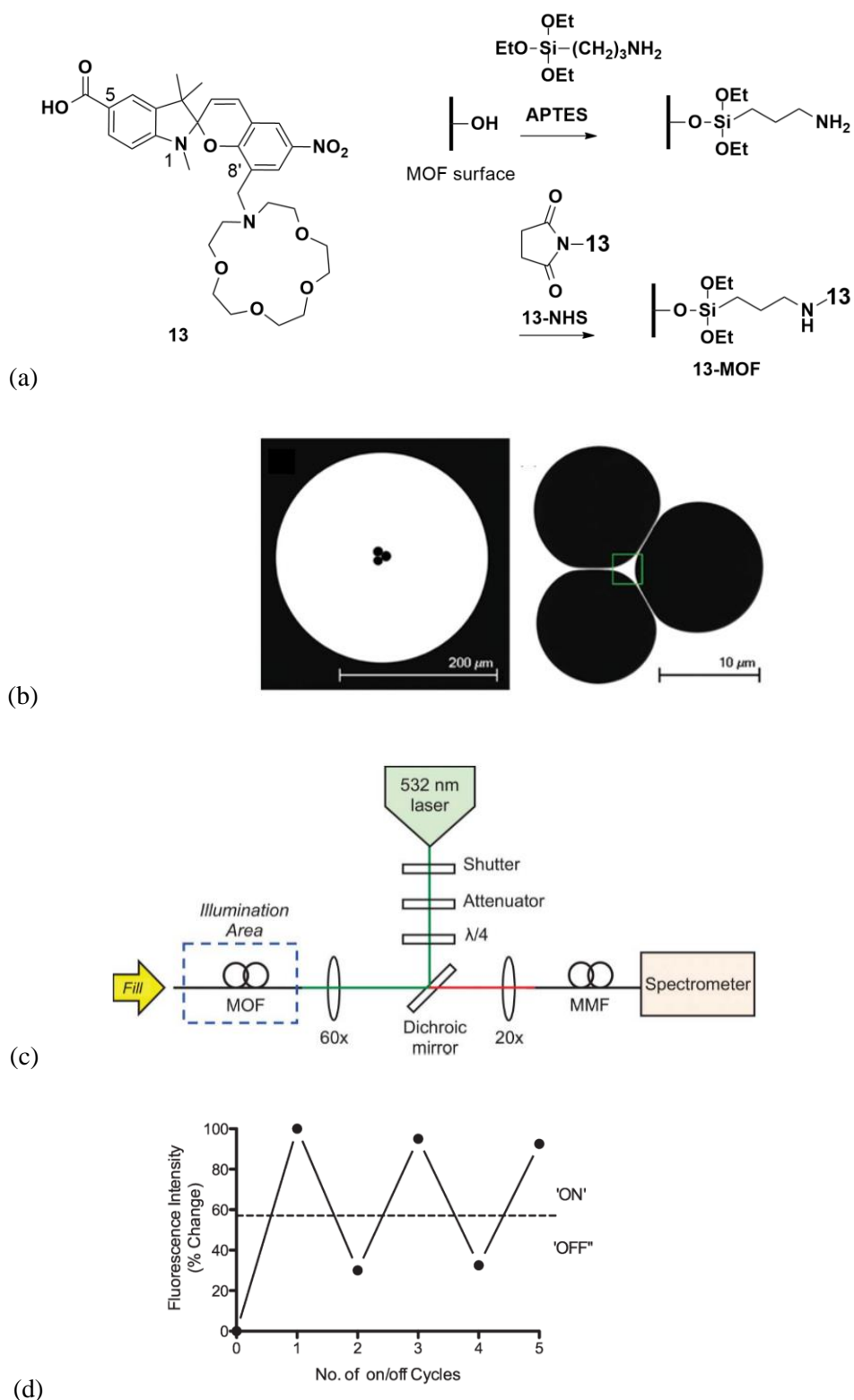


Figure 6. (a) Procedure for the covalent attachment of **13** to the MOF surface.⁵¹ (b) Scanning electron microscopy images of the silica microstructured optical fibre (MOF) with an outside diameter of 270 μm and an enlarged image of the air-holes and core (highlighted by the green box). (c) Optical setup used to measure the fluorescence from a MOF, where MMF is a multimode fibre. (d) Photoswitching of the surface functionalised MOF. Each ‘ON’ cycle denotes where the **13**-MOF was exposed to UV light ($\lambda = 365 \text{ nm}$) for 7 min. Each “OFF” cycle denotes where **13**-MOF was exposed to white light for 12 min.

Fluorescence of **13**-MOF gives an emission maximum of ~ 620 nm, which is consistent with solution-based experiments of **13** alone. One end of the functionalised **13**-MOF can be immersed in a 1 μM Li^+ solution, with the fibre filling via capillary forces. Photoswitching of **13**-MOF in the presence of Li^+ shows that ion binding and release is optically controlled and measured by the SP/MC state-dependent fluorescence (Figure 6d). Each ‘ON’ cycle involve exposure to UV light in order to stimulate formation of the active, fluorescent **13**(MC)- Li^+ complex on the MOF surface while each ‘OFF’ cycle is generated upon irradiation with white light to expel Li^+ back into the solution and regenerate the passive, weakly-fluorescent **13**(SP) surface. The entire photoswitching process occurs within the micron-scale holes of the MOF, with the sensor being unaffected by multiple rounds of photoswitching. Reusability of the sensor is demonstrated where unbound ions are flushed from **13**-MOF in the ‘OFF’ state, allowing the sensor to be reused for subsequent fluorescence measurements. Importantly, this work describes the first instance where a spiropyran-based metal ion sensor has been incorporated into a MOF sensing platform, to give a photoswitchable dip sensor detecting metal ions down to 100 nm, in nanolitre-scale volumes.

Sensors for Calcium (Ca^{2+})

Calcium ions play a vital role in intra- and extracellular signalling in mammalian cells involved in processes such as proliferation, differentiation and death.⁶⁰⁻⁶⁴ Total human cellular calcium concentration is estimated at 1-10 mM, however most of this is sequestered in organelles such as the endoplasmic reticulum and the Golgi or bound to protein complexes. Low concentrations of free Ca^{2+} in the cytosol (~ 100 nM) is tightly regulated by a range of membrane transport systems, such as pumps, exchanges and channels. As a signalling moiety, free- Ca^{2+} is an effective second messenger in cellular signal transduction pathways because it possesses a flexible coordination geometry which allows for binding to a range of biomolecules.⁶⁵⁻⁶⁶ Disruption of calcium homeostasis is associated with conditions such as chronic kidney disease-mineral bone disorder (CKD-MBD)⁶⁷⁻⁶⁸ and cancer.^{7, 69-70}

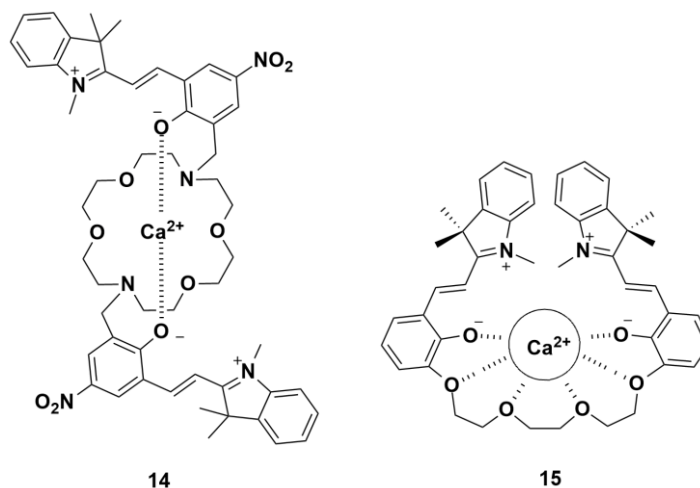


Figure 7. Ca^{2+} selective crowned bis(spirobenzopyran)s **14**⁷¹ and **15**.⁷²

Some of the earliest spiropyran-based sensors for calcium ions were the crowned bis(spirobenzopyrans),⁷¹⁻⁷² where two photoswitchable spiropyran units were attached to a central, crown ether ionophore (**14** and **15** Figure 7). Ca^{2+} binding was achieved by complexation of the ion in a crown ether ring, with additional chelation by phenolate anions from the two photoswitches when in the ring-opened, merocyanine form. While sensors composed of a single spiropyran with an azacrown ionophore at the C8 position were first reported for the detection of alkali metal ions (**10-12** Figure 5b),⁵⁰ more recent studies have confirmed a greater selectivity for divalent cations. In particular, the 1-aza-18-crown-6 analogue **12** shows selectivity for Ca^{2+} .⁷³⁻⁷⁴

We have recently developed three new, rationally designed photoswitchable spiropyran-based sensors for Ca^{2+} with reversible metal ion binding (**16-18**, Figure 8).³² The 1-aza-18-crown-6 moiety at the C8 position of the benzopyran ring imparts selectivity for Ca^{2+} over other biologically relevant metal ions, while functionalisation with methyl (**16**), hydroxyethyl (**17**) and butanoate (**18**) substituents at the N1-indole serves to further define metal ion binding and selectivity. Sensors **16** and **17** also possess an aryl carboxylate to increase hydrophilicity, as required for biological applications.

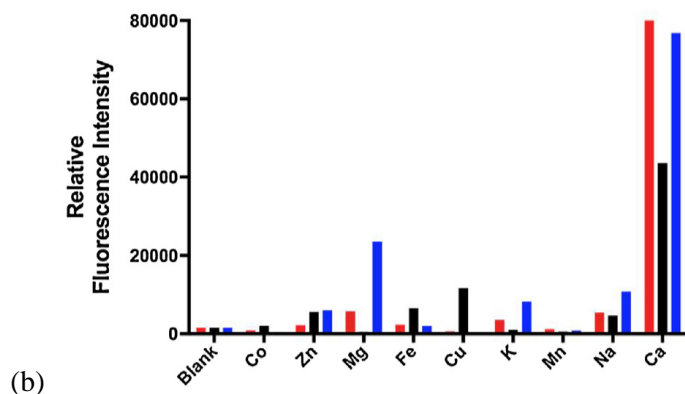
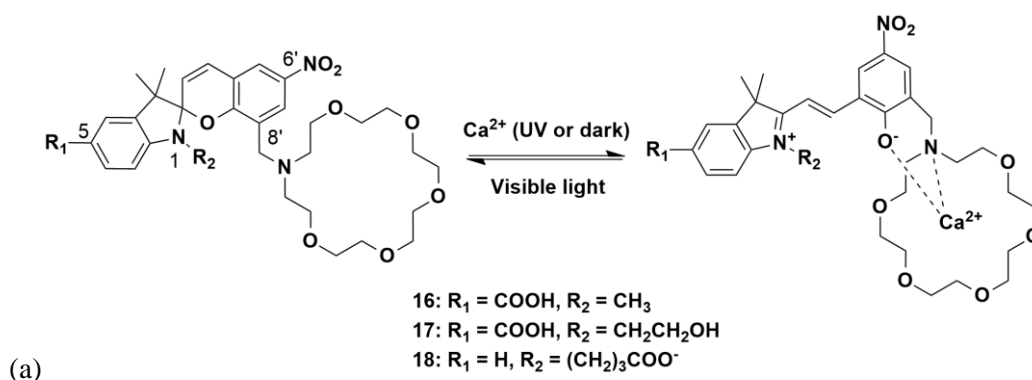


Figure 8. a) Isomeric structures of the Ca^{2+} sensor analogues **16-18**.³² The ring-closed spiropyran isomer is weakly fluorescent (SP, ‘OFF’). The ring-opened Ca^{2+} -induced merocyanine isomer is highly fluorescent (MC- Ca^{2+} , ‘ON’). (b) Fluorescence selectivity profile (where $\lambda_{\text{ex}} = 532 \text{ nm}$, $\sim \lambda_{\text{em}} = 630 \text{ nm}$) of **16** (50 μM , red), **17** (50 μM , black) and **18** (50 μM , blue) in the presence of various metal ions 100 μM .

Fluorescence assays of **16-18** against excess Ca^{2+} and other biologically relevant metal ions showed that while all three sensors gave rise to strong fluorescence in the presence of Ca^{2+} ($\sim \lambda_{\text{em}} 630 \text{ nm}$), only **16** showed high selectivity for Ca^{2+} over other ions assayed (Figure 8b). Sensor **17** showed some selectivity for Fe^{2+} , Cu^{2+} , Na^+ and Zn^{2+} , while **18** displayed moderate selectivity for Mg^{2+} , K^+ , Na^+ and Zn^{2+} . This selectivity trend is consistent with the sensor design, since the hydroxyethyl (**17**) and butanoate (**18**) groups were expected to provide an additional chelating site for metal ion binding. Cell-based validation of **16-18** in HEK 293 cells showed that sensor fluorescence is proportional to the amount of free Ca^{2+} within the cells (Figure 9a). Importantly, imaging via confocal microscopy confirmed that the observed red fluorescence intensity for **16** in the presence of Ca^{2+} was higher than **17** and **18**, in line with previous solution-based studies (Figure 9b).

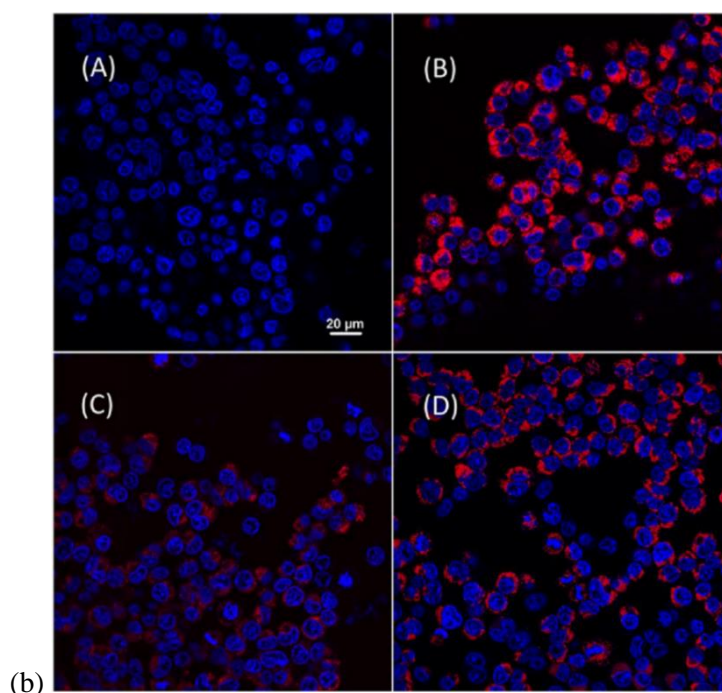
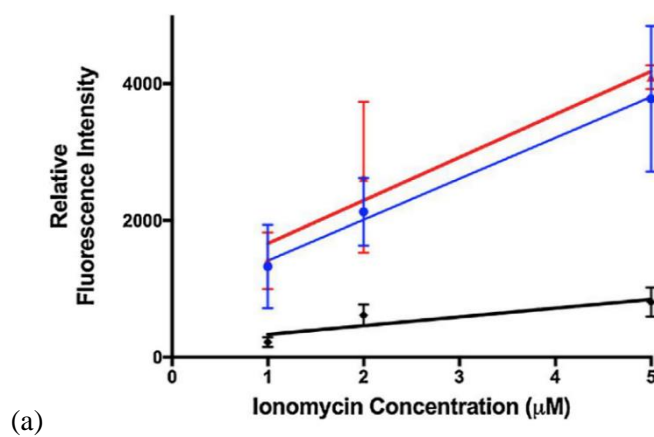


Figure 9. (a) Fluorescence emission ($\lambda_{\text{ex}} = 532 \text{ nm}$) of **16** (red), **17** (blue) and **18** (black) in the presence of HEK 293 cells treated with 1, 2 and 5 μM ionomycin. (b) Confocal microscopy images ($\lambda_{\text{ex}} = 559 \text{ nm}$ green laser) of HEK 293 cells treated with ionomycin (5 μM), Hoechst 33258 (10 μg) and (A) No sensor; (B) **16** (40 μM); (C) **17** (40 μM); (D) compound **18** (40 μM). Fluorescence is generated from the sensor (red) and from the Hoechst stain (blue).

In the final part of the study, the most selective sensor, **16**, was characterised using a microstructured optical fibre (MOF),⁵¹ as a first step towards developing a highly sensitive Ca^{2+} sensing platform for use in biological samples. With this in mind, one end of the MOF was dipped into solutions containing **16** premixed with 100 nM of Ca^{2+} , where approximately 0.1 nL of the solution was drawn into the air holes of the fibre by capillary action. Fluorescence of the sample was measured according to the setup described in Figure 6c, following irradiation with a 532 nm green laser to excite the resultant **16**(MC)- Ca^{2+} complex (Figure 10a). An approximate 1.5 – 2-fold increase in fluorescence intensity was

detected, a significant result given that the same concentration of Ca^{2+} was not detectable via plate reader experiments. Photoswitching between the **16**(MC)- Ca^{2+} complex and the weakly fluorescent SP isomer was also carried out in order to determine the reversibility and photostability of **16** under high intensity laser conditions broadly found within optical fibre-based systems. Subsequent irradiation of the MOF with UV (365 nm) and visible light (532 nm green laser), repeated over 50 cycles, resulted in the photoswitching profile displayed in Figure 10b. The results revealed that fluorescence intensities of the **16**(MC)- Ca^{2+} ‘ON’ complex decreased rapidly within the first 20 experimental cycles, falling to approximately 50% of the initial recorded fluorescence intensity but reached a promising steady-state between ‘ON’ and ‘OFF’ cycles after 20 photo-irradiations. This work demonstrates that the photoswitching and hence detection of Ca^{2+} can be controlled by irradiation with light of a specific wavelength, both in solution, within cells and integrated within a MOF platform.

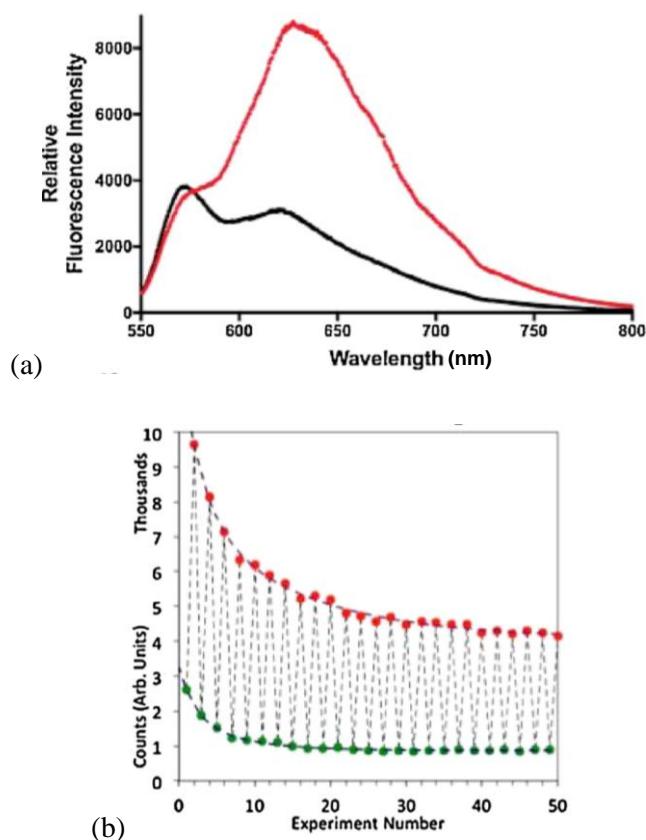


Figure 10. (a) Fibre-based fluorescence spectra of **16** in the absence (black) and presence of 100 nM Ca^{2+} (red). (b) Photoswitching between the **16**(MC)- Ca^{2+} complex (‘ON’ state, red) and the **16**(SP) isomer (‘OFF’ state, green) of the sensor using the fibre-based setup.

Sensors for Zinc (Zn^{2+})

Zinc is an essential trace element in biology and plays critical roles in a range of cellular processes such as antioxidant enzyme activity, DNA structural integrity, oocyte maturation, and fertilization.⁷⁵⁻⁷⁷ While most cellular zinc occurs as a structural component of proteins, there are pools of free Zn^{2+} in organs such as the brain,⁷⁸⁻⁷⁹ pancreas⁸⁰⁻⁸¹ and prostate.⁸²⁻⁸³ As such, disruption of zinc homeostasis is associated with numerous disease states including Alzheimer's,⁸⁴⁻⁸⁶ diabetes,⁸⁷⁻⁸⁸ and a range of cancers.^{8, 89-91}

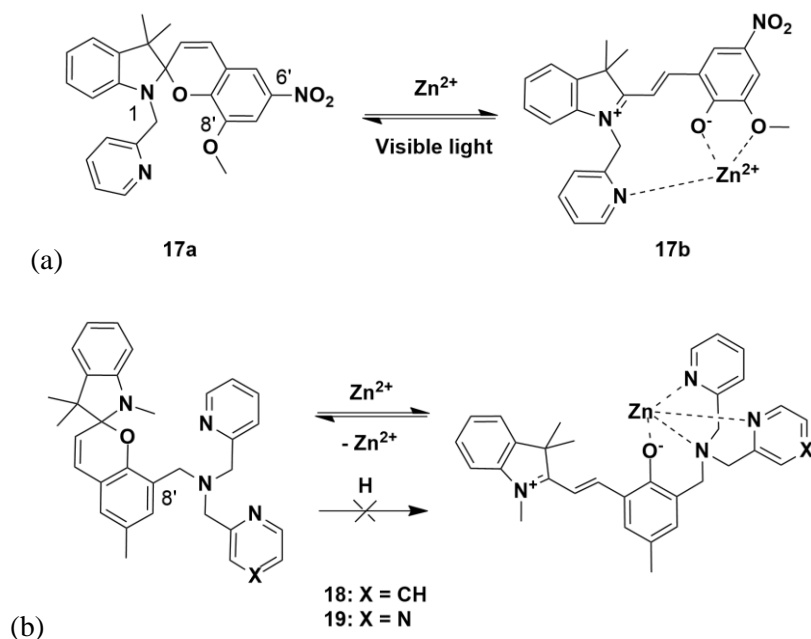


Figure 11. Zn^{2+} selective spiropyran-based sensors with the methylpyridinyl functionality. (a) The sensor presented by Natali *et al*, labelled as **17a** and **17b**⁹² and (b) the sensors presented by Rivera-Fuentes *et al*, labelled as **18** and **19**.³³⁻³⁴

One of the first Zn^{2+} selective spiropyran-based sensors (**17**, Figure 11a), was developed by Natali *et al*.⁹² The sensor is functionalised with a C8 methoxy group, which is known to chelate metal ions cooperatively with the phenolate anion of the ring-opened merocyanine isomer.⁹³⁻⁹⁶ A methyl pyridinyl was also incorporated at the N1-indole, as this group has been reported to be the chelating moiety of several Zn^{2+} -selected sensing systems.⁹⁷ The authors hypothesised that in the merocyanine isomer, the pyridine lone pair would be in close proximity to the phenolate anion and methoxy oxygen, thus producing a potentially selective, tridentate metal ion chelation site (see **17b**, Figure 11a). Metal binding experiments with **17** in the presence of Zn^{2+} and other biologically relevant metal ions revealed Zn^{2+} absorbance selectivity (λ_{abs} 504 nm) and fluorescence selectivity (λ_{em} 624 nm), consistent with formation of the **17(MC)**- Zn^{2+} complex. A strong preference for Zn^{2+} was also observed for **17** in competitive binding experiments, where multiple metal ions were

present, and absorbance-based photoswitching experiments confirmed reversibility of the **17**(MC)-Zn²⁺ complex/**17**(SP) isomer transition. Finally, ¹H NMR analysis of **17** in the presence of Zn²⁺ confirmed that all three potential coordinating sites on the spiropyran (methoxy, phenolate, pyridine) were involved with metal ion binding.

Further advancements in Zn²⁺-sensor development were reported by Rivera-Fuentes *et al.*³³ Their reversible, reaction-based sensor for the biological detection of Zn²⁺ is based on Zn²⁺-pyridine complexation with a bis(2-pyridinylmethyl)amine functionality at the C8' position of the spiropyran scaffold (labelled as **18** in Figure 11b).³³ Sensor **18** demonstrates selectivity for Zn²⁺ in aqueous solution at pH 7 and in conditions of high ionic strength, with biocompatibility of the probe demonstrated in live HeLa cells. Sensor **19** was later developed to expand on this work (Figure 11b),³⁴ where the probe detects zinc with nanomolar affinity. The red (λ_{em} 645 nm) fluorescence emission of **19** is compatible with the green-fluorescent protein, enabling multicolour imaging. To this end, the authors demonstrated that **19** responds reversibly to exogenously applied Zn²⁺ in lysosomes of HeLa cells, and to endogenous Zn²⁺ in the insulin granules of MIN6 cells and zinc-rich mossy fibre boutons in hippocampal tissue from mice.

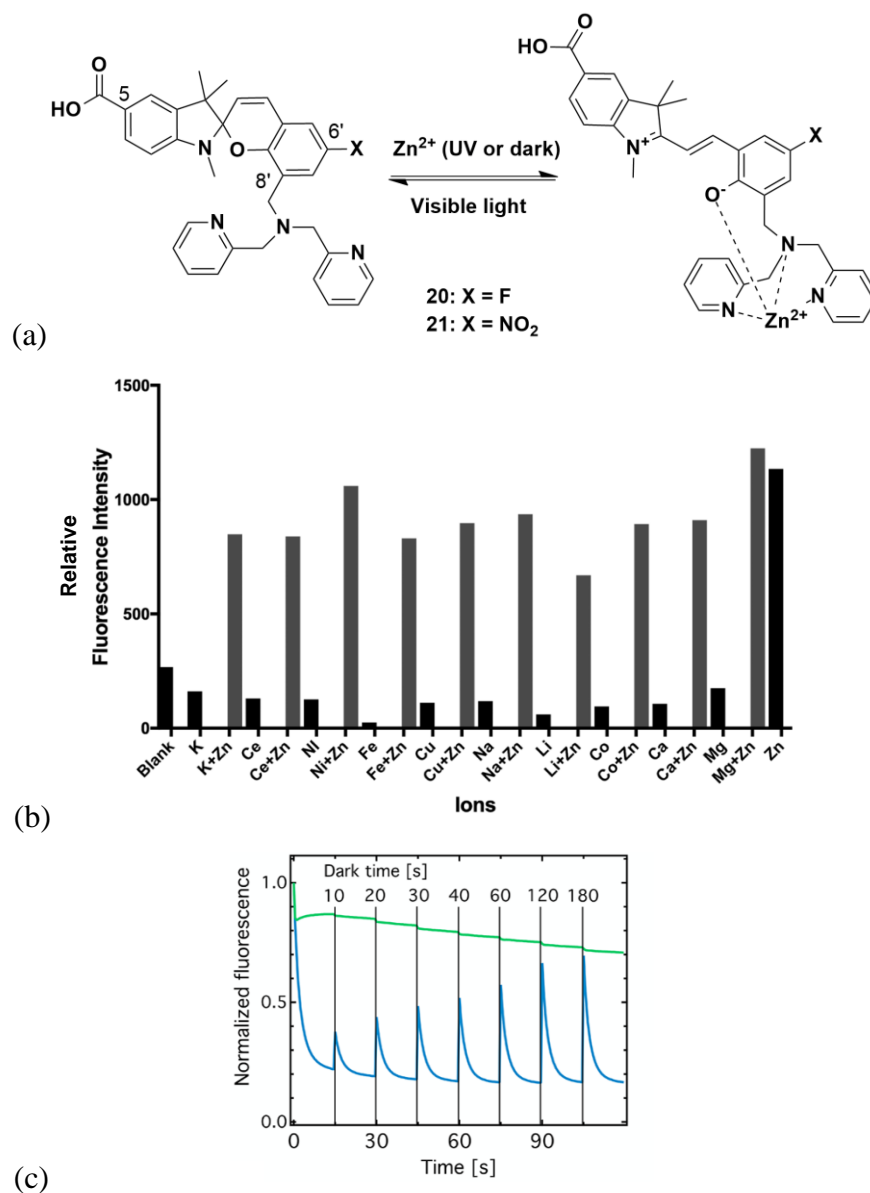


Figure 12. (a) Zn²⁺ selective spiropyran-based sensors **20** and **21**, with -NO₂ and -F functionality at the C6' position, respectively.³¹ (b) Selectivity of **20** (50 μM in water) against biologically relevant metal ions (100 μM in water). (c) Normalized fluorescence intensity as a function of time for **20** (blue) and **21** (green). Each 'ON' cycle is achieved by incubation in the dark for increasing periods of time (top axis), and each 'OFF' cycle is achieved by white light irradiation for 15s.

More recently, we reported a rationally designed a probe with a 6'-fluoro spiropyran scaffold for the reversible sensing of Zn²⁺ in biological environments (**20**, Figure 12a).³¹ Most reported spiropyran-based sensors possess a nitro group at the C6' of the benzopyran ring (see **21**, Figure 12a), as the electron withdrawing substituent imparts high quantum yields for fluorescence sensing. However, the ring-opened MC form is known to be favoured in polar solvents,⁹⁸⁻¹⁰⁰ which results in high background fluorescence and poor signal-to-noise ratio even in the absence of substrates, thus limiting sensitivity in sensor-based applications.

The introduction of an electron donating group such as t-butyl¹⁰¹ or methyl³⁴ renders the photochromic properties of spiropyran less susceptible to solvent effects, however such analogues lack solubility in water and display significantly lower quantum yields with the loss of switching efficiency.¹⁰² The 6'-fluoro substituent of sensor **20** overcomes several of these limitations to provide an improved signal-to-background ratio and faster photoswitching times in aqueous solution. A C8' bis(2-pyridylmethyl)amine substituent was incorporated into the spiropyran scaffold of **20** to promote binding of Zn²⁺ to the ring-opened MC form (depicted in Figure 12a), while a C5 aryl carboxylate was included for increased hydrophilicity as required for biological applications.

Spectroscopic analyses of sensor **20** and the C6'-nitro analogue **21** were performed in order to define the relative influence of the C6' substituent on Zn²⁺ binding. Absorbance spectra for **20** and **21** were essentially identical, with a uniform 10-fold increase in absorbance intensity between 510 – 535 nm in the presence of Zn²⁺ compared to spectra in the absence of metal ion. The fluorescence emission maximum for **20** (λ_{em} 670 nm) was found to be significantly red-shifted compared to **21** (λ_{em} 615 nm), an advantage for biological sensing as cellular autofluorescence is minimalised at these longer wavelengths.³³ Competitive fluorescence binding experiments of **20** showed a high selectivity for zinc in the presence of other biologically relevant metal ions (Figure 12b), in agreement with previous studies of **21**.¹⁰³ As expected, the quantum yield of **20** was found to be 10-fold lower than that of **21**, which is consistent with the more moderately electron donating nature of the C6'-fluoro substituent. Photoswitching between the MC-Zn²⁺ complexes and the SP isomers of sensors **20** and **21** was next studied in 20 μ m deep wells of a microscope slide, with the fluorescence measured using a modified commercial fluorescence microscope. As shown in Figure 12c, sensor **20** (blue line) showed clear photoswitching over the time course of the experiment, without any apparent signs of photobleaching. Comparatively, multiple cycles of irradiation did not give rise to photoswitching for **21** (green line), with a decrease in fluorescence over time, presumably due to photobleaching.

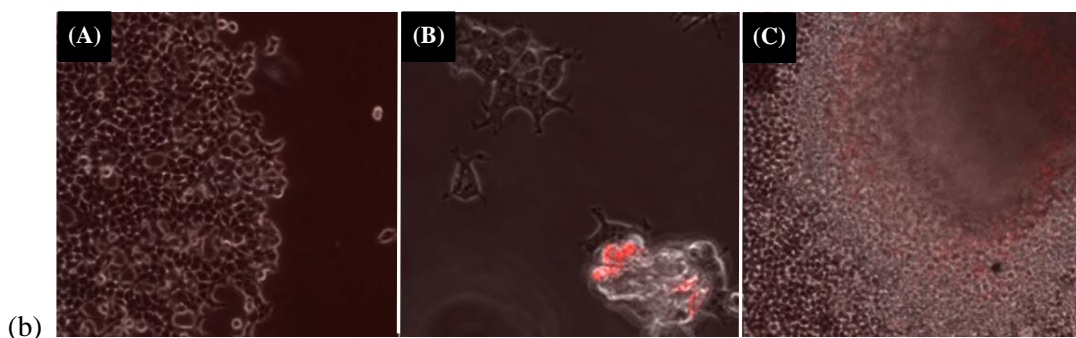
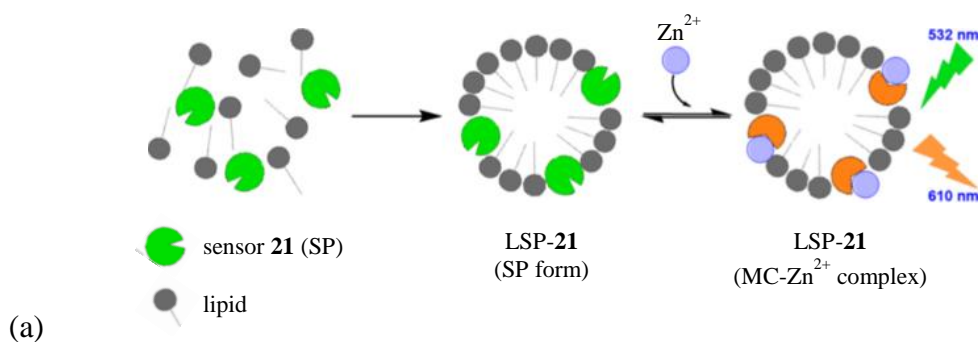


Figure 13. (a) A Zn^{2+} sensing spiropyran, **21**, embedded within the surface of a liposome derived from *Escherichia coli* lipids to generate a new, biologically compatible Zn^{2+} sensor (LSP-**21**).¹⁰³ (b) Confocal microscope images of LSP-**21** (8 μ L) incubated overnight at 37°C with HEK 293 cells; (A) image of LSP-**21** with healthy cells; (B, C) images of LSP-**21** with dying cells where Zn^{2+} efflux was detected.

Finally, improved biocompatibility of spiropyran-based zinc sensors can be achieved by embedding a Zn^{2+} sensing spiropyran, **21** (Figure 12a), within the surface of a liposome derived from *Escherichia coli* lipids (LSP-**21**, Figure 13a).¹⁰³ Solution-based fluorescence experiments indicate that LSP-**21** demonstrates improved aqueous solubility and Zn^{2+} sensitivity compared to the spiropyran sensor alone. HEK 293 cells were then used in biological validation of LSP-**21**, where the detection of Zn^{2+} efflux from dying cells suggests that sensing is localized near the cell surface membrane (Figure 13b). Fibre-based photoswitching experiments with a pre-mixed solution of LSP-**21** and Zn^{2+} taken up into the pores of a MOF show 100 μ M detection of the metal ion, with highly reproducible photoswitching and minimal photobleaching. This work represents a general method whereby existing spiropyran-based metal ion sensors can be made more biologically compatible, with applications in both cellular sensing and nanoscale sample-volume dip sensing.

1.3 Outline of Thesis

This thesis describes the functionalisation of spiropyran in order to improve fluorescence intensity (**Chapter 2**), develop selective metal ion sensors (**Chapter 3**) and investigate structure-metal ion selectivity relationships (**Chapter 4**).

Chapter 2 presents a unique approach to Ca^{2+} sensing with a rationally designed sensor which possesses all the desirable characteristics (brightness, photostability, red fluorescence emission) of both the traditional and spiropyran-based sensor. The synthesis, solution-based photophysical characterisation and optical fibre-based photostability of this photoswitchable pyrene-spiropyran hybrid are reported.

Chapter 3 details the development of the first rationally designed, spiropyran-based fluorescent Mg^{2+} sensors. DFT modelling in support of the sensor design, synthesis and solution-based photophysical characterisation are reported. Optical fibre-based photoswitching and photostability studies are presented, as a first step towards the development of a light-controlled, reversible dip-sensor for Mg^{2+} .

Chapter 4 explores the effects on metal ion selectivity for spiropyran-based sensors with different functional groups at the N1-indole position. The sensors presented possess a 1-aza-15-crown-5 ionophore at the C8' position, and N1-indole functionality in the form of hydroxyethyl, ethyl butanoate or butanoic acid groups. The rational design, synthesis and photophysical characterisation of these sensors are reported.

Chapter 5 contains the Supporting Information associated with research Chapters 2-4, detailing the experimental conditions, chemical syntheses, and characterisation spectra of the reported sensors.

In **Appendix A**, a sensor described in **Chapter 4** was utilized for a collaborative biological application, to study lithium 'hot-spots' in living colon cancer cells. Results pertaining to intracellular Li^{+} -binding and photoswitching of the sensor in living cells are presented.

Finally, **Appendix B** describes a different approach to biological sensing, targeted towards sensing of analytes in biological media. Here we describe fundamental surface-engineering strategies in nanoporous materials, and the effects of combined surface-functionalisation techniques, towards the development of optical-sensing systems with increased sensitivity.

1.4 References

1. Breydo, L.; Uversky, V. N., Role of metal ions in aggregation of intrinsically disordered proteins in neurodegenerative diseases. *Metallomics* **2011**, *3* (11), 1163-1180.
2. Lee, H. J.; Korshavn, K. J.; Kochi, A.; Derrick, J. S.; Lim, M. H., Cholesterol and metal ions in Alzheimer's disease. *Chemical Society Reviews* **2014**, *43* (19), 6672-6682.
3. Sarrafzadegan, N.; Khosravi-Boroujeni, H.; Lotfizadeh, M.; Pourmogaddas, A.; Salehi-Abargouei, A., Magnesium status and the metabolic syndrome: A systematic review and meta-analysis. *Nutrition* **2016**, *32* (4), 409-417.
4. Mooren, F. C., Magnesium and disturbances in carbohydrate metabolism. *Diabetes, Obesity and Metabolism* **2015**, *17* (9), 813-823.
5. Ranasinghe, P.; Pigera, S.; Galappatthy, P.; Katulanda, P.; Constantine, G. R., Zinc and diabetes mellitus: understanding molecular mechanisms and clinical implications. *DARU Journal of Pharmaceutical Sciences* **2015**, *23* (1), 44.
6. Theophanides, T.; Anastassopoulou, J., The effects of metal ion contaminants on the double stranded DNA helix and diseases. *Journal of Environmental Science and Health, Part A* **2017**, *52* (10), 1030-1040.
7. Dorota, S.; Barbara, B.-K.; Andrzej, T., Disorders of Mechanisms of Calcium Metabolism Control as Potential Risk Factors of Prostate Cancer. *Current Medicinal Chemistry* **2017**, *24* (38), 4229-4244.
8. Kolenko, V.; Teper, E.; Kutikov, A.; Uzzo, R., Zinc and zinc transporters in prostate carcinogenesis. *Nature reviews. Urology* **2013**, *10* (4), 219-226.
9. Carter, K. P.; Young, A. M.; Palmer, A. E., Fluorescent Sensors for Measuring Metal Ions in Living Systems. *Chemical Reviews* **2014**, *114* (8), 4564-4601.
10. Qian, X.; Xu, Z., Fluorescence imaging of metal ions implicated in diseases. *Chemical Society Reviews* **2015**, *44* (14), 4487-4493.
11. Dean, K. M.; Qin, Y.; Palmer, A. E., Visualizing metal ions in cells: An overview of analytical techniques, approaches, and probes. *Biochimica et Biophysica Acta (BBA) - Molecular Cell Research* **2012**, *1823* (9), 1406-1415.
12. Lakowicz, J. R., *Principles of fluorescence spectroscopy*. 3rd ed.; Springer: New York, 2006; p xxvi, 954 p.
13. *The Molecular Probes™ Handbook - A Guide to Fluorescent Probes and Labeling Technologies*. 11th ed.; Invitrogen™ by Thermo Fisher Scientific: 2010; p 975.
14. Lavis, L. D.; Raines, R. T., Bright building blocks for chemical biology. *ACS chemical biology* **2014**, *9* (4), 855-66.
15. Domaille, D. W.; Que, E. L.; Chang, C. J., Synthetic fluorescent sensors for studying the cell biology of metals. *Nature Chemical Biology* **2008**, *4*, 168.
16. Meier, S. D.; Kovalchuk, Y.; Rose, C. R., Properties of the new fluorescent Na⁺ indicator CoroNa Green: Comparison with SBFI and confocal Na⁺ imaging. *Journal of Neuroscience Methods* **2006**, *155* (2), 251-259.
17. Ohta, T.; Imagawa, T.; Ito, S., Novel gating and sensitizing mechanism of capsaicin receptor (TRPV1): tonic inhibitory regulation of extracellular sodium through the external protonation sites on TRPV1. *The Journal of biological chemistry* **2008**, *283* (14), 9377-87.
18. Bender, K. J.; Trussell, L. O., Axon Initial Segment Ca²⁺ Channels Influence Action Potential Generation and Timing. *Neuron* **2009**, *61* (2), 259-271.

19. Tu, P.; Kunert-Keil, C.; Lucke, S.; Brinkmeier, H.; Bouron, A., Diacylglycerol analogues activate second messenger-operated calcium channels exhibiting TRPC-like properties in cortical neurons. *Journal of Neurochemistry* **2009**, *108* (1), 126-138.
20. Sensi, S. L.; Ton-That, D.; Weiss, J. H.; Rothe, A.; Gee, K. R., A new mitochondrial fluorescent zinc sensor. *Cell Calcium* **2003**, *34* (3), 281-284.
21. Bonanni, L.; Chachar, M.; Jover-Mengual, T.; Li, H.; Jones, A.; Yokota, H.; Ofengeim, D.; Flannery, R. J.; Miyawaki, T.; Cho, C.-H.; Polster, B. M.; Pypaert, M.; Hardwick, J. M.; Sensi, S. L.; Zukin, R. S.; Jonas, E. A., Zinc-Dependent Multi-Conductance Channel Activity in Mitochondria Isolated from Ischemic Brain. *The Journal of Neuroscience* **2006**, *26* (25), 6851-6862.
22. Sensi, S. L.; Ton-That, D.; Sullivan, P. G.; Jonas, E. A.; Gee, K. R.; Kaczmarek, L. K.; Weiss, J. H., Modulation of mitochondrial function by endogenous Zn(2+) pools. *Proceedings of the National Academy of Sciences of the United States of America* **2003**, *100* (10), 6157-6162.
23. Monici, M., Cell and tissue autofluorescence research and diagnostic applications. In *Biotechnology Annual Review*, Elsevier: 2005; Vol. 11, pp 227-256.
24. Andersson; Baechli; Hoechl; Richter, Autofluorescence of living cells. *Journal of Microscopy* **1998**, *191* (1), 1-7.
25. Zipfel, W. R.; Williams, R. M.; Christie, R.; Nikitin, A. Y.; Hyman, B. T.; Webb, W. W., Live tissue intrinsic emission microscopy using multiphoton-excited native fluorescence and second harmonic generation. *Proceedings of the National Academy of Sciences of the United States of America* **2003**, *100* (12), 7075-7080.
26. Tsien, R. Y., A non-disruptive technique for loading calcium buffers and indicators into cells. *Nature* **1981**, *290*, 527.
27. Crichton, R. R., *Biological Inorganic Chemistry: A New Introduction to Molecular Structure and Function*. 2nd ed.; Elsevier: Oxford, 2012; p 460.
28. Natali, M.; Giordani, S., Molecular switches as photocontrollable "smart" receptors. *Chemical Society Reviews* **2012**, *41* (10), 4010-4029.
29. Klajn, R., Spiropyran-based dynamic materials. *Chemical Society Reviews* **2014**, *43* (1), 148-184.
30. Kolmakov, K.; Belov, V. N.; Bierwagen, J.; Ringemann, C.; Müller, V.; Eggeling, C.; Hell, S. W., Red-Emitting Rhodamine Dyes for Fluorescence Microscopy and Nanoscopy. *Chemistry – A European Journal* **2010**, *16* (1), 158-166.
31. Heng, S.; Reineck, P.; Vidanapathirana, A. K.; Pullen, B. J.; Drumm, D. W.; Ritter, L. J.; Schwarz, N.; Bonder, C. S.; Psaltis, P. J.; Thompson, J. G.; Gibson, B. C.; Nicholls, S. J.; Abell, A. D., Rationally Designed Probe for Reversible Sensing of Zinc and Application in Cells. *ACS Omega* **2017**, *2* (9).
32. Heng, S.; Mak, A. M.; Kosteki, R.; Zhang, X.; Pei, J.; Stubing, D. B.; Ebendorff-Heidepriem, H.; Abell, A. D., Photoswitchable calcium sensor: 'On'-'Off' sensing in cells or with microstructured optical fibers. *Sensors and Actuators B: Chemical* **2017**, *252*, 965-972.
33. Rivera-Fuentes, P.; Lippard, S. J., SpiroZin1: A Reversible and pH-Insensitive, Reaction-based, Red-fluorescent Probe for Imaging Biological Mobile Zinc. *ChemMedChem* **2014**, *9* (6), 1238-1243.
34. Rivera-Fuentes, P.; Wrobel, A. T.; Zastrow, M. L.; Khan, M.; Georgiou, J.; Luyben, T. T.; Roder, J. C.; Okamoto, K.; Lippard, S. J., A far-red emitting probe for unambiguous detection of mobile zinc in acidic vesicles and deep tissue. *Chemical Science* **2015**, *6* (3), 1944-1948.

35. Baldrighi, M.; Locatelli, G.; Desper, J.; Aakeröy, C. B.; Giordani, S., Probing Metal Ion Complexation of Ligands with Multiple Metal Binding Sites: The Case of Spiropyran. *Chemistry (Weinheim an der Bergstrasse, Germany)* **2016**, *22* (39), 13976-13984.
36. Tanaka, M.; Kamada, K.; Ando, H.; Kitagaki, T.; Shibutani, Y.; Yajima, S.; Sakamoto, H.; Kimura, K., Metal-ion stabilization of photoinduced open colored isomer in crowned spirobenzothiapyran. *Chemical Communications* **1999**, (16), 1453-1454.
37. Zakharova, M. I.; Pimienta, V.; Metelitsa, A. V.; Minkin, V. I.; Micheau, J. C., Thermodynamic and kinetic analysis of metal ion complexation by photochromic spiropyran. *Russian Chemical Bulletin* **2009**, *58* (7), 1329-1337.
38. T.C. Wojtyk, J.; Buncel, E.; M. Kazmaier, P., Effects of metal ion complexation on the spiropyran-merocyanine interconversion: development of a thermally stable photo-switch. *Chemical Communications* **1998**, (16), 1703-1704.
39. E. Collins, G.; Choi, L.-S.; J. Ewing, K.; Michelet, V.; M. Bowen, C.; D. Winkler, J., Photoinduced switching of metal complexation by quinolinospiropyranindolines in polar solvents. *Chemical Communications* **1999**, (4), 321-322.
40. Salhin, Abdussalam M. A.; Tanaka, M.; Kamada, K.; Ando, H.; Ikeda, T.; Shibutani, Y.; Yajima, S.; Nakamura, M.; Kimura, K., Decisive Factors in the Photoisomerisation Behavior of Crowned Spirobenzopyrans: Metal Ion Interaction with Crown Ether and Phenolate Anion Moieties. *European Journal of Organic Chemistry* **2002**, *2002* (4), 655-662.
41. Yin, J.; Hu, Y.; Yoon, J., Fluorescent probes and bioimaging: alkali metals, alkaline earth metals and pH. *Chemical Society Reviews* **2015**, *44* (14), 4619-4644.
42. Clausen, M. J. V.; Poulsen, H., Sodium/Potassium Homeostasis in the Cell. In *Metallomics and the Cell*, Banci, L., Ed. Springer Netherlands: Dordrecht, 2013; pp 41-67.
43. Crichton, R. R., Chapter 9 - Sodium and Potassium – Channels and Pumps. In *Biological Inorganic Chemistry: A New Introduction to Molecular Structure and Function*, 2nd ed.; Elsevier: Oxford, 2012; pp 177-195.
44. Alda, M., Lithium in the treatment of bipolar disorder: pharmacology and pharmacogenetics. *Mol Psychiatry* **2015**, *20* (6), 661-70.
45. Tobe, B. T. D. *et al*, Probing the lithium-response pathway in hiPSCs implicates the phosphoregulatory set-point for a cytoskeletal modulator in bipolar pathogenesis. *Proceedings of the National Academy of Sciences* **2017**, *114* (22), E4462-E4471.
46. de Leon, J., A Practitioner's Guide to Prescribing Lithium for Adults with Intellectual Disabilities. In *A Practitioner's Guide to Prescribing Antiepileptics and Mood Stabilizers for Adults with Intellectual Disabilities*, de Leon, J., Ed. Springer US: Boston, MA, 2012; pp 207-234.
47. Zarse, K.; Terao, T.; Tian, J.; Iwata, N.; Ishii, N.; Ristow, M., Low-dose lithium uptake promotes longevity in humans and metazoans. *European Journal of Nutrition* **2011**, *50* (5), 387-389.
48. Inouye, M.; Ueno, M.; Kitao, T.; Tsuchiya, K., Alkali metal recognition induced isomerization of spiropyran. *Journal of the American Chemical Society* **1990**, *112* (24), 8977-8979.
49. Inouye, M.; Ueno, M.; Tsuchiya, K.; Nakayama, N.; Konishi, T.; Kitao, T., Alkali-metal cation recognition induced isomerization of spirobenzopyrans and spironaphthoxazines possessing a crown ring as a recognition site: multifunctional artificial receptors. *The Journal of Organic Chemistry* **1992**, *57* (20), 5377-5383.

50. Kimura, K.; Yamashita, T.; Yokoyama, M., Syntheses, cation complexation, isomerization and photochemical cation-binding control of spirobenzopyrans carrying a monoazacrown moiety at the 8-position. *Journal of the Chemical Society, Perkin Transactions 2* **1992**, (4), 613-619.
51. Heng, S.; Nguyen, M.-C.; KostECKI, R.; Monroe, T. M.; Abell, A. D., Nanoliter-scale, regenerable ion sensor: sensing with a surface functionalized microstructured optical fibre. *Rsc Adv* **2013**, 3 (22), 8308-8317.
52. Monroe, T. M.; Belardi, W.; Furusawa, K.; Baggett, J. C.; Broderick, N. G. R.; Richardson, D. J., Sensing with microstructured optical fibres. *Measurement Science and Technology* **2001**, 12 (7), 854.
53. Monroe, T. M.; Warren-Smith, S.; Schartner, E. P.; François, A.; Heng, S.; Ebendorff-Heidepriem, H.; Afshar, S., Sensing with suspended-core optical fibers. *Optical Fiber Technology* **2010**, 16 (6), 343-356.
54. Schartner, E. P.; Henderson, M. R.; Purdey, M.; Dhattrak, D.; Monroe, T. M.; Gill, P. G.; Callen, D. F., Cancer Detection in Human Tissue Samples Using a Fiber-Tip pH Probe. *Cancer Res* **2016**, 76 (23), 6795-6801.
55. Purdey, M. S.; Schartner, E. P.; Sutton-McDowall, M. L.; Ritter, L. J.; Thompson, J.; Monroe, T. M.; Abell, A. D. In *Localised hydrogen peroxide sensing for reproductive health*, SPIE Optics + Optoelectronics, SPIE: 2015; p 10.
56. Ebendorff-Heidepriem, H.; Warren-Smith, S. C.; Monroe, T. M., Suspended nanowires: Fabrication, design and characterization of fibers with nanoscale cores. *Opt. Express* **2009**, 17 (4), 2646-2657.
57. KostECKI, R.; Ebendorff-Heidepriem, H.; Davis, C.; McAdam, G.; Warren-Smith, S. C.; Monroe, T. M., Silica exposed-core microstructured optical fibers. *Opt. Mater. Express* **2012**, 2 (11), 1538-1547.
58. Kubodera, S.; Wisoff, P. J. K.; Tittel, F. K.; Sauerbrey, R. A., Coupling of high-power UV laser radiation into fused silica fibers using pressurized gases. *Appl. Opt.* **1988**, 27 (9), 1638-1640.
59. Kawamura, K., In situ UV-VIS Detection of Hydrothermal Reactions Using Fused-Silica Capillary Tubing within 0.08 - 3.2 s at High Temperatures. *Analytical Sciences* **2002**, 18 (6), 715-716.
60. Clapham, D. E., Calcium Signaling. *Cell* **2007**, 131 (6), 1047-1058.
61. Berridge, M. J.; Lipp, P.; Bootman, M. D., The versatility and universality of calcium signalling. *Nature Reviews Molecular Cell Biology* **2000**, 1, 11.
62. Bhosale, G.; Sharpe, J. A.; Sundier, S. Y.; Duchen, M. R., Calcium signaling as a mediator of cell energy demand and a trigger to cell death. *Annals of the New York Academy of Sciences* **2015**, 1350 (1), 107-116.
63. Tonelli, F. M. P.; Santos, A. K.; Gomes, D. A.; da Silva, S. L.; Gomes, K. N.; Ladeira, L. O.; Resende, R. R., Stem Cells and Calcium Signaling. *Advances in experimental medicine and biology* **2012**, 740, 891-916.
64. Brini, M.; Carafoli, E., Calcium Pumps in Health and Disease. *Physiological Reviews* **2009**, 89 (4), 1341-1378.
65. Brini, M.; Ottolini, D.; Calì, T.; Carafoli, E., Calcium in Health and Disease. In *Interrelations between Essential Metal Ions and Human Diseases*, Sigel, A.; Sigel, H.; Sigel, R. K. O., Eds. Springer Netherlands: Dordrecht, 2013; pp 81-137.
66. Brini, M.; Calì, T.; Ottolini, D.; Carafoli, E., Intracellular Calcium Homeostasis and Signaling. In *Metallomics and the Cell*, Banci, L., Ed. Springer Netherlands: Dordrecht, 2013; pp 119-168.

67. Peacock, M., Calcium metabolism in health and disease. *Clinical journal of the American Society of Nephrology : CJASN* **2010**, *5 Suppl 1*, S23-30.
68. Felsenfeld, A. J.; Levine, B. S.; Rodriguez, M., Pathophysiology of Calcium, Phosphorus, and Magnesium Dysregulation in Chronic Kidney Disease. *Seminars in Dialysis* **2015**, *28* (6), 564-577.
69. Stewart, T. A.; Yapa, K. T. D. S.; Monteith, G. R., Altered calcium signaling in cancer cells. *Biochimica et Biophysica Acta (BBA) - Biomembranes* **2015**, *1848* (10, Part B), 2502-2511.
70. Marchi, S.; Pinton, P., Alterations of calcium homeostasis in cancer cells. *Current Opinion in Pharmacology* **2016**, *29*, 1-6.
71. Kimura, K.; Teranishi, T.; Yokoyama, M., Highly calcium-ion-accelerated coloration of bis(spirobenzopyran) bridged by diaza-18-crown-6 moiety at the 8-position. *Supramolecular Chemistry* **1996**, *7* (1), 11-13.
72. Yagi, S.; Nakamura, S.; Watanabe, D.; Nakazumi, H., Colorimetric sensing of metal ions by bis(spiropyran) podands: Towards naked-eye detection of alkaline earth metal ions. *Dyes and Pigments* **2009**, *80* (1), 98-105.
73. Kimura, K.; Teranishi, T.; Yokoyama, M.; Yajima, S.; Miyake, S.; Sakamoto, H.; Tanaka, M., Cation complexation, isomerization, and photoresponsive ionic conduction of a crown ether derivative carrying two spirobenzopyran units. *Journal of the Chemical Society, Perkin Transactions 2* **1999**, (2), 199-204.
74. Kimura, K.; Sakamoto, H.; Kado, S.; Arakawa, R.; Yokoyama, M., Studies on metal-ion complex formation of crown ether derivatives incorporating a photoionizable spirobenzopyran moiety by electrospray ionization mass spectrometry. *Analyst* **2000**, *125* (6), 1091-1095.
75. Maret, W., Zinc and the Zinc Proteome. In *Metallomics and the Cell*, Banci, L., Ed. Springer Netherlands: Dordrecht, 2013; pp 479-501.
76. Crichton, R. R., Zinc – Lewis Acid and Gene Regulator. In *Biological Inorganic Chemistry: A New Introduction to Molecular Structure and Function*, 2nd ed.; Elsevier: Oxford, 2012; pp 229-246.
77. Kim, A. M.; Bernhardt, M. L.; Kong, B. Y.; Ahn, R. W.; Vogt, S.; Woodruff, T. K.; O'Halloran, T. V., Zinc sparks are triggered by fertilization and facilitate cell cycle resumption in mammalian eggs. *ACS chemical biology* **2011**, *6* (7), 716-723.
78. Frederickson, C. J.; Koh, J.-Y.; Bush, A. I., The neurobiology of zinc in health and disease. *Nature Reviews Neuroscience* **2005**, *6*, 449.
79. Takeda, A.; Nakamura, M.; Fujii, H.; Tamano, H., Synaptic Zn²⁺ homeostasis and its significance. *Metallomics* **2013**, *5* (5), 417-423.
80. Taylor, C. G., Zinc, the Pancreas, and Diabetes: Insights from Rodent Studies and Future Directions. *Biometals* **2005**, *18* (4), 305-312.
81. Maret, W., Zinc in Pancreatic Islet Biology, Insulin Sensitivity, and Diabetes. *Preventive Nutrition and Food Science* **2017**, *22* (1), 1-8.
82. Costello, L. C.; Franklin, R. B., A comprehensive review of the role of zinc in normal prostate function and metabolism; and its implications in prostate cancer. *Archives of biochemistry and biophysics* **2016**, *611*, 100-112.
83. Franklin, R. B.; Milon, B.; Feng, P.; Costello, L. C., ZINC AND ZINC TRANSPORTERS IN NORMAL PROSTATE FUNCTION AND THE PATHOGENESIS OF PROSTATE CANCER. *Frontiers in bioscience : a journal and virtual library* **2005**, *10*, 2230-2239.

84. Morris, D. R.; Levenson, C. W., Neurotoxicity of Zinc. In *Neurotoxicity of Metals*, Aschner, M.; Costa, L. G., Eds. Springer International Publishing: Cham, 2017; pp 303-312.
85. Wang, C.-Y.; Wang, T.; Zheng, W.; Zhao, B.-L.; Danscher, G.; Chen, Y.-H.; Wang, Z.-Y., Zinc Overload Enhances APP Cleavage and A β Deposition in the Alzheimer Mouse Brain. *PLOS ONE* **2010**, *5* (12), e15349.
86. Maynard, C. J.; Bush, A. I.; Masters, C. L.; Cappai, R.; Li, Q.-X., Metals and amyloid- β in Alzheimer's disease. *International Journal of Experimental Pathology* **2005**, *86* (3), 147-159.
87. Jansen, J.; Karges, W.; Rink, L., Zinc and diabetes — clinical links and molecular mechanisms. *The Journal of Nutritional Biochemistry* **2009**, *20* (6), 399-417.
88. Long, A. E.; Gillespie, K. M.; Aitken, R. J.; Goode, J. C.; Bingley, P. J.; Williams, A. J. K., Humoral Responses to Islet Antigen-2 and Zinc Transporter 8 Are Attenuated in Patients Carrying HLA-A*24 Alleles at the Onset of Type 1 Diabetes. *Diabetes* **2013**, *62* (6), 2067-2071.
89. Formigari, A.; Gregianin, E.; Irato, P., The effect of zinc and the role of p53 in copper-induced cellular stress responses. *Journal of Applied Toxicology* **2013**, *33* (7), 527-536.
90. Hoang, B. X.; Han, B.; Shaw, D. G.; Nimni, M., Zinc as a possible preventive and therapeutic agent in pancreatic, prostate, and breast cancer. *European Journal of Cancer Prevention* **2016**, *25* (5), 457-461.
91. Riesop, D.; Hirner, A. V.; Rusch, P.; Bankfalvi, A., Zinc distribution within breast cancer tissue: A possible marker for histological grading? *Journal of Cancer Research and Clinical Oncology* **2015**, *141* (7), 1321-1331.
92. Natali, M.; Soldi, L.; Giordani, S., A photoswitchable Zn (II) selective spiropyran-based sensor. *Tetrahedron* **2010**, *66* (38), 7612-7617.
93. Gorner, H.; Chibisov, A. K., Complexes of spiropyran-derived merocyanines with metal ions Thermally activated and light-induced processes. *Journal of the Chemical Society, Faraday Transactions* **1998**, *94* (17), 2557-2564.
94. Chibisov, A. K.; Görner, H., Complexes of spiropyran-derived merocyanines with metal ions: relaxation kinetics, photochemistry and solvent effects. *Chemical Physics* **1998**, *237* (3), 425-442.
95. Görner, H.; Atabekyan, L. S.; Chibisov, A. K., Photoprocesses in spiropyran-derived merocyanines: singlet versus triplet pathway. *Chemical Physics Letters* **1996**, *260* (1), 59-64.
96. Chibisov, A. K.; Gorner, H., Photochromism of spirobenzopyranindolines and spironaphthopyranindolines. *Physical Chemistry Chemical Physics* **2001**, *3* (3), 424-431.
97. Kimura, E.; Aoki, S.; Kikuta, E.; Koike, T., A macrocyclic zinc(II) fluorophore as a detector of apoptosis. *Proceedings of the National Academy of Sciences* **2003**, *100* (7), 3731-3736.
98. Tian, W.; Tian, J., An insight into the solvent effect on photo-, solvato-chromism of spiropyran through the perspective of intermolecular interactions. *Dyes and Pigments* **2014**, *105*, 66-74.
99. Swansburg, S.; Buncel, E.; Lemieux, R. P., Thermal Racemization of Substituted Indolinobenzospiropyran: Evidence of Competing Polar and Nonpolar Mechanisms. *Journal of the American Chemical Society* **2000**, *122* (28), 6594-6600.

100. Shiraishi, Y.; Inoue, T.; Sumiya, S.; Hirai, T., Entropy-Driven Thermal Isomerization of Spiropyran in Viscous Media. *The Journal of Physical Chemistry A* **2011**, *115* (33), 9083-9090.
101. Shao, N.; Wang, H.; Gao, X.; Yang, R.; Chan, W., Spiropyran-Based Fluorescent Anion Probe and Its Application for Urinary Pyrophosphate Detection. *Analytical Chemistry* **2010**, *82* (11), 4628-4636.
102. Shao, N.; Jin, J.; Wang, H.; Zheng, J.; Yang, R.; Chan, W.; Abliz, Z., Design of Bis-spiropyran Ligands as Dipolar Molecule Receptors and Application to in Vivo Glutathione Fluorescent Probes. *Journal of the American Chemical Society* **2010**, *132* (2), 725-736.
103. Heng, S.; McDevitt, C. A.; Stubing, D. B.; Whittall, J. J.; Thompson, J. G.; Engler, T. K.; Abell, A. D.; Monro, T. M., Microstructured optical fibers and live cells: a water-soluble, photochromic zinc sensor. *Biomacromolecules* **2013**, *14* (10), 3376-3379.

CHAPTER 2

A spiropyran with enhanced fluorescence: A bright, photostable and red-emitting calcium sensor

Georgina M. Sylvia,¹ Sabrina Heng,¹ Akash Bachhuka,¹ Heike Ebendorff-Heidepriem¹ and Andrew D. Abell¹

¹ARC Centre of Excellence for Nanoscale BioPhotonics (CNBP), Institute for Photonics and Advanced Sensing (IPAS) and School of Physical Sciences, The University of Adelaide, South Australia, Australia 5005.

Tetrahedron, **2018**, 74(12), 1240-1244; doi:10.1016/j.tet.2017.11.020.

(Impact Factor 2016: 2.645, Ranking in Chemistry, Organic: Q2.)

Statements of Authorship

Title of Paper	A spiropyran with enhanced fluorescence: a bright, photostable and red-emitting calcium sensor.
Publication Status	<input checked="" type="checkbox"/> Published <input type="checkbox"/> Accepted for Publication <input type="checkbox"/> Submitted for Publication <input type="checkbox"/> Unpublished and Unsubmitted work written in manuscript style
Publication Details	Sylvia, G. M.; Heng, S.; Bachhuka, A.; Ebendorff-Heidepriem, H.; Abell, A. D. <i>Tetrahedron</i> , 2018 , 74, 1240-1244. DOI: 10.1016/j.tet.2017.11.020

Principal Author

Name of Principal Author (Candidate)	Georgina M. Sylvia		
Contribution to the Paper	Performed analysis on all samples, interpreted data and wrote manuscript.		
Overall percentage (%)	70 %		
Certification:	This paper reports on original research I conducted during the period of my Higher Degree by Research candidature and is not subject to any obligations or contractual agreements with a third party that would constrain its inclusion in this thesis. I am the primary author of this paper.		
Signature		Date	08/11/2017

Co-Author Contributions

By signing the Statement of Authorship, each author certifies that:

- i. the candidate's stated contribution to the publication is accurate (as detailed above);
- ii. permission is granted for the candidate to include the publication in the thesis; and
- iii. the sum of all co-author contributions is equal to 100% less the candidate's stated contribution.

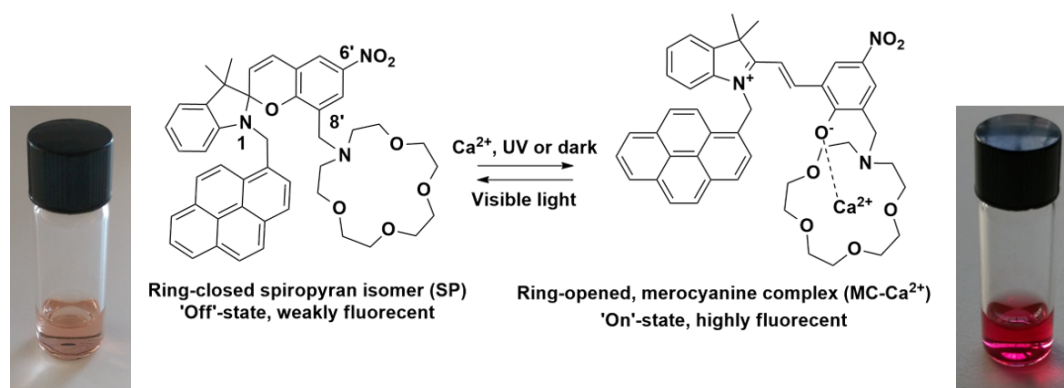
Name of Co-Author	Heike Ebendorff-Heidepriem		
Contribution to the Paper	Helped in manuscript evaluation.		
Signature		Date	8/11/2017

Name of Co-Author	Andrew D. Abell		
Contribution to the Paper	Helped to evaluate and edit the manuscript and acted as corresponding author.		
Signature		Date	14/11/2017

Name of Co-Author	Sabrina Heng		
Contribution to the Paper	Supervised development of work, helped in data interpretation and manuscript evaluation.		
Signature		Date	10/11/17

Name of Co-Author	Akash Bachhuka		
Contribution to the Paper	Performed fibre-based experiments.		
Signature		Date	08/11/17

2.1 Abstract



A rationally designed, pyrene-spiropyran hybrid Ca²⁺ sensor (**Py-1**) with enhanced fluorescence intensity compared to a standalone spiropyran analogue is presented. Importantly, **Py-1** retains the characteristic red emission profile of the spiropyran, while fibre-based photostability studies show the sensor is stable after multiple cycles of photoswitching, without any sign of photodegradation. Such properties are of real advantage for cell-based sensing applications. An interesting observation is that, **Py-1** presents with two excitation options; direct green excitation (532 nm) of the photoswitch for a red emission, and UV excitation (344 nm) of the component pyrene, which gives rise to distinct blue and red emissions. This proof-of-concept hybrid sensing system presents as a more general approach to brighter spiropyran-based sensors.

2.2 Introduction

Calcium ions (Ca²⁺) act as a ubiquitous chemical signalling in cell proliferation, differentiation and death; and as such are essential for cellular function.¹⁻⁴ It is thus important to sense and quantify Ca²⁺ in cells and this is typically achieved using small molecule fluorescence-based sensors, in combination with fluorescence microscopy.⁵⁻⁷ These fluorescent sensors are commonly based on fluorescein (e.g. Calcein, Fluo-4)⁸⁻¹⁰ and coumarin (e.g. Calcein Blue, BTC)^{11,12} which present a high fluorescence emission intensity (i.e. brightness) when bound to Ca²⁺. However, most of these sensors suffer from photostability^{13,14} and high background fluorescence signal in the absence of the ion. In addition, the high excitation energies (i.e. UV/blue) of these fluorophores are damaging to cells,^{15,16} and cause autofluorescence, which overlaps with the desired fluorescence signal of the sensors.^{17,18}

On the other hand, ion sensors based on photochromic molecules, such as spiropyrans,^{19,20} are known to exhibit excellent photostability.²¹ A spiropyran undergoes photochromic conversion between a ring-opened, polar merocyanine (MC) isomer and the ring-closed, non-polar spiropyran (SP), on irradiation with UV (or dark) and white light, respectively (see Figure 1). In addition, the MC state is highly fluorescent when chelating to an appropriate analyte compared to the SP state, resulting in a low background signal in the absence of the analyte. Furthermore, the green excitation and red emission profiles typical of the highly fluorescent MC isomer are not damaging to cells, and do not overlap with cellular autofluorescence.¹⁷⁻²⁰ Finally, these sensors can be prepared in a modular fashion to allow the incorporation of a range of metal-specific ionophores to target a given metal ion.²²⁻²⁴

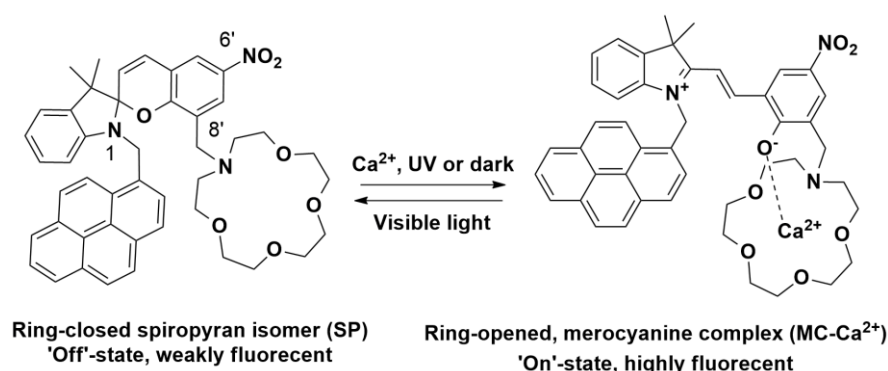


Figure 1. Structures of **Py-1** as the ring-closed, weakly fluorescent spiropyran (SP, 'off') isomer, and the ring-opened, highly fluorescent merocyanine (MC-Ca²⁺, 'on') complex.

While many spiropyran-based, photoswitchable metal ion sensors have been reported, these are somewhat limited by an inherent lack of brightness. An ability to enhance the fluorescence signal of spiropyran would thus extend the range of sensing capability for live-cell imaging using confocal microscopy. One way to address this limitation is to couple a traditional fluorophore to a spiropyran, in order to combine the beneficial properties of both types of sensors, while overcoming the limitations of each in isolation. A few such coupled molecules have been described,²⁵⁻²⁹ however these use the photo-stationary state of spiropyran as an 'on/off' switch to control the fluorescence output of the fluorophore through Förster resonance electron transfer (FRET).^{30,31} As such, the focus of these studies has been on photocontrol of a non-photoswitchable core fluorophore, rather than potential enhancement of the spiropyran in isolation.

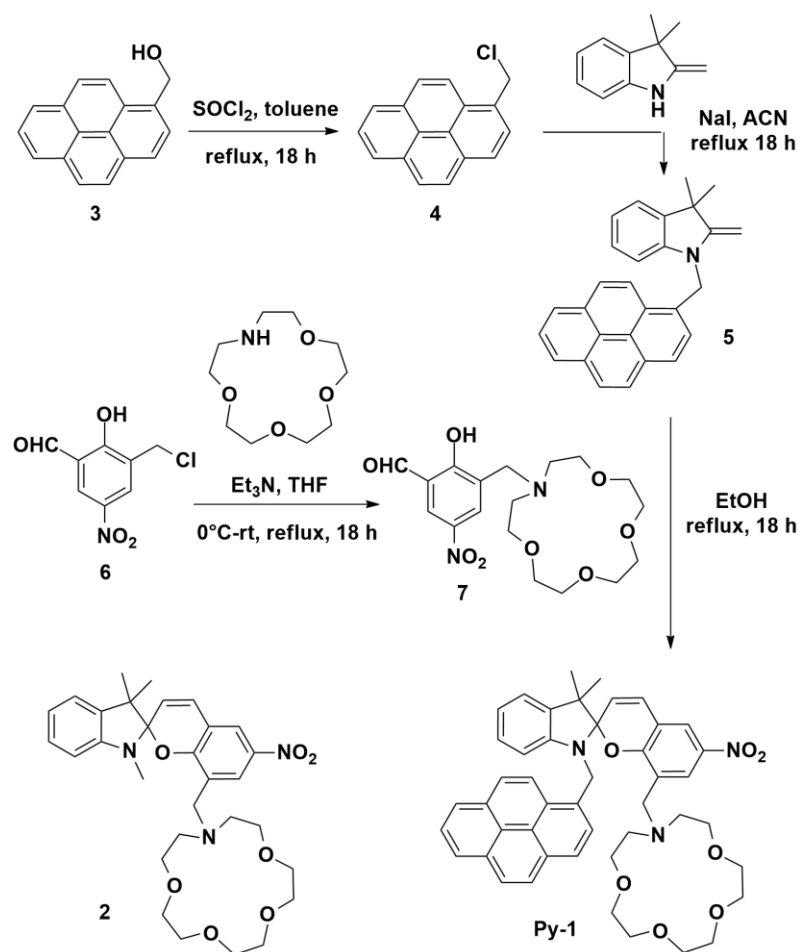
In this work, we demonstrate that coupling of a traditional fluorophore (pyrene) to a photoswitch (spiropyran) with Ca^{2+} -selective ionophore (**Py-1**, Figure 1), gives rise to an 80-fold brighter fluorescence emission in the presence of Ca^{2+} , when compared to a non-coupled spiropyran analogue. Importantly, **Py-1** retains the photostability, red emission profile and low background fluorescence signal typical of spiropyran-based sensors. Pyrene was chosen as the traditional fluorophore in this proof-of-concept study for ease of synthesis, and given that it has a distinct fluorescence emission profile to that of spiropyran.³² We present a detailed characterisation of this novel Ca^{2+} sensor, **Py-1**, and propose that the incorporation of a suitable traditional fluorophore may be a general method for improving the brightness of spiropyran-based sensors.

2.3 Results and Discussion

2.3.1 Design

The pyrene-modified spiropyran sensor, **Py-1**, was designed to be selective for Ca^{2+} with the incorporation of a 1-aza-15-crown-5-ether ionophore at C8' of the benzopyran ring (see Figure 1). The phenolic oxygen of the MC isomer also serves to stabilize metal ion binding in the ionophore (as shown by the dotted line in Figure 1), to define the ion-binding domain.³³ The pyrene fluorophore was attached at the N1 indolic nitrogen (labelled in Figure 1) through a short alkyl tether. Previous work from our group has shown that in general, substitution at this position does not affect photoswitching of the spiropyran.^{34,35} An electron withdrawing C6'- NO_2 group was incorporated to promote formation of the MC(**Py-1**)- Ca^{2+} complex, and hence improve the Ca^{2+} -responsive fluorescence signal.³⁶

2.3.2 Synthesis



Scheme 1. Synthesis of **Py-1**.

Py-1 was prepared as outlined in Scheme 1. Commercially available 1-pyrenemethanol was reacted with thionyl chloride in toluene to give chloromethylpyrene **4**. 2,3,3-Trimethylindolenine was then reacted with **4** in the presence of sodium iodide, followed by treatment with aqueous sodium hydroxide to give the indoline **5**. 1-Aza-15-crown-5-ether was alkylated with chloride **6** to give the benzaldehyde **7**. Finally, a condensation reaction between the aldehyde **7** and indoline **5** in refluxing ethanol, followed by purification of the product by normal-phase column chromatography, gave the pyrene-modified spiropyran **Py-1** in 16 % yield over four steps. The non-pyrene modified sensor **2** was prepared as a control, as previously described in the literature.³⁷

2.3.3 Absorbance Characterisation

Absorbance spectra of **Py-1** were first measured in the absence and presence of excess Ca^{2+} , in order to characterise metal binding-induced SP to MC isomerisation. First, the absorbance of **Py-1** (50 μM in acetonitrile) was measured. Results displayed in Figure 2 (black line), show strong absorbance maxima for the pyrene fluorophore (329 nm and 344 nm)³² with weaker absorbances for the SP (405 nm) and MC (554 nm) isomers.¹⁹ The presence of these two, distinct absorption bands allows for excitation of the sensor at 344 nm and 532 nm. Next, the absorbance of **Py-1** (50 μM) in the presence of excess Ca (100 μM) was measured. Binding of **Py-1** to Ca^{2+} (red line) caused a 4-fold increased intensity and hypsochromic shift of the MC absorbance to 520 nm. Thus, metal ion binding induces isomerisation of **Py-1** to the more coloured MC(**Py-1**)- Ca^{2+} complex.²²⁻²⁴

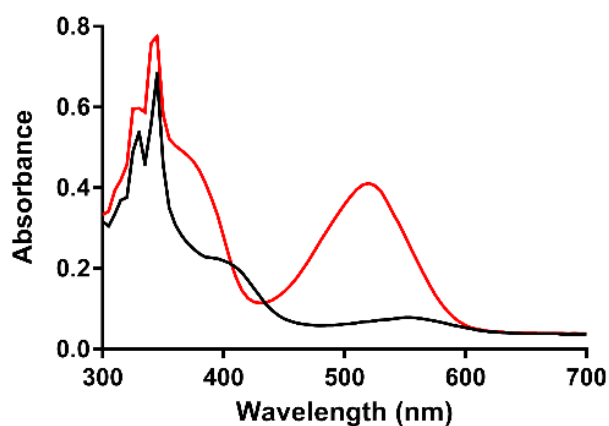


Figure 2. Absorbance of **Py-1** (50 μM , black line) and in the presence of a 2-fold excess of Ca^{2+} (100 μM , red line).

2.3.4 Fluorescence Characterisation

Excitation at 532 nm

The fluorescence emission spectra of **Py-1** were next measured in order to characterise the emission profile and determine the effect of the pyrene moiety on sensor brightness. Sensor **2** was included for comparative studies, as this azacrown-bearing spiropyran does not contain the N1 indolic pyrene moiety (see Scheme 1). Results displayed in Figure 3a show that, in the presence of excess Ca^{2+} , **Py-1** gives a strong, red emission maximum (605 nm), 8-fold higher than that observed in the absence of the ion (635 nm). Similar emission maxima were observed for sensor **2** (Figure 3b) in the presence of Ca^{2+} (600 nm), but with a higher background fluorescence in the absence of the ion (625 nm). Despite both sensors sharing a common aza-crown ether-based Ca^{2+} -binding domain, **Py-1** shows enhanced selectivity for Ca^{2+} compared to **2**. This suggests that the pyrene moiety may stabilize the ring-opened MC isomer, which we know binds metal ions. Importantly, **Py-1** was found to be approx. 80-fold brighter than sensor **2** in the presence of Ca^{2+} . Other information, such as quantum yield calculations, can be found in the Supporting Information.

Next, the ion selectivity profiles of **Py-1** and **2** were investigated in order to determine the effect of the pyrene substitution on metal ion binding. The fluorescence emission spectra in the presence of excess of Ca^{2+} and other biologically relevant ions (Li^+ , Na^+ , K^+ , Cs^+ , Mg^{2+} , Mn^{2+} , Cu^{2+} and Zn^{2+}) were measured, with results displayed in Figure 3c. The sensors showed a similar selectivity profile with 2 to 4-fold affinity measured for Ca^{2+} over all other ions. Critically, these fluorescence results demonstrate that the pyrene-spiropyran sensor, **Py-1**, is brighter than the non-modified sensor **2** with an improved signal-to-noise ratio, while retaining the red emission profile and metal-ion selectivity, in agreement with our design strategy.

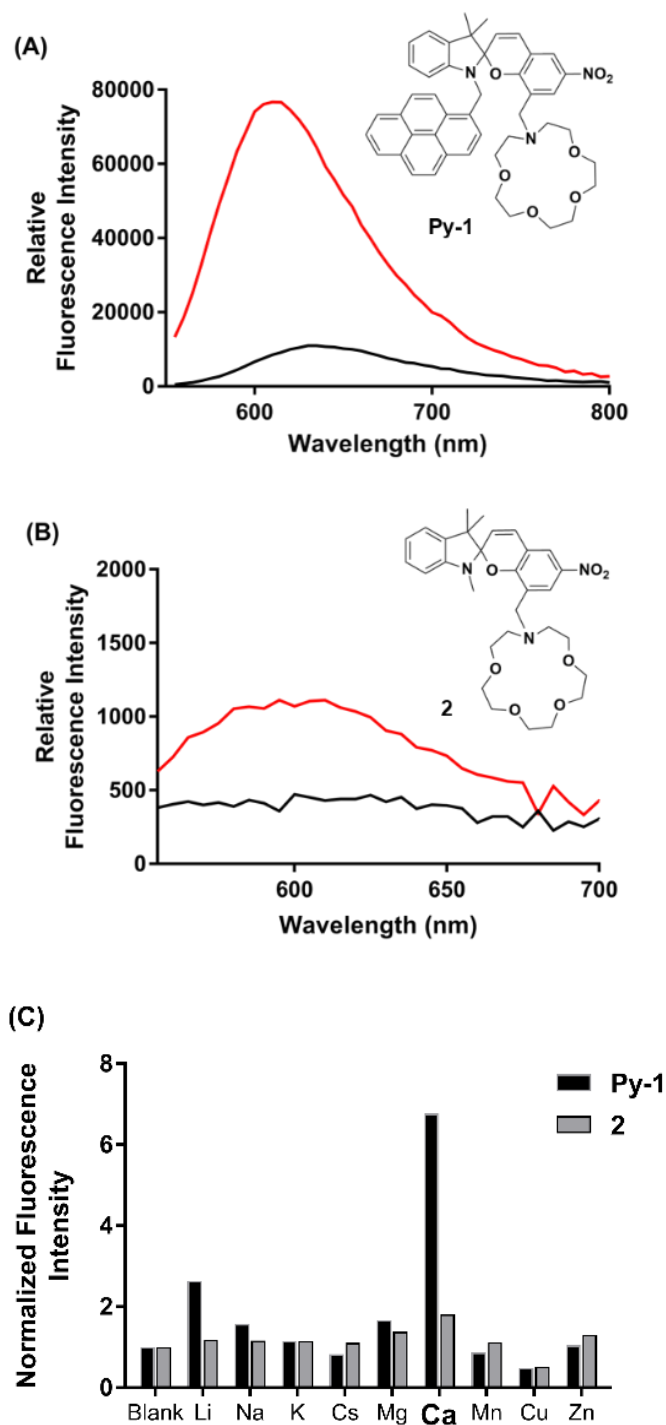


Figure 3. Fluorescence spectra of (A) **Py-1** and (B) **2** (black lines) and in the presence of Ca^{2+} (red lines). Excitation was at 532 nm. (C) Fluorescence emission selectivity of **Py-1** (black) and **2** (red) in the presence of a 2-fold excess of biologically relevant metal ions.

Excitation at 344 nm

The fluorescence emission of **Py-1** with excitation at the pyrene absorbance maximum (344 nm) was next investigated, with results displayed in Figure 4a. In the absence of Ca^{2+} , two distinct maxima are observed for the pyrene fluorophore (390 nm) and merocyanine (635 nm) isomer, respectively, with a 2:1 emission intensity ratio. Binding of **Py-1** to Ca^{2+} caused a hypsochromic shift of the MC emission to 605 nm, and a change in the intensity ratio of the two emissions to approx. 1:3. These separate emission maxima with a single excitation may be explained by Förster resonance electron transfer (FRET) occurring within the **Py-1** sensor, where pyrene acts as the FRET ‘donor’ and MC the ‘acceptor’ (see Figure 4a, inset). In support of this explanation, excitation of literature sensor **2** at 344 nm, which lacks the pyrene moiety, gives no such emission (see 5.2 Supporting Information for Chapter 2, Figure S2-3). Additionally, the resulting change in emission intensity of the two maxima in response to Ca^{2+} suggests that the efficiency of FRET between the pyrene and MC is affected by metal chelation to **Py-1**. The absorbance spectra from Figure 2 shows a hypsochromic shift and increase in the MC absorbance of **Py-1** in the presence of Ca^{2+} . This ion-induced change is likely causing better overlap with the fluorescence emission of pyrene, and hence allowing for greater FRET transfer to occur between donor and acceptor fluorophores. Interestingly, the FRET-induced MC emission profile of **Py-1** is identical to that observed with excitation at 532 nm, albeit of a lower intensity.

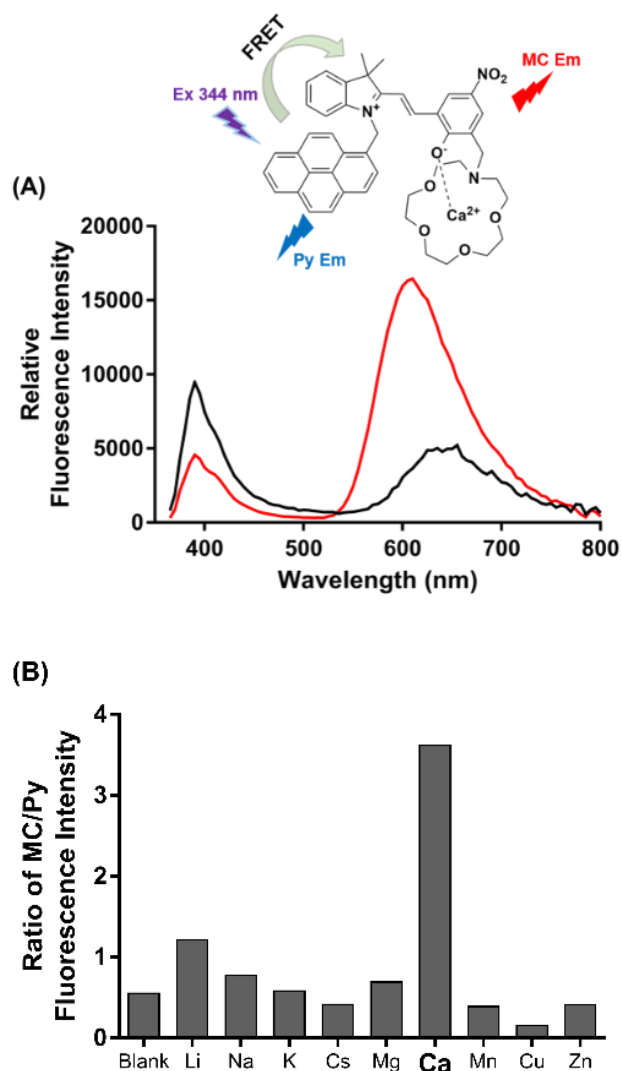


Figure 4. (A) Fluorescence emission spectrum of **Py-1** (black) and in the presence of Ca²⁺ (red) with excitation at 344 nm. Inset: Proposed mechanism of fluorescence emission of MC(**Py-1**)-Ca²⁺ complex. (B) Selectivity of **Py-1** with excitation at 344 nm showing ratio of the MC/Py fluorescence emission intensities in the presence of biologically relevant metal ions.

The fluorescence intensity ratio of MC/pyrene emissions in the presence of various metal ions was next measured, to further investigate the effect of ionophore selectivity on the FRET efficiency. From the results in Figure 4b, the greatest transfer efficiency is seen in the presence of Ca²⁺, with a MC/pyrene ratio 8-fold greater than that of sensor in the absence of metal ion. Importantly, this trend in fluorescence ratio is consistent with the selectivity of the azacrown ionophore with excitation at 532nm established earlier.

2.3.5 Photostability Characterisation

In the final part of this study, photoswitching between the highly fluorescent MC and weakly fluorescent SP isomers of **Py-1** was characterised using an in-house fabricated silica-based suspended core microstructured optical fibre (SCF), in order to assess the photostability of the sensor. Microstructured optical fibers offer the advantage that interaction between the light and chemical species can be extended along the entire length of the fiber, while maintaining the integrity of the device. In SCFs, the glass core is suspended in air by thin struts, allowing a portion of the guided light to extend outside the fiber core into the surrounding holes which serve as low-volume sample chambers (Figure S2-5).^{38,39}

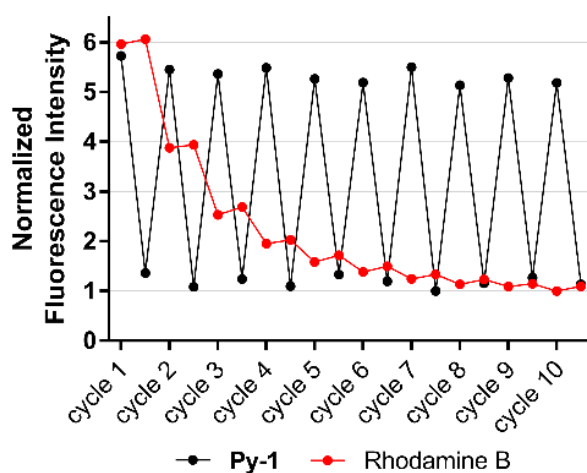


Figure 5. Photostability of **Py-1** (black) within an optical fibre over 10 cycles of photoswitching, where each cycle denotes photoconversion from the highly fluorescent MC isomer to the weakly fluorescent SP isomer upon irradiation with 532 nm green laser light for 2 min. Incubation in the dark for 5 min results in reversion to the MC state. Excitation for fluorescence measurements was at 532 nm, with 5 x 15 ms pulses at 1.5 μ W power. The photostability of Rhodamine B (red) was investigated under the same irradiation conditions.

The SCF was immersed in a solution of **Py-1** sensor (500 μ M in acetonitrile), with **Py-1** taken up into the holes of the fibre by capillary action. Fluorescence measurement in the SCF revealed the highly fluorescent MC form of **Py-1** (λ_{em} max \sim 635 nm), presented as the first point in Figure 5. Next, irradiation with the 532 nm laser light to photoswitch to the weakly fluorescent SP isomer resulted in a 6-fold decreased fluorescence intensity. The second switching cycle in the dark allowed the sensor to photoswitch back to the highly fluorescent MC form, with the fluorescence intensity returned to pre-irradiation levels. In all cases, excitation was achieved with 5 x 15 ms pulses of the 532 nm green laser. This process was repeated over 10 cycles, demonstrating the photo-reversibility of the system. For

comparison, the fluorescence emission of Rhodamine B (100 μM in acetonitrile) was recorded under the same experimental conditions, with results displayed in Figure 5 (red line). Rhodamine B suffers from considerable photobleaching, with a 6-fold decrease in the normalized fluorescence intensity by the eighth photoswitching cycle. These results clearly demonstrate that **Py-1** can photoswitch without photobleaching, compared to the commercially available sensor.

2.4 Conclusion

In this work, we present a new rationally designed, photostable, red-emitting Ca^{2+} sensor. This hybrid pyrene-spiropyran sensor (**Py-1**) has enhanced fluorescence intensity compared to a non-coupled analogue, while retaining the characteristic red emission profile of the spiropyran. It presents two other excitation options; direct green excitation (532 nm) of the photoswitch for a red emission and UV excitation (344 nm) of the pyrene moiety, which gives rise to distinct blue and red emissions. Fibre-based photostability studies show that **Py-1** is stable after multiple cycles of photoswitching, without any sign of photobleaching. Importantly, this new pyrene-spiropyran coupled system presents an opportunity for a general method towards the fluorescence enhancement of spiropyran-based sensors.

2.5 Acknowledgements

The authors would like to acknowledge funding support from the Centre for Nanoscale BioPhotonics (CNBP), through the Australian Research Council (ARC) CE140100 003. This work was performed in part at the OptoFab node of the Australian National Foundation Facility utilizing Commonwealth and South Australian State Government funding.

2.6 References

1. Clapham, D. E., Calcium signaling. *Cell* **2007**, *131* (6), 1047-1058.
2. Berridge, M. J.; Lipp, P.; Bootman, M. D., The versatility and universality of calcium signalling. *Nature reviews. Molecular cell biology* **2000**, *1* (1), 11-21.
3. Tonelli, F. M. P.; Santos, A. K.; Gomes, D. A.; da Silva, S. L.; Gomes, K. N.; Ladeira, L. O.; Resende, R. R., Stem Cells and Calcium Signaling. *Adv Exp Med Biol* **2012**, *740*, 891-916.
4. Bhosale, G.; Sharpe, J. A.; Sundier, S. Y.; Duchen, M. R., Calcium signaling as a mediator of cell energy demand and a trigger to cell death. *Ann Ny Acad Sci* **2015**, *1350*, 107-116.
5. Dean, K. M.; Qin, Y.; Palmer, A. E., Visualizing metal ions in cells: An overview of analytical techniques, approaches, and probes. *Bba-Mol Cell Res* **2012**, *1823* (9), 1406-1415.
6. Carter, K. P.; Young, A. M.; Palmer, A. E., Fluorescent Sensors for Measuring Metal Ions in Living Systems. *Chem Rev* **2014**, *114* (8), 4564-4601.
7. Lichtman, J. W.; Conchello, J. A., Fluorescence microscopy. *Nat Methods* **2005**, *2* (12), 910-919.
8. Lavis, L. D., Teaching Old Dyes New Tricks: Biological Probes Built from Fluoresceins and Rhodamines. *Annu Rev Biochem* **2017**, *86*, 825-843.
9. Minta, A.; Kao, J. P. Y.; Tsien, R. Y., Fluorescent Indicators for Cytosolic Calcium Based on Rhodamine and Fluorescein Chromophores. *Journal of Biological Chemistry* **1989**, *264* (14), 8171-8178.
10. Gee, K. R.; Brown, K. A.; Chen, W. N. U.; Bishop-Stewart, J.; Gray, D.; Johnson, I., Chemical and physiological characterization of fluo-4 Ca²⁺-indicator dyes. *Cell calcium* **2000**, *27* (2), 97-106.
11. Smith, G. A.; Hesketh, R. T.; Metcalfe, J. C.; Feeney, J.; Morris, P. G., Intracellular Calcium Measurements by F-19 Nmr of Fluorine-Labeled Chelators. *P Natl Acad Sci Biol* **1983**, *80* (23), 7178-7182.
12. Rahn, B. A.; Perren, S. M., Calcein Blue as a Fluorescent Label in Bone. *Experientia* **1970**, *26* (5), 519-&.
13. Song, L. L.; Hennink, E. J.; Young, I. T.; Tanke, H. J., Photobleaching Kinetics of Fluorescein in Quantitative Fluorescence Microscopy. *Biophys J* **1995**, *68* (6), 2588-2600.
14. Eggeling, C.; Widengren, J.; Rigler, R.; Seidel, C. A. M., Photobleaching of fluorescent dyes under conditions used for single-molecule detection: Evidence of two-step photolysis. *Analytical chemistry* **1998**, *70* (13), 2651-2659.
15. Godley, B. F.; Shamsi, F. A.; Liang, F. Q.; Jarrett, S. G.; Davies, S.; Boulton, M., Blue light induces mitochondrial DNA damage and free radical production in epithelial cells. *Journal of Biological Chemistry* **2005**, *280* (22), 21061-21066.
16. Pattison, D. I.; Davies, M. J., Actions of ultraviolet light on cellular structures. *Exs* **2006**, (96), 131-57.
17. Monici, M., Cell and tissue autofluorescence research and diagnostic applications. *Biotechnology annual review* **2005**, *11*, 227-56.
18. Andersson, H.; Baechi, T.; Hoehl, M.; Richter, C., Autofluorescence of living cells. *J Microsc-Oxford* **1998**, *191*, 1-7.
19. Lukyanov, B. S.; Lukyanova, M. B., Spiropyran: Synthesis, Properties, and Application. *Chem Heterocycl Com+* **2005**, *41* (3), 32.

20. Klajn, R., Spiropyran-based dynamic materials. *Chemical Society reviews* **2014**, *43* (1), 148-84.
21. Stubing, D. B.; Heng, S.; Monro, T. M.; Abell, A. D., A comparative study of the fluorescence and photostability of common photoswitches in microstructured optical fibre. *Sensor Actuat B-Chem* **2017**, *239*, 474-480.
22. Tanaka, M.; Kamada, K.; Ando, H.; Kitagaki, T.; Shibutani, Y.; Yajima, S.; Sakamoto, H.; Kimura, K., Metal-ion stabilization of photoinduced open colored isomer in crowned spirobenzothiapyran. *Chem Commun* **1999**, (16), 1453-1454.
23. Zakharova, M. I.; Pimienta, V.; Metelitsa, A. V.; Minkin, V. I.; Micheau, J. C., Thermodynamic and kinetic analysis of metal ion complexation by photochromic spiropyran. *Russ Chem B+* **2009**, *58* (7), 1329-1337.
24. Wojtyk, J. T. C.; Kazmaier, P. M.; Buncel, E., Effects of metal ion complexation on the spiropyran-merocyanine interconversion: development of a thermally stable photo-switch. *Chem Commun* **1998**, (16), 1703-1704.
25. Ahmed, S. A.; Tanaka, M.; Ando, H.; Tawa, K.; Kimura, K., Fluorescence emission control and switching of oxymethylcrowned spirobenzopyrans by metal ion. *Tetrahedron* **2004**, *60* (28), 6029-6036.
26. Beyer, C.; Wagenknecht, H. A., Synthesis of Spiropyran As Building Blocks for Molecular Switches and Dyads. *J Org Chem* **2010**, *75* (8), 2752-2755.
27. Seefeldt, B.; Kasper, R.; Beining, M.; Mattay, J.; Arden-Jacob, J.; Kemnitzer, N.; Drexhage, K. H.; Heilemann, M.; Sauer, M., Spiropyran as molecular optical switches. *Photoch Photobio Sci* **2010**, *9* (2), 213-220.
28. Xiong, Y. Y.; Rivera-Fuentes, P.; Sezgin, E.; Jentsch, A. V.; Eggeling, C.; Anderson, H. L., Photoswitchable Spiropyran Dyads for Biological Imaging. *Org Lett* **2016**, *18* (15), 3666-3669.
29. Remon, P.; Hammarson, M.; Li, S. M.; Kahnt, A.; Pischel, U.; Andreasson, J., Molecular Implementation of Sequential and Reversible Logic Through Photochromic Energy Transfer Switching. *Chem-Eur J* **2011**, *17* (23), 6492-6500.
30. Yuan, L.; Lin, W. Y.; Zheng, K. B.; Zhu, S. S., FRET-Based Small-Molecule Fluorescent Probes: Rational Design and Bioimaging Applications. *Accounts Chem Res* **2013**, *46* (7), 1462-1473.
31. Zadran, S.; Standley, S.; Wong, K.; Otiniano, E.; Amighi, A.; Baudry, M., Fluorescence resonance energy transfer (FRET)-based biosensors: visualizing cellular dynamics and bioenergetics. *Appl Microbiol Biot* **2012**, *96* (4), 895-902.
32. Castanheira, E. M. S.; Martinho, J. M. G., Solvatochromic Shifts of Pyrene Excimer Fluorescence. *Chem Phys Lett* **1991**, *185* (3-4), 319-323.
33. Salhin, A. M. A.; Tanaka, M.; Kamada, K.; Ando, H.; Ikeda, T.; Shibutani, Y.; Yajima, S.; Nakamura, M.; Kimura, K., Decisive factors in the photoisomerization behavior of crowned spirobenzopyran: Metal ion interaction with crown ether and phenolate anion moieties. *Eur J Org Chem* **2002**, (4), 655-662.
34. Heng, S.; Mak, A. M.; Kostecky, R.; Zhang, X. Z.; Pei, J. X.; Stubing, D. B.; Ebendorff-Heidepriem, H.; Abell, A. D., Photoswitchable calcium sensor: 'On'-'Off' sensing in cells or with microstructured optical fibers. *Sensor Actuat B-Chem* **2017**, *252*, 965-972.
35. Heng, S.; Mak, A. M.; Stubing, D. B.; Monro, T. M.; Abell, A. D., Dual Sensor for Cd(II) and Ca(II): Selective Nanoliter-Scale Sensing of Metal Ions. *Anal Chem* **2014**, *86* (7), 3268-3272.

36. Collins, G. E.; Choi, L. S.; Ewing, K. J.; Michelet, V.; Bowen, C. M.; Winkler, J. D., Photoinduced switching of metal complexation by quinolinospiropyranindolines in polar solvents. *Chem Commun* **1999**, (4), 321-322.
37. Kimura, K.; Yamashita, T.; Yokoyama, M., Syntheses, Cation Complexation, Isomerization and Photochemical Cation-Binding Control of Spirobenzopyrans Carrying a Monoazacrown Moiety at the 8-Position. *J Chem Soc Perk T 2* **1992**, (4), 613-619.
38. Zhao, J. B.; Jin, D. Y.; Schartner, E. P.; Lu, Y. Q.; Liu, Y. J.; Zvyagin, A. V.; Zhang, L. X.; Dawes, J. M.; Xi, P.; Piper, J. A.; Goldys, E. M.; Monro, T. M., Single-nanocrystal sensitivity achieved by enhanced upconversion luminescence. *Nat Nanotechnol* **2013**, 8 (10), 729-734.
39. Schartner, E. P.; Tsiminis, G.; Francois, A.; Kostecki, R.; Warren-Smith, S. C.; Nguyen, L. V.; Heng, S.; Reynolds, T.; Klantsataya, E.; Rowland, K. J.; Abell, A. D.; Ebendorff-Heidepriem, H., Taming the Light in Microstructured Optical Fibers for Sensing. *Int J Appl Glass Sci* **2015**, 6 (3), 229-239.
40. Magde, D.; Rojas, G. E.; Seybold, P. G., Solvent dependence of the fluorescence lifetimes of xanthene dyes. *Photochem Photobiol* **1999**, 70 (5), 737-744.
41. Stubing, D. B.; Heng, S.; Abell, A. D., Crowned spiropyran fluoroionophores with a carboxyl moiety for the selective detection of lithium ions. *Organic & biomolecular chemistry* **2016**, 14 (15), 3752-7.

CHAPTER 3

A rationally designed, spiropyran-based chemosensor for magnesium

Georgina M. Sylvia,¹ Adrian M. Mak,² Sabrina Heng,¹ Akash Bachhuka,¹ Heike Ebendorff-Heidepriem¹ and Andrew D. Abell¹

¹ARC Centre of Excellence for Nanoscale BioPhotonics (CNBP), Institute for Photonics and Advanced Sensing (IPAS) and School of Physical Sciences, The University of Adelaide, South Australia, Australia 5005.

² Institute of High Performance Computing, 1 Fusionopolis Way, No. 16-16 Connexis, 138632, Singapore.

Chemosensors, **2018**, 6(2), 17; doi:10.3390/chemosensors6020017.

Statements of Authorship

Title of Paper	A rationally designed, spiropyran-based chemosensor for magnesium.
Publication Status	<input checked="" type="checkbox"/> Published <input type="checkbox"/> Accepted for Publication <input type="checkbox"/> Submitted for Publication <input type="checkbox"/> Unpublished and Unsubmitted work written in manuscript style
Publication Details	Sylvia, G. M.; Mak, A. M.; Heng, S.; Bachhuka, A.; Ebendorff-Heidepriem, H.; Abell, A. D. <i>Chemosensors</i> , 2018 , <i>6</i> , 17. DOI: 10.3390/chemosensors6020017

Principal Author

Name of Principal Author (Candidate)	Georgina M. Sylvia		
Contribution to the Paper	Performed analysis on all samples, interpreted data and wrote manuscript.		
Overall percentage (%)	70 %		
Certification:	This paper reports on original research I conducted during the period of my Higher Degree by Research candidature and is not subject to any obligations or contractual agreements with a third party that would constrain its inclusion in this thesis. I am the primary author of this paper.		
Signature		Date	08/11/2017

Co-Author Contributions

By signing the Statement of Authorship, each author certifies that:

- i. the candidate's stated contribution to the publication is accurate (as detailed above);
- ii. permission is granted for the candidate to include the publication in the thesis; and
- iii. the sum of all co-author contributions is equal to 100% less the candidate's stated contribution.

Name of Co-Author	Adrian M. Mak		
Contribution to the Paper	Performed DFT calculations and helped in data interpretation.		
Signature		Date	22nd March 2018

Name of Co-Author	Sabrina Heng		
Contribution to the Paper	Supervised development of work, helped in data interpretation and manuscript evaluation.		
Signature		Date	10/11/17

Name of Co-Author	Akash Bachhuka		
Contribution to the Paper	Performed all fibre-based experiments.		
Signature		Date	08/11/17

Name of Co-Author	Heike Ebendorff-Heidepriem		
Contribution to the Paper	Helped to evaluate the manuscript.		
Signature		Date	8/11/2017

Name of Co-Author	Andrew D. Abell		
Contribution to the Paper	Helped to evaluate and edit the manuscript, acted as corresponding author.		
Signature		Date	14/11/2017

3.1 Abstract

Magnesium ions (Mg^{2+}) play an important role in mammalian cell function; however, relatively little is known about the mechanisms of Mg^{2+} regulation in disease states. An advance in this field would come from the development of selective, reversible fluorescent chemosensors, capable of repeated measurements. To this end, the rational design and fluorescence-based photophysical characterisation of two spiropyran-based chemosensors for Mg^{2+} are presented. The most promising analogue, chemosensor **1**, exhibits 2-fold fluorescence enhancement factor and 3-fold higher binding affinity for Mg^{2+} (K_d 6.0 μM) over Ca^{2+} (K_d 18.7 μM). Incorporation of spiropyran-based sensors into optical fibre sensing platforms has been shown to yield significant signal-to-background changes with minimal sample volumes, a real advance in biological sensing that enables measurement on subcellular-scale samples. In order to demonstrate chemosensor compatibility within the light intense microenvironment of an optical fibre, photoswitching and photostability of **1** within a suspended core optical fibre (SCF) was subsequently explored, revealing reversible Mg^{2+} binding with improved photostability compared to the non-photoswitchable Rhodamine B fluorophore. The spiropyran-based chemosensors reported here highlight untapped opportunities for a new class of photoswitchable Mg^{2+} probe and present a first step in the development of a light-controlled, reversible dip-sensor for Mg^{2+} .

3.2 Introduction

Magnesium ions (Mg^{2+}) play an important role in mammalian cell function,¹⁻⁴ as an enzymatic cofactor,⁵ regulator of cellular ion channels⁶⁻⁸ and energy metabolism.⁹ Conditions such as Type 2 Diabetes,¹⁰⁻¹² Alzheimer's¹³⁻¹⁴ and cardiovascular disease¹⁵⁻¹⁶ have been linked with magnesium deficiency, however the mechanisms of Mg^{2+} regulation in such disease states are poorly understood.¹⁷⁻¹⁸ Fluorescent chemosensors, in combination with specialised imaging technologies, provide a useful tool to study the role of metal ions in cellular processes as they enable detection in and around cells with spatial and temporal resolution.¹⁹

Mag-fura-2 (FURAPTRA)²⁰⁻²¹ is one such commercially available chemosensor for Mg^{2+} , based on a benzofuran fluorophore scaffold and functionalised with the *O*-aminophenol-*N,N,O*-triacetic acid (APTRA) Mg^{2+} chelator.²² Mag-fura-2 has been shown to detect cytosolic Mg^{2+} in various cells,²³⁻²⁵ however as it is structurally analogous to the calcium (Ca^{2+}) chelator fura-2, intracellular Mg^{2+} detection is complicated by an affinity for Ca^{2+} .²⁶⁻

²⁷ More recently, other probes based on fluorophore scaffolds such as fluorescein and rhodamine have been reported to display improved selectivity.²⁸⁻³⁰ For example, the KMG series of chemosensors possess a bidentate, charged beta-diketone binding domain, which gives rise to excellent Mg^{2+} selectivity over Ca^{2+} (Figure 1B).²⁹ Similar selectivity has been observed with the MGQ series, which possess a range of tridentate carboxy binding domains (Figure 1C).³⁰ These studies represent significant developments in the field of Mg^{2+} detection, but further work is required in order to advance this area.³¹⁻³²

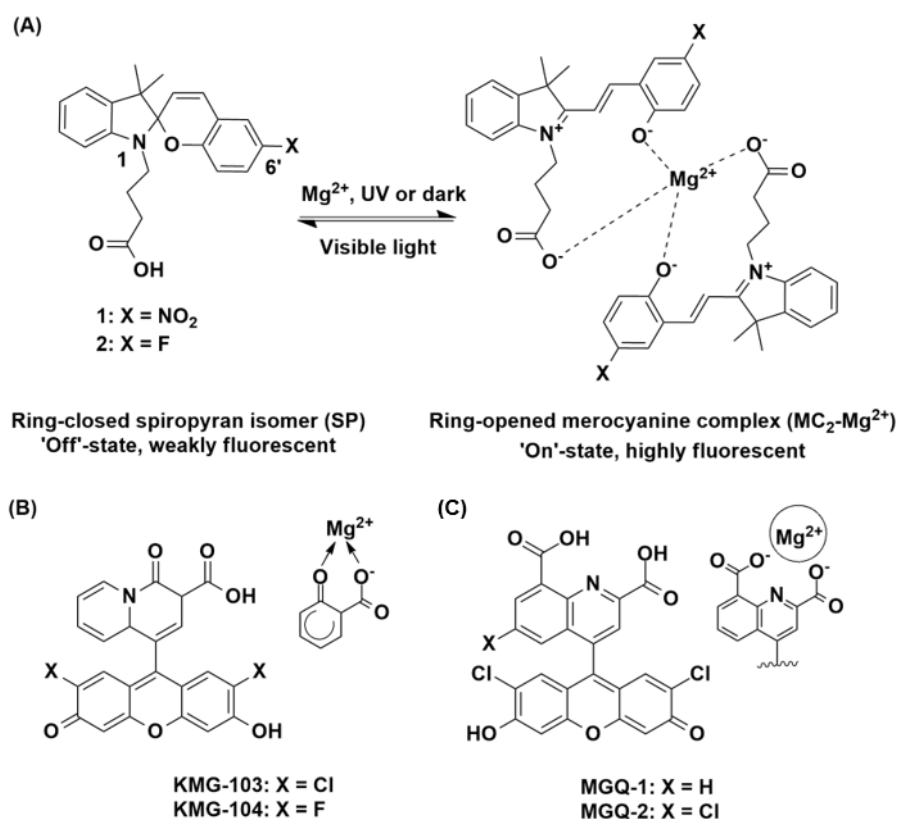


Figure 1. (A) Structures of **1** and **2** as the ring-closed, weakly fluorescent spiropyran (SP, 'off') isomer, and the proposed ring-opened, highly fluorescent merocyanine (MC_2-Mg^{2+} , 'on') complex. Structures of the (B) KMG²⁹ and (C) MGQ³⁰ chemosensors with the proposed Mg^{2+} -binding domains highlighted.

For example, the ability to turn metal ion sensing on and off, with an external and non-invasive stimulus such as light, would extend the range of sensing capability for live-cell imaging. A photoswitchable spiropyran presents as one such sensing moiety, where these structures form the basis of a chemosensor when functionalised with a suitable ionophore that is capable of complexing with a metal ion.³³⁻³⁴ Photo-controlled switching between the weakly fluorescent spiropyran (SP) and highly fluorescent merocyanine (MC) isomers occurs on irradiation with UV light or in the presence of the target metal ion, while visible light reverses the isomerisation (see **1** and **2** Figure 1A).³⁵⁻³⁷ Recently, we have reported the

combination of spiropyran-based chemosensors with microstructured optical fibres for the nanoscale detection of metal ions.³⁸⁻⁴⁰ These systems have been shown to yield significant signal-to-background changes with minimal sample volumes, a real advance in biological sensing that enables measurement on subcellular-scale samples. Importantly, spiropyrans are among the most stable photoswitches in the light intense microenvironment of an optical fibre.⁴¹ The fibre also provides a platform for sensing metal ions in confined spaces such as the medium surrounding cell clusters, oocytes and embryos, and in the *in vivo* environment.⁴²⁻⁴⁴

Here we present two rationally designed, spiropyran-based chemosensors for Mg^{2+} (**1** and **2**, Figure 1A). Chemosensor **1** consists of a photoswitchable spiropyran fluorophore scaffold, functionalised with a butanoic acid at the N1-indole. The molecule is designed to chelate Mg^{2+} through the free carboxyl group, in combination with the phenoxide of the ring-opened merocyanine isomer. We envisaged that **1** would bind Mg^{2+} in a 2:1 chemosensor to metal ion ratio (depicted in Figure 1A), in a design inspired by the Mg^{2+} -selective, literature chemosensors described above.²⁸⁻³⁰ An electron withdrawing NO_2 group was incorporated at the C6' position of the benzopyran ring, since such groups are known to further promote metal ion binding by stabilising the ring-opened MC isomer.⁴⁵ The fluorinated analogue **2** was also investigated as a moderately electron withdrawing fluoro-substituent is known to give rise to relatively high fluorescence yields compared to a nitro analogue.³⁹ It is interesting to note that while absorbance-based photophysical studies have previously been reported on **1**,^{33, 46} the fluorescence properties of this chemosensor in the presence of Mg^{2+} are unknown. As such, this work reports on the rational design and photophysical characterisation of the first spiropyran-based fluorescence chemosensors for Mg^{2+} and demonstrates the photo-compatibility of chemosensor **1** within a suspended core optical fibre (SCF) as a first step in the development of a light-controlled, reversible dip-sensor for Mg^{2+} .

3.3 Results and Discussion

3.3.1 DFT Modelling

Structures of chemosensors **1** and **2**, bound with both Mg^{2+} and Ca^{2+} , were calculated by density functional theory based on a 2:1 binding of ring opened merocyanine isomer to metal ion (see Figure 1). This proposed coordination geometry has precedent for similarly functionalised spiropyran-based chemosensors with divalent metal ions.⁴⁷⁻⁴⁹ Two water molecules were included in the initial calculations to provide additional coordinating sites, based on the metal-bound crystal structure reported for a similar spiropyran.⁴⁷ Geometry optimised structures were obtained using the B3LYP functionals⁵⁰ and 6-311G** basis set for all atoms, within the Gaussian09 package.⁵¹

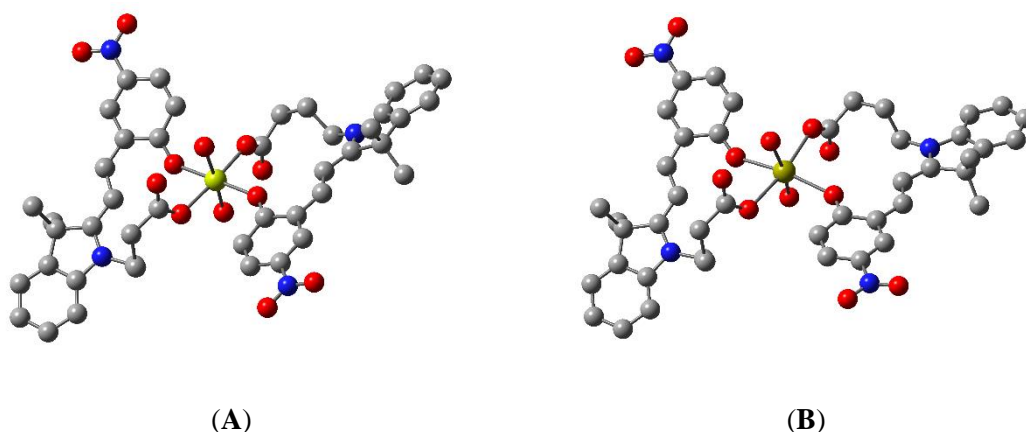


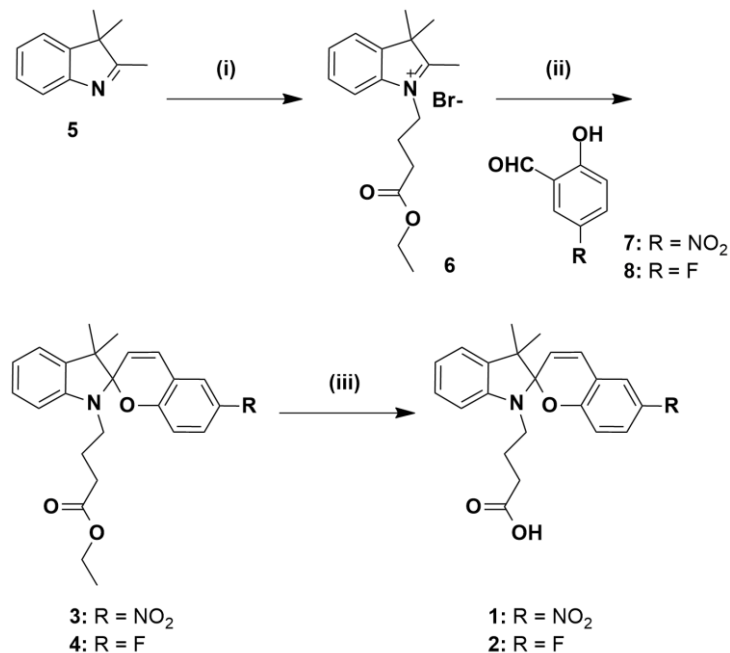
Figure 2. B3LYP/6-311G** optimised structure of **1** bound to (A) Mg^{2+} (yellow) and (B) Ca^{2+} (gold), respectively, in a 2:1 ratio, showing oxygen atoms (red) chelating to the metal ion. Hydrogen atoms are omitted for clarity.

The optimised structures for chemosensor **1** bound to Mg^{2+} and Ca^{2+} are presented in Figure 2. The resulting complexes of **1** bound with Mg^{2+} and Ca^{2+} are both hexa-coordinated, such that the ion is bound by two, bidentate MC ligands, with two water molecules fulfilling the coordination of the metal in each case. The $\text{Mg}^{2+}\cdots\text{O}$ distances are between 2.07 and 2.13 Å, and $\text{Ca}^{2+}\cdots\text{O}$ distances are between 2.37 and 2.46 Å. The reaction energies for the formation of the $\text{M}[\mathbf{1}(\text{MC})_2(\text{H}_2\text{O})_2]$ species were calculated to be -299.0 kJ/mol and -137.8 kJ/mol for Mg^{2+} and Ca^{2+} , respectively. Similar results were observed for the fluorinated chemosensor **2** (see 5.3 Supporting Information for Chapter 3, Figure S3-9). Taken together, the more negative ΔG_{298} for the formation of the $\text{Mg}[\mathbf{1}(\text{MC})_2(\text{H}_2\text{O})_2]$ and $\text{Mg}[\mathbf{2}(\text{MC})_2(\text{H}_2\text{O})_2]$, and the shorter $\text{Mg}^{2+}\cdots\text{O}$ distances compared with Ca^{2+} analogues in

this study suggest stronger binding of the Mg^{2+} compared to the Ca^{2+} by chemosensors **1** and **2**.

3.3.2 Synthesis

Compounds **1** and **2** were prepared as outlined in Scheme 1. Commercially available 3,3-dimethyl-2-methyleneindoline **5** was alkylated with ethyl-4-bromobutanoate to give the previously reported indoline **6**.³⁸ Separate condensation reactions of 2-hydroxy-5-nitrobenzaldehyde **7** or 5-fluoro-2-hydroxybenzaldehyde **8**, with indoline **6** in refluxing ethanol, gave the ester-protected spiropyrans **3** and **4**, respectively which were fully characterised by 1H , ^{13}C -NMR and HRMS (see Figures S3-1 –S3-4 and S3-8). Spiropyrans **3** and **4** were then separately treated with 2 M aqueous NaOH in order to hydrolyse the ester protecting groups, and the crude, free-acid products were then purified by reverse-phase HPLC, respectively. The resulting compounds were characterised by 1H , ^{13}C -NMR and HRMS, with details reported in Supporting Information (Figures S3-5 –S3-8). The proton NMR spectrum of **1** shows the chemosensor fully in the ring-closed SP form, as is consistent with previous studies.³³ Interestingly, the proton NMR spectrum of **2** suggests a mixture of SP and MC isomers. Based on this, subsequent work was focused on chemosensor **1**.



Scheme 1. Synthesis of chemosensors **1** and **2**. Reagents and conditions: (i) ethyl-4-bromobutyrate, $CHCl_3$, reflux 24 h; (ii) EtOH, reflux 18 h; (iii) 2 M NaOH, MeOH, 50 °C, 5h.

3.3.3 Sensor Characterisation

Absorbance and fluorescence emission spectra of chemosensor **1** (50 μM in acetonitrile) were first measured in the presence of an excess of Mg^{2+} (100 μM), as well as other biologically relevant metal ions (Li^+ , Na^+ , K^+ , Cs^+ , Ca^{2+} , Mn^{2+} , Cu^{2+} and Zn^{2+}), to characterise its selectivity profile. Spectra were recorded in ambient light conditions, in order to characterise the metal-induced SP to MC isomerisation.³⁶⁻³⁷ Results displayed in Figure 3 show that chemosensor **1** has the highest fluorescence emission in the presence of Mg^{2+} , 2-fold higher than that of Ca^{2+} and 3–4-fold higher than for Li^+ and Zn^{2+} . In the presence of excess Mg^{2+} , **1** gives an emission maximum at 590 nm, hypsochromically shifted compared to the chemosensor in the presence of Ca^{2+} (605 nm) or in the absence of metal ions (605 nm). These maxima are characteristic of the MC-form of the spiropyran, and thus, metal ion binding induces isomerisation of chemosensor **1** to the more coloured MC(**1**)- M^{2+} complex.³⁶ As has been reported previously,³³ chemosensor **1** exhibits a significant increase in the characteristic MC absorbance in the presence of Cu^{2+} (Figure S3-10), while the absorbance spectra of the **1**- Mg^{2+} and **1**- Ca^{2+} species are similar to the SP form of **1** under ambient light conditions (see Figure 3A).

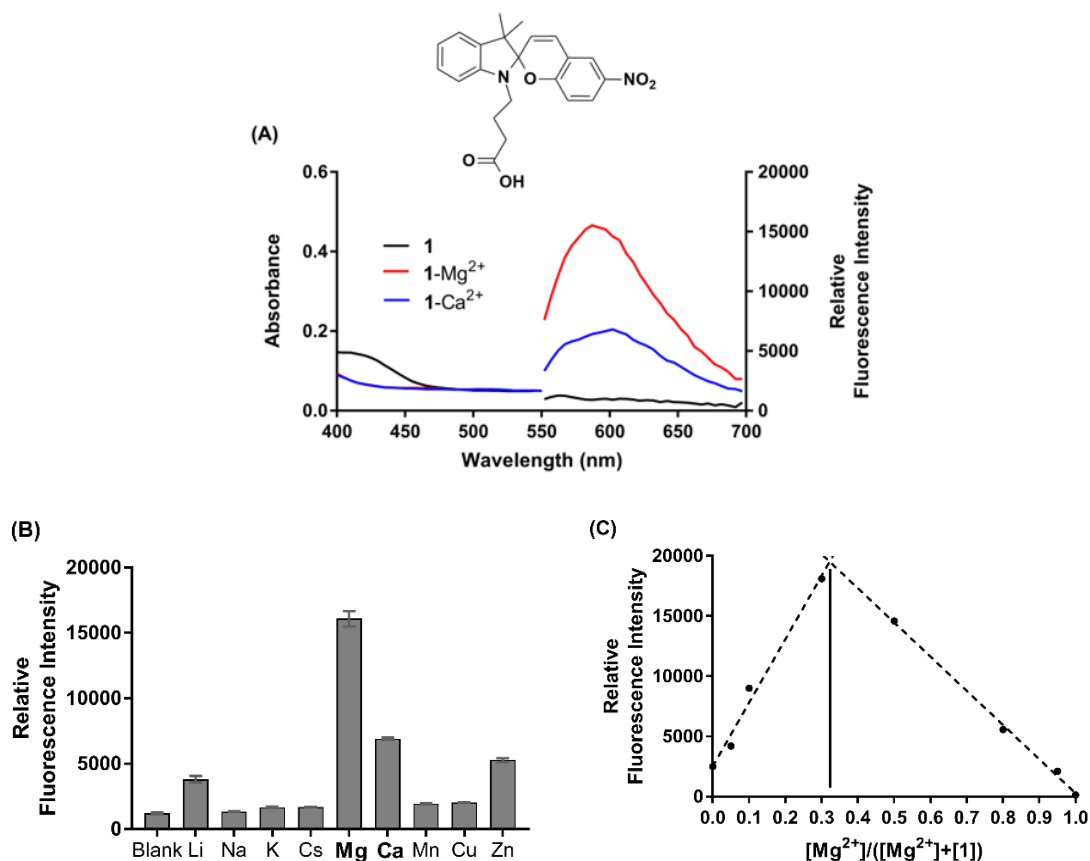


Figure 3. (A) Absorbance and fluorescence emission spectra of chemosensor **1** in the absence (black, 50 μM) and presence of excess Mg²⁺ (red, 100 μM) and Ca²⁺ (blue, 100 μM), respectively. (B) Selectivity profile of **1** (50 μM) in the presence of various biologically relevant metal ions (100 μM). (C) Job's plot analysis of MC(**1**)-Mg²⁺ complex, where [SP] + [Mg²⁺] = 100 μM in acetonitrile. Excitation was at 532 nm, and all experiments were performed under ambient light conditions.

Data pertaining to the photophysical characterisation of chemosensor **1** is presented in Table 1. The binding stoichiometry of **1** in the presence of excess Mg²⁺ was next defined by Job's plot analysis, as displayed in Figure 3C. Chemosensor **1** binds Mg²⁺ in a 2:1 ratio (Job's plot apex at 0.33), in agreement with the design proposal and DFT modelling discussed above. Similarly, Job's analysis showed that **1** also binds Ca²⁺ in a 2:1 ratio (apex at 0.33, Figure S3-11). Dissociation constants (K_d) for the binding of **1** with Mg²⁺ and Ca²⁺, respectively, were determined by fitting a saturation binding model to concentration curves of the chemosensor (50 μM) with increasing concentrations of metal ions (1–200 μM) (Figure S3-12). The dissociation constant for chemosensor **1** with Mg²⁺ was calculated to be 6.0 μM, and a 3-fold weaker affinity was observed with Ca²⁺ (K_d = 18.7 μM). Finally, the quantum yields of fluorescence for chemosensor **1** in the presence of Mg²⁺ (Φ = 0.20) and Ca²⁺ (Φ = 0.06) were determined via the method described in the Supporting Information, using Rhodamine B as the calibration standard (Figure S3-13).⁵²

Table 1. Photophysical properties of Chemosensor **1**.

Chemosensor [†]	Em λ_{\max} (nm)	Stoichiometry [‡]	Φ [°]	K _d (μ M)
MC(1)	605	*	*	*
MC(1)-Mg ²⁺	590	2:1 (0.33)	0.20	6.0
MC(1)-Ca ²⁺	605	2:1 (0.33)	0.06	18.7

[†] Measurements recorded at 25 °C in acetonitrile solvent, under ambient light conditions.

[‡] Stoichiometric ratio of chemosensor to metal ion determined from Job's plot (apex). [°] Relative fluorescence quantum yield determined in acetonitrile using Rhodamine B ($\Phi = 0.31$) as a standard.

* No data obtained.

The absorbance and fluorescence emission spectra for the fluorinated chemosensor **2** were similarly analysed. Fluorescence emission spectra gave two distinct emission maxima, which are attributable to the SP (~560 nm) and MC (~605 nm) isomers of chemosensor **2**³⁶ and suggest the presence of both these species in solution (Figure S3-14), as per the earlier proton NMR spectrum. The chemosensor shows a similar fluorescence response in the presence of Mg²⁺ and Zn²⁺ with non-significant response for all other ions. In particular, a diminished fluorescence is observed in the presence of Ca²⁺ compared to chemosensor **1**. In all cases, while the presence of metal ions appears to affect the fluorescence intensity of chemosensor **2**, no shifts in the emission maxima are observed. Interestingly, chemosensor **2** exhibits no absorbance in the characteristic MC region and unlike chemosensor **1**, no absorbance was observed for the **2**-Cu²⁺ species (Figure S3-10). Job's plot analysis of chemosensor **2** suggests multiple potential binding stoichiometries may be present (Figure S3-15). Based on these results, subsequent optical fibre-based studies were only performed on chemosensor **1**. Finally, fluorescence emission spectra of the ester-protected precursors **3** and **4** revealed a loss of fluorescence intensity in the presence of all ions (see Figure S3-16), indicating that the free carboxylic acid (of **1** and **2**) is important for metal ion chelation, and hence chemosensor brightness and selectivity as per the earlier discussion and modelling results.

3.3.4 Photoswitching in an Optical Fibre

In the final part of the study, chemosensor **1** was combined with a microstructured optical fibre in order to demonstrate compatibility and as a first step in the development of a light-controlled, dip-sensor for Mg²⁺. Photostability and photo-reversibility of analyte binding to **1** were defined on a silica-based, in-house fabricated suspended core optical fibre (SCF),⁵³⁻⁵⁴ which allows rapid photoswitching using a laser. Interaction between the light and **1** in

microstructured optical fibres is extended along the entire length of the fiber, while maintaining the integrity of the device. In SCFs, the glass core is suspended in air by thin struts, allowing a portion of the guided light to extend outside the fiber core into the surrounding holes which serve as low-volume sample chambers (see Figure 4A, schematic).

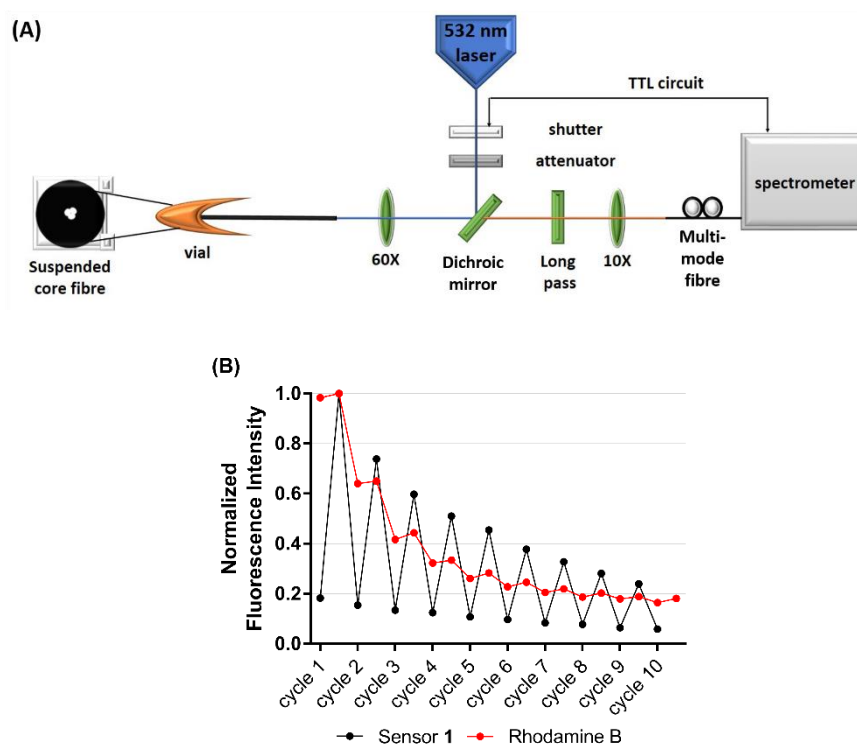


Figure 4. (A) Schematic of the optical setup used to measure fluorescence from a suspended core microstructured optical fibre (SCF). (B) Photostability of chemosensor **1** (500 μM) in the presence of Mg^{2+} (1 mM) (black), compared to the photostability of Rhodamine B (red) in an SCF. Excitation was at 532 nm, with 10×50 ms pulses at 1 mW power. Results are normalised to the highest fluorescence measurement, respectively.

Photoswitching between the weakly fluorescent SP isomer and the highly fluorescent MC(1)- Mg^{2+} complex was achieved by irradiation with UV ('on'-cycle, 365 nm lamp) and visible light ('off'-cycle, 532 nm green laser), respectively, within the SCF platform. A significant decrease in signal was observed in the first 4 experimental cycles, falling to 50% of the initial fluorescence, as seen in Figure 4B. This decrease is likely the result of the sensor switching back to the weakly-fluorescent SP isomer under the influence of the 532 nm laser light and/or light induced parasitic side reactions that led to the formation of non-switchable by-products, a process that is not completely understood and beyond the scope of this work.⁵⁵ In comparison, the fluorescence of Rhodamine B (a fluorophore capable of excitation under the same 532 nm laser but not photoswitchable) fell to 30% of the initial fluorescence by the same photoswitching cycle in a similar experiment. These results demonstrate that

chemosensor **1** is capable of photoswitching over multiple cycles in the SCF platform, however future work is needed to optimise the laser power and intensity to reduce the initial photo-decolouration.

3.4 Conclusions

Here we present the rational design and photophysical characterisation of spiropyran-based chemosensors for Mg^{2+} , **1** and **2**. Fluorescence characterisation revealed that the C6'-nitro functionalised chemosensor **1** exhibits a 2-fold fluorescence enhancement factor for Mg^{2+} over Ca^{2+} ions, comparable to the commercially available mag-fura-2.²¹ Importantly, the dissociation constant (K_d) of **1**- Mg^{2+} was calculated to be 6.0 μM , with a 3-fold weaker affinity observed for **1**- Ca^{2+} (18.7 μM). As proposed by DFT modelling, stoichiometric studies support 2:1 chemosensor to metal ion binding of **1** with Mg^{2+} . Interestingly, structural and fluorescence characterisation of the C6'-fluorinated analogue **2** suggests the presence of both SP and MC species in solution, while stoichiometric studies indicate a complex metal binding relationship with Mg^{2+} . Subsequent studies were thus focused on **1**, which was combined with a suspended core optical fiber (SCF) as a first step towards the development of a light-controlled, reversible dip-sensor for Mg^{2+} . Fibre-based photoswitching experiments revealed reversible Mg^{2+} binding with improved photostability, as compared to the non-photoswitchable Rhodamine B fluorophore.

3.5 Acknowledgements

The authors (G. M. S., S. H., A. B., H. E. -H. and A. D. A.) acknowledge funding support from the Centre of Nanoscale BioPhotonics, through the Australian Research Council (ARC) CE140100 003. This work was performed in part at the OptoFab node of the Australian National Fabrication Facility utilising Commonwealth and South Australian State Government funding. The authors would like to acknowledge Yow Yu Ting and Nicole Tan Jia Ling for assistance with fluorescence characterisation. This work was supported with high-performance computing resources provided by the Phoenix HPC service at the University of Adelaide and the A*STAR Computational Resource Center (A*CRC).

3.6 References

1. Glasdam, S. M.; Glasdam, S.; Peters, G. H., The Importance of Magnesium in the Human Body: A Systematic Literature Review. *Advances in clinical chemistry* **2016**, *73*, 169-93.
2. Wolf, F. I.; Trapani, V., Cell (patho)physiology of magnesium. *Clinical science* **2008**, *114* (1), 27-35.
3. Gunther, T., Concentration, compartmentation and metabolic function of intracellular free Mg²⁺. *Magnesium research* **2006**, *19* (4), 225-36.
4. Romani, A. M., Cellular magnesium homeostasis. *Archives of biochemistry and biophysics* **2011**, *512* (1), 1-23.
5. Ryan, M. F., The role of magnesium in clinical biochemistry: an overview. *Annals of clinical biochemistry* **1991**, *28* (Pt 1), 19-26.
6. Shi, J.; Krishnamoorthy, G.; Yang, Y.; Hu, L.; Chaturvedi, N.; Harilal, D.; Qin, J.; Cui, J., Mechanism of magnesium activation of calcium-activated potassium channels. *Nature* **2002**, *418* (6900), 876-80.
7. Mubagwa, K.; Gwanyanya, A.; Zakharov, S.; Macianskiene, R., Regulation of cation channels in cardiac and smooth muscle cells by intracellular magnesium. *Archives of biochemistry and biophysics* **2007**, *458* (1), 73-89.
8. Nadler, M. J.; Hermosura, M. C.; Inabe, K.; Perraud, A. L.; Zhu, Q.; Stokes, A. J.; Kurosaki, T.; Kinet, J. P.; Penner, R.; Scharenberg, A. M.; Fleig, A., LTRPC7 is a Mg.ATP-regulated divalent cation channel required for cell viability. *Nature* **2001**, *411* (6837), 590-5.
9. Ko, Y. H.; Hong, S.; Pedersen, P. L., Chemical mechanism of ATP synthase. Magnesium plays a pivotal role in formation of the transition state where ATP is synthesized from ADP and inorganic phosphate. *The Journal of biological chemistry* **1999**, *274* (41), 28853-6.
10. Sarrafzadegan, N.; Khosravi-Boroujeni, H.; Lotfizadeh, M.; Pourmogaddas, A.; Salehi-Abargouei, A., Magnesium status and the metabolic syndrome: A systematic review and meta-analysis. *Nutrition* **2016**, *32* (4), 409-17.
11. Mooren, F. C., Magnesium and disturbances in carbohydrate metabolism. *Diabetes, obesity & metabolism* **2015**, *17* (9), 813-23.
12. Volpe, S. L., Magnesium, the metabolic syndrome, insulin resistance, and type 2 diabetes mellitus. *Critical reviews in food science and nutrition* **2008**, *48* (3), 293-300.
13. Veronese, N.; Zurlo, A.; Solmi, M.; Luchini, C.; Trevisan, C.; Bano, G.; Manzano, E.; Sergi, G.; Rylander, R., Magnesium Status in Alzheimer's Disease: A Systematic Review. *American journal of Alzheimer's disease and other dementias* **2016**, *31* (3), 208-13.
14. Barbagallo, M.; Belvedere, M.; Di Bella, G.; Dominguez, L. J., Altered ionized magnesium levels in mild-to-moderate Alzheimer's disease. *Magnesium research* **2011**, *24* (3), S115-21.
15. Kolte, D.; Vijayaraghavan, K.; Khera, S.; Sica, D. A.; Frishman, W. H., Role of magnesium in cardiovascular diseases. *Cardiology in review* **2014**, *22* (4), 182-92.
16. Kupetsky-Rincon, E. A.; Uitto, J., Magnesium: novel applications in cardiovascular disease--a review of the literature. *Annals of nutrition & metabolism* **2012**, *61* (2), 102-10.
17. Geiger, H.; Wanner, C., Magnesium in disease. *Clinical Kidney Journal* **2012**, *5* (Suppl 1), i25-i38.

18. Long, S.; Romani, A. M. P., Role of Cellular Magnesium in Human Diseases. *Austin journal of nutrition and food sciences* **2014**, 2 (10), 1051.
19. Carter, K. P.; Young, A. M.; Palmer, A. E., Fluorescent Sensors for Measuring Metal Ions in Living Systems. *Chemical Reviews* **2014**, 114 (8), 4564-4601.
20. Raju, B.; Murphy, E.; Levy, L. A.; Hall, R. D.; London, R. E., A fluorescent indicator for measuring cytosolic free magnesium. *American Journal of Physiology-Cell Physiology* **1989**, 256 (3), C540-C548.
21. Fluorescent Mg²⁺ Indicators. In *The Molecular Probes Handbook - A Guide to Fluorescent Probes and Labeling Technologies*, 11 ed.; ThermoFisher Scientific: 2010; pp 862-864.
22. Levy, L. A.; Murphy, E.; Raju, B.; London, R. E., Measurement of cytosolic free magnesium ion concentration by fluorine-19 NMR. *Biochemistry* **1988**, 27 (11), 4041-4048.
23. Schachter, M.; Gallagher, K. L.; Sever, P. S., Measurement of intracellular magnesium in a vascular smooth muscle cell line using a fluorescent probe. *Biochimica et Biophysica Acta (BBA) - General Subjects* **1990**, 1035 (3), 378-380.
24. Murphy, E.; Freudenrich, C. C.; Levy, L. A.; London, R. E.; Lieberman, M., Monitoring cytosolic free magnesium in cultured chicken heart cells by use of the fluorescent indicator Fura-2. *P Natl Acad Sci USA* **1989**, 86 (8), 2981-2984.
25. Grubbs, R.; Walter, A., *Determination of cytosolic Mg²⁺ activity and buffering in BC3H-1 cells with mag-fura-2*. 1994; Vol. 136, p 11-22.
26. Martínez-Zaguilán, R.; Parnami, J.; Martinez, G. M., Mag-Fura-2 (Fura-2) Exhibits both Low (μM) and High (nM) Affinity for Ca²⁺. *Cellular Physiology and Biochemistry* **1998**, 8 (3), 158-174.
27. Hurley, T. W.; Ryan, M. P.; Brinck, R. W., Changes of cytosolic Ca²⁺ interfere with measurements of cytosolic Mg²⁺ using mag-fura-2. *American Journal of Physiology-Cell Physiology* **1992**, 263 (2), C300-C307.
28. Shindo, Y.; Fujii, T.; Komatsu, H.; Citterio, D.; Hotta, K.; Suzuki, K.; Oka, K., Newly developed Mg²⁺-selective fluorescent probe enables visualization of Mg²⁺ dynamics in mitochondria. *PLoS one* **2011**, 6 (8), e23684.
29. Komatsu, H.; Iwasawa, N.; Citterio, D.; Suzuki, Y.; Kubota, T.; Tokuno, K.; Kitamura, Y.; Oka, K.; Suzuki, K., Design and synthesis of highly sensitive and selective fluorescein-derived magnesium fluorescent probes and application to intracellular 3D Mg²⁺ imaging. *Journal of the American Chemical Society* **2004**, 126 (50), 16353-60.
30. Matsui, Y.; Sadhu, K. K.; Mizukami, S.; Kikuchi, K., Highly selective tridentate fluorescent probes for visualizing intracellular Mg²⁺ dynamics without interference from Ca²⁺ fluctuation. *Chem Commun (Camb)* **2017**, 53 (77), 10644-10647.
31. Trapani, V.; Farruggia, G.; Marraccini, C.; Iotti, S.; Cittadini, A.; Wolf, F. I., Intracellular magnesium detection: imaging a brighter future. *The Analyst* **2010**, 135 (8), 1855-66.
32. Trapani, V.; Schweigel-Rontgen, M.; Cittadini, A.; Wolf, F. I., Intracellular magnesium detection by fluorescent indicators. *Methods in enzymology* **2012**, 505, 421-44.
33. Natali, M.; Giordani, S., Interaction studies between photochromic spiropyran and transition metal cations: the curious case of copper. *Organic & biomolecular chemistry* **2012**, 10 (6), 1162-1171.
34. Natali, M.; Giordani, S., Molecular switches as photocontrollable "smart" receptors. *Chemical Society reviews* **2012**.

35. Lukyanov, B. S.; Lukyanova, M. B., Spiropyran: Synthesis, Properties, and Application. *Chem Heterocycl Com+* **2005**, *41* (3), 32.
36. Klajn, R., Spiropyran-based dynamic materials. *Chemical Society reviews* **2014**, *43* (1), 148-84.
37. Zakharova, M. I.; Pimienta, V.; Metelitsa, A. V.; Minkin, V. I.; Micheaua, J. C., Thermodynamic and kinetic analysis of metal ion complexation by photochromic spiropyran. *Russ Chem B+* **2009**, *58* (7), 1329-1337.
38. Heng, S.; Mak, A. M.; KostECKI, R.; Zhang, X. Z.; Pei, J. X.; Stubing, D. B.; Ebendorff-Heidepriem, H.; Abell, A. D., Photoswitchable calcium sensor: 'On'-'Off' sensing in cells or with microstructured optical fibers. *Sensor Actuat B-Chem* **2017**, *252*, 965-972.
39. Heng, S.; McDevitt, C. A.; KostECKI, R.; Morey, J. R.; Eijkelkamp, B. A.; Ebendorff-Heidepriem, H.; Monroe, T. M.; Abell, A. D., Microstructured Optical Fiber-based Biosensors: Reversible and Nanoliter-Scale Measurement of Zinc Ions. *ACS applied materials & interfaces* **2016**, *8* (20), 12727-12732.
40. Heng, S.; Nguyen, M.-C.; KostECKI, R.; Monroe, T. M.; Abell, A. D., Nanoliter-scale, regenerable ion sensor: sensing with a surface functionalized microstructured optical fibre. *Rsc Adv* **2013**, *3* (22), 8308-8317.
41. Stubing, D. B.; Heng, S.; Monroe, T. M.; Abell, A. D., A comparative study of the fluorescence and photostability of common photoswitches in microstructured optical fibre. *Sensor Actuat B-Chem* **2017**, *239*, 474-480.
42. Monroe, T. M.; Warren-Smith, S.; Schartner, E. P.; François, A.; Heng, S.; Ebendorff-Heidepriem, H.; Afshar, S., Sensing with suspended-core optical fibers. *Opt Fiber Technol* **2010**, *16* (6), 343-356.
43. Schartner, E. P.; Henderson, M. R.; Purdey, M.; Dhattrak, D.; Monroe, T. M.; Gill, P. G.; Callen, D. F., Cancer Detection in Human Tissue Samples Using a Fiber-Tip pH Probe. *Cancer Res* **2016**, *76* (23), 6795-6801.
44. Purdey, M. S.; Schartner, E. P.; Sutton-McDowall, M. L.; Ritter, L. J.; Thompson, J.; Monroe, T. M.; Abell, A. D. In *Localised hydrogen peroxide sensing for reproductive health*, SPIE Optics + Optoelectronics, SPIE: 2015; p 10.
45. Collins, G. E.; Choi, L.-S.; Ewing, K. J.; Michelet, V.; Bowen, C. M.; Winkler, J. D., Photoinduced switching of metal complexation by quinolinospiropyranindolines in polar solvents. *Chem. Commun.* **1999**, 321-322.
46. Garcia, A. A.; Cherian, S.; Park, J.; Gust, D.; Jahnke, F.; Rosario, R., Photon-controlled phase partitioning of spiropyran. *Journal of Physical Chemistry A* **2000**, *104* (26), 6103-6107.
47. Baldrighi, M.; Locatelli, G.; Desper, J.; Aakeroy, C. B.; Giordani, S., Probing Metal Ion Complexation of Ligands with Multiple Metal Binding Sites: The Case of Spiropyran. *Chem-Eur J* **2016**, *22* (39), 13976-13984.
48. Heng, S.; Mak, A. M.; Stubing, D. B.; Monroe, T. M.; Abell, A. D., Dual sensor for Cd(II) and Ca(II): selective nanoliter-scale sensing of metal ions. *Analytical chemistry* **2014**, *86* (7), 3268-72.
49. Filley, J.; Ibrahim, M. A.; Nimlos, M. R.; Watt, A. S.; Blake, D. M., Magnesium and calcium chelation by a bis-spiropyran. *Journal of Photochemistry and Photobiology A: Chemistry* **1998**, *117* (3), 193-198.
50. Becke, A. D., Density - functional thermochemistry. III. The role of exact exchange. *The Journal of Chemical Physics* **1993**, *98* (7), 5648-5652.
51. Frisch, M. J. *e. a. Gaussian 09*, Gaussian, Inc: Wallingford CT, 2009.

52. Magde, D.; Rojas, G. E.; Seybold, P. G., Solvent Dependence of the Fluorescence Lifetimes of Xanthene Dyes. *Photochem Photobiol* **1999**, 70 (5), 737-744.
53. Zhao, J. B.; Jin, D. Y.; Schartner, E. P.; Lu, Y. Q.; Liu, Y. J.; Zvyagin, A. V.; Zhang, L. X.; Dawes, J. M.; Xi, P.; Piper, J. A.; Goldys, E. M.; Monro, T. M., Single-nanocrystal sensitivity achieved by enhanced upconversion luminescence. *Nat Nanotechnol* **2013**, 8 (10), 729-734.
54. Schartner, E. P.; Tsiminis, G.; Francois, A.; Kostecki, R.; Warren-Smith, S. C.; Nguyen, L. V.; Heng, S.; Reynolds, T.; Klantsataya, E.; Rowland, K. J.; Abell, A. D.; Ebendorff-Heidepriem, H., Taming the Light in Microstructured Optical Fibers for Sensing. *Int J Appl Glass Sci* **2015**, 6 (3), 229-239.
55. Wiedemann, U.; Alt, W.; express, M.-D., Switching photochromic molecules adsorbed on optical microfibres. *Optics express* **2012**.

CHAPTER 4

Investigating the effect of *N*-indole functionalisation on metal ion selectivity in crowned spiropyran sensors

Georgina M. Sylvia, Sabrina Heng, and Andrew D. Abell.

ARC Centre of Excellence for Nanoscale BioPhotonics (CNBP), Institute for Photonics and Advanced Sensing (IPAS), School of Physical Sciences, The University of Adelaide, South Australia, Australia 5005.

Unpublished and unsubmitted work prepared in a manuscript-style.

Statements of Authorship

Title of Paper	Investigating the effect of N-indole functionalisation on metal ion selectivity in crowned spiropyran sensors.
Publication Status	<input type="checkbox"/> Published <input type="checkbox"/> Accepted for Publication <input type="checkbox"/> Submitted for Publication <input checked="" type="checkbox"/> Unpublished and Unsubmitted work written in manuscript style
Publication Details	

Principal Author

Name of Principal Author (Candidate)	Georgina M. Sylvia		
Contribution to the Paper	Performed analysis on all samples, interpreted data and wrote manuscript.		
Overall percentage (%)	70 %		
Certification:	This paper reports on original research I conducted during the period of my Higher Degree by Research candidature and is not subject to any obligations or contractual agreements with a third party that would constrain its inclusion in this thesis. I am the primary author of this paper.		
Signature		Date	08/11/2017

Co-Author Contributions

By signing the Statement of Authorship, each author certifies that:

- i. the candidate's stated contribution to the publication is accurate (as detailed above);
- ii. permission is granted for the candidate to include the publication in the thesis; and
- iii. the sum of all co-author contributions is equal to 100% less the candidate's stated contribution.

Name of Co-Author	Sabrina Heng		
Contribution to the Paper	Supervised development of work, helped in data interpretation and manuscript evaluation.		
Signature		Date	10/11/17

Name of Co-Author	Andrew D. Abell		
Contribution to the Paper	Helped to evaluate and edit the manuscript, acted as corresponding author.		
Signature		Date	14/11/2017

4.1 Abstract

A series of spiropyran-based sensors are presented, incorporating both C8' and N1-indole metal ion binding domains, in order to explore the influence of multiple chelating groups on calcium ion (Ca^{2+}) selectivity. The sensors possess N1-indole functionalisation in the form of hydroxyethyl (**SP-1**), ethoxycarbonylbutyl (**SP-2**) and carboxybutyl (**SP-3**) groups, while all three sensors incorporate a 1-aza-15-crown-5 ionophore at the C8' position. Absorbance and fluorescence characterisation of metal ion binding revealed that in particular, sensor **SP-3** gave excellent Ca^{2+} -selectivity, improved dissociation constant ($K_d \text{MC}(\text{SP-3})\text{-Ca}^{2+} = 22 \mu\text{M}$) and increased quantum yield of fluorescence ($\Phi \text{MC}(\text{SP-3})\text{-Ca}^{2+} = 0.37$), compared to the other sensors. These results suggest the carboxybutyl N1-indole functionality of **SP-3** may play a role in stabilizing Ca^{2+} in the 1-aza-15-crown-5 ionophore, promoting metal-induced isomerisation to the $\text{MC}(\text{SP-3})\text{-Ca}^{2+}$ complex and thus a bright, Ca^{2+} -selective, red fluorescence signal.

4.2 Introduction

Calcium ions (Ca^{2+}) are a ubiquitous chemical signalling molecule in cell proliferation, differentiation and death.¹⁻⁵ The concentration of Ca^{2+} is known to fluctuate within a typical cell cycle, in response to external stimuli,^{3,6-7} and in disease states such as chronic kidney disease-mineral bone disorder (CKD-MBD)⁸⁻⁹ and cancer.¹⁰⁻¹¹ Fluorescent sensors, in combination with specialised imaging technologies, are typically used to sense Ca^{2+} in and around cells.¹²⁻¹⁴

An ability to turn sensing on and off, with an external and non-invasive stimulus such as light, would extend the range of sensing capability for live cell imaging. Our group¹⁵⁻²⁰ and others²¹⁻²³ have reported extensively on reversible metal ion sensors that contain a photoswitchable spiropyran core to allow the fluorescence signal to be turned on and off on demand. Spiroyrans can be reversibly switched between a weakly fluorescent spiropyran (SP), and a highly fluorescent merocyanine (MC) isomer upon irradiation with UV and visible light, respectively (see Figure 1a).²⁴⁻²⁵ The spiropyran scaffold is easily modified in order to tailor selectivity for one analyte over another, and this is commonly achieved by incorporating a metal ion binding domain at the N1-indole and/or C8' position of the benzopyran ring (see Figure 1).

For example, previous work has shown that spiropyran-based sensors C8'-functionalised with various sizes of azacrown-ether ionophores (1-aza-12-crown-4, 1-aza-15-crown-5 and 1-aza-18-crown-6), generally favour binding of the Li^+ cation over other alkali metals.^{16, 26}

Later studies with a wider range of metal ions for analysis confirmed that these sensors, in particular the 1-aza-18-crown-6 ionophore analogue, possesses a greater affinity for divalent metal ions such as Ca^{2+} .²⁷⁻²⁸ Importantly, the phenolate anion of the ring-opened merocyanine isomer was found to bind cooperatively with metal ions in the ionophore, providing an additional chelating site when the sensor is in the ring-opened form.²⁹

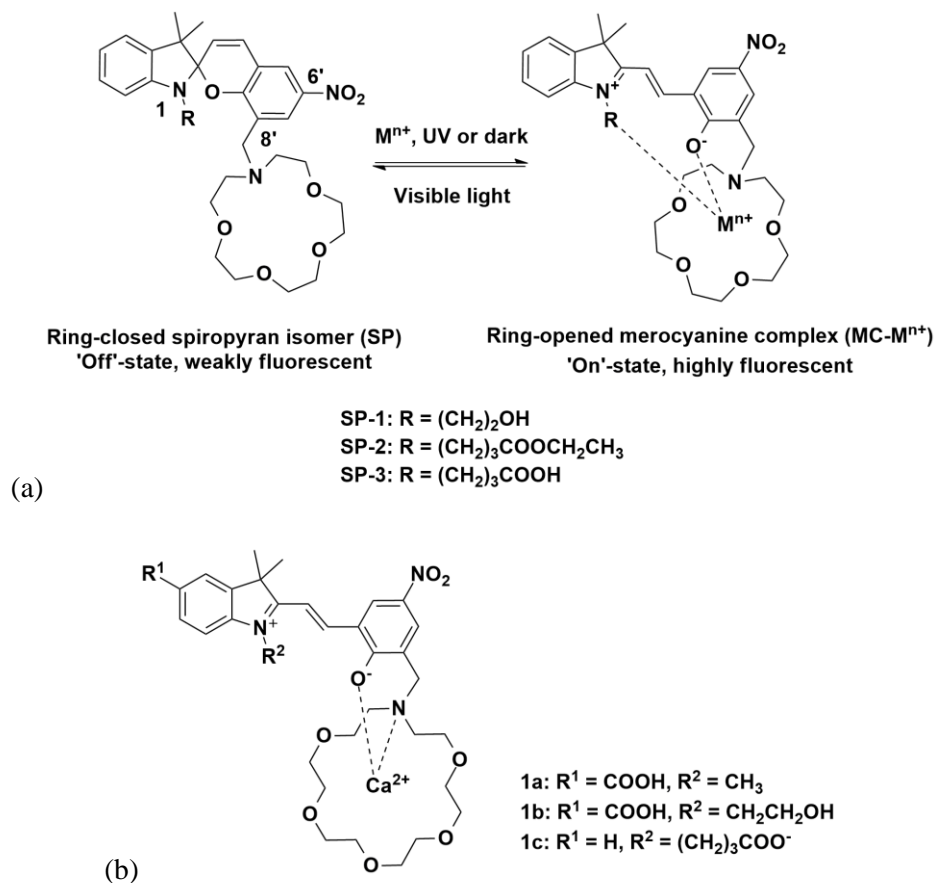


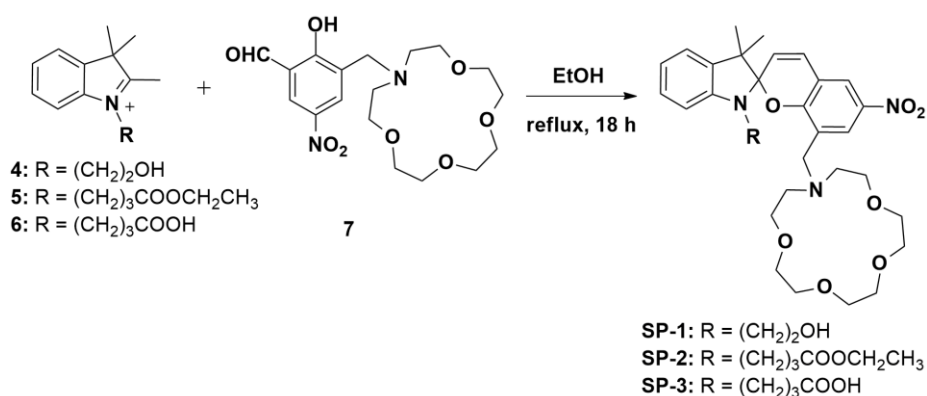
Figure 1. (a) Structures of sensors **SP-1**, **SP-2** and **SP-3** as the ring-closed, weakly fluorescent spiropyran (SP, 'off') isomer, and the proposed ring-opened, highly fluorescent merocyanine (MC- M^{n+} , 'on') complex. (b) Structure of the earlier sensor analogues **1a**, **1b** and **1c** in the merocyanine- Ca^{2+} metal bound complex.¹⁸

Introducing a chelating moiety at the N1-indole position has also been shown to influence metal ion selectivity.^{22-23, 30-33} In an earlier study, we demonstrated that sensors with both a C8' ionophore (1-aza-18-crown-6) and N1-indole functionalisation (methyl, hydroxyethyl and carboxybutyl substituents, sensors **1a**, **1b** and **1c** Figure 1b, respectively) give rise to selectivity for Ca^{2+} over other biologically relevant metal ions.¹⁸ The N1-methyl substituted sensor was found to be the most selective of this series, binding Ca^{2+} in the azacrown ionophore without contribution of a chelating substituent on the N1-indole (binding as depicted in Figure 1b).

In this Chapter we present a series of spiropyran-based sensors incorporating both C8' and N1-indole metal ion binding domains, in order to determine the effect of multiple chelating groups on Ca²⁺ selectivity. The sensors possess N1-indole functionalisation in the form of hydroxyethyl (**SP-1**), ethoxycarbonylbutyl (**SP-2**) carboxybutyl (**SP-3**) groups, with a 1-aza-15-crown-5 ionophore incorporated at the C8' position (Figure 1a). This 15-membered azacrown ether ionophore is a smaller analogue to the 18-membered azacrown reported for Ca²⁺-selective sensors, **1a**, **1b** and **1c**.¹⁸ We hypothesize that in the presence of a smaller C8' ionophore, the N1-indole functionality of spiropyran may contribute to stabilizing Ca²⁺ in the 15-membered azacrown, promoting metal-induced isomerisation to the MC-Ca²⁺ complex for improved fluorescence intensity and Ca²⁺ selectivity.

4.3 Results and Discussion

4.3.1 Synthesis



Scheme 1. Synthesis of sensors **SP-1**, **SP-2** and **SP-3**.

Sensors **SP-1**, **SP-2** and **SP-3** were prepared as outlined in Scheme 1. Separate condensation reactions of indolines **4**, **5**¹⁸ and **6**³⁴ with aldehyde **7**,³⁵ gave the N1-functionalized, C8'-azacrown spiropyran **SP-1**, **SP-2** and **SP-3**, respectively. The crude products were purified by reverse-phase silica chromatography or high-performance liquid chromatography, and characterized by ¹H, ¹³C NMR and HRMS (see 5.4 Supporting Information for Chapter 4, Figures S4-1 –S4-7). All compounds showed resonances at ~ δ 7.02 and ~ δ 5.95 ppm with coupling constant value of *J* = 10.5 Hz, characteristic of the *cis* alkene protons of spiropyran.

4.3.2 Sensor Characterisation

Absorbance and fluorescence emission spectra of sensors **SP-1**, **SP-2** and **SP-3** (50 μM in acetonitrile) were measured separately in the presence of an excess of Ca^{2+} and other biologically relevant metal ions (Li^+ , Na^+ , K^+ , Cs^+ , Mg^{2+} , Mn^{2+} , Cu^{2+} and Zn^{2+} ; each 100 μM in acetonitrile) to determine the influence of N1-indole functionalisation on the metal ion selectivity of the sensors. All spectra were recorded in ambient light conditions, in order to characterise the metal-induced spiropyran to merocyanine isomerisation.^{24, 36}

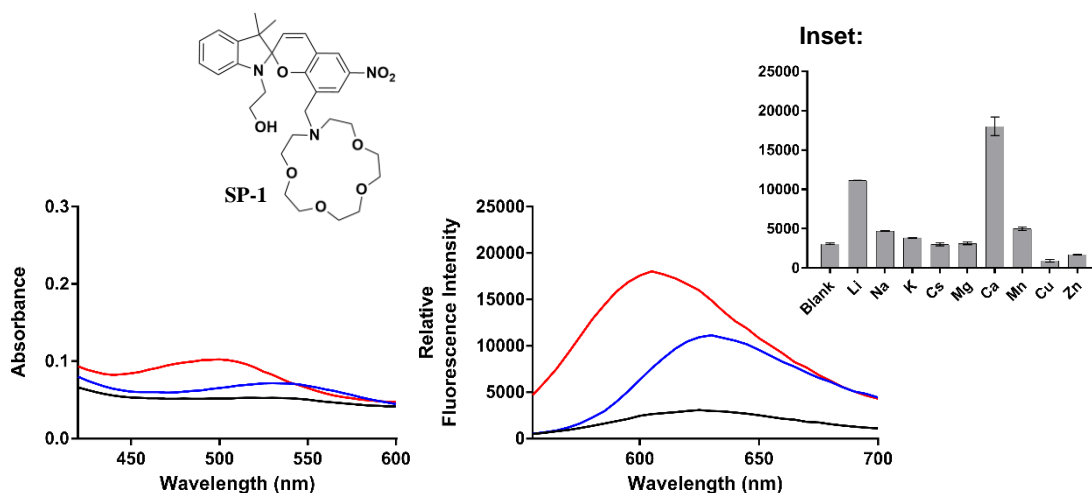


Figure 2. Absorbance and fluorescence emission spectra of **SP-1** (50 μM , black) in the absence and presence of excess Li^+ (100 μM , blue) and Ca^{2+} (100 μM , red). Inset: Fluorescence selectivity profile of **SP-1** (50 μM) in the presence of various biologically relevant metal ions (100 μM). Fluorescence spectra were recorded with 532 nm excitation, at 100 gain.

Fluorescence emission spectra displayed in Figure 2 show the hydroxyethyl substituted sensor **SP-1**, exhibits a 6-fold fluorescence enhancement in the presence of Ca^{2+} with a hypsochromic shift in the emission maxima (λ_{em} 605 nm) compared to the sensor in the absence of metal ion (λ_{em} 625 nm). **SP-1** also exhibits a 4-fold fluorescent enhancement in the presence of Li^+ with a bathochromic shift (λ_{em} 630 nm) compared to the sensor alone. This observation of Li^+ -selectivity is consistent with the literature, where the C8' azacrown ionophore is known to chelate Li^+ with a greater affinity than other monovalent metal ions such as Na^+ and K^+ .^{16, 26} Absorbance spectra of **SP-1** show a similar trend for the absorbance maxima in the presence of Ca^{2+} (λ_{abs} 500 nm) and Li^+ (λ_{abs} 530 nm) relative to the sensor alone (λ_{abs} 520 nm). Importantly, these maxima are characteristic of the MC isomer of the spiropyran sensor, which indicates metal ion binding to the sensor induces isomerisation to the more coloured MC(**SP-1**)- Ca^{2+} and MC(**SP-1**)- Li^+ complexes.^{24, 36} Dissociation constants (K_{d}) for the binding of **SP-1** with Ca^{2+} and Li^+ , respectively, were calculated with

fluorescence concentration curve data (see Figure S4-10). The dissociation constant for **SP-1** bound to Ca^{2+} ($K_d 43 \pm 2 \mu\text{M}$) was almost double that of the Li^+ complex ($K_d 24 \pm 3 \mu\text{M}$), indicating a greater binding affinity for Li^+ over Ca^{2+} .

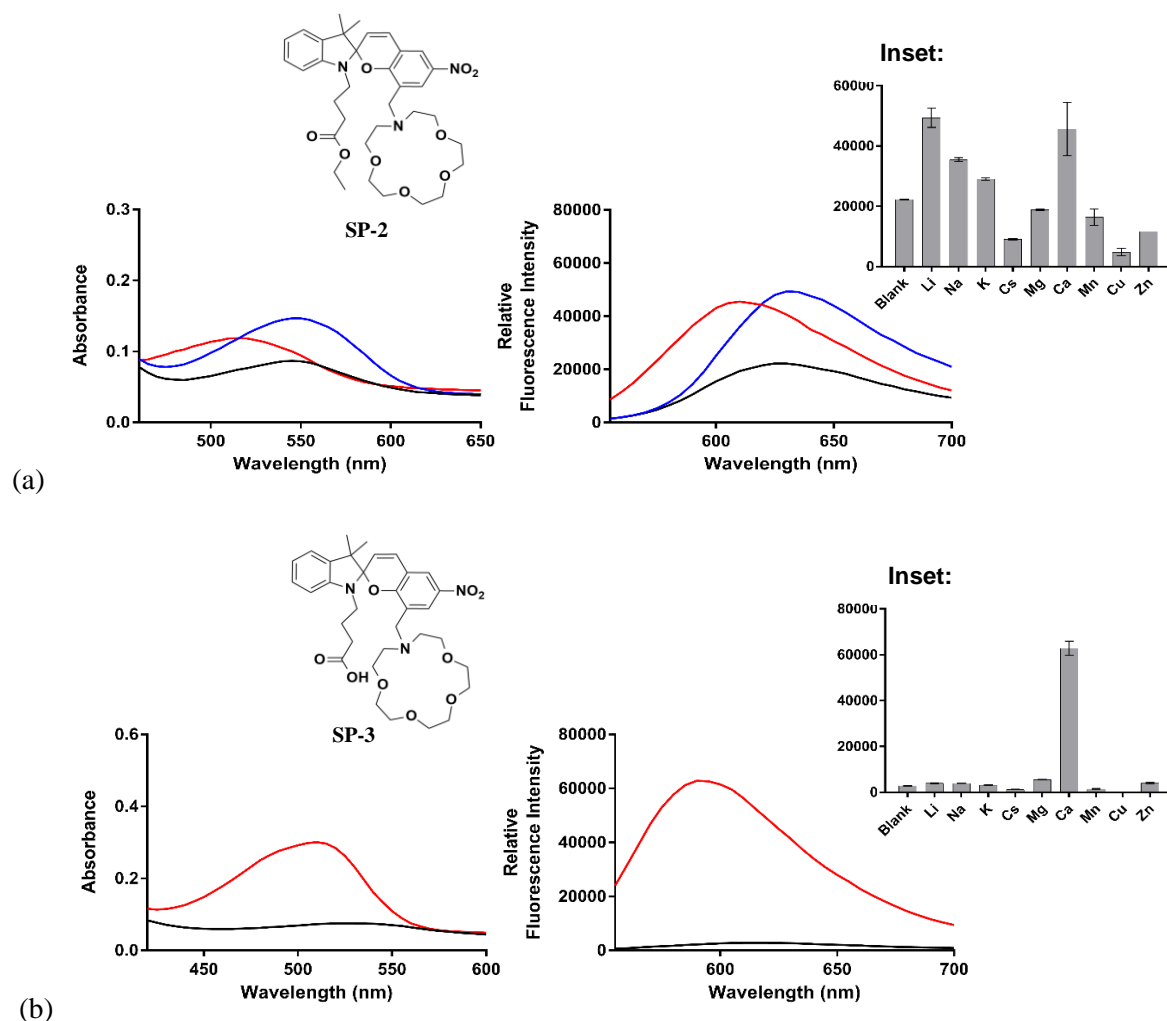


Figure 3. Absorbance and fluorescence emission spectra of (a) **SP-2** (50 μM) and (b) **SP-3** (50 μM) in the absence (black) and presence of excess Li^+ (100 μM , blue) and Ca^{2+} (100 μM , red). Inset: Fluorescence selectivity profiles for **SP-2** and **SP-3**, respectively. Fluorescence spectra were recorded with 532 nm excitation, at 100 gain for **SP-2**, and 75 gain for **SP-3**.

Absorbance and fluorescence emission spectra of the N1-ethoxycarbonylbutyl sensor **SP-2** and the N1-carboxybutyl sensor **SP-3** are presented in Figure 3. Sensor **SP-2** displays a similar selectivity profile to **SP-1**, with some affinity for both Li^+ ($\lambda_{\text{em}} 630 \text{ nm}$) and Ca^{2+} ($\lambda_{\text{em}} 610 \text{ nm}$) compared to the other metal ions and relative to the sensor alone ($\lambda_{\text{em}} 625 \text{ nm}$), however with a higher background fluorescence (see inset, Figure 3a). Absorbance spectra gave a consistent trend, with the $\text{MC}(\text{SP-2})\text{-Ca}^{2+}$ complex absorbance maximum ($\lambda_{\text{abs}} 515 \text{ nm}$) hypsochromically shifted relative to the sensor alone or in the presence of Li^+ ($\lambda_{\text{abs}} 545 \text{ nm}$). In comparison, fluorescence spectra of sensor **SP-3** (the free acid analogue of **SP-2**)

displays excellent Ca^{2+} selectivity, with no response for Li^+ or any of the other metal ions examined and improved signal-to-background fluorescence ratio relative to **SP-1** and **SP-2**. The sensor exhibits a 23-fold increased emission in the presence of Ca^{2+} (λ_{em} 590 nm), hypsochromically shifted relative to the sensor alone (λ_{em} 620 nm) (Figure 3b). Interestingly, sensor **SP-3** is significantly brighter than **SP-1** and **SP-2**, such that fluorescence spectra of **SP-3** were recorded at 75% gain of the other two sensors. Additionally, absorbance spectra depicted in Figure 3b show a 4-fold increase in absorbance intensity for **SP-3** in the presence of Ca^{2+} (λ_{abs} 510 nm), again hypsochromically shifted compared to the sensor alone (λ_{abs} 525 nm). This increased absorbance signal compared to the other sensors suggests a strong interaction between Ca^{2+} and the merocyanine isomer of **SP-3**.³⁷ The dissociation constant (K_d) for binding of **SP-3** with Ca^{2+} was next determined from concentration curve data (Figure S4-10), and calculated to be $22 \pm 1 \mu\text{M}$. This value is almost half that of the K_d calculated for **SP-1** and thus **SP-3** exhibits the highest binding affinity for Ca^{2+} of the two sensors. Results pertaining to the photophysical characterisation of **SP-1**, **SP-2** and **SP-3** is presented in Table 1.

Table 1. Photophysical properties of **SP-1**, **SP-2** and **SP-3**.

Sensor [†]	Em λ_{max} (nm)	Em λ_{max} (nm)	Stoichiometry [‡]	Φ^{δ}	K_d (μM)
MC(SP-1)	520	625	*	*	*
MC(SP-1)- Li^+	530	630	1:1 (0.5)	0.03	24 ± 3
MC(SP-1)- Ca^{2+}	500	605	3:1 (0.72)	0.03	43 ± 2
MC(SP-2)	545	625	*	*	*
MC(SP-2)- Li^+	545	630	*	0.04	*
MC(SP-2)- Ca^{2+}	515	610	*	0.06	*
MC(SP-3)	525	620	*	*	*
MC(SP-3)- Ca^{2+}	510	590	\sim 1:1 or 2:1 (0.58)	0.37	22 ± 1

[†] Measurements recorded at 25 °C in HPLC-grade acetonitrile. [‡] Sensor-to- $\text{M}^{\text{n+}}$ stoichiometric ratio derived from Job's plot, where the x-axis is mole fraction of metal ion, $[\text{M}^{\text{n+}}]/([\text{M}^{\text{n+}}]+[\text{SP}])$. ^δ Relative fluorescence quantum yield determined by using Rhodamine B ($\Phi = 0.31$ in water)³⁸ as a standard. * No value was obtained as binding was too weak or not relevant.

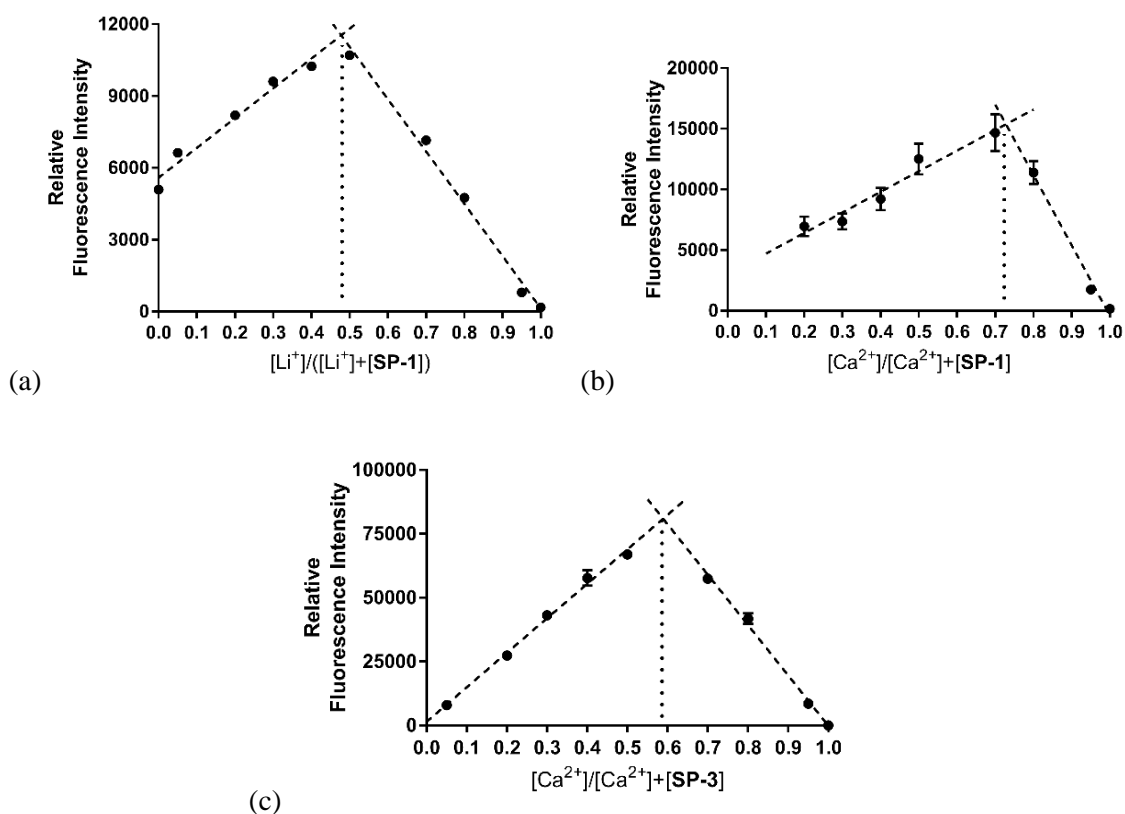


Figure 4. Job's plot analysis of binding stoichiometry of **SP-1** with Li⁺ (left) and Ca²⁺ (right), respectively. The concentration of sensor and metal ion are varied, where ($[SP-1] + [M^{n+}] = 100 \mu M$). (c) Job's plot analysis of binding stoichiometry of **SP-3** with Ca²⁺, where ($[SP-3] + [Ca^{2+}] = 100 \mu M$).

Job's method of continuous variation³⁹ was next employed to determine the stoichiometry of binding of metal ions to the sensors, with plots presented in Figure 4. Binding relationships of MC(**SP-1**)-Li⁺, MC(**SP-1**)-Ca²⁺ and MC(**SP-3**)-Ca²⁺ were investigated, as these sensor-metal ion pairs gave the greatest fluorescence emission intensity and selectivity of those investigated. Sensor **SP-1** appears to bind Li⁺ in a 1:1 ratio (Job's plot apex at ~ 0.50), which is consistent with previous studies of spiropyrans bearing a 1-aza-15-crown-5 ionophore.¹⁶ Conversely, **SP-1** binding to Ca²⁺ appears to occur in a 3:1 ratio of metal ion to sensor (apex at ~ 0.72). These results suggest that while **SP-1** likely binds Li⁺ in the manner proposed in Figure 1, the **SP-1**-Ca²⁺ interaction is more complicated. Analysis of **SP-3** binding with Ca²⁺ revealed a possible 1:1 or 2:1 metal ion to sensor ratio (Job's plot apex at ~ 0.58). Future work will be focused on high level DFT calculations in order to better understand the metal binding mechanisms of the sensors. Finally, quantum yield of fluorescence values (Φ) were determined for **SP-1** and **SP-2** in the presence of Li⁺ and Ca²⁺,

and for **SP-3** in the presence of Ca^{2+} , using Rhodamine B as the calibration standard* with values displayed in Table 1. The quantum yield of **SP-3** in the presence of Ca^{2+} (Φ 0.37) was found to be significantly higher than the MC- Li^+ and MC- Ca^{2+} complexes of **SP-1** and **SP-2** (Φ 0.03 – 0.06), respectively. This result is consistent with the earlier fluorescence studies and may explain the observed brightness of the MC(**SP-3**)- Ca^{2+} complex.

4.4 Conclusions and Future Work

The design, synthesis and photophysical characterisation of a series of spiropyran-based sensors incorporating both C8' and N1-indole metal ion binding domains are presented. Fluorescence-based metal ion selectivity studies revealed that the hydroxyethyl (**SP-1**) and ethoxycarbonylbutyl (**SP-2**) N1-functionalised spiropyrans exhibited affinity for both Li^+ and Ca^{2+} ions, while the N1-carboxybutyl sensor (**SP-3**) gave excellent Ca^{2+} -selectivity. Further solution-based studies showed an improved dissociation constant (K_d MC(**SP-3**)- Ca^{2+} = $22 \pm 1 \mu\text{M}$) and quantum yield of fluorescence (Φ MC(**SP-3**)- Ca^{2+} = 0.37), compared to the other sensors. Job's analysis of binding stoichiometry was inconclusive (**SP-3**- Ca^{2+} binding apex at 0.58, indicating 1:1 or 2:1 metal-sensor binding) and so future work will be focused on high level DFT calculations in order to clarify possible binding mechanisms. These results suggest the carboxybutyl N1-indole functionality of **SP-3** may play a role in stabilizing Ca^{2+} in the 15-membered azacrown ionophore, promoting metal-induced isomerisation to the MC(**SP-3**)- Ca^{2+} complex and thus a bright, Ca^{2+} -selective, red fluorescence signal.

4.5 Acknowledgements

The authors acknowledge funding support from the Centre of Nanoscale BioPhotonics, through the Australian Research Council (ARC) CE140100 003. This work was performed in part at the OptoFab node of the Australian National Fabrication Facility utilizing Commonwealth and South Australian State Government funding. The authors would like to acknowledge Ms Yow Yu Ting and Ms Nicole Tan Jia Ling for assistance with fluorescence experiments.

* Rhodamine B was selected as the standard for quantum yield of fluorescence calculations, because the fluorophore can be excited at 514 nm, a compatible excitation for spiropyran-based sensors.

4.6 References

1. Clapham, D. E., Calcium signaling. *Cell* **2007**, *131* (6), 1047-1058.
2. Berridge, M. J.; Lipp, P.; Bootman, M. D., The versatility and universality of calcium signalling. *Nat Rev Mol Cell Bio* **2000**, *1* (1), 11-21.
3. Berridge, M. J.; Bootman, M. D.; Roderick, H. L., Calcium signalling: Dynamics, homeostasis and remodelling. *Nat Rev Mol Cell Bio* **2003**, *4* (7), 517-529.
4. Bhosale, G.; Sharpe, J. A.; Sundier, S. Y.; Duchen, M. R., Calcium signaling as a mediator of cell energy demand and a trigger to cell death. *Ann Ny Acad Sci* **2015**, *1350*, 107-116.
5. Raffaello, A.; Mammucari, C.; Gherardi, G.; Rizzuto, R., Calcium at the Center of Cell Signaling: Interplay between Endoplasmic Reticulum, Mitochondria, and Lysosomes. *Trends Biochem Sci* **2016**, *41* (12), 1035-1049.
6. Gaspers, L. D.; Bartlett, P. J.; Politi, A.; Burnett, P.; Metzger, W.; Johnston, J.; Joseph, S. K.; Hofer, T.; Thomas, A. P., Hormone-Induced Calcium Oscillations Depend on Cross-Coupling with Inositol 1,4,5-Trisphosphate Oscillations. *Cell Rep* **2014**, *9* (4), 1209-1218.
7. Humeau, J.; Bravo-San Pedro, J. M.; Vitale, I.; Nuñez, L.; Villalobos, C.; Kroemer, G.; Senovilla, L., Calcium signaling and cell cycle: Progression or death. *Cell Calcium* **2017**.
8. Peacock, M., Calcium metabolism in health and disease. *Clinical journal of the American Society of Nephrology : CJASN* **2010**, *5 Suppl 1*, S23-30.
9. Felsenfeld, A. J.; Levine, B. S.; Rodriguez, M., Pathophysiology of Calcium, Phosphorus, and Magnesium Dysregulation in Chronic Kidney Disease. *Seminars in Dialysis* **2015**, *28* (6), 564-577.
10. Stewart, T. A.; Yapa, K. T. D. S.; Monteith, G. R., Altered calcium signaling in cancer cells. *Biochimica et Biophysica Acta (BBA) - Biomembranes* **2015**, *1848* (10, Part B), 2502-2511.
11. Marchi, S.; Pinton, P., Alterations of calcium homeostasis in cancer cells. *Current Opinion in Pharmacology* **2016**, *29*, 1-6.
12. Carter, K. P.; Young, A. M.; Palmer, A. E., Fluorescent Sensors for Measuring Metal Ions in Living Systems. *Chem Rev* **2014**, *114* (8), 4564-4601.
13. Thomas, D.; Tovey, S. C.; Collins, T. J.; Bootman, M. D.; Berridge, M. J.; Lipp, P., A comparison of fluorescent Ca²⁺-indicator properties and their use in measuring elementary and global Ca²⁺-signals. *Cell Calcium* **2000**, *28* (4), 213-223.
14. Paredes, R. M.; Etzler, J. C.; Watts, L. T.; Zheng, W.; Lechleiter, J. D., Chemical calcium indicators. *Methods* **2008**, *46* (3), 143-151.
15. Heng, S.; Mak, A. M.; Stubing, D. B.; Monro, T. M.; Abell, A. D., Dual Sensor for Cd(II) and Ca(II): Selective Nanoliter-Scale Sensing of Metal Ions. *Anal Chem* **2014**, *86* (7), 3268-3272.
16. Stubing, D. B.; Heng, S.; Abell, A. D., Crowned spiropyran fluoroionophores with a carboxyl moiety for the selective detection of lithium ions. *Org Biomol Chem* **2016**, *14* (15), 3752-3757.
17. Heng, S.; McDevitt, C. A.; Stubing, D. B.; Whittall, J. J.; Thompson, J. G.; Engler, T. K.; Abell, A. D.; Monro, T. M., Microstructured Optical Fibers and Live Cells: A Water-Soluble, Photochromic Zinc Sensor. *Biomacromolecules* **2013**, *14* (10), 3376-3379.

18. Heng, S.; Mak, A. M.; Kostecki, R.; Zhang, X. Z.; Pei, J. X.; Stubing, D. B.; Ebendorff-Heidepriem, H.; Abell, A. D., Photoswitchable calcium sensor: 'On'-'Off' sensing in cells or with microstructured optical fibers. *Sensor Actuat B-Chem* **2017**, *252*, 965-972.
19. Heng, S.; Reineck, P.; Vidanapathirana, A. K.; Pullen, B. J.; Drumm, D. W.; Ritter, L. J.; Schwarz, N.; Bonder, C. S.; Psaltis, P. J.; Thompson, J. G.; Gibson, B. C.; Nicholls, S. J.; Abell, A. D., Rationally Designed Probe for Reversible Sensing of Zinc and Application in Cells. *ACS Omega* **2017**, *2* (9), 6201-6210.
20. Sylvia, G. M.; Heng, S.; Bachhuka, A.; Ebendorff-Heidepriem, H.; Abell, A. D., A spiropyran with enhanced fluorescence: A bright, photostable and red-emitting calcium sensor. *Tetrahedron* **2017**.
21. Natali, M.; Giordani, S., Molecular switches as photocontrollable "smart" receptors. *Chemical Society reviews* **2012**, *41* (10), 4010-4029.
22. Baldrighi, M.; Locatelli, G.; Desper, J.; Aakeroy, C. B.; Giordani, S., Probing Metal Ion Complexation of Ligands with Multiple Metal Binding Sites: The Case of Spiropyran. *Chem-Eur J* **2016**, *22* (39), 13976-13984.
23. Kho, Y. M.; Shin, E. J., Spiropyran-Isoquinoline Dyad as a Dual Chemosensor for Co(II) and In(III) Detection. *Molecules* **2017**, *22* (9).
24. Klajn, R., Spiropyran-based dynamic materials. *Chemical Society reviews* **2014**, *43* (1), 148-84.
25. Lukyanov, B. S.; Lukyanova, M. B., Spiropyran: Synthesis, Properties, and Application. (Review). *Chemistry of Heterocyclic Compounds* **2005**, *41* (3), 281-311.
26. Kimura, K.; Yamashita, T.; Yokoyama, M., Syntheses, Cation Complexation, Isomerization and Photochemical Cation-Binding Control of Spirobenzopyrans Carrying a Monoazacrown Moiety at the 8-Position. *J Chem Soc Perk T 2* **1992**, (4), 613-619.
27. Kimura, K.; Teranishi, T.; Yokoyama, M.; Yajima, S.; Miyake, S.; Sakamoto, H.; Tanaka, M., Cation complexation, isomerization, and photoresponsive ionic conduction of a crown ether derivative carrying two spirobenzopyran units. *Journal of the Chemical Society, Perkin Transactions 2* **1999**, (2), 199-204.
28. Kimura, K.; Sakamoto, H.; Kado, S.; Arakawa, R.; Yokoyama, M., Studies on metal-ion complex formation of crown ether derivatives incorporating a photoionizable spirobenzopyran moiety by electrospray ionization mass spectrometry. *Analyst* **2000**, *125* (6), 1091-1095.
29. Salhin, A. M. A.; Tanaka, M.; Kamada, K.; Ando, H.; Ikeda, T.; Shibutani, Y.; Yajima, S.; Nakamura, M.; Kimura, K., Decisive factors in the photoisomerization behavior of crowned spirobenzopyrans: Metal ion interaction with crown ether and phenolate anion moieties. *Eur J Org Chem* **2002**, (4), 655-662.
30. Wojtyk, J. T. C.; Kazmaier, P. M.; Buncel, E., Modulation of the Spiropyran-Merocyanine Reversion via Metal-Ion Selective Complexation: Trapping of the "Transient" cis-Merocyanine. *Chemistry of Materials* **2001**, *13* (8), 2547-2551.
31. Natali, M.; Aakeroy, C.; Desper, J.; Giordani, S., The role of metal ions and counterions in the switching behavior of a carboxylic acid functionalized spiropyran. *Dalton T* **2010**, *39* (35), 8269-8277.
32. Natali, M.; Soldi, L.; Giordani, S., A photoswitchable Zn (II) selective spiropyran-based sensor. *Tetrahedron* **2010**, *66* (38), 7612-7617.
33. Natali, M.; Giordani, S., Interaction studies between photochromic spiropyran and transition metal cations: the curious case of copper. *Org Biomol Chem* **2012**, *10* (6), 1162-1171.

34. Garcia, A. A.; Cherian, S.; Park, J.; Gust, D.; Jahnke, F.; Rosario, R., Photon-controlled phase partitioning of spiropyrans. *J Phys Chem A* **2000**, *104* (26), 6103-6107.
35. Heng, S.; Nguyen, M. C.; KostECKI, R.; Monro, T. M.; Abell, A. D., Nanoliter-scale, Regenerable Ion Sensor: Sensing with Surface Functionalized Microstructured Optical Fiber. *Proc Spie* **2013**, 8774.
36. Zakharova, M. I.; Pimienta, V.; Metelitsa, A. V.; Minkin, V. I.; Micheau, J. C., Thermodynamic and kinetic analysis of metal ion complexation by photochromic spiropyrans. *Russian Chemical Bulletin* **2009**, *58* (7), 1329-1337.
37. Tanaka, M.; Kamada, K.; Ando, H.; Kitagaki, T.; Shibutani, Y.; Yajima, S.; Sakamoto, H.; Kimura, K., Metal-ion stabilization of photoinduced open colored isomer in crowned spirobenzothiapyran. *Chem Commun* **1999**, (16), 1453-1454.
38. Magde, D.; Rojas Gail, E.; Seybold Paul, G., Solvent Dependence of the Fluorescence Lifetimes of Xanthene Dyes. *Photochemistry and Photobiology* **2008**, *70* (5), 737-744.
39. Renny, J. S.; Tomasevich, L. L.; Tallmadge, E. H.; Collum, D. B., Method of Continuous Variations: Applications of Job Plots to the Study of Molecular Associations in Organometallic Chemistry[**]. *Angewandte Chemie (International ed. in English)* **2013**, *52* (46), 11998-12013.

CHAPTER 5

Supporting Information

5.1 Experimental Techniques described in Chapters 2-4

5.1.1 General Synthesis

All ^{13}C NMR and ^1H NMR spectra were recorded on an Agilent Technologies 500 MHz NMR with DD2 console in CD_3CN or $\text{DMSO-}d_6$ (Cambridge Isotope Laboratories, Cambridge, MA). Chemical shifts (δ) are reported in ppm. Chemical shifts of CD_3CN ($\delta_{\text{C}} = 118.26$ ppm), $\text{DMSO-}d_6$ ($\delta_{\text{C}} = 39.52$ ppm) or TMS ($\delta_{\text{H}} = 0.0$ ppm) were used as internal standards in all ^{13}C NMR and ^1H NMR experiments, respectively. High resolution mass spectrometry was performed on the Agilent 6230 TOF LC-MS. HPLC grade acetonitrile was used in all related experiments. All other reagents were purchased from Sigma-Aldrich and used without further purification.

5.1.2 Absorbance and Fluorescence Selectivity

Stock solutions of spiropyrans (5 mM) were prepared in HPLC-grade acetonitrile. Stock solutions of metal ion salts (10 mM) were prepared in water from dried perchlorate salts of Li^+ , Na^+ , K^+ , Mg^{2+} , Ca^{2+} , Mn^{2+} , Cu^{2+} , Zn^{2+} , and Cs^+ (from Cs_2SO_4). For the selectivity studies, solutions were prepared (in triplicate) on the same microplate tray from 2 μL spiropyran and 2 μL of ion stock solutions, such that each replicate contained a 2:1 molar ratio of ion: spiropyran. 196 μL of HPLC grade acetonitrile was then added to dilute each replicate, such that the final concentrations of spiropyran and ions in each solution were 50 μM and 100 μM , respectively. The microplate tray was then incubated in the dark for 10 mins before reading. Absorbance and fluorescence spectra were recorded between 300 and 700 nm, and 555 and 800 nm, respectively, at 25 $^\circ\text{C}$ using a BioTek Synergy H4 Hybrid Multi-Mode Microplate Reader. The scanning resolution was 5 nm, with a band pass of 9 nm. Fluorescence excitation was at 532 nm, with 100 gain setting, unless otherwise specified. All absorbance and fluorescence measurements were repeated in triplicate. The error bars presented represent a standard deviation about the mean value.

5.1.3 Quantum Yield of Fluorescence (Φ)

A stock solution containing spiropyran chemosensor (SP, 50 μM) and metal ion salt (M, 100 μM) was prepared in HPLC-grade acetonitrile. Solutions were prepared (in triplicate) on the same clear-bottom microplate tray from varying volumes of the combined spiropyran/metal ion stock solution and HPLC-grade acetonitrile, until the volume of each replicate was 200 μL . The concentration ratios of ([SP], [M]) in μM were (10, 20), (20, 40), (30, 60), (40, 80), (50, 100), (60, 120), (80, 160) and (100, 200). The microplate tray was then incubated in the dark for 10 mins before reading. Absorbance (400-600 nm, 2nm band pass) and fluorescence emission spectra (535-800 nm, 5nm band pass, excitation 514 nm, 80 gain) were recorded at 25 $^{\circ}\text{C}$ using a BioTek Synergy H4 Plate Reader. These absorbance and fluorescence measurements was repeated for Rhodamine B (0, 1, 2, 3, 4, 5 μM), and a graph of integrated fluorescence *vs* absorbance at 514 nm (up to an approximate absorbance value of 0.1) was obtained. Quantum yield was calculated using the following equation:

$$\Phi_x = \Phi_{\text{ST}} (\text{Grad}_x/\text{Grad}_{\text{ST}})(\eta_x^2/\eta_{\text{ST}}^2)$$

Where subscripts ST and X denote standard (Rhodamine B) and the unknown (spiropyran), respectively. Φ is fluorescence quantum yield, Grad is the gradient from the plot of integrated fluorescence intensity *vs* absorbance and η is the refractive index of the solvent ($\eta_{\text{(water)}} = 1.330$, $\eta_{\text{(acetonitrile)}} = 1.344$). The fluorescence quantum yield of Rhodamine B in water at $\lambda_{\text{ex}} = 514$ nm is 0.31, as reported in the literature.¹

5.1.4 Job's Plot Analysis

Stock solutions of spiropyran chemosensor (SP, 100 μM) and metal ion salts (M, 100 μM) were prepared separately in HPLC-grade acetonitrile. Solutions were prepared (in triplicate) in the same clear-bottom microplate tray from varying volumes of the spiropyran stock solution and of the ion stock solutions, respectively, until the total volume of each replicate was 200 μL . The concentration ratios of ([SP], [M]) in μM were (100, 0), (95, 5), (80, 20), (70, 30), (50, 50), (40, 60), (30, 70), (20, 80), (5, 95) and (0, 100). As such, each solution contained a constant total combined concentration of spiropyran and metal ion ([SP]+ [M] = 100 μM). The microplate tray was then incubated in the dark for 10 mins before reading. Fluorescence emission spectra were recorded between 555 and 800 nm, respectively, at 25 $^{\circ}\text{C}$ using a BioTek Synergy H4 Hybrid Multi-Mode Microplate Reader. Fluorescence excitation was at 532 nm, with 100 gain setting and scanning resolution was 5nm, with band

pass of 9 nm. Job's plots were derived by plotting the mean fluorescence at the maximum emission wavelength for each concentration ratio of (SP), [M]).

5.1.5 Dissociation Constants (K_d)

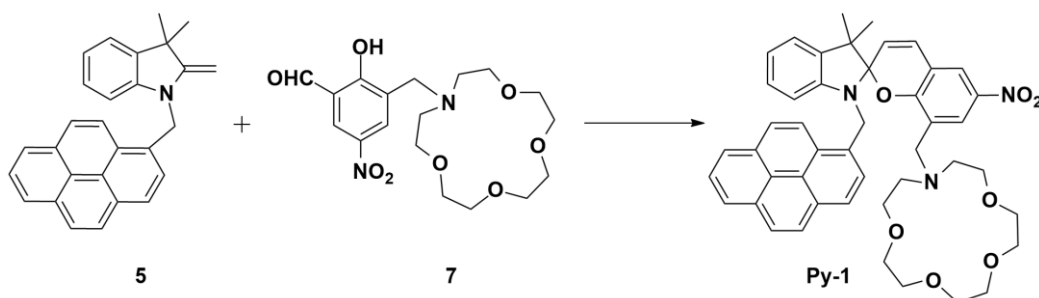
Stock solutions of metal ion salts (0.02-2 mM) were prepared separately in HPLC-grade acetonitrile. Replicate solutions were prepared (in triplicate) in the same clear-bottom microplate tray from 2 μ L of spiropyran stock (5 mM) and 10 μ L of the respective ion stock solutions. 188 μ L of HPLC grade acetonitrile was then added to dilute each replicate, such that the final concentrations of spiropyran and metal ions in each solution were 50 μ M and 1-100 μ M, respectively. The microplate tray was then incubated in the dark for 10 mins before reading. Fluorescence emission spectra were recorded between 555 and 800 nm, at 25 °C using a BioTek Synergy H4 Hybrid Multi-Mode Microplate Reader. Fluorescence excitation was at 532 nm, with 100 gain setting and scanning resolution was 5nm, with band pass of 9 nm. Concentration curves were prepared from the fluorescence emission maxima for each ion concentration. The apparent dissociation constants (K_d) of spiropyrans for metal ions were then calculated by fitting an appropriate non-linear regression in GraphPad Prism version 7.02. The 'Hill Plot with Specific Binding' model was selected, as it represents a saturation binding experiment, where concentration of 'radioligand' (i.e. metal ion) is varied and binding to the 'receptor' (i.e. merocyanine isomer) is measured, in this case as a fluorescence emission. The model uses the following equation,

$$Y = B_{max} * X^h / (K_d^h + X^h)$$

Where Y is the relative fluorescence intensity at any given concentration of metal ion, B_{max} is the maximum specific binding in the same units as Y (i.e. in this case the fluorescence at sensor saturation), X is the concentration of metal ion and K_d is the metal ion concentration needed to achieve the half-maximum binding at equilibrium, expressed in the same units as X. The parameter h is the Hill slope, and $h = 1.0$ when a monomer binds with no cooperativity to one site. If $h > 0$, i.e. the 'receptor' (merocyanine) or 'radioligand' (metal ion) has multiple binding sites with positive cooperativity, and the graph will have a sigmoidal appearance.²

5.2 Supporting Information to Chapter 2

5.2.1 Chemical Syntheses



8-((1,4,7,10-Tetraoxa-13-azacyclopentadecan-13-yl)methyl)-3',3'-dimethyl-6-nitro-1'-(pyren-1-ylmethyl)spiro [chromene-2,2'-indoline] (**Py-1**).

To a solution of **5** (196 mg, 0.5 mmol) in dry ethanol (15 mL) was added **7** (209 mg, 0.5 mmol) and the reaction heated at reflux for 18 hrs. The solvent was removed in vacuo to give a dark red solid (209 mg). A sample (100 mg) of the crude material was purified on silica by gradient column chromatography using 0-10 % methanol in dichloromethane to give **Py-1** as a purple-red solid (10 mg, 10 %).

^1H NMR (500 MHz, $\text{DMSO-}d_6$) δ 8.34 – 8.32 (m, 1H, ArH), 8.30 (m, 2H, ArH), 8.21 (m, 1H, ArH), 8.19 (m, 1H, ArH), 8.15 (m, 2H, ArH), 8.10 (m, 1H, ArH), 8.03 – 8.01 (m, 2H, ArH), 7.99 (m, 1H, ArH), 7.23 (d, 1H, ArH, $J = 7.0$ Hz), 7.01 - 6.98 (m, 2H, ArH), 6.83 (t, 1H, ArH, $J = 7.5$ Hz), 6.36 (d, 1H, ArH, $J = 7.5$ Hz), 5.97 (d, 1H, ArH, $J = 10.0$ Hz), 5.14 (d, 1H, CHH, $J = 16.5$ Hz), 5.04 (d, 1H, CHH, $J = 17.0$ Hz), 3.58- 3.42 (m, 20H, 10 x CH_2), 2.58 – 2.46 (m, 2H, CH_2), 1.30 (s, 3H CH_3), 1.22 (s, 2H, CH_3) ppm;

^{13}C NMR (126 MHz, $\text{DMSO-}d_6$) δ 157.1, 147.1, 140.2, 132.0, 130.9, 127.3, 127.1, 126.6, 125.5, 125.4, 124.2, 124.1, 121.5, 119.9, 118.7, 72.5, 70.5, 70.0, 69.9, 69.8, 69.9, 69.7, 69.2, 60.4, 54.1, 52.5, 35.3, 31.5, 31.4, 29.2, 29.0, 28.9, 28.8, 26.8, 26.1, 25.3, 22.3, 19.9, 15.7, 14.2 ppm;

HRMS-ESI (m/z) calculated for $\text{C}_{46}\text{H}_{47}\text{N}_3\text{O}_7$ $[\text{M} + \text{H}]^+$ 754.3487, found 754.3480, and $[\text{M} + \text{Na}]^+$ 776.3306, found 776.3305.

5.2.2 NMR and HRMS Characterisation Spectra

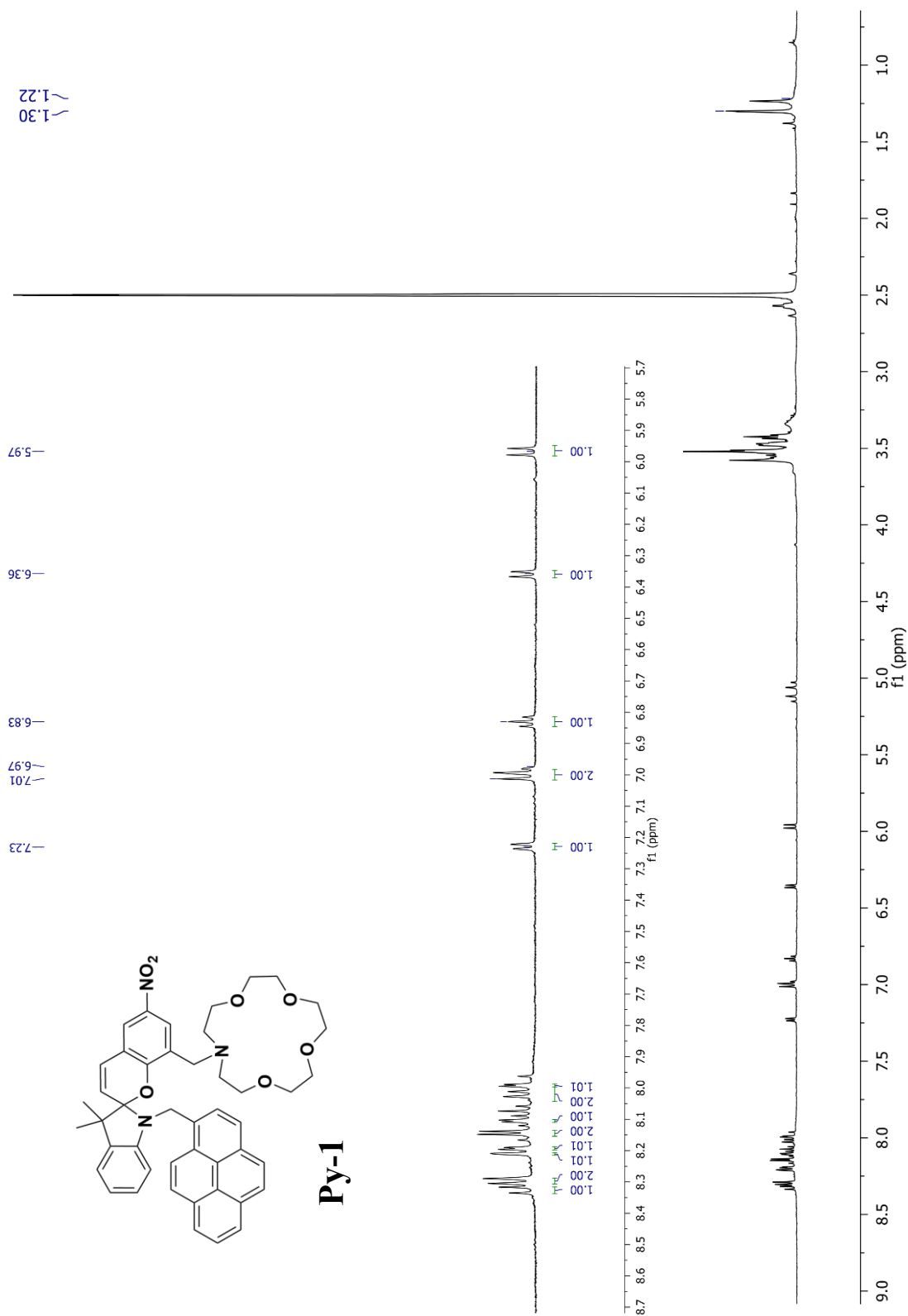


Figure S2-1. ^1H NMR spectrum of compound **Py-1** recorded in $\text{DMSO-}d_6$ at 500 MHz.

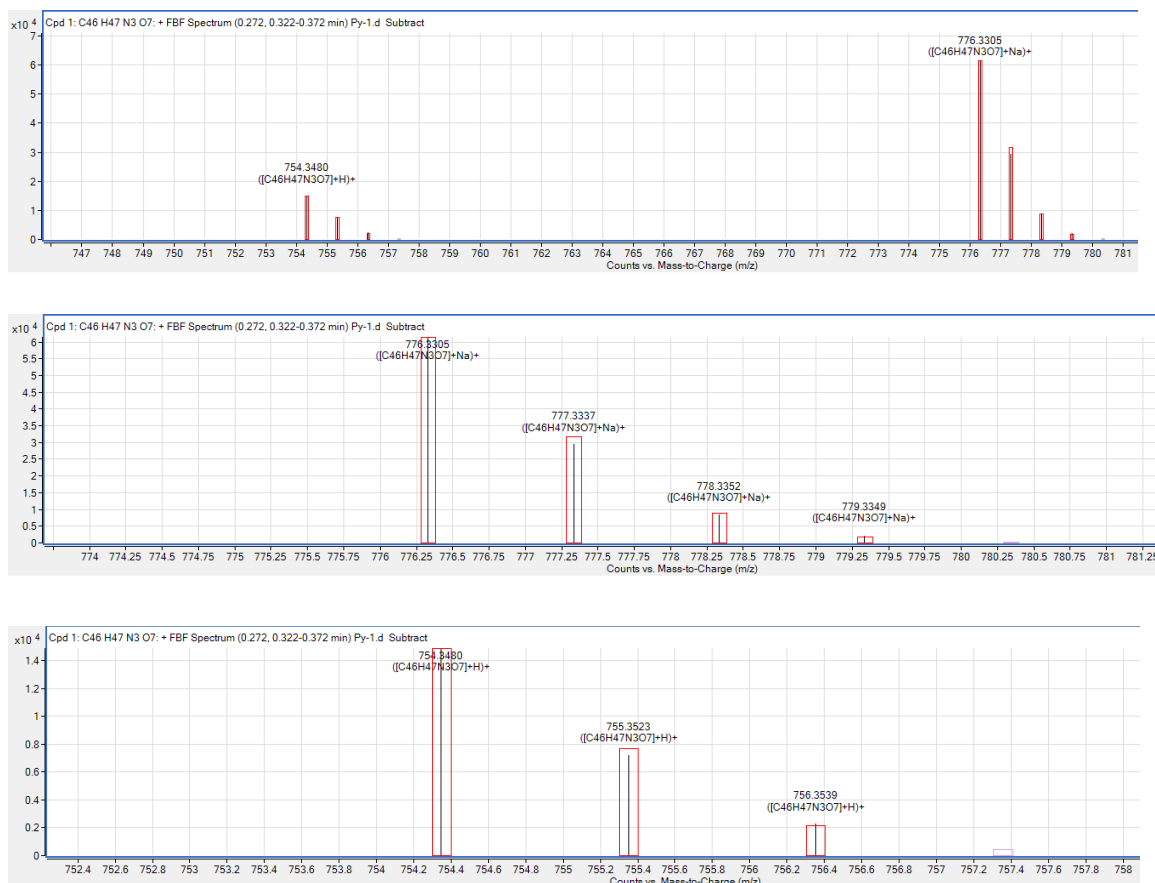


Figure S2-2. HRMS-ESI of compound **Py-1** recorded in acetonitrile.

5.2.3 Absorbance and Fluorescence Spectra

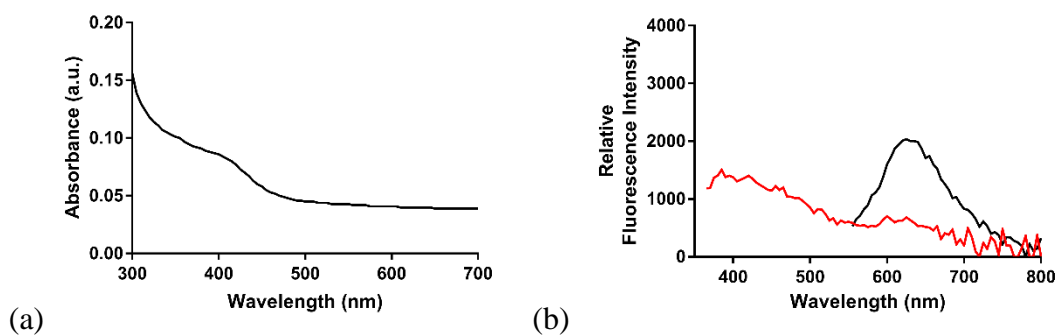


Figure S2-3. (a) Absorbance spectrum of sensor **2**, and (b) fluorescence emission with excitation at 532 nm (black) and with excitation at 344 nm (red). Fluorescence spectra recorded at 120 gain.

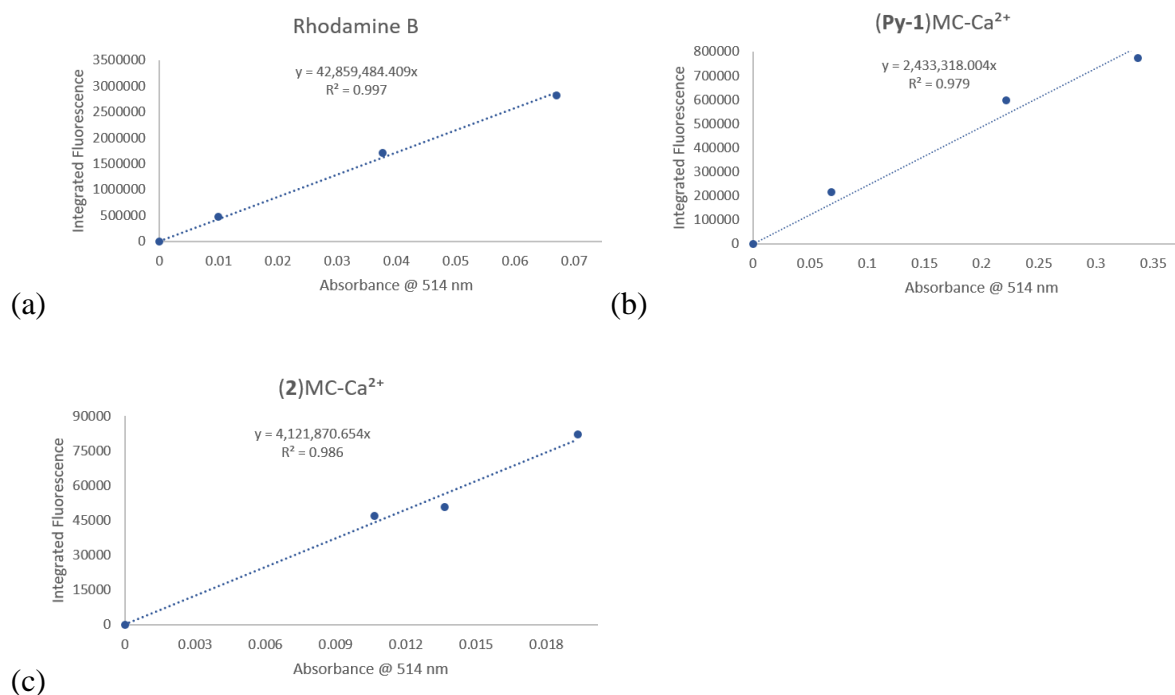


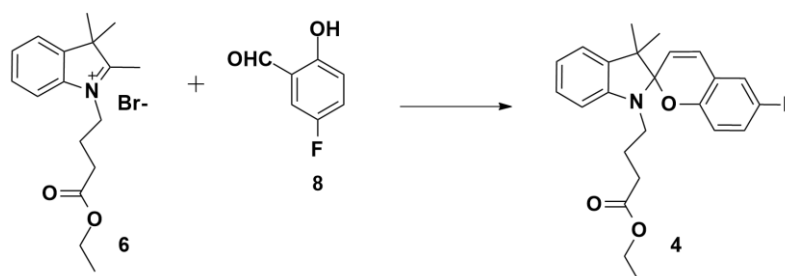
Figure S2-4. Integrated fluorescence spectra after excitation at 514 nm versus the absorbance at 514 nm for (a) Rhodamine B (0–5 μM , water), (b) (Py-1)MC-Ca²⁺ (0-100 μM , acetonitrile) in the presence of a 2-fold excess of Ca²⁺ and (c) (2)MC-Ca²⁺ (0-100 μM , acetonitrile) in the presence of a 2-fold excess of Ca²⁺. The quantum yields of (Py-1)MC-Ca²⁺ and (2)MC-Ca²⁺ were calculated to be $\Phi = 0.02$ and $\Phi = 0.03$, respectively.

5.2.4 Photoswitching in Optical Fibre

A 5 mW laser was coupled into the core of a suspended core fibre (SCF) via dichromic mirror at a wavelength of 532 nm using 60X objective as described previously.² One end of the SCF was filled by capillary action by dipping in an acetonitrile solution containing sensor **Py-1** (500 μ M). Fluorescence of the sensor-filled SCF was measured after excitation with a 532 nm green laser (5 x 15 ms pulses). Next, the sensor-filled SCF was exposed to a 532 nm green laser for 2 min in order to facilitate photoswitching to the weakly fluorescent SP isomer, and fluorescence was measured after excitation with the same 532 nm laser. Finally, incubation in the dark for 5 min, followed by excitation with the 532 nm laser allowed the sensor to photoswitch back to the highly fluorescent MC isomer. This process was repeated for 10 cycles to investigate the photoswitching and photostability of sensor **Py-1**. The fluorescence of Rhodamine B was similarly recorded.

5.3 Supporting Information to Chapter 3

5.3.1 Chemical Syntheses



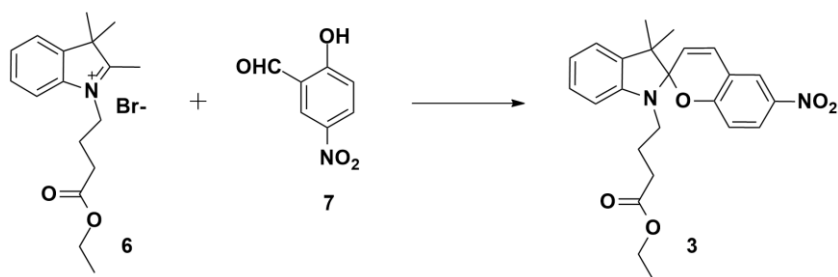
Ethyl 4-(3',3'-dimethyl-6-fluorospiro[chromene-2,2'-indolin]-1'-yl)butanoate (4).

To a solution of 5-fluoro-2-hydroxybenzaldehyde **8** (44 mg, 0.31 mmol) in dry ethanol (5 mL) was added 1-(4-ethoxy-4-oxobutyl)-2,3,3-trimethyl-3H-indolium bromide **6** (100 mg, 0.28 mmol) and the reaction heated at reflux for 18 h. The solvent was removed in vacuo to give an orange crude oil (150 mg). The crude compound was purified on normal-phase silica by gradient column chromatography in 0–10% methanol in dichloromethane to give **4** as a yellow oil (44 mg, 39%).

$^1\text{H-NMR}$ (500 MHz, $\text{DMSO-}d_6$) δ 7.10–7.06 (m, 3H, ArH), 6.97 (d, 1H, ArH, $J = 10.5$ Hz), 6.90 (td, 1H, ArH, $J = 8.5, 3.5$ Hz), 6.75 (t, 1H, ArH, $J = 7.5$ Hz), 6.65 (dd, 1H, ArH, $J = 8.5, 4.5$ Hz), 6.61 (d, 1H, ArH, $J = 8.0$ Hz), 5.84 (d, 1H, ArH, $J = 7.5$ Hz), 4.00 (q, 2H, CH_2 , $J = 7.5$ Hz), 3.19–3.12 (m, 1H, CHH), 3.10–3.04 (m, 1H, CHH), 2.35–2.30 (m, 2H, CH_2), 1.86–1.80 (m, 1H, CHH), 1.78–1.72 (m, 1H, CHH), 1.19 (s, 3H, CH_3), 1.13 (t, 3H, CH_3 , $J = 7.5$ Hz), 1.07 (s, 3H, CH_3) ppm;

$^{13}\text{C-NMR}$ (126 MHz, $\text{DMSO-}d_6$) δ 172.6, 156.8, 155.0, 149.8, 147.0, 135.9, 128.5, 128.4, 127.4, 121.6, 121.1, 118.6, 112.9, 112.7, 106.3, 104.3, 59.7, 51.8, 42.3, 31.0, 25.7, 23.7, 19.7, 14.0 ppm;

HRMS-ESI (m/z) calculated for $\text{C}_{24}\text{H}_{26}\text{FNO}_3$ [$\text{M} + \text{Na}$] $^+$ 418.1789, found 418.1769.



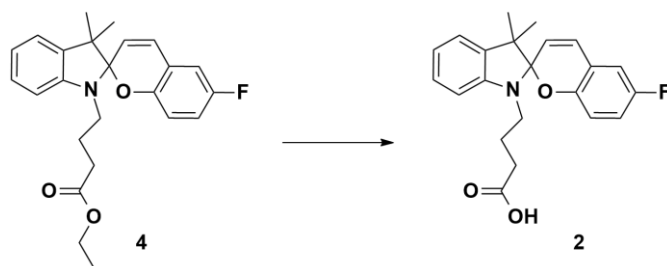
Ethyl 4-(3',3'-dimethyl-6-nitrospiro[chromene-2,2'-indolin]-1'-yl)butanoate (3).

To a solution of 2-hydroxy-5-nitrobenzaldehyde **7** (52 mg, 0.31 mmol) in dry ethanol (5 mL) was added **6** (100 mg, 0.28 mmol) and the solution heated at reflux for 18 h. The solvent was removed in vacuo to give a brown crude solid (156 mg). The crude compound was purified on normal-phase silica by gradient column chromatography in 0–10% methanol in dichloromethane to give **3** as a purple solid (64 mg, 54%).

$^1\text{H-NMR}$ (500 MHz, $\text{DMSO-}d_6$) δ 8.21 (d, 1H, ArH, $J = 3.0$ Hz), 7.99 (dd, 1H, ArH, $J = 2.5, 8.5$ Hz), 7.20 (d, 1H, ArH, $J = 10.0$ Hz), 7.13–7.10 (m, 2H, ArH), 6.85 (d, 1H, ArH, $J = 9.0$ Hz), 6.79 (t, 1H, ArH, $J = 7.5$ Hz), 6.66 (d, 1H, ArH, $J = 8.0$ Hz), 5.98 (d, 1H, ArH, $J = 10.0$ Hz), 4.00 (q, 2H, CH_2 , $J = 7.0$ Hz), 3.20–3.10 (m, 2H, CH_2), 2.36–2.30 (m, 2H, CH_2), 1.86–1.81 (m, 1H, CHH), 1.76–1.71 (m, 1H, CHH), 1.19 (m, 3H, CH_3), 1.13–1.09 (m, 6H, $2 \times \text{CH}_3$) ppm;

$^{13}\text{C-NMR}$ (126 MHz, $\text{DMSO-}d_6$) δ 172.6, 159.1, 146.7, 140.5, 135.6, 129.6, 128.1, 127.6, 125.7, 122.8, 121.7, 121.6, 119.1, 115.4, 106.5, 106.4, 59.8, 52.3, 42.3, 30.9, 25.8, 23.6, 19.6, 14.0 ppm;

HRMS-ESI (m/z) calculated for $\text{C}_{24}\text{H}_{26}\text{N}_2\text{O}_5$ found $[\text{M} + \text{Na}]^+$ 445.1734, found 445.1720.



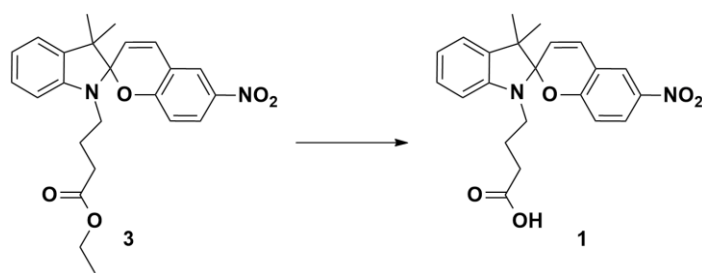
4-(6-Fluoro-3',3'-dimethylspiro[chromene-2,2'-indolin]-1'-yl)butanoic acid (2).

To a solution of **4** (200 mg, 0.51 mmol) in methanol (10 mL) was added 2 M aqueous NaOH (5 mL) and the reaction heated at 50 °C for 5 h. The solvent was removed in vacuo to give an orange solid (1.362 g). A sample of the crude material (100 mg) was purified by reverse-phase HPLC eluting water and acetonitrile (60–100%) to give a purple solid consisting of **2** in mixture with its MC isomer (41 mg);

¹H-NMR (500 MHz, CD₃CN/DMSO-*d*₆) selected data for SP isomer from mixture δ 7.08–6.48 (m, aromH), 6.84 (d, 1H, CH, *J* = 10.0 Hz), 5.83 (d, 1H, CH, *J* = 10.0 Hz), 3.18–3.12 (m, 2H, CH₂), 2.31 (d, 2H, CH₂, *J* = 8.0 Hz), 1.74–1.69 (m, CH₂), 1.18 (s, 3H, CH₃), 1.06 (s, 3H, CH₃);

Selected data for the MC isomer from mixture δ 7.08–6.48 (m, aromH), 4.46 (d, 1H, CHH, *J* = 10.0 Hz), 4.12 (m, 1H, CHH), 2.06–2.03 (m, 2H, CH₂), 1.74–1.69 (m, CH₂), 1.23 (s, 3H, CH₃), 1.19 (s, 3H, CH₃);

HRMS-ESI (*m/z*) calculated for C₂₂H₂₂FNO₃ [M + H]⁺ 368.1656, found 368.1646.



4-(3',3'-Dimethyl-6-nitrospiro[chromene-2,2'-indolin]-1'-yl)butanoic acid (**1**).

To a solution of **3** (224 mg, 0.53 mmol) in methanol (10 mL) was added 2M aqueous NaOH (5 mL) and the reaction heated at 50 °C for 5 h. The solvent was removed in vacuo to give an orange solid (1.441 g). The crude material was purified by reverse-phase HPLC eluting with water and acetonitrile (60–100%) to give **1** as an orange solid (104 mg, 50%).

$^1\text{H-NMR}$ (500 MHz, CD_3CN) δ 8.06 (d, 1H, ArH, $J = 2.5$ Hz), 7.98 (dd, 1H, ArH, $J = 3.0, 9.0$ Hz), 7.14 (t, 1H, ArH, $J = 7.5$ Hz), 7.10 (d, 1H, ArH, $J = 10.0$ Hz), 7.02 (d, 1H, ArH, $J = 10.0$ Hz), 6.83 (t, 1H, ArH, $J = 7.5$ Hz), 6.70 (d, 1H, ArH, $J = 9.0$ Hz), 6.68 (d, 1H, ArH, $J = 7.5$ Hz), 5.96 (d, 1H, ArH, $J = 10.5$ Hz), 3.24–3.11 (m, 2H, CH_2), 2.31–2.27 (m, 2H, CH_2), 1.92–1.76 (m, 2H, CH_2), 1.24 (s, 3H, CH_3), 1.14 (s, 3H, CH_3) ppm;

$^{13}\text{C-NMR}$ (126 MHz, CD_3CN) δ 174.6, 160.4, 148.2, 142.1, 137.10, 129.1, 128.7, 126.6, 123.7, 122.8, 122.7, 120.4, 120.0, 116.2, 107.9, 107.8, 53.3, 43.6, 31.5, 26.3, 24.7, 20.00 ppm;

HRMS-ESI (m/z) calculated for $\text{C}_{22}\text{H}_{22}\text{N}_2\text{O}_5$ $[\text{M} + \text{H}]^+$ 395.1579, found 395.1587.

5.3.2 NMR and HRMS Characterisation Spectra

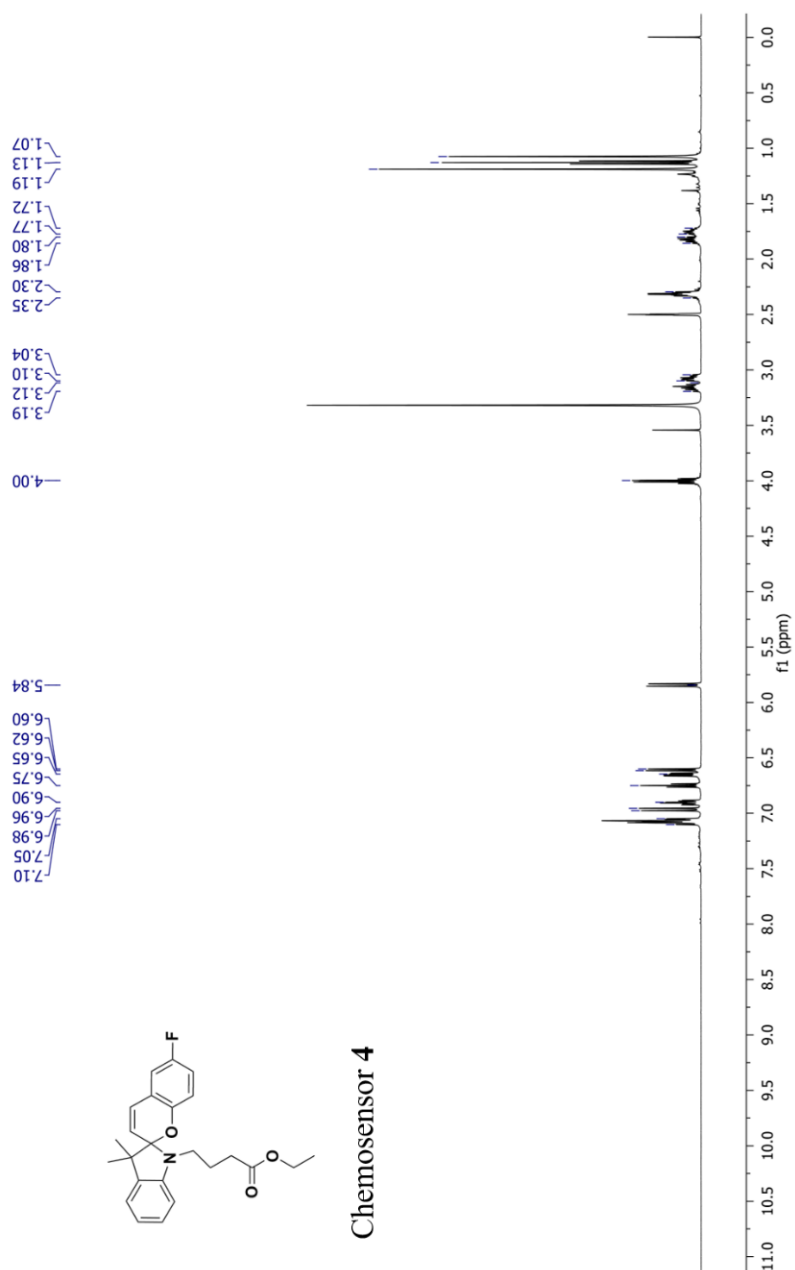


Figure S3-1. ^1H NMR spectrum of chemosensor **4** recorded in $\text{DMSO-}d_6$ at 500 MHz.

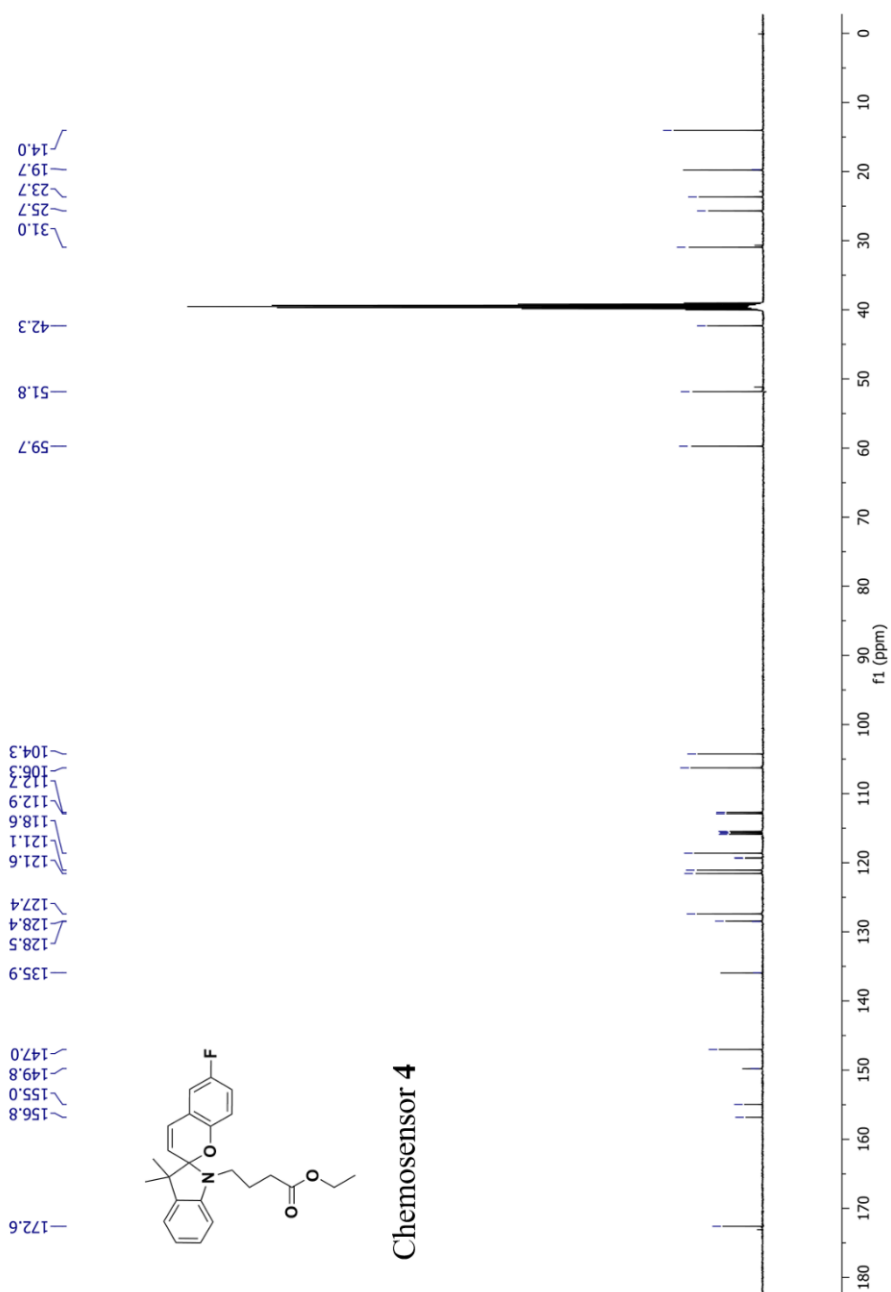


Figure S3-2. ¹³C NMR spectrum of chemosensor **4** recorded in DMSO-D₆ at 500 MHz.

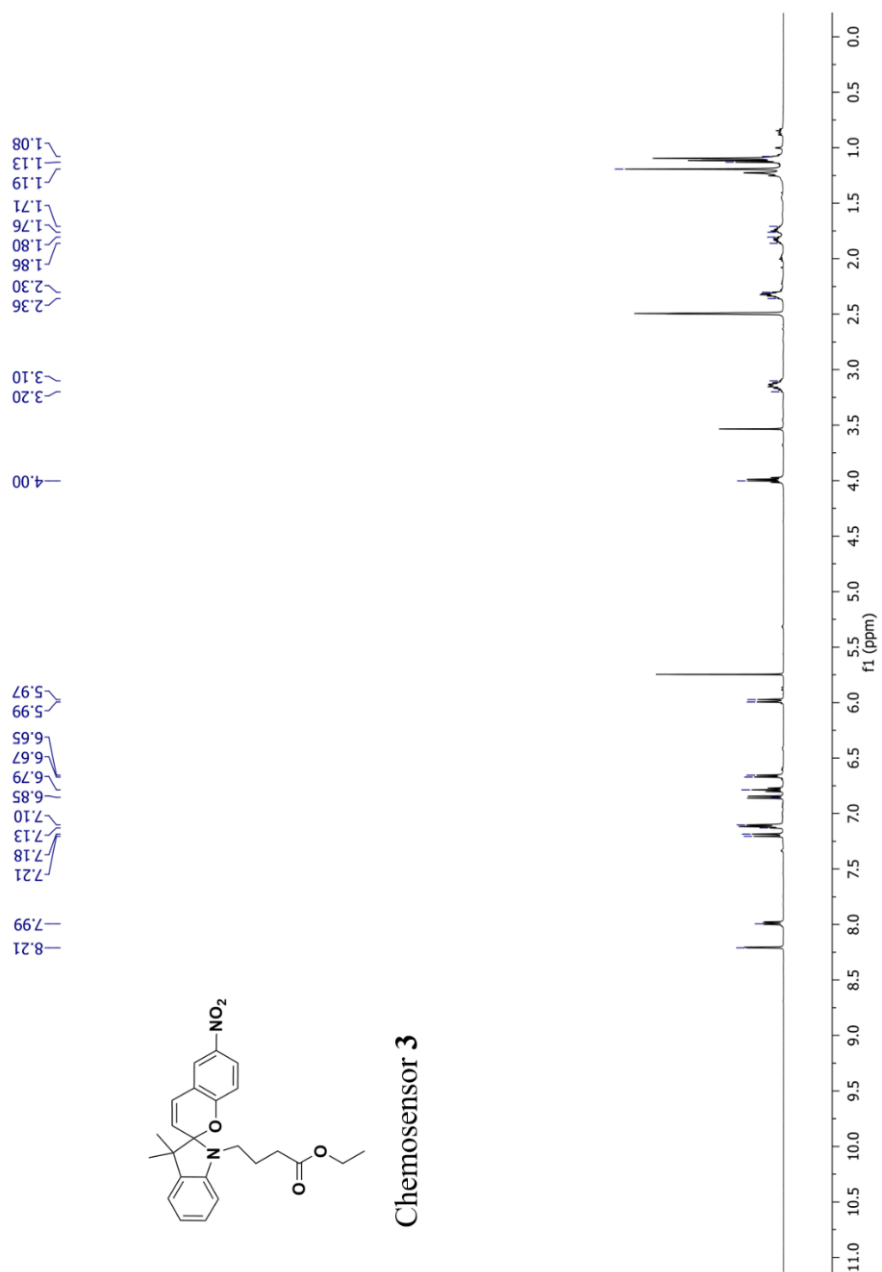


Figure S3-3. ¹H NMR spectrum of chemosensor **3** recorded in DMSO-D₆ at 500 MHz.

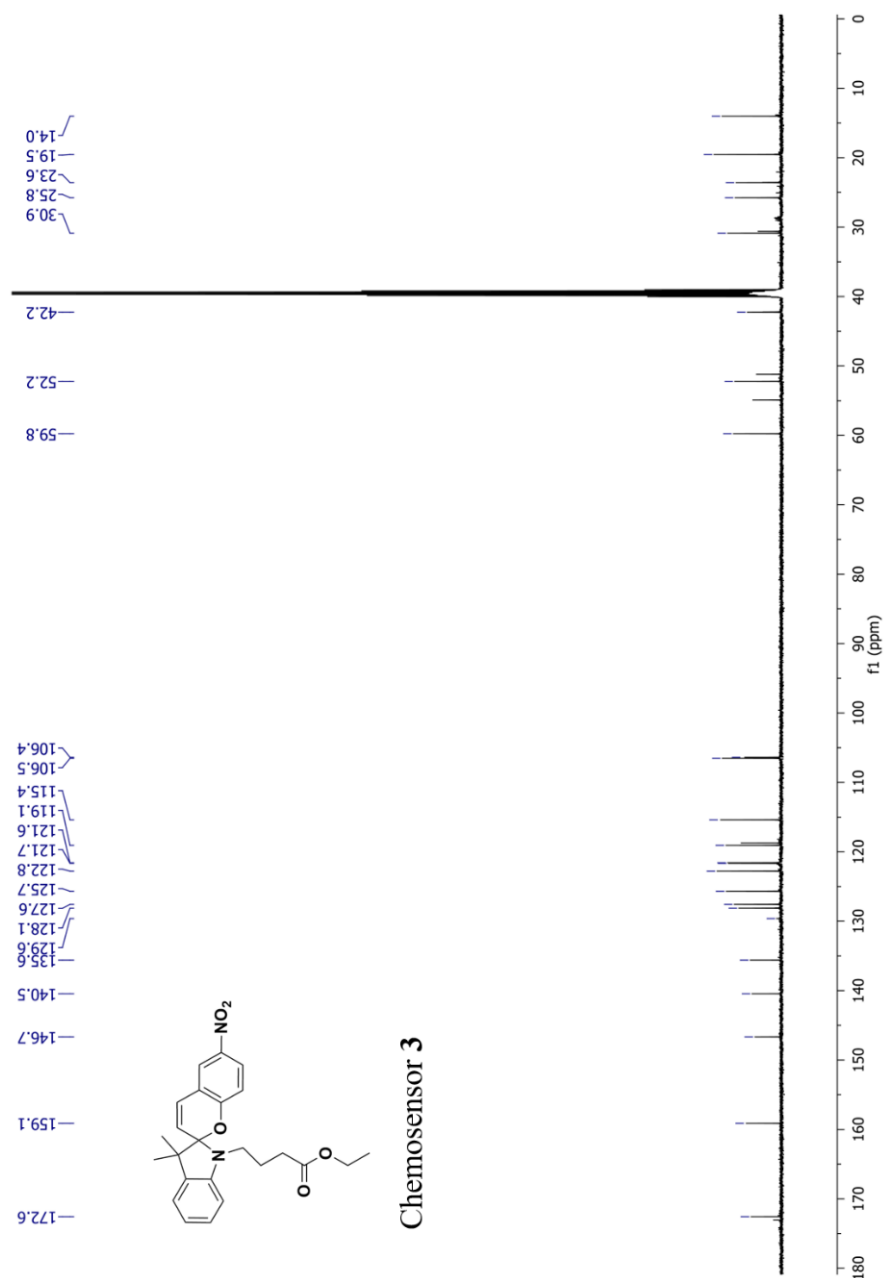


Figure S3-4. ^{13}C NMR spectrum of chemosensor **3** recorded in DMSO-D_6 at 500 MHz.

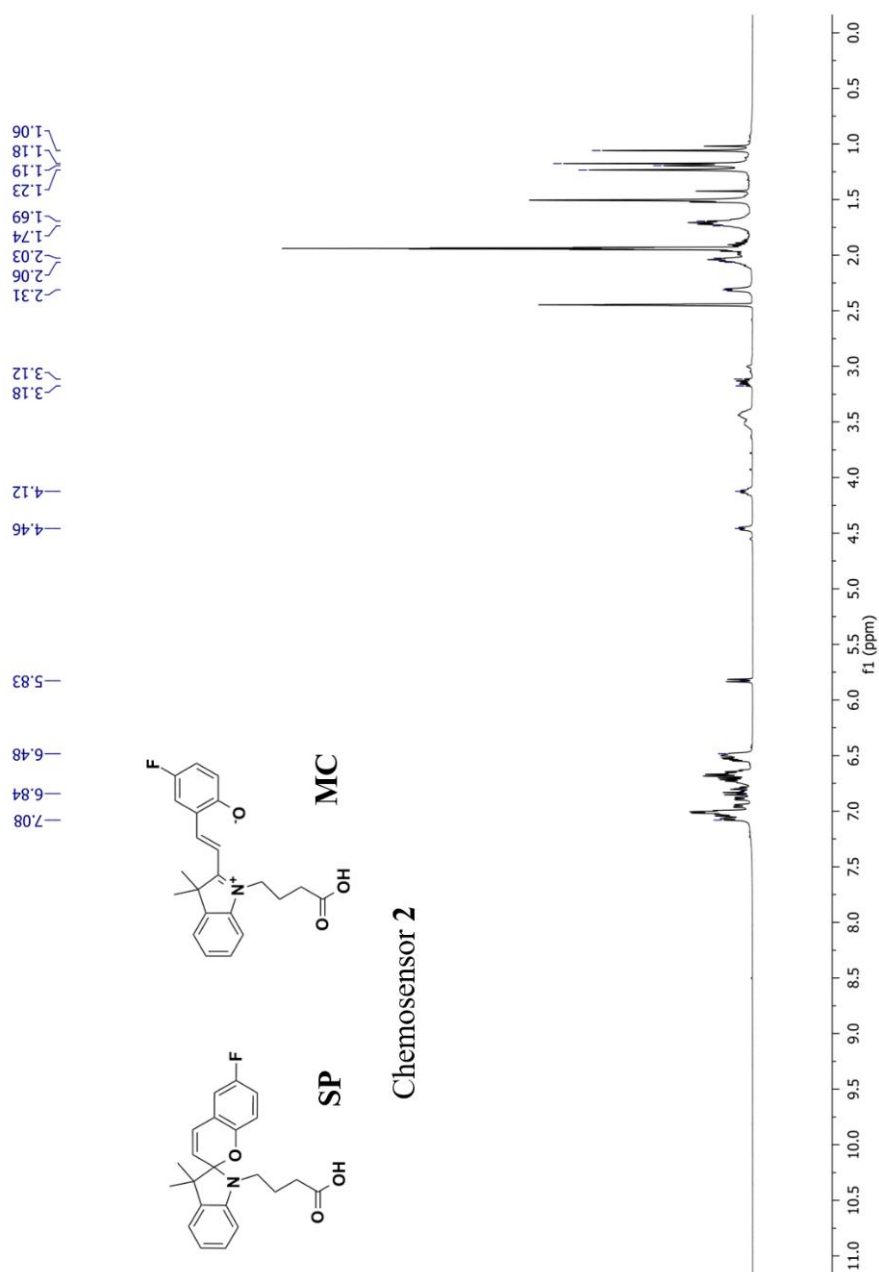


Figure S3-5. ¹H NMR spectrum of chemosensor **2** recorded in CD₃CN and d₆-DMSO at 500 MHz. The sensor is present in both the merocyanine and spiropyran forms in the spectrum. H₂O signal at δ 3.1 ppm suppressed.

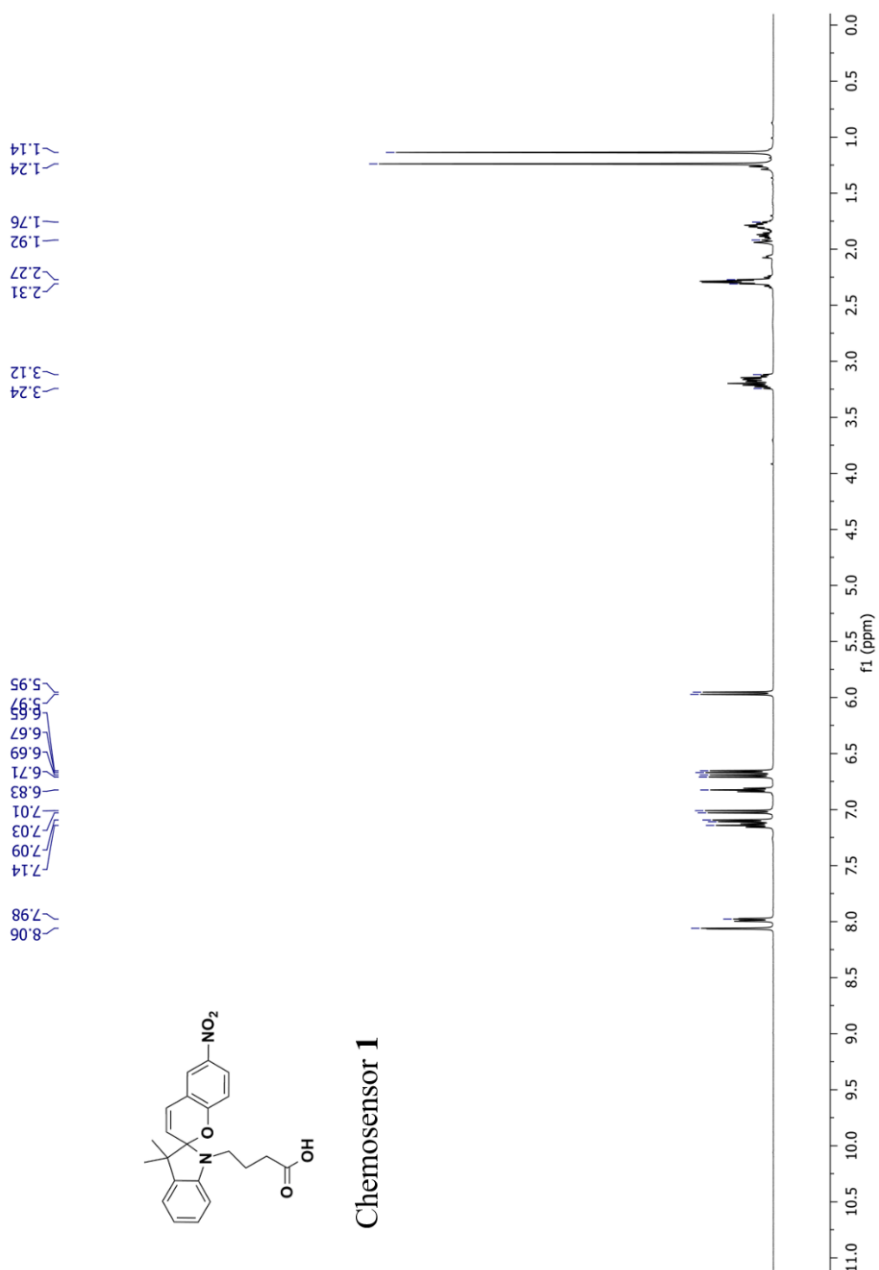


Figure S3-6. ¹H NMR spectrum of chemosensor **1** recorded in CD₃CN at 500 MHz.

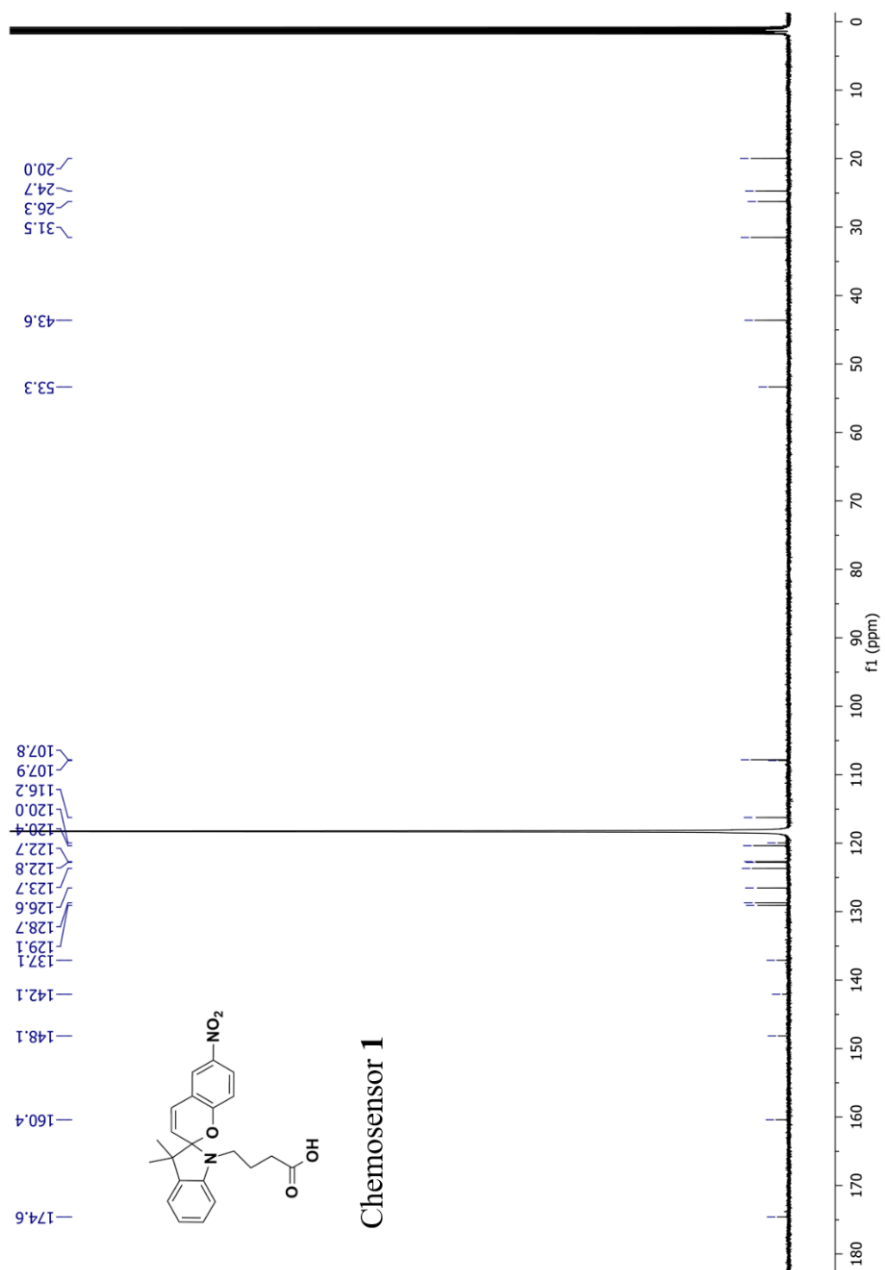


Figure S3-7. ¹³C NMR spectrum of chemosensor **1** recorded in CD₃CN at 500 MHz.

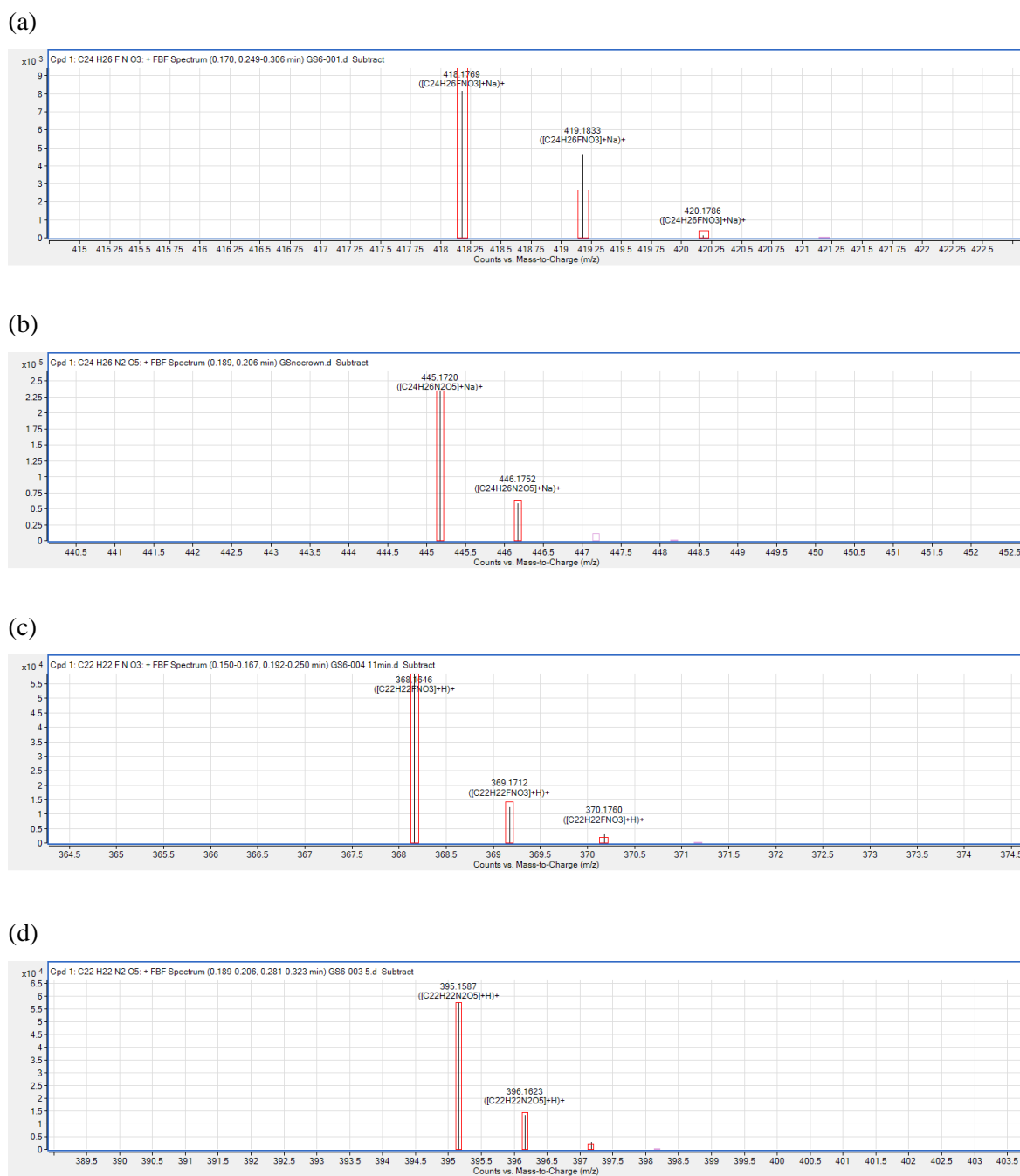


Figure S3-8. ESI-HRMS spectra of chemosensors (a) **4**, (b) **3**, (c) **2** and (d) **1**.

5.3.3 DFT Calculations

Reaction energies were calculated based on the following equation, where ‘M’ denotes Mg^{2+} or Ca^{2+} , and ‘MC’ denotes the merocyanine form of sensor **1** or **2**.

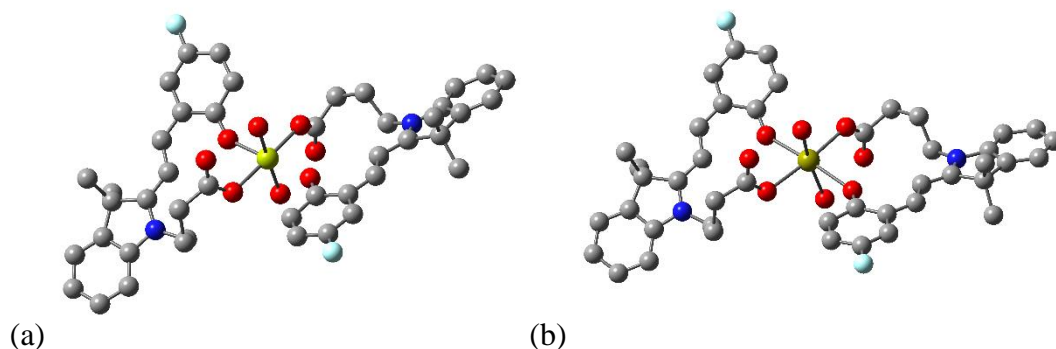
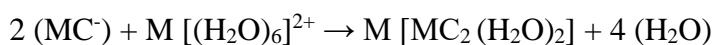


Figure S3-9. B3LYP/6-311G** optimized structure of sensor **2** bound to (A) Mg^{2+} (yellow) and (B) Ca^{2+} (gold), respectively, in a 2:1 ratio, showing oxygen atoms (red) chelating to the metal ion. Hydrogen atoms are omitted for clarity. The $\text{Mg}^{2+} \cdots \text{O}$ distances are between 2.08 and 2.12 Å, and $\text{Ca}^{2+} \cdots \text{O}$ distances are between 2.36 and 2.45 Å. Reaction energies for the formation of the $\text{M}[\mathbf{2}(\text{MC})_2(\text{H}_2\text{O})_2]$ species were calculated to be -315.7 kJ/mol and -151.2 kJ/mol for Mg^{2+} and Ca^{2+} , respectively.

$\text{Mg}[(1\text{MC})_2(\text{OH}_2)_2]^{2+}$ structural coordinates

C	-9.7382	-2.39273	-0.54798	C	-3.95854	-2.89702	-0.75039
C	-8.87202	-3.2718	-1.20323	C	-2.66296	-3.36218	-1.43183
C	-7.52126	-2.95646	-1.38327	C	-1.66747	-2.19761	-1.52686
C	-7.08145	-1.73431	-0.88255	O	-1.34872	-1.66068	-0.41583
C	-7.93223	-0.84443	-0.22548	O	-1.28239	-1.83632	-2.66599
C	-9.27104	-1.16691	-0.0557	C	9.18571	2.88535	-1.41215
N	-5.78434	-1.17661	-0.93401	C	8.14126	3.7884	-1.62533
C	-5.73025	0.02647	-0.31428	C	6.80687	3.40416	-1.45829
C	-7.14816	0.39615	0.16917	C	6.56533	2.08803	-1.07215
O	-1.66707	1.19762	0.03309	C	7.59713	1.17238	-0.85884
C	-1.93797	2.42205	0.21574	C	8.91722	1.56536	-1.02702
C	-3.31945	2.87881	0.42033	N	5.32412	1.44881	-0.84912
C	-4.45858	2.0476	0.29223	C	5.49117	0.1486	-0.49843
C	-4.52934	0.73487	-0.15626	C	6.99965	-0.16796	-0.46795
C	-0.90636	3.43212	0.24791	O	1.668	-1.45168	-0.06084
C	-1.18322	4.74063	0.52665	C	2.04201	-2.5826	0.36824
C	-2.52098	5.14616	0.78367	C	3.46534	-2.93974	0.43283
C	-3.55454	4.24287	0.73063	C	4.51382	-2.0384	0.12753
C	-7.19331	0.61189	1.69913	C	4.40953	-0.69916	-0.23026
C	-7.71777	1.6217	-0.59249	C	1.09185	-3.5766	0.80721
C	-4.67018	-1.84589	-1.61489	C	1.48887	-4.81801	1.21652
Mg	-0.00768	-0.13283	-0.00115	C	2.87038	-5.15644	1.22841

C	3.82739	-4.24498	0.85261	H	-5.07873	-2.30317	-2.5216
C	7.38235	-1.24429	-1.51364	H	-3.96826	-1.07835	-1.94341
C	7.47021	-0.56908	0.95209	H	-3.7004	-2.45748	0.21735
C	4.049	2.16693	-1.01577	H	-4.62917	-3.74349	-0.56478
C	3.69056	3.08214	0.1667	H	-2.2121	-4.16048	-0.83273
C	3.36822	2.36982	1.48434	H	-2.85514	-3.75541	-2.43453
C	2.0898	1.51788	1.51054	H	10.21294	3.20848	-1.54642
O	1.48707	1.31391	0.40186	H	8.36413	4.80774	-1.92435
O	1.7455	1.07584	2.63151	H	6.00277	4.11153	-1.62327
O	-0.25121	-0.43107	2.05714	H	9.73269	0.86611	-0.86603
O	0.38039	0.06833	-2.07103	H	5.50574	-2.4728	0.2134
N	-2.80268	6.53712	1.09163	H	3.40959	-0.29102	-0.27361
O	-3.97486	6.86179	1.31297	H	0.04723	-3.28823	0.78121
O	-1.85117	7.32484	1.11584	H	0.77391	-5.56636	1.53669
N	3.27817	-6.48402	1.65388	H	4.87089	-4.53752	0.89295
O	4.48501	-6.75262	1.65833	H	8.47102	-1.34598	-1.54852
O	2.39298	-7.27843	1.98845	H	6.95961	-2.22076	-1.26935
H	-10.7815	-2.6619	-0.4184	H	7.03676	-0.96245	-2.51177
H	-9.24854	-4.2183	-1.57794	H	7.19826	0.19427	1.6858
H	-6.85268	-3.64574	-1.88619	H	7.03738	-1.5186	1.27269
H	-9.94991	-0.48622	0.44998	H	8.55925	-0.67261	0.95833
H	-5.39081	2.55043	0.53222	H	3.24799	1.44841	-1.17057
H	-3.59577	0.25168	-0.41625	H	4.14659	2.75791	-1.93191
H	0.10517	3.09023	0.06301	H	2.82243	3.66794	-0.154
H	-0.40251	5.49099	0.56291	H	4.50609	3.79565	0.3349
H	-4.56365	4.59575	0.91291	H	3.27753	3.1074	2.28874
H	-8.22856	0.76645	2.01721	H	4.19427	1.71531	1.7903
H	-6.61073	1.48444	2.00218	H	-1.07838	-0.03345	2.35485
H	-6.80215	-0.26012	2.2298	H	0.50159	0.14396	2.42784
H	-7.65258	1.47701	-1.67406	H	-0.26919	-0.61842	-2.43856
H	-8.77235	1.74866	-0.33133	H	1.24239	-0.36552	-2.13824
H	-7.19645	2.54631	-0.33883				

Mg[(2MC)₂(OH₂)₂]²⁺ structural coordinates

C	-9.77165	-1.76887	-0.99545	C	-0.98841	4.85751	1.01967
C	-8.90115	-2.73158	-1.51186	C	-2.32198	5.30478	1.1868
C	-7.51948	-2.51549	-1.54449	C	-3.38027	4.47459	0.9806
C	-7.05048	-1.30377	-1.04304	C	-7.29231	1.12271	1.44017
C	-7.90645	-0.332	-0.52084	C	-7.48013	2.10511	-0.91417
C	-9.27506	-0.55709	-0.49608	C	-4.5887	-1.61738	-1.47021
N	-5.72242	-0.83857	-0.96665	F	-2.52111	6.59387	1.5517
C	-5.6494	0.38907	-0.3825	Mg	0.07669	-0.05726	0.3008
C	-7.0855	0.86601	-0.07059	C	-4.03918	-2.62708	-0.45173
O	-1.55253	1.39633	0.14366	C	-2.72079	-3.23894	-0.95203
C	-1.8045	2.60961	0.44184	C	-1.66679	-2.13397	-1.09937
C	-3.17562	3.10914	0.58729	O	-1.3448	-1.53856	-0.02139
C	-4.32794	2.33839	0.34198	O	-1.25855	-1.85761	-2.256
C	-4.43349	1.02766	-0.12845	C	9.29145	2.00875	-1.88277
C	-0.73946	3.5606	0.65698	C	8.31061	2.97953	-2.09674

C	6.96531	2.72776	-1.80653	H	-6.69865	1.96751	1.79548
C	6.64215	1.47162	-1.29642	H	-7.01662	0.24257	2.02696
C	7.61248	0.48929	-1.08011	H	-7.31185	1.92311	-1.97894
C	8.94294	0.75104	-1.3714	H	-8.54408	2.31647	-0.77143
N	5.37725	0.96602	-0.93767	H	-6.91809	2.99598	-0.6274
C	5.4636	-0.32182	-0.48874	H	-4.92444	-2.12719	-2.37866
C	6.94132	-0.7607	-0.53662	H	-3.80878	-0.92023	-1.7792
O	1.60205	-1.46091	0.42988	H	-3.84619	-2.11469	0.49553
C	1.8897	-2.61714	0.86245	H	-4.78636	-3.40654	-0.26241
C	3.26723	-3.12268	0.84155	H	-2.36784	-3.97494	-0.22251
C	4.36075	-2.35962	0.39457	H	-2.85511	-3.74166	-1.91449
C	4.34791	-1.04285	-0.07738	H	10.32874	2.22859	-2.11433
C	0.87311	-3.49347	1.39664	H	8.59212	3.94988	-2.49419
C	1.17549	-4.75032	1.84539	H	6.21231	3.48895	-1.9743
C	2.51248	-5.22192	1.79668	H	9.70716	-0.00421	-1.21001
C	3.52618	-4.45072	1.31814	H	5.31523	-2.87716	0.44552
C	7.15553	-1.9448	-1.51002	H	3.38087	-0.5615	-0.10373
C	7.48653	-1.0865	0.87509	H	-0.13909	-3.10613	1.41161
C	4.15539	1.77355	-1.06934	H	0.40959	-5.40843	2.24534
F	2.75838	-6.47618	2.24921	H	4.53865	-4.8431	1.30446
C	3.97062	2.80576	0.05653	H	8.22579	-2.15205	-1.60565
C	3.67318	2.22683	1.44437	H	6.66275	-2.85376	-1.15948
C	2.30599	1.54628	1.61274	H	6.76569	-1.7088	-2.5037
O	1.60007	1.37732	0.56131	H	7.32999	-0.24663	1.55719
O	1.98954	1.20199	2.77612	H	7.00422	-1.9666	1.30517
O	-0.22028	-0.06698	2.38103	H	8.56206	-1.28076	0.81747
O	0.26235	0.19099	-1.79301	H	3.28891	1.11713	-1.1124
H	-10.8396	-1.96105	-0.97885	H	4.22522	2.28524	-2.03509
H	-9.29879	-3.66708	-1.89285	H	3.14188	3.45238	-0.25143
H	-6.8494	-3.27097	-1.93869	H	4.86316	3.44054	0.115
H	-9.95623	0.18882	-0.09624	H	3.73575	3.01827	2.19948
H	-5.25399	2.87685	0.52023	H	4.43413	1.49214	1.73573
H	-3.50819	0.49576	-0.31002	H	-0.96962	0.49362	2.61589
H	0.2707	3.18939	0.52707	H	0.61715	0.42847	2.67914
H	-0.17934	5.56237	1.18721	H	-0.28036	-0.60563	-2.10915
H	-4.38976	4.85496	1.10446	H	-0.2928	0.96139	-1.97346
H	-8.34656	1.34278	1.63386				

Ca[(1MC)₂(OH)₂]²⁺ structural coordinates

C	9.92152	2.45964	-1.42888	C	2.29089	-2.29233	0.56391
C	8.97202	3.43805	-1.73433	C	3.68806	-2.74676	0.52855
C	7.60272	3.18143	-1.61054	C	4.78881	-1.9205	0.20014
C	7.22961	1.91356	-1.17272	C	4.79688	-0.58612	-0.18568
C	8.16453	0.9258	-0.86016	C	1.29094	-3.29022	0.87452
C	9.52036	1.19149	-0.98861	C	1.61776	-4.58796	1.14674
N	5.92993	1.39687	-0.97254	C	2.979	-4.99667	1.12548
C	5.96159	0.12296	-0.51419	C	3.97837	-4.10358	0.82639
C	7.43346	-0.33259	-0.4231	C	7.83296	-0.70947	1.02356
O	1.96521	-1.08881	0.33915	C	7.74206	-1.48296	-1.41518

C	4.72374	2.19153	-1.23277	H	10.26273	0.43447	-0.75247
Ca	0.01642	0.30535	0.53418	H	5.74334	-2.43575	0.24571
C	4.30175	3.04453	-0.02647	H	3.83935	-0.08508	-0.23591
C	2.99343	3.80858	-0.30424	H	0.25725	-2.9586	0.88501
C	1.86777	2.805	-0.58261	H	0.86112	-5.32616	1.38412
O	1.30667	2.28677	0.43396	H	5.00352	-4.45716	0.81428
O	1.65155	2.51031	-1.78819	H	8.90811	-0.90699	1.06429
C	-8.71098	-3.58511	-2.27919	H	7.311	-1.60259	1.37235
C	-7.55369	-4.36578	-2.3392	H	7.61209	0.10665	1.71648
C	-6.31191	-3.84992	-1.95505	H	7.4411	-1.21531	-2.43147
C	-6.27904	-2.52962	-1.51269	H	8.81879	-1.67588	-1.42083
C	-7.42424	-1.73511	-1.45264	H	7.23501	-2.41033	-1.14247
C	-8.65158	-2.25819	-1.83448	H	4.93543	2.82532	-2.09842
N	-5.16413	-1.76993	-1.08589	H	3.92144	1.52073	-1.53855
C	-5.52145	-0.50482	-0.75837	H	4.15756	2.39418	0.8433
C	-7.04393	-0.35211	-0.95513	H	5.10542	3.74702	0.22351
O	-2.00353	1.58809	0.18238	H	2.74284	4.4123	0.57232
C	-2.58925	2.67125	0.48257	H	3.11407	4.46863	-1.16913
C	-4.04691	2.8135	0.3962	H	-9.66303	-4.00948	-2.58107
C	-4.91733	1.7677	-0.00274	H	-7.61444	-5.39178	-2.688
C	-4.59344	0.45932	-0.33636	H	-5.41979	-4.46295	-2.00311
C	-1.83971	3.82539	0.91992	H	-9.55301	-1.65346	-1.79481
C	-2.45074	5.00731	1.23377	H	-5.96261	2.06028	-0.03583
C	-3.86346	5.12271	1.13309	H	-3.55193	0.18171	-0.25354
C	-4.63511	4.06006	0.72589	H	-0.76099	3.7115	0.9726
C	-7.3843	0.70608	-2.03338	H	-1.88412	5.87242	1.55686
C	-7.76403	-0.05205	0.38309	H	-5.70992	4.19164	0.66531
C	-3.8142	-2.35841	-1.04147	H	-8.46008	0.68954	-2.23097
C	-3.5894	-3.2925	0.15943	H	-7.11389	1.71553	-1.7186
C	-3.55913	-2.60273	1.52623	H	-6.86514	0.49086	-2.97108
C	-2.3574	-1.67688	1.77617	H	-7.51698	-0.80366	1.13742
O	-1.55241	-1.47828	0.80471	H	-7.49853	0.92924	0.78058
O	-2.26621	-1.1823	2.92458	H	-8.84628	-0.07311	0.2254
O	-0.14661	0.30877	2.92943	H	-3.0726	-1.5639	-1.02442
O	-0.18056	0.61432	-1.89582	H	-3.68793	-2.90932	-1.97888
N	3.31827	-6.37836	1.41537	H	-2.62791	-3.78559	-0.01589
O	4.51052	-6.70533	1.39554	H	-4.35583	-4.07611	0.16221
O	2.39255	-7.1574	1.66596	H	-3.55525	-3.35661	2.32098
N	-4.50408	6.38376	1.46465	H	-4.46846	-2.01292	1.69684
O	-5.73376	6.45944	1.36302	H	-0.2327	1.06973	3.51344
O	-3.78219	7.31665	1.83143	H	-0.97142	-0.26779	3.05865
H	10.97825	2.68411	-1.53174	H	0.52633	1.32741	-1.97795
H	9.29782	4.41685	-2.07183	H	-1.01214	1.11012	-1.8976
H	6.87252	3.94792	-1.84359				

Ca[(2MC)₂(OH₂)₂]²⁺ structural coordinates

C	10.1262	1.6176	-1.01688	C	7.88933	2.48087	-1.44437
C	9.2791	2.63956	-1.45173	C	7.38749	1.26461	-0.98748

C	8.22019	0.23466	-0.54556	O	-1.75682	-1.45677	0.52804
C	9.59712	0.40303	-0.55982	O	-0.031	-0.01684	2.73986
N	6.04418	0.84824	-0.88829	O	0.30953	0.02931	-2.07947
C	5.94186	-0.40576	-0.36995	H	11.2013	1.76544	-1.0313
C	7.36644	-0.94832	-0.1184	H	9.70186	3.57649	-1.80077
O	1.81452	-1.32633	0.11034	H	7.2389	3.28123	-1.77792
C	2.04551	-2.53149	0.45677	H	10.2598	-0.3892	-0.22298
C	3.40199	-3.06876	0.59455	H	5.48532	-2.89643	0.50471
C	4.57339	-2.33292	0.33203	H	3.79851	-0.46708	-0.29873
C	4.71167	-1.0211	-0.12575	H	-0.05081	-3.04203	0.62487
C	0.95483	-3.43568	0.73882	H	0.34133	-5.39921	1.34745
C	1.16908	-4.72943	1.13398	H	4.56988	-4.84106	1.12802
C	2.49117	-5.21828	1.27316	H	8.65866	-1.52586	1.53079
C	3.57081	-4.43051	1.01636	H	6.99582	-2.09914	1.72328
C	7.6075	-1.26372	1.37702	H	7.38112	-0.39486	2.00067
C	7.68693	-2.17085	-1.01429	H	7.50352	-1.94251	-2.06755
C	4.92703	1.70789	-1.29048	H	8.74317	-2.43441	-0.90448
F	2.65729	-6.50326	1.66778	H	7.09121	-3.04558	-0.74664
Ca	-0.06606	0.23258	0.33666	H	5.25362	2.27527	-2.16697
C	4.46677	2.65655	-0.17213	H	4.10442	1.07856	-1.62897
C	3.21928	3.45847	-0.58812	H	4.22935	2.0701	0.72217
C	2.06603	2.48615	-0.86634	H	5.28631	3.33515	0.09252
O	1.43771	2.05215	0.14852	H	2.94475	4.1346	0.22628
O	1.89719	2.12814	-2.06298	H	3.42554	4.04802	-1.48713
C	-9.41212	-2.35984	-1.92603	H	-10.4358	-2.6409	-2.15155
C	-8.37112	-3.25087	-2.19575	H	-8.59228	-4.22041	-2.63136
C	-7.04168	-2.91953	-1.91309	H	-6.24123	-3.61823	-2.12574
C	-6.79695	-1.66695	-1.35269	H	-9.95254	-0.40843	-1.16742
C	-7.82695	-0.7621	-1.08604	H	-5.77661	2.69963	0.46846
C	-9.14147	-1.10265	-1.36885	H	-3.6555	0.57098	-0.14199
N	-5.56287	-1.09148	-0.98836	H	-0.33794	3.61634	1.01586
C	-5.72592	0.17428	-0.50037	H	-1.10625	5.87076	1.79147
C	-7.2325	0.51333	-0.51415	H	-5.19279	4.74598	1.25293
O	-1.91833	1.69596	0.31979	H	-8.63285	1.82988	-1.52962
C	-2.32902	2.8365	0.69344	H	-7.12111	2.63804	-1.09049
C	-3.75509	3.17305	0.75162	H	-7.15914	1.51878	-2.45954
C	-4.7774	2.28311	0.37721	H	-7.55701	-0.085	1.56843
C	-4.65871	0.97074	-0.09314	H	-7.35034	1.65952	1.36414
C	-1.39234	3.86725	1.08005	H	-8.86427	0.88512	0.87309
C	-1.81316	5.09981	1.49937	H	-3.46971	-1.11439	-1.14072
C	-3.19937	5.3951	1.55771	H	-4.32641	-2.25646	-2.16897
C	-4.1411	4.48082	1.19941	H	-3.18888	-3.48377	-0.45122
C	-7.54859	1.70212	-1.45465	H	-4.91492	-3.61158	-0.12036
C	-7.77761	0.76179	0.91309	H	-3.86905	-3.25597	2.01442
C	-4.29757	-1.81862	-1.1652	H	-4.62234	-1.73396	1.62883
F	-3.56664	6.62941	1.98073	H	0.66061	-0.48721	3.21814
C	-4.06518	-2.91886	-0.11629	H	-0.87994	-0.56414	2.85308
C	-3.82533	-2.41748	1.31061	H	0.86595	0.86191	-2.19686
C	-2.48827	-1.69691	1.54602	H	0.96159	-0.68592	-2.07069
O	-2.22314	-1.39588	2.73529				

Sensor 1(MC) structural coordinates

C	5.27391	-2.4027	-0.46016	O	1.61985	1.21483	2.80677
C	5.62874	-1.16485	-1.00067	N	-6.0465	-1.04299	0.64108
C	4.6906	-0.13544	-1.13021	O	-5.72276	-1.97821	1.39201
C	3.39042	-0.38943	-0.69761	O	-7.23036	-0.73717	0.41515
C	3.01521	-1.63123	-0.17694	H	6.02032	-3.18583	-0.36529
C	3.95628	-2.64122	-0.04575	H	6.65036	-0.99267	-1.3274
N	2.26593	0.45748	-0.73396	H	4.9708	0.82138	-1.55261
C	1.13931	-0.20969	-0.367	H	3.67806	-3.60745	0.36632
C	1.52982	-1.61182	0.13587	H	-1.23349	-1.12223	0.5672
O	-2.11432	1.85488	-1.98539	H	-0.2555	1.23287	-1.12414
C	-2.97096	1.2165	-1.34748	H	-4.64149	2.30743	-2.19444
C	-2.64148	0.12406	-0.39614	H	-6.42254	0.99849	-1.0296
C	-1.31277	-0.2709	-0.10378	H	-3.45801	-1.39872	0.91313
C	-0.14187	0.31889	-0.55687	H	1.19902	-3.71178	-0.30702
C	-4.39699	1.49527	-1.51684	H	-0.261	-2.72671	-0.47401
C	-5.37014	0.78461	-0.88485	H	0.99622	-2.65822	-1.71749
C	-5.01359	-0.28076	-0.00376	H	1.64567	-0.83115	2.19359
C	-3.68676	-0.5886	0.22862	H	0.22865	-1.84521	1.88829
C	0.81752	-2.74146	-0.64113	H	1.81298	-2.61912	2.03952
C	1.29337	-1.72867	1.66815	H	1.36671	2.31867	-0.7776
C	2.34917	1.90772	-0.9962	H	2.59137	2.05823	-2.05583
C	3.33904	2.6548	-0.07371	H	3.02408	3.70182	-0.12396
C	3.28493	2.19672	1.38841	H	4.36348	2.60168	-0.46456
C	1.8216	2.11555	1.95165	H	3.84863	2.91685	1.99734
O	1.02096	2.95906	1.4759	H	3.78048	1.22911	1.52155

Sensor 2(MC) structural coordinates

C	4.89339	-2.27376	-0.35189	C	-0.67795	0.08343	-0.49027
C	5.13107	-1.11982	-1.10065	C	-5.04467	0.77387	-1.40679
C	4.12441	-0.17131	-1.3121	C	-5.93547	0.1381	-0.5908
C	2.87322	-0.41403	-0.74556	C	-5.45984	-0.70325	0.45015
C	2.61478	-1.58035	-0.01515	C	-4.13077	-0.89345	0.66859
C	3.62313	-2.50762	0.19501	C	0.47081	-2.87833	-0.08915
N	1.70321	0.3573	-0.82063	C	1.03932	-1.43586	1.95366
C	0.63545	-0.32058	-0.29162	C	1.66465	1.76589	-1.25466
C	1.15613	-1.58877	0.41121	F	-6.38742	-1.32282	1.23642
O	-2.82145	1.19375	-2.0613	C	2.70648	2.67248	-0.56393
C	-3.59625	0.62389	-1.26534	C	2.83047	2.43316	0.94458
C	-3.14832	-0.24615	-0.15231	C	1.44537	2.46059	1.68491
C	-1.79527	-0.49089	0.12708	O	0.60741	3.26861	1.21247

O	1.33825	1.67678	2.66428
H	5.69118	-2.99431	-0.19664
H	6.11465	-0.94948	-1.53008
H	4.31605	0.71854	-1.89858
H	3.43317	-3.40955	0.77116
H	-1.61787	-1.1913	0.93982
H	-0.88199	0.88327	-1.19026
H	-5.37728	1.42265	-2.21123
H	-7.00925	0.25627	-0.71212
H	-3.80999	-1.53651	1.4838
H	0.93843	-3.75054	0.38029
H	-0.59247	-2.8912	0.15761
H	0.56767	-2.98317	-1.17409
H	1.37895	-0.44479	2.28465
H	0.0001	-1.55271	2.27523
H	1.63222	-2.22117	2.43708
H	0.69014	2.14977	-0.95852
H	1.75804	1.80842	-2.3479
H	2.33173	3.68943	-0.71833
H	3.6848	2.60351	-1.05756
H	3.4582	3.23017	1.36779
H	3.34337	1.49036	1.16104

5.3.4 Absorbance and Fluorescence Spectra

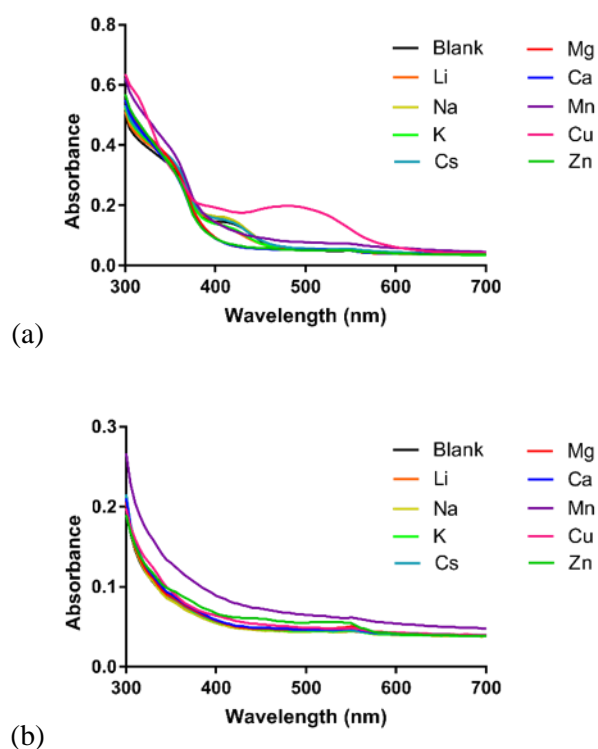


Figure S3-10. Absorbance spectra of (a) chemosensor **1** (50 μM) and (b) chemosensor **2** (50 μM) in the presence of an excess of biologically relevant metal ions (100 μM). Experiments were performed under ambient light conditions in acetonitrile solvent.

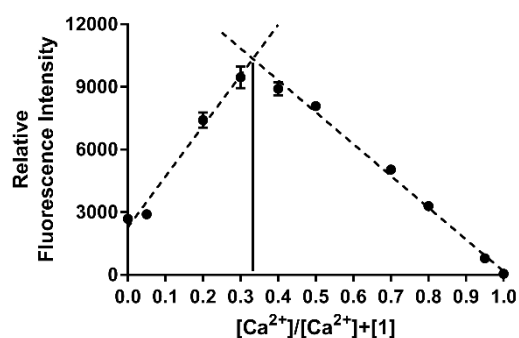


Figure S3-11. Job's plot of chemosensor **1** (50 μM) in the presence of Ca²⁺ ions (100 μM). Fluorescence excitation was at 532 nm, with experiments performed under ambient light conditions in acetonitrile solvent.

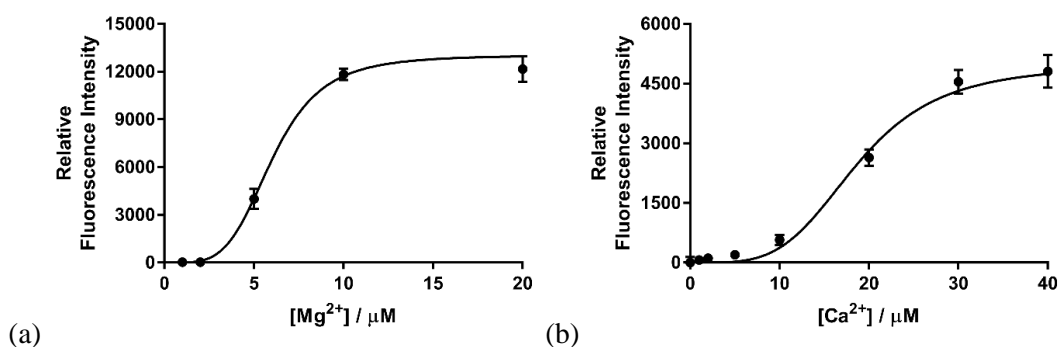


Figure S3-12. Metal ion titration curves of chemosensor **1** (50 μM) with (a) Mg^{2+} ($K_d(\text{Mg}^{2+}) = 6.0 \pm 0.3 \mu\text{M}$, $h = 4.3 \pm 0.9$) and (b) Ca^{2+} ($K_d(\text{Ca}^{2+}) = 18.7 \pm 0.6 \mu\text{M}$, $h = 4.0 \pm 0.5$) measured from their respective maximum emissions. Experiments were recorded in HPLC-grade acetonitrile, with excitation at 532 nm under ambient light conditions.

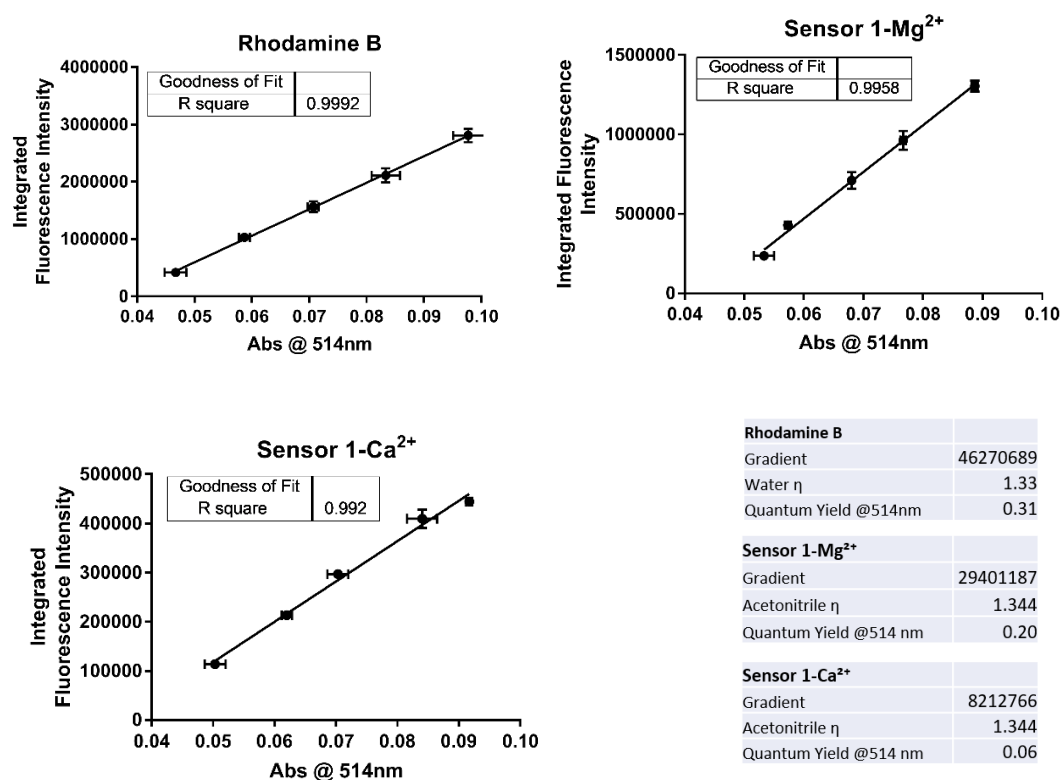


Figure S3-13. Integrated fluorescence spectra after excitation at 514 nm versus the absorbance at 514 nm for Rhodamine B (0 – 5 μM , water); **1**MC-Mg²⁺ (0-100 μM , acetonitrile) in the presence of a 2-fold excess of Mg²⁺; and **1**MC-Ca²⁺ (0-100 μM , acetonitrile) in the presence of a 2-fold excess of Ca²⁺. Spectra were recorded under ambient light conditions, in acetonitrile solvent. The quantum yield of **1**MC-Mg²⁺ was calculated to be $\Phi = 0.20$, and the quantum yield of **1**MC-Ca²⁺ was calculated to be $\Phi = 0.06$.

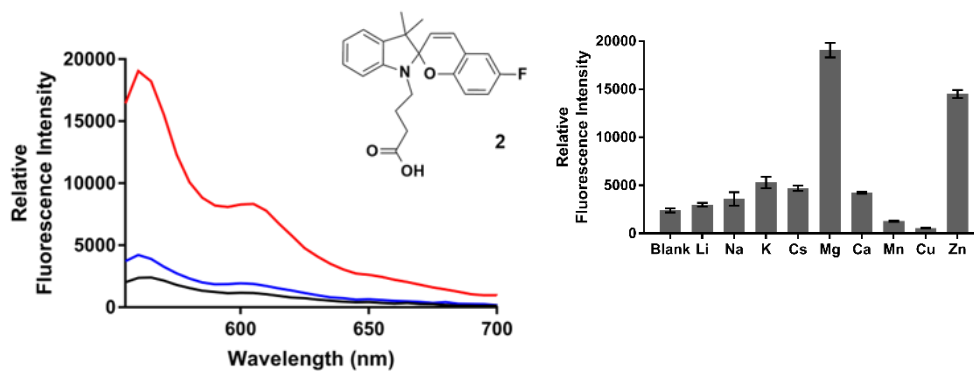


Figure S3-14. Fluorescence emission spectra of chemosensor **2** (50 μM) in the absence (black) and presence of excess Mg^{2+} (red, 100 μM) and Ca^{2+} (blue, 100 μM), respectively. Inset: Selectivity profile of chemosensor **2** in the presence of various biologically relevant metal ions (100 μM), with λ_{max} at 560 nm. Excitation was at 532 nm, and all experiments were performed under ambient light conditions, in HPLC-grade acetonitrile solvent.

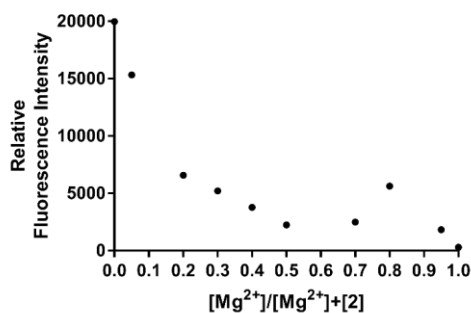


Figure S3-15. Job's plot of chemosensor **2** (50 μM) in the presence of Mg^{2+} ions (100 μM), with λ_{max} at 560 nm. Fluorescence excitation was at 532 nm, with experiments performed under ambient light conditions in acetonitrile solvent. The plot suggests a more complex binding stoichiometry for chemosensor **2**.

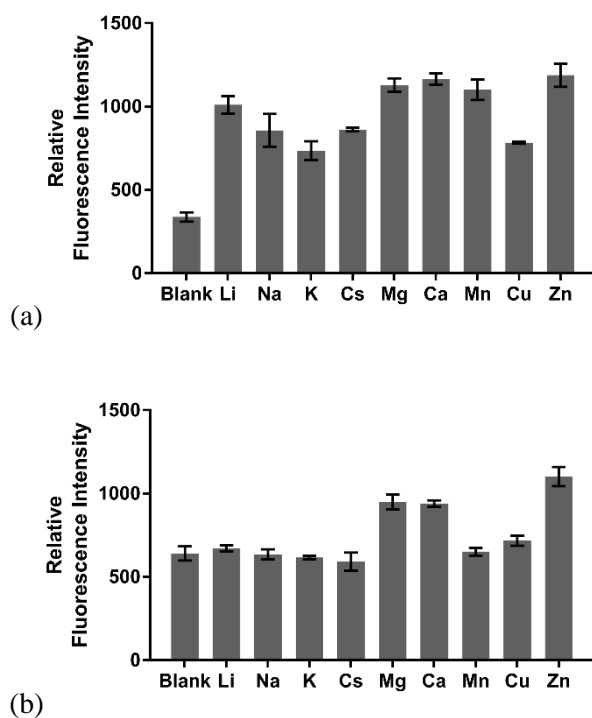


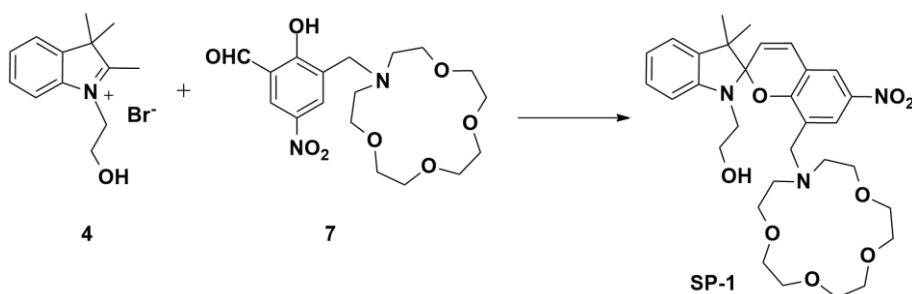
Figure S3-16. Selectivity profiles of (a) compound **3** (50 μM) and (b) compound **4** (50 μM) in the presence of an excess of biologically relevant metal ions (100 μM) in HPLC-grade acetonitrile. Fluorescence excitation was at 532 nm.

5.3.1 Photoswitching in Optical Fibre

A 5 mW laser was coupled into the core of a suspended core fibre (SCF) via dichroic mirror at a wavelength of 532 nm using 60X objective as described previously.³ One end of the SCF was filled by capillary action by dipping in an acetonitrile solution containing sensor **1** (500 μM) and Mg^{2+} (1 mM). The sensor-filled SCF was then exposed to a 532 nm green laser for 2 min, and fluorescence was measured after excitation with the same 532 nm laser (10 x 50 ms). Next, the sensor-filled SCF was exposed to UV light (365 nm) for 5 min to facilitate photoswitching to the ring-opened MC(**1**)- Mg^{2+} complex, and fluorescence was measured again after excitation with the 532 nm green laser (10 x 50 ms). This process was repeated for 10 cycles to investigate photoswitching of sensor **1** in the presence of Mg^{2+} . Fluorescence of Rhodamine B was similarly recorded; however, UV irradiation was not required for the ‘on’ cycles as this fluorophore does not photoswitch.

5.4 Supporting Information to Chapter 4

5.4.1 Chemical Syntheses



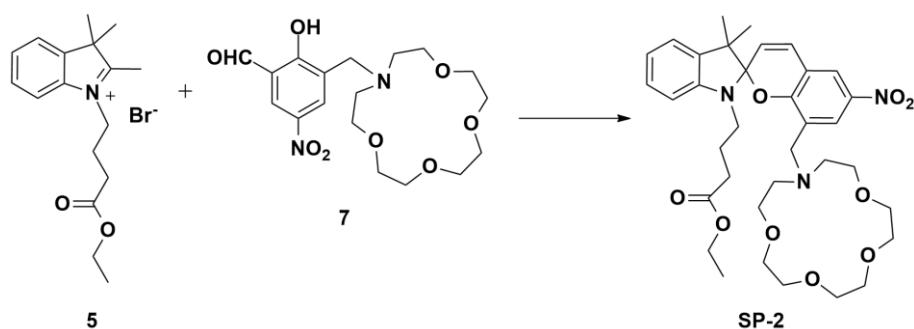
2-(8-((1,4,7,10-Tetraoxa-13-azacyclopentadecan-13-yl)methyl)-3',3'-dimethyl-6-nitrospiro[chromene-2,2'-indolin]-1'-yl)ethanol (**SP-1**).

Compound **7** (566 mg, 1.4 mmol) and indoline **4** (230 mg, 1.1 mmol) were combined and dissolved in ethanol (10 mL) and the mixture was heated to reflux for 18 h. Excess solvent was removed *in vacuo* to give a purple crude solid (0.68 g) which was purified by C18 reverse phase silica chromatography eluting with 0 - 30% water / acetonitrile to give **SP-1** as a purple solid (120 mg, 18 % yield).

^1H NMR (500 MHz, DMSO- d_6) δ 8.13 (dd, 2H, ArH, $J = 12.5, 2.5$ Hz), 7.22 (d, 1H, ArH, $J = 10.5$ Hz), 7.15 – 7.12 (m, 2H, ArH), 6.81 (t, 1H, ArH, $J = 7.5$ Hz), 6.62 (d, 1H, ArH, $J = 7.5$ Hz), 5.99 (d, 1H, ArH, $J = 10.5$ Hz), 3.61 – 3.53 (m, 4H, CH₂), 3.51-3.47 (m, 9H, CH₂), 3.45 – 3.41 (m, 5H, CH₂), 3.39 – 3.33 (m, 5H, CH₂), 2.64 (s, 3H, CH₂), 1.23 (s, 3H, CH₃), 1.13 (s, 3H, CH₃) ppm;

^{13}C NMR (126 MHz, DMSO- d_6) δ 157.1, 147.4, 140.1, 136.0, 128.5, 127.6, 127.0, 125.6, 121.5, 121.4, 121.0, 119.5, 118.7, 107.1, 106.1, 70.3, 69.8, 69.5, 69.1, 53.9, 52.3, 51.6, 28.5, 25.8, 19.7 ppm;

HRMS-ESI (m/z) calculated for C₃₁H₄₁N₃O₈ [M + H]⁺ 584.2972, found 584.2943 and [M + Na]⁺ 606.2791, found 606.2773.



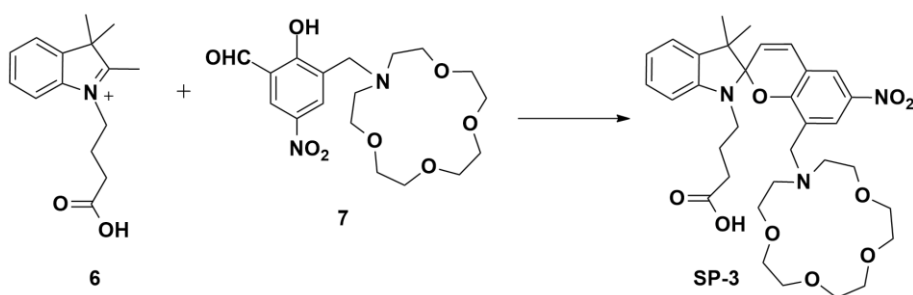
Ethyl 4-(8-((1,4,7,10-tetraoxa-13-azacyclopentadecan-13-yl)methyl)-3',3'-dimethyl-6-nitrospiro [chromene-2,2'-indolin]-1'-yl)butanoate (SP-2).

Compound **7** (383 mg, 1.0 mmol) and indoline **5** (263 mg, 1.0 mmol) were combined and dissolved in ethanol (10 mL) and the mixture was heated to reflux for 8 h. Excess solvent was removed *in vacuo* to give a purple crude solid. A portion of the crude compound (12 mg) was purified by reverse phase HPLC eluting with water and acetonitrile (60 - 100%) to give **SP-2** as a purple solid (2 mg, 17 % yield).

^1H NMR (500 MHz, CD_3CN) δ 8.18 – 8.16 (m, 1H, ArH), 7.97 (d, 1H, ArH, $J = 3.0$ Hz), 7.17-7.11 (m, 2H, ArH), 7.02 (d, 1H, ArH, $J = 10.5$ Hz), 6.85 – 6.82 (m, 1H, ArH), 6.67 (d, 1H, ArH, $J = 8.0$ Hz), 5.95 (d, 1H, ArH, $J = 10.5$ Hz), 4.05 – 4.01 (m, 2H, CH_2), 3.56 – 3.37 (m, 18H, 9 x CH_2), 3.18 – 3.14 (m, 2H, CH_2), 2.59 – 2.49 (m, 4H, 2 x CH_2), 2.38 – 2.32 (m, 2H, CH_2), 1.84 – 1.78 (m, 2H, CH_2), 1.25 (s, 2H, CH_3), 1.17 – 1.15 (m, 6H, 2 x CH_3) ppm;

^{13}C NMR (126 MHz, CD_3CN) δ 173.9, 148.1, 141.6, 137.2, 129.3, 128.6, 122.6, 122.4, 120.3, 107.7, 71.3, 70.9, 70.8, 70.7, 61.0, 53.2, 43.6, 32.2, 26.3, 24.8, 20.1, 14.5 ppm;

HRMS-ESI (m/z) calculated for $\text{C}_{35}\text{H}_{47}\text{N}_3\text{O}_9$ $[\text{M} + \text{Na}]^+$ 676.3210, found 676.3200.



4-(8-((1,4,7,10-Tetraoxa-13-azacyclopentadecan-13-yl)methyl)-3',3'-dimethyl-6-nitrospiro[chromene-2,2'-indolin]-1'-yl)butanoic acid (**SP-3**).

Compound **7** (470 mg, 1.2 mmol), indoline **6** (418 mg, 1.2 mmol) and triethylamine (164 μ L, 1.2 mmol) were combined and dissolved in ethanol (10 mL) and the mixture was heated to reflux for 18 h. Excess solvent was removed *in vacuo* to give a purple crude solid (1.15 g). A portion of the crude compound (15 mg) was purified by reverse phase HPLC eluting with water and acetonitrile (60 - 100%) to give **SP-3** as a purple solid (4 mg, 27 % yield).

^1H NMR (500 MHz, CD_3CN) δ 8.17 (d, 1H, ArH, $J = 7.5$ Hz), 7.96 (d, 1H, ArH, $J = 2.5$ Hz), 7.16-7.11 (m, 2H, ArH), 7.01 (d, 1H, ArH, $J = 10.5$ Hz), 6.83 (t, 1H, ArH, $J = 7.5$ Hz), 6.68 (d, 1H, ArH, $J = 7.5$ Hz), 5.95 (d, 1H, ArH, $J = 10.5$ Hz), 3.55 – 3.53 (m, 8H, 4 x CH_2), 3.48 – 3.46 (m, 4H, 2x CH_2), 3.42 – 3.38 (m, 6H, 3 x CH_2), 3.18 – 3.13 (m, 2H, CH_2), 2.59 – 2.49 (m, 4H, 2 x CH_2), 2.29 – 2.24 (m, 2H, CH_2), 1.90 – 1.81 (m, 2H, CH_2), 1.24 (s, 2H, CH_3), 1.14 (s, 3H, CH_3) ppm;

^{13}C NMR (126 MHz, CD_3CN) δ 158.1, 148.1, 141.6, 137.1, 129.3, 128.6, 126.9, 122.6, 122.4, 122.2, 120.2, 119.6, 107.8, 71.3, 70.8, 70.7, 70.2, 55.2, 53.1, 43.7, 31.9, 27.4, 26.3, 24.9, 20.1 ppm;

HRMS-ESI (m/z) calculated for $\text{C}_{33}\text{H}_{43}\text{N}_3\text{O}_9$ [$\text{M} + \text{H}$] $^+$ 626.3078, found 626.3070.

5.4.2 NMR and HRMS Characterisation Spectra

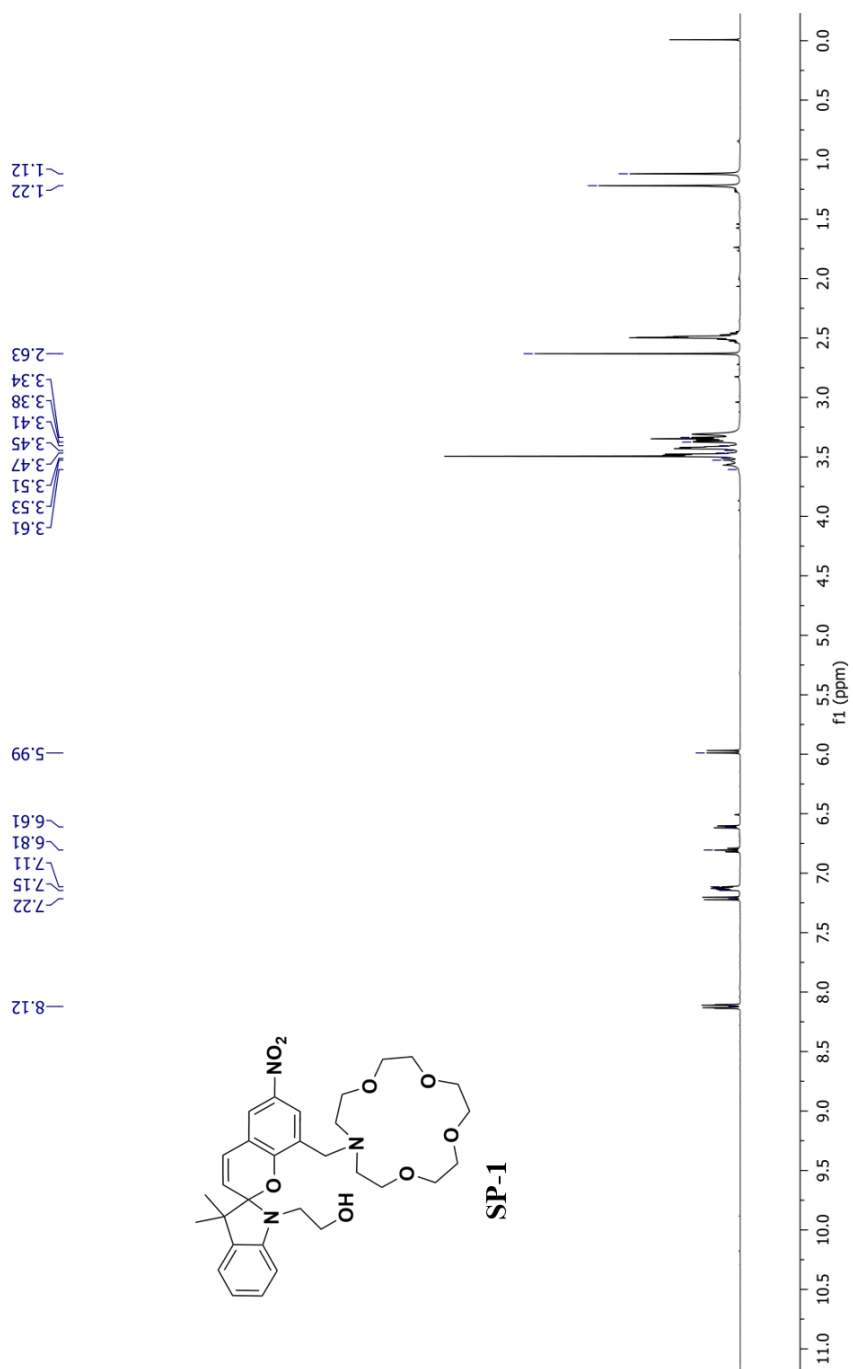


Figure S4-1. ¹H NMR spectrum of **SP-1** recorded in DMSO-*d*₆ at 500 MHz.

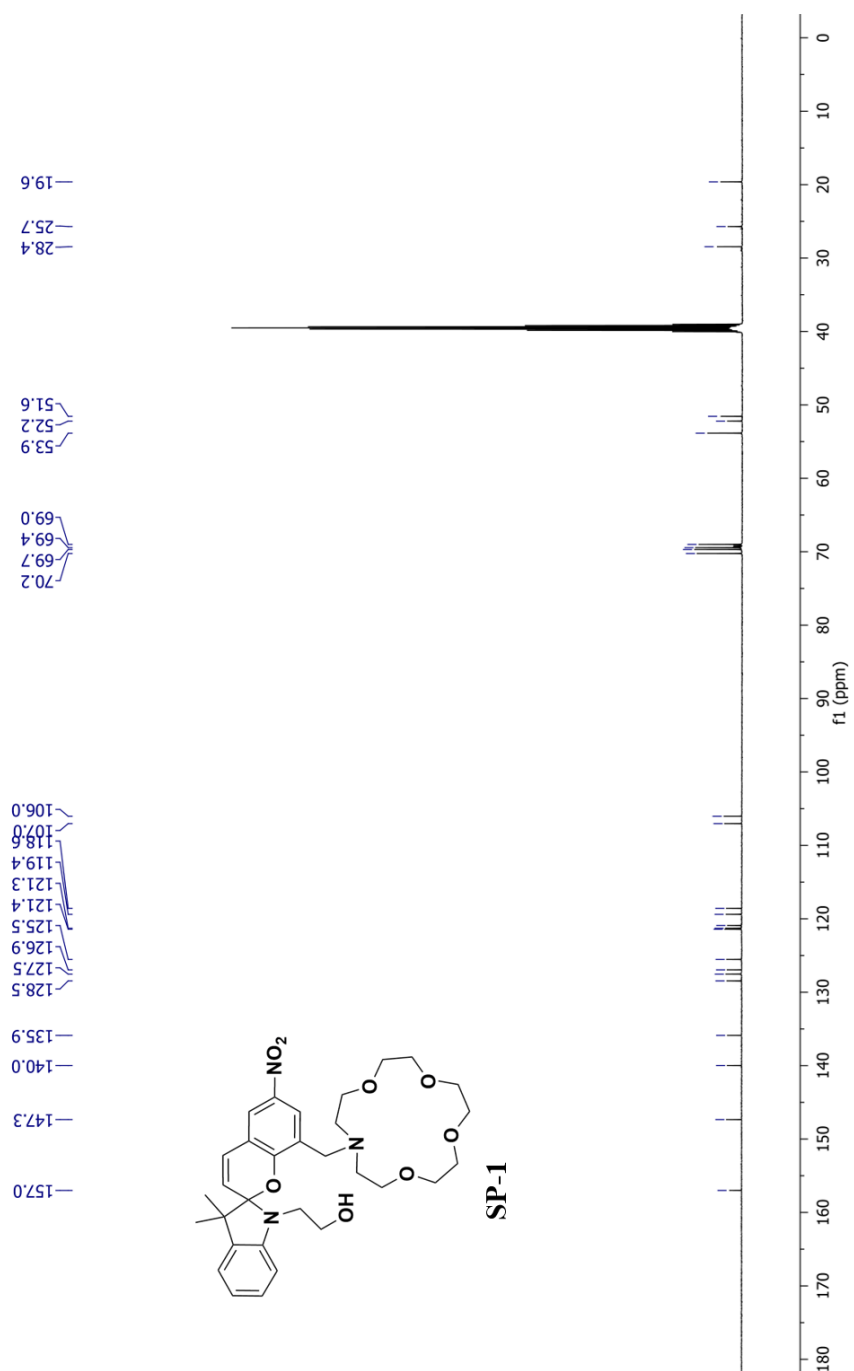


Figure S4-2. ^{13}C NMR spectrum of **SP-1** recorded in $\text{DMSO-}d_6$ at 500 MHz.

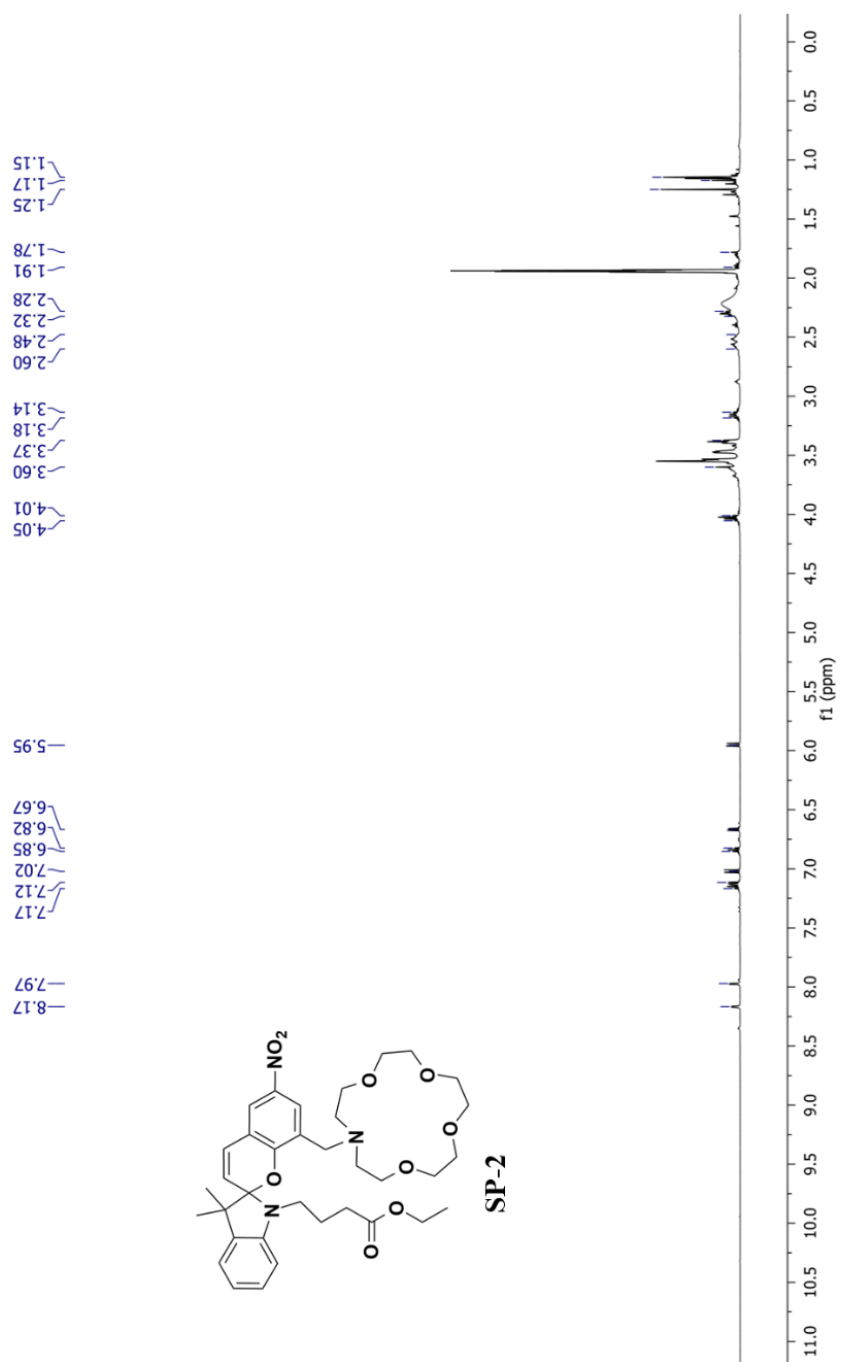


Figure S4-3. ^1H NMR spectrum of **SP-2** recorded in CD_3CN at 500 MHz.

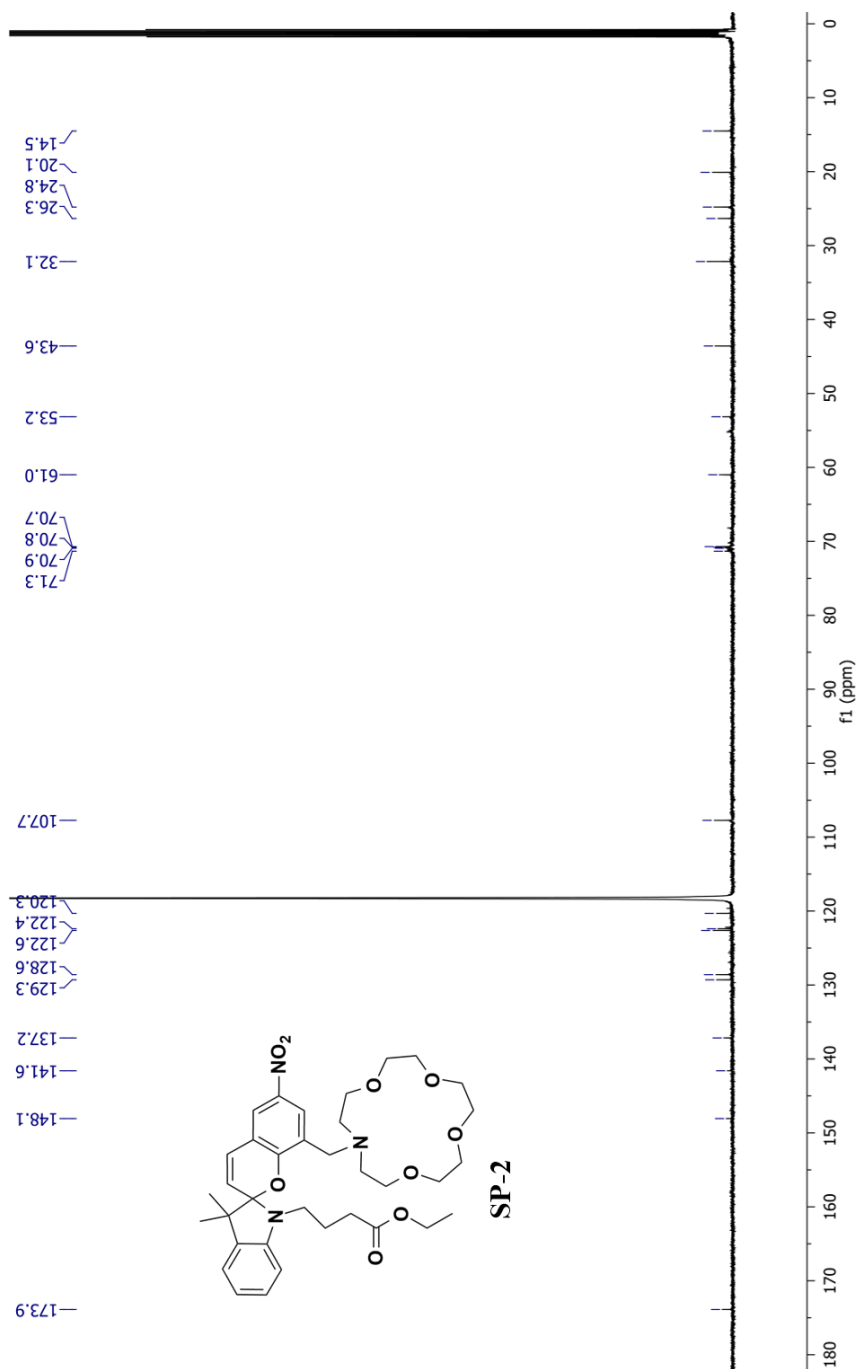


Figure S4-4. ^{13}C NMR spectrum of **SP-2** recorded in CD_3CN at 500 MHz.

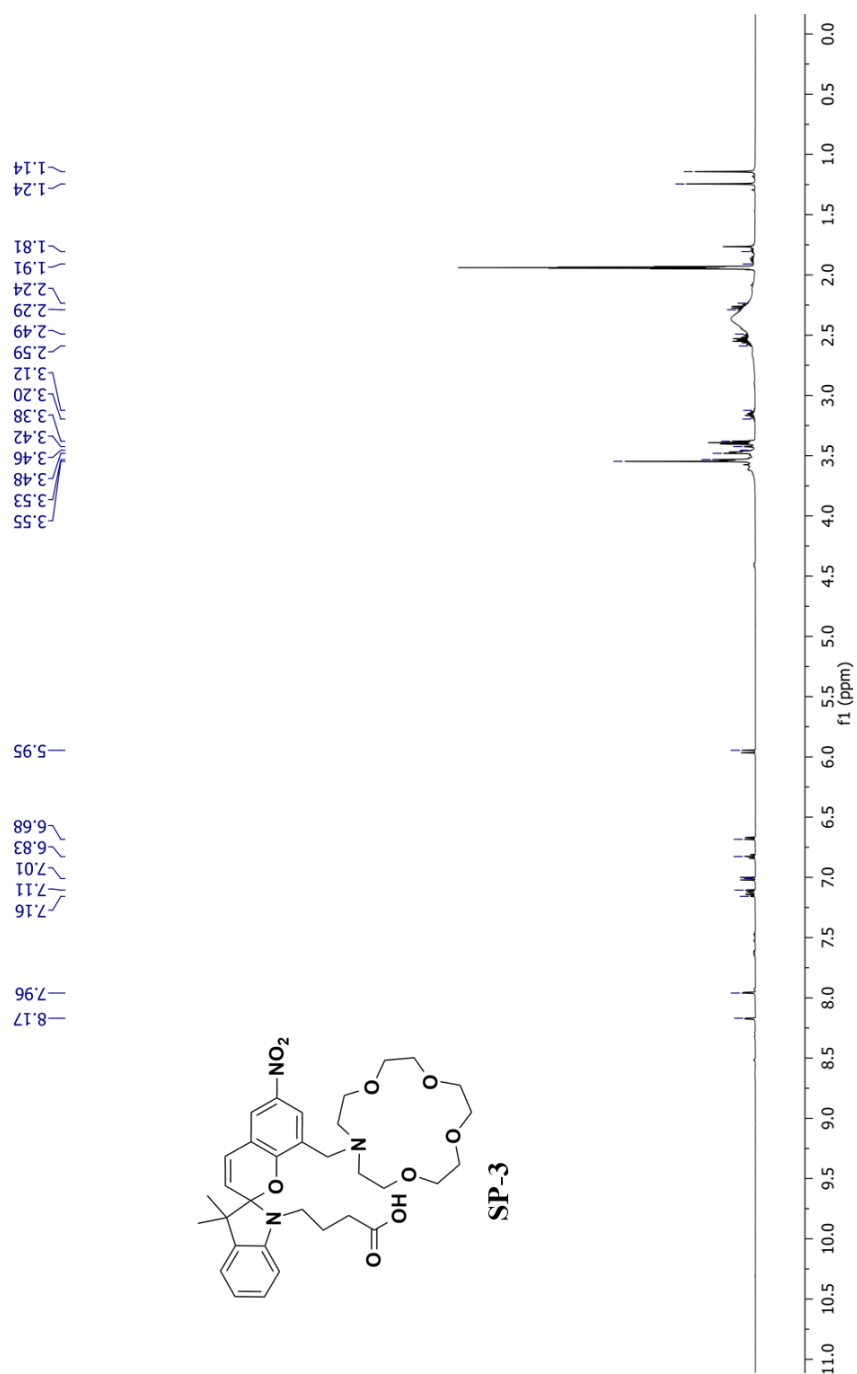


Figure S4-5. ¹H NMR spectrum of **SP-3** recorded in CD₃CN at 500 MHz.

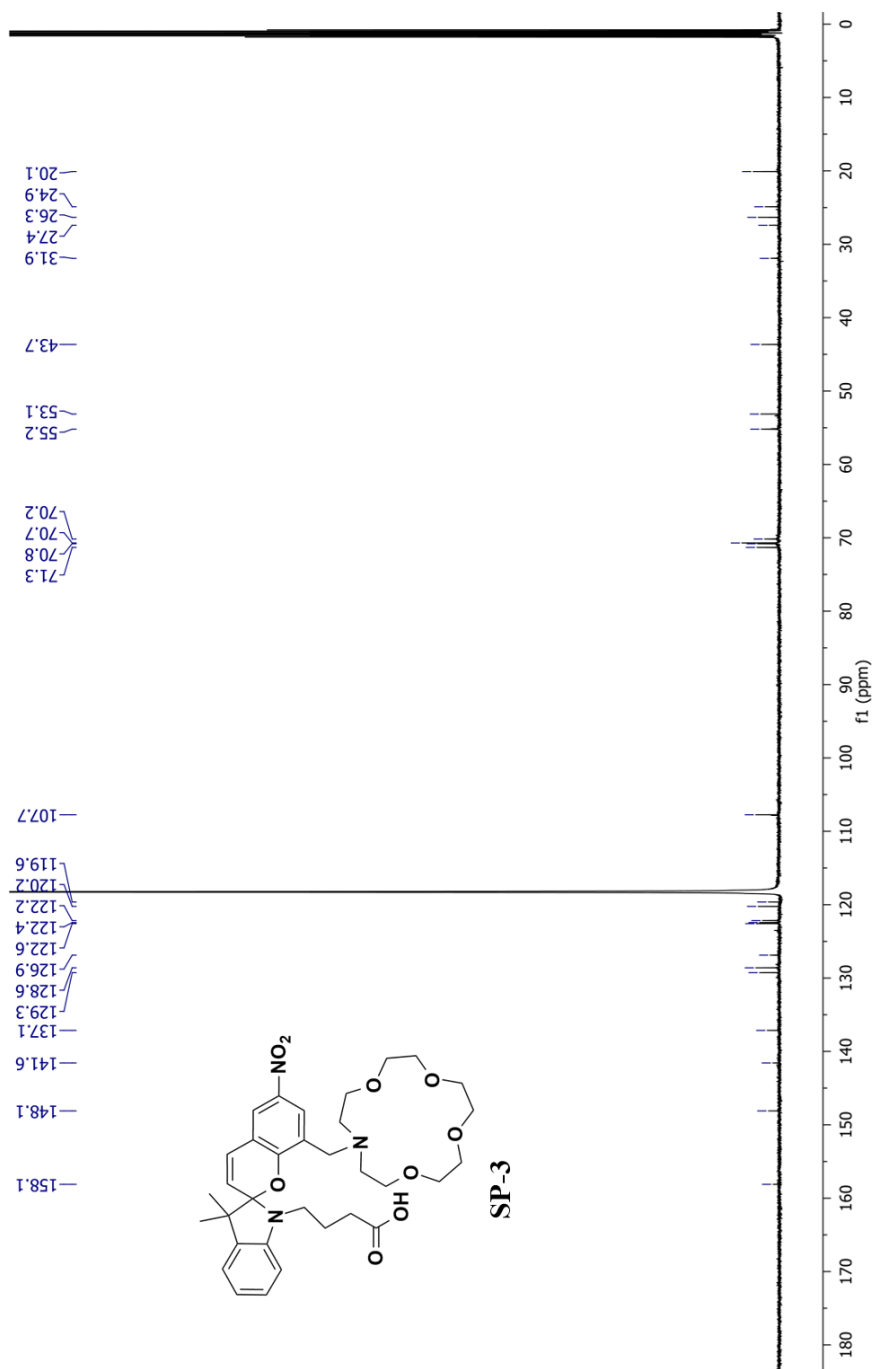


Figure S4-6. ^{13}C NMR spectrum of **SP-3** recorded in CD_3CN at 500 MHz.

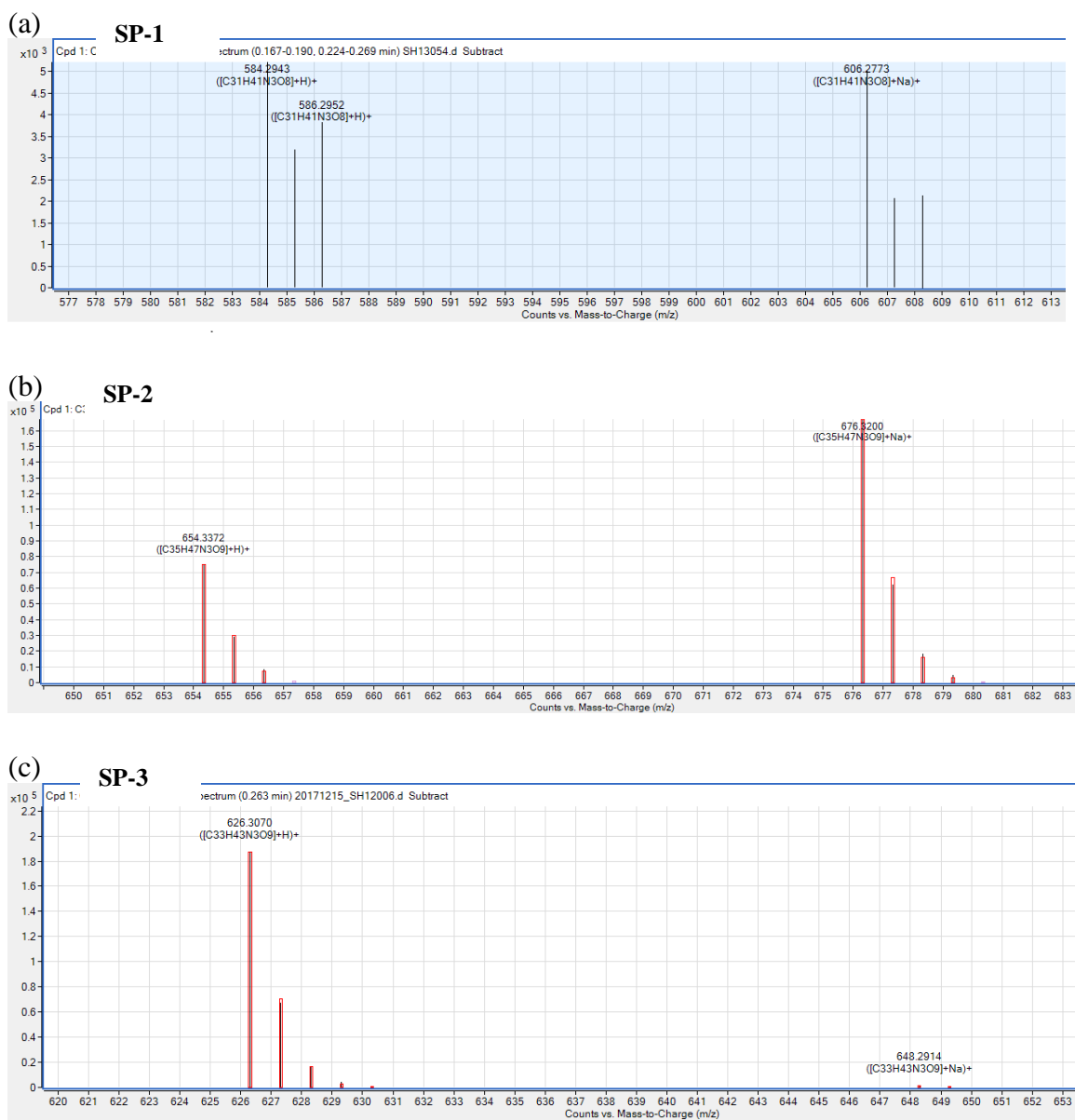


Figure S4-7. HRMS-ESI spectra of sensors (a) **SP-1**, (b) **SP-2** and (c) **SP-3**.

5.4.3 Absorbance and Fluorescence Spectra

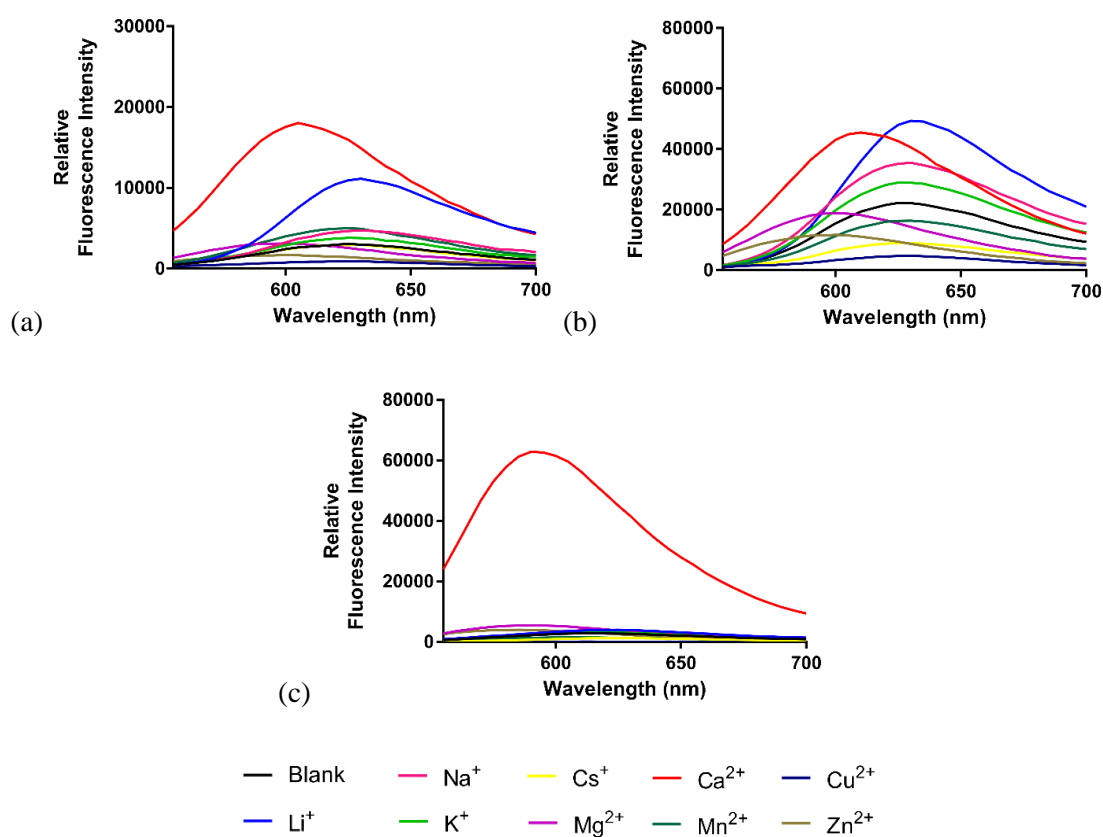


Figure S4-8. Fluorescence emission spectra of sensors (a) **SP-1**, (b) **SP-2** and (c) **SP-3** (50 μM) in the presence of biologically relevant metal ions (100 μM). Spectra were recorded at 100 gain for sensors **SP-1** and **SP-2**, and at 75 gain for sensor **SP-3**. Excitation was at 532 nm, and all experiments were performed under ambient light conditions.

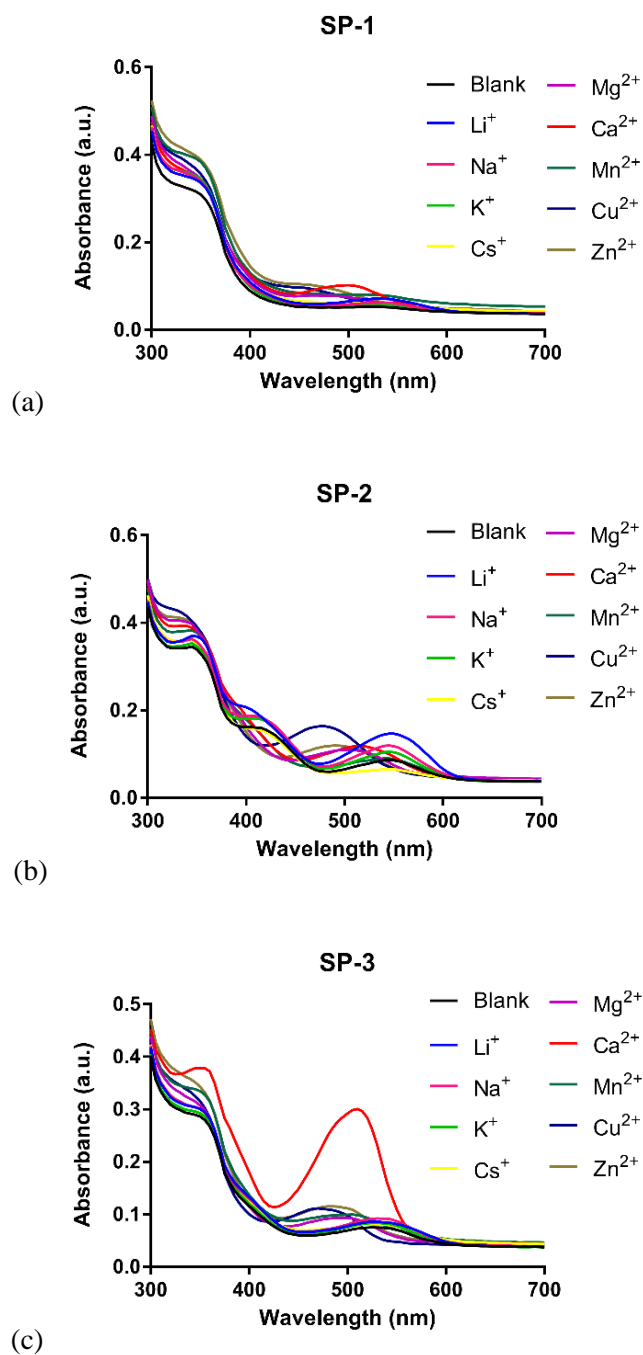


Figure S4-9. Absorbance spectra of sensors (a) **SP-1**, (b) **SP-2** and (c) **SP-3** (50 μ M) in the presence of biologically relevant metal ions (100 μ M). All experiments were performed under ambient light conditions.

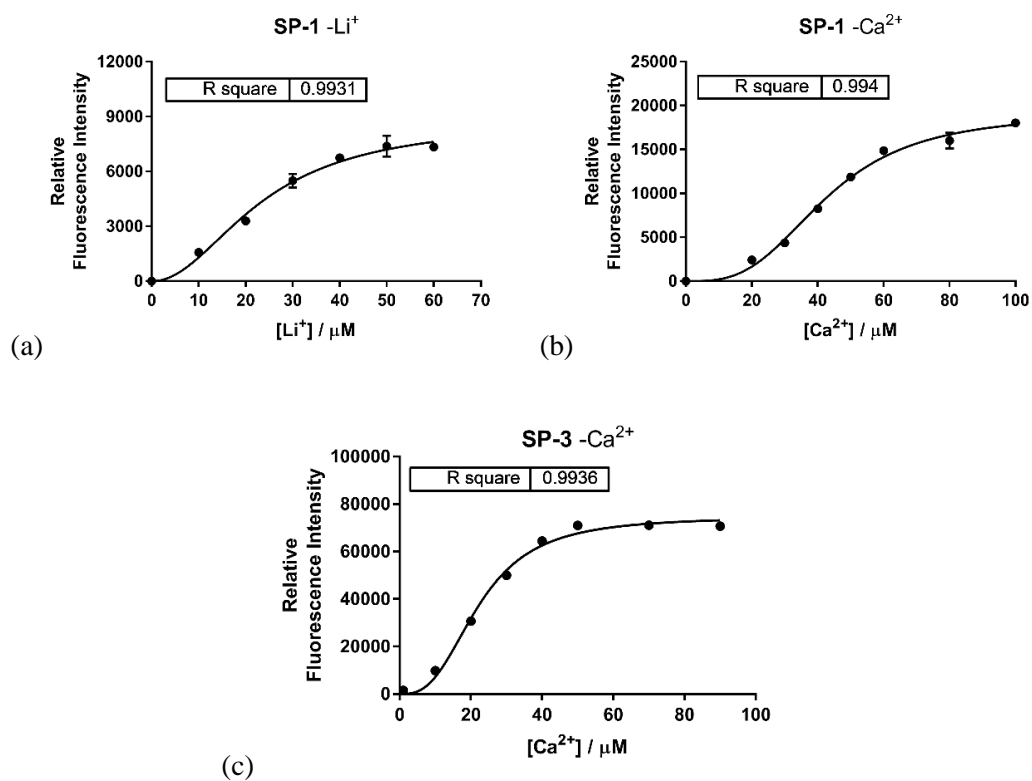


Figure S4-10. Metal ion titration curves of sensors (50 μM), in the presence of increasing concentrations of metal ions (1-90 μM). Each data point is measured from the sensor emission maxima. (a) **SP-1** -Li⁺ ($K_d = 24 \pm 3 \mu\text{M}$); (b) **SP-1** -Ca²⁺ ($K_d = 43 \pm 2 \mu\text{M}$); (c) **SP-3** -Ca²⁺ ($K_d = 22 \pm 1 \mu\text{M}$).

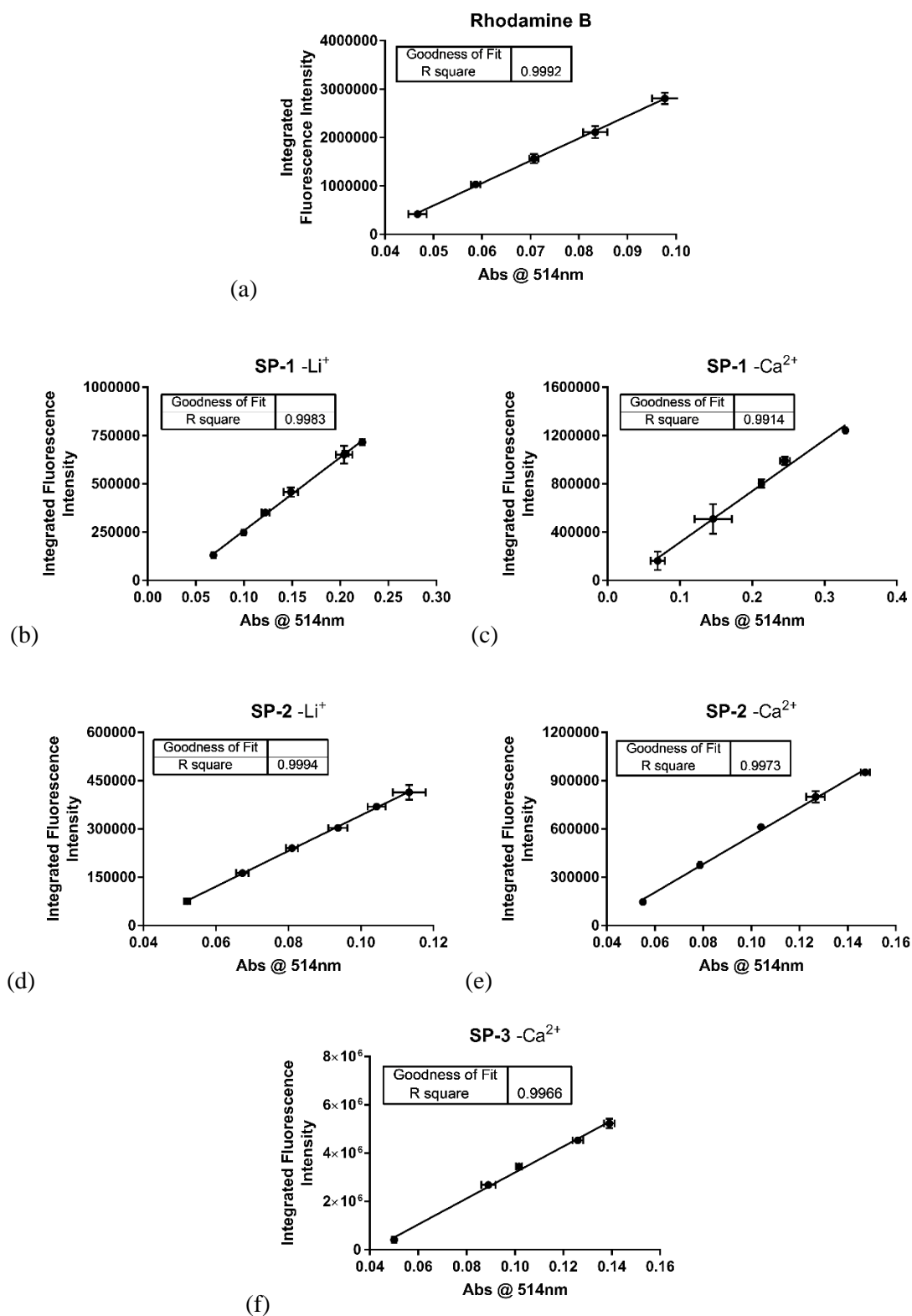


Figure S4-11. Integrated fluorescence spectra after excitation at 514 nm versus the absorbance at 514 nm for (a) Rhodamine B; (b) **SP-1** -Li⁺ ($\Phi = 0.03$); (c) **SP-1** -Ca²⁺ ($\Phi = 0.03$); (d) **SP-2** -Li⁺ ($\Phi = 0.04$); (e) **SP-2** -Ca²⁺ ($\Phi = 0.06$); (f) **SP-3** -Ca²⁺ ($\Phi = 0.37$). Spectra were recorded under ambient light conditions.

5.5 References

1. "Equation: Specific binding with Hill slope", GraphPad Curve Fitting Guide. Accessed 10 April 2018. https://www.graphpad.com/guides/prism/7/curve-fitting/index.htm?reg_specific_hill.htm.
2. Magde, D.; Rojas Gail, E.; Seybold Paul, G., Solvent Dependence of the Fluorescence Lifetimes of Xanthene Dyes. *Photochemistry and Photobiology* **2008**, 70 (5), 737-744.
3. Heng, S.; McDevitt, C.A.; Kostecki, R.; Morey, J.R.; Eijkelkamp, B.A.; Ebendorff-Heidepriem, H.; Monro, T.M.; Abell, A.D., Microstructured Optical Fiber-based Biosensors: Reversible and Nanoliter-Scale Measurement of Zinc Ions. *ACS Appl. Mater. Interfaces* **2016**, 8(20), 12727-12732.

CHAPTER 6

Conclusion and Further Studies

Fluorescent chemosensors, in combination with specialised imaging technologies, provide a useful tool to study the role of metal ions in cellular processes. However, one drawback of current sensors is a lack of reusability. As detailed in **Chapter 1**, the photoswitchable, photochromic spiropyran has been employed in the development of reversible fluorescent metal ion sensors, for use in biological applications. This thesis has described functionalisation of spiropyran in order to improve fluorescence intensity (**Chapter 2**), develop selective metal ion sensors for Mg^{2+} (**Chapter 3**) and investigate structure-metal ion selectivity relationships (**Chapter 4**).

Chapter 2 presented a new, rationally designed, photostable and red-emitting Ca^{2+} sensor. This hybrid pyrene-spiropyran sensor (**Py-1**) has enhanced fluorescence intensity compared to a non-coupled analogue, while retaining the characteristic red emission profile of the spiropyran. It presents two excitation options; direct green excitation (532 nm) of the photoswitch for a red emission, and UV excitation (344 nm) of the pyrene moiety which gives rise to distinct blue and red emissions. Fibre-based photostability studies show that **Py-1** is stable after multiple cycles of photoswitching, without any sign of photobleaching. Importantly, this new pyrene-spiropyran coupled system presents an opportunity for a general method towards the fluorescence enhancement of spiropyran-based sensors.

Chapter 3 detailed the rational design and photophysical characterisation of spiropyran-based chemosensors for Mg^{2+} , **1** and **2**. Fluorescence characterisation revealed that the C6'-nitro functionalised chemosensor **1** exhibits a 2-fold fluorescence enhancement factor for Mg^{2+} over Ca^{2+} ions, comparable to the commercially available mag-fura-2.¹ Importantly, the dissociation constant (K_d) of **1**- Mg^{2+} was calculated to be 6.0 μM , with a 3-fold weaker affinity observed for **1**- Ca^{2+} (18.7 μM). As proposed by DFT modelling, stoichiometric studies supported 2:1 chemosensor to metal ion binding of **1** with Mg^{2+} . Interestingly, structural and fluorescence characterisation of the C6'-fluorinated analogue **2** suggests the presence of both SP and MC species in solution, while stoichiometric studies indicate a complex metal binding relationship with Mg^{2+} . Subsequent studies were thus focused on **1**, which was combined with a suspended core optical fiber (SCF) as a first step towards the development of a light-controlled, reversible dip-sensor for Mg^{2+} . Fibre-based photoswitching experiments revealed reversible Mg^{2+} binding with improved photostability, as compared to the non-photoswitchable Rhodamine B fluorophore. The spiropyran-based chemosensors reported here highlight untapped opportunities for a new class of photoswitchable Mg^{2+} probe and present a first step in the development of a light-controlled, reversible dip-sensor for Mg^{2+} .

In **Chapter 4**, the photophysical characterisation of metal ion binding for a series of spiropyran-based sensors, incorporating both C8' and N1-indole metal ion binding domains, was presented. Fluorescence-based metal ion selectivity studies revealed that the hydroxyethyl (**SP-1**) and ethoxycarbonylbutyl (**SP-2**) N1-functionalised spiropyrans exhibited affinity for both Li^+ and Ca^{2+} ions, while the N1-carboxybutyl sensor (**SP-3**) gave excellent Ca^{2+} -selectivity. Further solution-based studies showed an improved dissociation constant ($K_d \text{ MC}(\text{SP-3})\text{-Ca}^{2+} = 22 \pm 1 \mu\text{M}$) and quantum yield of fluorescence ($\Phi \text{ MC}(\text{SP-3})\text{-Ca}^{2+} = 0.37$), compared to the other sensors. Job's analysis of binding stoichiometry was inconclusive (**SP-3**- Ca^{2+} binding apex at 0.58, indicating 1:1 or 2:1 metal-sensor binding), and so future work will be focused on high level DFT calculations in order to clarify possible binding mechanisms. These results suggest the carboxybutyl N1-indole functionality of **SP-3** may play a role in stabilizing Ca^{2+} in the 15-membered azacrown ionophore, promoting metal-induced isomerisation to the $\text{MC}(\text{SP-3})\text{-Ca}^{2+}$ complex and thus a bright, Ca^{2+} -selective, red fluorescence signal.

Finally, the ideas developed in this thesis – of tailored selectivity, enhancement of detection signal and of biological applicability – have already been extended into other areas, which are further discussed in the appendices.

Appendix A Lithium 'Hot-spots': Real-time Analysis of Ion Conductance in Aquaporin-1

Aquaporins are transmembrane channels which allow the flux of small solutes and water in and out of mammalian cells.²⁻³ Aquaporin-1 (AQP1) channels, an aquaporin subtype associated with highly motile cells, are located at the leading edges of aggressive cancer cells, where they are necessary to enable fast migration.⁴⁻⁷ Previously, it has been suggested that monovalent cation conductance through AQP1 channels may contribute to cancer cell migration, though this has not been proved directly.⁸⁻¹¹ Defining the role of AQP1 ion channel function in cell migration would advance knowledge of how aquaporins enhance the motility of cancer cells and provide a potential therapeutic target.

This biological challenge presents the need for a selective, fluorescent monovalent metal ion sensor compatible with confocal microscopy. In addition, reversible metal ion binding is a desirable sensor characteristic for visualizing ion transport into the cell. Sensor **SP-1** from **Chapter 4** (named 'SHL') shows improved Li^+ -selectivity over potassium (K^+) and sodium (Na^+) compared to previously reported spiropyran-based sensors.¹²⁻¹³ HT29 colon cancer cells were utilized in this study to investigate the ion conductance of aquaporins as they are

known to have high AQP1 expression.¹⁴ Here **SHL** was used to detect intracellular Li⁺, while a previously reported ion channel blocker (AqB011)¹⁵ modulated the AQP1-mediated Li⁺ entry into the cells. The results presented in this manuscript show that ion binding to the sensor intracellularly is dependent on exogenous Li⁺ transport into the cell, and repeated cycles of photoswitching gave reproducible changes in fluorescence, demonstrating the ability of **SHL** to reversibly photoswitch in living cells. Furthermore, ‘hot-spots’ of Li⁺-**SHL** binding induced fluorescence were observed at the leading edges of migrating cells, which correlates with ion movement through AQP1 channels. These results suggest that the AQP1 ion channel could be a novel candidate for therapeutic interventions to manage metastasis in AQP1-dependent cancers.

Appendix B Engineering of Surface Chemistry for Enhanced Sensitivity in Nanoporous Interferometric Sensing Platforms

Optical-based sensing platforms are an emerging area for biomedical sensing applications.¹⁶ Recent work by Dusan Losic and Abel Santos has demonstrated the application of optical-based sensing materials, for the detection of bio-analytes.¹⁷ In these systems, sensing is achieved by reflectometric interference spectroscopy (RIfS), whereby white light interaction with solid thin-films, such as nanoporous anodic alumina (NAA),¹⁸ results in the formation of a characteristic interference pattern.¹⁹⁻²⁰ The nanoporous structure of NAAs allows the development of photonic structures with precisely engineered optical properties. In addition, the surface of the NAAs can be chemically modified with different functional groups, to attain chemical sensitivity for analytes of interest.²¹

The work described in this thesis has thus far been focused on the development of photoswitchable fluorescent dyes, mainly for intracellular sensing applications. Complementarily, the work described in Appendix B utilises a different approach to biological sensing, targeted towards sensing of analytes in biological media. Here we describe fundamental surface-engineering strategies in NAA/RIfS materials, and the effects of combined surface-functionalisation techniques, towards the development of more sensitive optical-sensing systems. Three sensing approaches were used in this study, namely attachment of functional molecules to the (i) inner pores and (ii) top surface of the NAA, as well as a combination of the two (approach iii). The strong molecular interaction of Au³⁺ ions with thiol-containing functional molecules provides a model sensing system with which to assess sensitivity of the NAA platforms by surface engineering, as well as molecular structure.

My role in this work was in the development of a library of functional molecules for surface attachment. The sensitivity of optical sensing platforms based on RIfS/NAA and analogous nanoporous materials relies on the magnitude of the interaction between the nanoporous matrix and analyte molecules.²²⁻²³ This interaction is translated into changes in the effective optical medium of the nanoporous film. Thus, the greater the structural or conformational change in the surface-attached molecules upon analyte-binding, the greater optical signal measurement. Functional molecules of various molecular lengths were selected, with alkane chain and peptide-like character, in order to assess the effects of molecular length and molecular feature on NAA sensitivity. Molecules for sensing approach (i) were selected with terminal amine and thiol groups, for attachment to the NAA pore surface and to facilitate Au³⁺ binding, respectively. Functional molecules for sensing approach (ii) required di-thiol terminal groups, as attachment to the outer surface of the NAA was achieved by coating of the surface with Au, such that the functional molecules were attached via one terminal thiol, with the other vacant for binding to the Au³⁺ analyte solution. Alkane chain compounds for sensing approaches (i) and (ii) were sourced commercially, while the compounds of peptide character were synthesised in-house. Briefly, synthesis of the alanine-rich tripeptide, AAC, was performed via solid-phase synthesis, and the methyl ester-protected L-cysteine was simultaneously methyl ester protected and Boc-deprotected from commercially available Boc-cysteine by reaction of thionyl chloride in methanol.

Finally, the most sensitive functional molecules from sensing approaches (i) and (ii) were combined into a third sensing strategy whereby the NAA platforms are functionalised on both the top and inner surfaces concurrently. Engineering of the surface according to this approach resulted in an additive enhancement in sensitivity of up to 5-fold compared to previously reported systems. The work described in this Appendix advances the rational engineering of surface chemistry for interferometric sensing on nanoporous platforms. Moreover, this technology has potential applications for real-time monitoring of multiple analytes in dynamic environments.

6.1 References

1. Fluorescent Mg²⁺ Indicators. In *The Molecular Probes Handbook - A Guide to Fluorescent Probes and Labeling Technologies*, 11 ed.; ThermoFisher Scientific: 2010; pp 862-864.
2. Agre, P.; Preston, G. M.; Smith, B. L.; Jung, J. S.; Raina, S.; Moon, C.; Guggino, W. B.; Nielsen, S., Aquaporin CHIP: the archetypal molecular water channel. *American Journal of Physiology-Renal Physiology* **1993**, 265 (4), F463-F476.
3. King, L. S.; Kozono, D.; Agre, P., From structure to disease: the evolving tale of aquaporin biology. *Nature Reviews Molecular Cell Biology* **2004**, 5, 687.
4. Papadopoulos, M. C.; Saadoun, S.; Verkman, A. S., Aquaporins and cell migration. *Pflugers Arch* **2008**, 456 (4), 693-700.
5. Olson, M. F.; Sahai, E., The actin cytoskeleton in cancer cell motility. *Clinical & Experimental Metastasis* **2008**, 26 (4), 273.
6. Friedl, P.; Wolf, K., Tumour-cell invasion and migration: diversity and escape mechanisms. *Nature Reviews Cancer* **2003**, 3, 362.
7. Pei, J.; Burton, J.; Kourghi, M.; De Ieso, M.; Yool, A., *Drug Discovery and Therapeutic Targets for Pharmacological Modulators of Aquaporin Channels*. 2015; p 356.
8. Hu, J.; Verkman, A. S., Increased migration and metastatic potential of tumor cells expressing aquaporin water channels. *The FASEB Journal* **2006**, 20 (11), 1892-1894.
9. McCoy, E.; Sontheimer, H., Expression and function of water channels (aquaporins) in migrating malignant astrocytes. *Glia* **2007**, 55 (10), 1034-1043.
10. Anthony, T. L.; Brooks, H. L.; Boassa, D.; Leonov, S.; Yanochko, G. M.; Regan, J. W.; Yool, A. J., Cloned Human Aquaporin-1 Is a Cyclic GMP-Gated Ion Channel. *Molecular Pharmacology* **2000**, 57 (3), 576-588.
11. Boassa, D.; Yool, A. J., Single amino acids in the carboxyl terminal domain of aquaporin-1 contribute to cGMP-dependent ion channel activation. *BMC Physiology* **2003**, 3, 12-12.
12. Heng, S.; Nguyen, M.-C.; KostECKI, R.; Monro, T. M.; Abell, A. D., Nanoliter-scale, regenerable ion sensor: sensing with a surface functionalized microstructured optical fibre. *RSC Advances* **2013**, 3 (22), 8308-8317.
13. Stubing, D. B.; Heng, S.; Abell, A. D., Crowned spiropyran fluoroionophores with a carboxyl moiety for the selective detection of lithium ions. *Organic & Biomolecular Chemistry* **2016**, 14 (15), 3752-3757.

14. Pei, J. V.; Kourghi, M.; De Ieso, M. L.; Campbell, E. M.; Dorward, H. S.; Hardingham, J. E.; Yool, A. J., Differential Inhibition of Water and Ion Channel Activities of Mammalian Aquaporin-1 by Two Structurally Related Bacopaside Compounds Derived from the Medicinal Plant *Bacopa monnieri*. *Molecular Pharmacology* **2016**, *90* (4), 496-507.
15. Kourghi, M.; Pei, J. V.; De Ieso, M. L.; Flynn, G.; Yool, A. J., Bumetanide Derivatives AqB007 and AqB011 Selectively Block the Aquaporin-1 Ion Channel Conductance and Slow Cancer Cell Migration. *Molecular Pharmacology* **2016**, *89* (1), 133-140.
16. Fan, X.; White, I. M.; Shopova, S. I.; Zhu, H.; Suter, J. D.; Sun, Y., Sensitive optical biosensors for unlabeled targets: A review. *Analytica Chimica Acta* **2008**, *620* (1), 8-26.
17. Santos, A.; Kumeria, T.; Losic, D., Nanoporous Anodic Alumina: A Versatile Platform for Optical Biosensors. *Materials* **2014**, *7* (6), 4297-4320.
18. Chen, Y.; Santos, A.; Wang, Y.; Kumeria, T.; Wang, C.; Li, J.; Losic, D., Interferometric nanoporous anodic alumina photonic coatings for optical sensing. *Nanoscale* **2015**, *7* (17), 7770-7779.
19. Belge, G.; Beyerlein, D.; Betsch, C.; Eichhorn, K.-J.; Gauglitz, G.; Grundke, K.; Voit, B., Suitability of hyperbranched polyester for sensoric applications – investigation with reflectometric interference spectroscopy. *Analytical and Bioanalytical Chemistry* **2002**, *374* (3), 403-411.
20. Birkert, O.; Tünnemann, R.; Jung, G.; Gauglitz, G., Label-Free Parallel Screening of Combinatorial Triazine Libraries Using Reflectometric Interference Spectroscopy. *Analytical Chemistry* **2002**, *74* (4), 834-840.
21. Santos, A.; Kumeria, T.; Losic, D., Optically Optimized Photoluminescent and Interferometric Biosensors Based on Nanoporous Anodic Alumina: A Comparison. *Analytical Chemistry* **2013**, *85* (16), 7904-7911.
22. Pacholski, C.; Sartor, M.; Sailor, M. J.; Cunin, F.; Miskelly, G. M., Biosensing Using Porous Silicon Double-Layer Interferometers: Reflective Interferometric Fourier Transform Spectroscopy. *Journal of the American Chemical Society* **2005**, *127* (33), 11636-11645.
23. Pacholski, C.; Yu, C.; Miskelly, G. M.; Godin, D.; Sailor, M. J., Reflective Interferometric Fourier Transform Spectroscopy: A Self-Compensating Label-Free Immunosensor Using Double-Layers of Porous SiO₂. *Journal of the American Chemical Society* **2006**, *128* (13), 4250-4252.

APPENDIX A

Lithium ‘Hot-spots’: Real-time Analysis of Ion Conductance in Aquaporin-1

Jinxin V. Pei,¹ Sabrina Heng,² Michael De Ieso,¹ Georgina M. Sylvia,² Mohamad Kourghi,¹ Saeed Nourmohammadi,¹ Andrew D. Abell,² and Andrea Yool.¹

¹Adelaide Medical School, Institute for Photonics and Advanced Sensing (IPAS), The University of Adelaide, Adelaide, SA 5005, Australia.

²ARC Centre of Excellence for Nanoscale BioPhotonics (CNBP), Institute for Photonics and Advanced Sensing (IPAS), School of Physical Sciences, The University of Adelaide, Adelaide, SA 5005, Australia.

Manuscript in preparation.

Abstract

Non-selective cation channels serve key roles in enabling cell motility, detecting sensory signals, regulating cell volume, and other important life processes. Work here is the first to use a newly designed Li^+ -selective photoswitchable probe ('SHL') in living colon cancer cells to non-invasively monitor cation channel activity in real time by the appearance of lithium hot spots, detected by confocal microscopy. Punctate Li^+ hot spots are clustered in the lamellipodial leading edges of HT29 human colon cancer cells, co-localized with aquaporin-1 (AQP1) channels. AQP1 is a dual water and cyclic-nucleotide-gated cation channel, located in lamellipodia and essential for rapid cell migration in a subset of aggressive cancers. Both the Li^+ hot spots and cell migration are blocked in HT29 cells by the AQP1 ion channel antagonist AqB011. In contrast, Li^+ hot spots are not evident in a poorly-migrating colon cancer cell line SW620, which lacks comparable membrane expression of AQP1. Knockdown of AQP1 by small interfering RNA in HT29 cells significantly impairs Li^+ hot spot activity. The SHL probe loaded in living cells induces no appreciable cytotoxicity, and shows signature chemical properties of ionic selectivity and reversibility (capacity to be reset for signaling by illumination at bandwidths that induce photoswitching). Dynamic properties of the Li^+ hot spots, turning on and off, are confirmed by time-lapse imaging. SHL is a powerful tool for evaluating cation channel function in living cells in real time, with particular promise for studies of motile cells or interlinked networks not easily analyzed by electrophysiological methods. The ability to reset SHL by photoswitching allows monitoring of dynamic signals over time. Future applications of the Li^+ probe could include high-throughput optical screening for discovering new classes of channels, or finding new pharmacological modulators for non-selective cation channels.

Introduction

Cell migration is central to critical processes of repair, regeneration, immune protection, development and maintenance of multicellular organisms, and in disease conditions such as cancer metastasis¹⁻⁵. In addition to regulating fluid balance^{6,7}, some classes of aquaporins facilitate rapid cell migration. Aquaporin-1 (AQP1) for example enhances mobility of some of the most motile cells such as T-cells, fibroblasts, cancers and amoebae⁸. While the exact mechanisms have yet to be determined, we do know that elevated expression of AQP1 is apparent at the leading edges of lamellipodia in these classes of migrating cells. Genetic knockdown of AQP1 expression can impair cell migration significantly^{9,10}, whereas reintroduction of AQP1 but not other channels such as AQP4 can restore motility¹⁰. A major

difference is that AQP1 but not AQP4 can function as a non-selective monovalent cation channel gated by cGMP, as well as a water channel^{11,12}. Dissecting the role of AQP1 ion channels in cell migration would advance our knowledge of basic mechanisms that enhance motility in cancer, stem cells and regenerating tissues, and identify possible targets for intervention for example in cancer metastasis.

Here we demonstrate that a newly designed reversible lithium sensor (SHL) can be used to monitor cation channel activity in living cells, and demonstrate proof of principle using a metastatic colon cancer cell line (HT29) that relies on high levels of AQP1 expression for rapid migration capability, as compared to a relatively sedentary colon cancer line (SW620) which lacks high AQP1 expression. SHL was designed to be selective for a low abundance monovalent ion, Li^+ , over Na^+ and K^+ . AQP1 ion channels have properties that make them an excellent choice for this study; once activated, they show long open times, a high single channel conductance (150 pS in physiological salines), and high permeability to monovalent cations Na^+ , K^+ and Cs^+ ¹¹. Work here shows the AQP1 ion channel also is permeable to Li^+ , and thus can be hypothesized to enable Li^+ ion influx which could be detected by the SHL probe. The exciting finding that launched this study was the observation that the punctate SHL signals are clustered in the lamellipodia of migrating cancer cells. Subsequent confirmation that SHL is detecting AQP1-mediated Li^+ entry took advantage of the selective AQP1 ion channel inhibitor (AqB011), cation-substituted extracellular salines, and molecular knockdown of AQP1 to show that Li^+ entry into the cells and the punctate hot spot signals depended on the presence of ion-conducting AQP1 channels.

Results here show that activation of the sensor intracellularly is dependent on transport of extracellular Li^+ into the cell. Selective blocking of AQP1 with AqB011 and knockdown of AQP1 with small interfering RNA shows that the Li^+ transport is occurring through AQP1 channels. These results provide the first evidence of hot-spots that co-localize with non-selective monovalent cation channels, as confirmed by properties of pharmacological sensitivity, ion selectivity, and levels of expression. These data illustrate the selectivity and applicability of the SHL probe as a powerful biological tool, and add further support to the idea that the ion channel function of AQP1 is an intriguing target for new strategies to manage AQP1-expressing cancers.

Results and Discussion

Design and characterisation of the reversible and selective lithium (Li⁺) sensor (SHL).

The sensor described here (see Figure 1A for SHL structure) contains a photochromic spiropyran that can be reversibly switched between a non-fluorescent isomer (SP) and a charge-delocalized fluorescent merocyanine isomer (MC) when interacting with an appropriate metal ion¹³ such as Li⁺ (Figure 1A). The ability to switch between the two states is advantageous for visualizing Li⁺ transport into the cell. SHL shows enhanced fluorescence when complexed to Li⁺ (MC-Li⁺ complex in Figure 1A), while maintaining low background fluorescence in the absence of the ion (SP isomer in Figure 1A). This sensor characteristic is desirable for visualizing ion binding with confocal microscopy, and is predicted to yield better resolution than conventional fluorescent probes due to its enhanced signal-to-background ratio.^{14,15} A critical characteristic of the SHL sensor is its selectivity for Li⁺ over other biologically abundant ions. We showed that incorporation of suitable ionophores on the spiropyran nucleus provides selective binding of defined ions¹⁶. Here we incorporated a 1-aza-15-crown-5 substituent at C8' and a hydroxyethyl substituent at N1 to impart selectivity for Li⁺ (Figure 1A). Finally, we incorporated a NO₂ substituent at C6' of the benzopyran ring as an electron-withdrawing group at that position, known to stabilize the ring-opened MC form, thus favoring ion binding. Details on the synthesis of SHL are reported in the Synthesis section of the Supporting Information. Briefly, the Li⁺ sensor was prepared from 1-aza-15-crown-5 and 1-(2-hydroxyethyl)-2,3,3-trimethyl-3*H*-indol-1-ium to give SHL with an overall yield of 20 % using a modification to existing methodology^{17,18}.

The addition of excess Li⁺ (100 μM) to SHL (50 μM) gave rise to strong fluorescence ($\lambda_{\text{ex}} = 532 \text{ nm}$) at approximately $\lambda_{\text{em}} = 635 \text{ nm}$ as shown in Figure 1B (inset), which is consistent with the formation of the MC(SHL)-Li⁺ complex as expected based on our sensor design. Importantly, the red fluorescence represents an emission bandwidth that is distinct from the blue nuclear stain (Hoescht 33258) and green AQP1 immunofluorescence signals. Additional spectroscopic properties of SHL such as absorbance, detection limits, photoswitching and quantum yields are detailed in the 'Supplementary Note' section. The selectivity of SHL for Li⁺ over other biologically relevant ions was confirmed through ion binding assays with addition of excess ions (Li⁺, Na⁺, K⁺, Cs⁺, Mg²⁺, Mn²⁺, Cu²⁺ or Zn²⁺). Results in Figure 1B show that SHL had highest affinity for Li⁺, and relatively little response to similar monovalent ions such as Na⁺ and K⁺. The red-emitting properties and selectivity

of SHL for Li^+ demonstrated that the emission observed in the cell was not due to auto-fluorescence or interaction of the sensor with other endogenous ions; the signal was specific to the MC(SHL)- Li^+ complex.

AQP1 ion channel is permeable to Li^+ and can be blocked by AqB011.

AQP1-expressing *Xenopus* oocytes were recorded by two-electrode voltage clamp in isotonic saline with 137 mM Li^+ substituted for standard physiological Na^+ . Currents (Figure 2A) in isotonic Li^+ saline were measured for human AQP1-expressing *Xenopus* oocytes and non-expressing control oocytes before ('initial') and after treatment with a membrane permeable analog of cGMP (CPT-cGMP; see Methods for details), demonstrating Li^+ permeability of the ion conductance in AQP1-expressing oocytes, and not in controls. Oocytes were then incubated 2 h in 30 μM AqB011 and tested for reactivation by cGMP ("AqB011") in Li^+ saline. Results (Figure 2B) showed that approximately 90% of the cGMP-induced current in AQP1-expressing oocytes was successfully blocked by AqB011; whereas control oocytes (AQP1-) lacked appreciable cGMP-activated current responses and showed no effect of the inhibitor.

AqB011 blocks migration in AQP1-expressing HT29 colon cancer cells

Live-cell imaging was used to map the trajectories of cultured HT29 cells (Figure 2C) to quantify migration rates in the presence and absence of the AQP1 ion channel blocker, AqB011. Histogram summaries of the distances moved by individual cells per unit time interval show that the Gaussian distribution was substantially shifted to shorter distances in the presence of the AQP1 inhibitor (Figure 2D), demonstrating that block of the ion channel activity impaired cell migration.

Li^+ entry through hot spots in AQP1-expressing HT29 cells.

The ability of SHL to detect Li^+ in live cells was investigated using confocal microscopy. HT29 colon cancer cells are known to have high AQP1 expression¹⁹, and were chosen as a useful model for testing cellular imaging of Li^+ permeation through non-selective cation channels. SHL (50 μM in physiological saline) was incubated with the HT29 cells for 2 h prior to imaging to allow loading of SHL into the cells. The cells were counterstained with Hoescht 33258 to label nuclei.

Illumination with green laser light activated the MC(SHL)- Li^+ complex, which resulted in a red fluorescence signal characteristic of this chemical interaction (Figure 3A, ON1).

Exposure of the cells to continuous white light for 10 min progressively shifted the signal to a low level of fluorescence, consistent with the expected photoswitching from the fluorescent MC(SHL)-Li⁺ complex to the non-fluorescent SP isomer. After prolonged white light illumination, the probe was reset to a responsive state by 10 min recovery in darkness, which allowed reactivation of the probe signal (ON2). Fluorescence intensity decreased as a single-phase decay function over time when cells were illuminated with standard white light (Figure 3B), as illustrated by images taken at 2 min intervals. The normalized signal intensity decreased from 100 Relative Fluorescence Units (RFU) to 44.51 RFU after 10 min of visible light radiation (Figure 3C). Under these experimental conditions, the half-life was determined to be 4.13 minutes with a τ value estimated at 5.95 minutes. Recovery in darkness for 10 min allowed the formation of the MC isomer. The binding of Li⁺ regenerated the MC(SHL)-Li⁺ complex at a normalized intensity of 84.65 RFU (Figure 3C; ON2). Repeated cycles of photoswitching performed on same cells gave reproducible changes in fluorescence, demonstrating the ability of SHL to reversibly photoswitch in living cells. This innovation defines a new probe for monitoring changes in intracellular Li⁺ in a biological sample over time, without loss of sensitivity imposed by photobleaching of a sensor. The photoswitching property allows repeated comparisons of function across multiple experimental treatments, and provides additional advantages for biological assays in which sample availability can be limited.

Distinctive punctate signals referred to here as lithium 'hot spots' were observed in HT29 cells when imaged in Li⁺-containing saline (Figure. 4A-1). A loss of hot spot events was observed after treatment with the AQP1 ion channel antagonist AqB011 (20 μ M for 2 h), after which only a faint background fluorescence was observed (Figure 4A-2). The removal of Li⁺ from the extracellular saline by equimolar substitution with tetraethylammonium ion (TEA⁺) also caused a loss of hot spots (Figure 4A-3), showing that the observed events resulted from Li⁺ ion entry. In saline with TEA⁺, application of the blocker AqB011 had no additional effect on hot spot activity (Figure 4A-4). The fluorescent signal for the entire cell was reduced two-fold in HT29 cells when Li⁺ entry was compromised by pharmacological block of the ion channel with AqB011 or by removal of extracellular Li⁺ ion via replacement with other cations as chloride salts (Figure 4B). Collectively, these data confirmed that the bright punctate Li⁺ signals depended on the presence of extracellular Li⁺ and the presence of functional AQP1 ion channels, and ruled out the possibility that hot spots were due indirectly to non-specific interactions with other intracellular cations or entry of Li⁺ through other cation pathways. The most parsimonious interpretation is that the lithium 'hot spots' represent Li⁺ entry across the plasma membrane through AQP1 cation channels.

Knockdown of AQP1 expression with small interfering (si)-RNA resulted in a dramatic loss of red Li⁺ hot spots specifically in transfected HT29 cells (labelled green with co-transfected siGLO transfection indicator), and not in non-transfected cells in the same culture plate (Figure 4C). The fluorescence intensity of the SHL Li⁺ probe signals (Figure 4D) and the levels of AQP1 transcript assessed by quantitative PCR (Figure 4E) both were reduced significantly with AQP1-siRNA treatment, but not with control scrambled siRNA treatment. These data confirm that in HT29 cells, the appearance of Li⁺ hot spots requires the expression of AQP1 channels.

Li⁺ hot spots were not observed in SW620 cells lacking high levels of AQP1 expression.

The role of AQP1 ion channels in mediating the lithium hot spot events was tested by comparison with another colon cancer cell line (SW620) which is similar to HT29 in having an adherent epithelial phenotype²⁰, but different in that rates of migration are slower. Levels of AQP1 expression are approximately 2.6-fold lower in SW620 than in HT29 cells (Figure 5C). HT29 cells and SW620 cells were pre-incubated in SHL for 2 hours, transferred into Li⁺-substituted saline and imaged. Results show that the lithium hot spots are more abundant and brighter in HT29 cells (Figure 5C, 1-3) than in SW620 cells (Figure 5C, 4-6). In migrating HT29 cells, lithium hot spots are concentrated in leading edges (Figure 5C, 2,3), in contrast to the uniform distribution seen in non-migrating cells (Figure 5C, 1). This observation is consistent with the known clustering of AQP1 channels in the leading edges of specific classes of cells during migration¹⁰, where these channels are proposed to facilitate fluid movements needed for volume changes during extension, and possibly to compensate for changes in osmotic pressure associated with actin polymerization and depolymerization⁹.

AQP1 expression and localization were determined by immunofluorescent imaging using confocal microscopy (as detailed in the Supporting Information section). AQP1 protein was immunolabeled with anti-AQP1 and green fluorescent AlexaFluor 488 secondary antibody, visualized by 488 nm laser excitation. HT29 cells demonstrated high AQP1 signal intensities as compared to SW620 cells (Figure 6A, B). Comparison with SW620 cells confirmed that a reduced abundance of lithium hot spots correlated with lower levels of AQP1 expression. In combination, results here based on pharmacology, ion substitution, and a comparison of cell lines with different levels of AQP1 expression provide evidence that the lithium hot spots measured by the novel probe SHL mark the locations of active AQP1 ion channels.

Lithium hot spots are colocalized with AQP1 channels in HT29 cells

The spatial correlation between the locations of the lithium hot-spots and AQP1 channels was assessed using confocal microscopy. Signal intensities using Z-stack compiled images were measured as a function of distance across the cell diameter (indicated by straight lines crossing the cell centers; two cross-sections per cell). Signals were plotted as a function of X-Y distance to quantify the correspondence between the SHL Li⁺ fluorescence intensity (red channel; MC(SHL)-Li⁺ complex) and the AQP1 protein signal intensity (green channel; immunofluorescence). Results in Figure 6C show that the two fluorescence signals were strongly colocalized in HT29 cells (with superimposed red and green signals represented as yellow), yielding relative fluorescence units (RFU) ranging from 50 to 200 that were consistent with data shown in Figure 5A. The spatial profiles of the red and green signals across the cell diameter are illustrated by plots of signal intensity (Figure 6D). Li⁺ and AQP1 signals in HT29 cells were strongly correlated, with R² values ranging 0.61 to 0.68. In contrast, SW620 cells (Figure 6D) showed low signal intensities and poor spatial correlation, with signal values mainly at 0 to 50 RFU, and R² values ranging from 0.06 to 0.09. This work opens avenues never before imagined for the real-time visualization of cation channel function and the localization of active channel domains in living cells, with insight into the relevance of cation channels such as AQP1 in dynamic cellular responses.

Lithium hot spots are dynamic when imaged in HT29 cells

The ability of SHL to detect dynamic Li⁺ entry through AQP1 was tested using a 300 s time lapse video of a SHL-loaded cell directly after perfusion with Li⁺-substituted extracellular saline. The intensity of Li⁺ hot spots increased during the first half of the recording then cycled between increasing and decreasing during the second half (Figure 7). The montage shows the time series for a 2 μm x 3 μm region of interest (rectangle), illustrating the dynamic fluorescence emission properties. A movie depicting Li⁺ hot spot activity in HT29 cells in real time is available as a Supplemental File.

Conclusion

Work here with confocal imaging is the first to demonstrate the use of a new Li⁺-selective photoswitchable probe as a tool for monitoring non-selective cation entry in living cells, with AQP1 ion channels of migrating cancer cells selected as a model for illustrating feasibility and potential significance. Nonselective monovalent cation channel activity was monitored with the probe SHL which is selective for Li⁺. Lithium hot spots were abundant in HT29 colon cancer cells expressing high levels of AQP1, and rare in SW620 colon cancer cells which have comparatively little AQP1. The spatial localization of Li⁺ hot spots at the leading

edges of HT29 cells was an exciting observation, fitting the predicted location of AQP1 ion channels. Future studies characterizing the dynamic temporal and spatial properties of ion fluxes in migrating cells at higher resolution will be of interest.

The initial proposal that AQP1 works as a non-selective cation channel in addition to its known role as a water channel²¹ generated controversy. Subsequent analyses confirmed the capacity of AQP1 to function as a dual water and ion channel, showing the ion channel activity was gated directed by intracellular cGMP and indirectly regulated by intracellular signalling cascades including tyrosine phosphorylation^{11,12,22,23}, but left unclear the physiological relevance of the dual water and ion channel function²³. Recent work has since demonstrated that the AQP1 ion conductance is essential for rapid cell movement in a subset of cancer cells which show high metastasis or invasiveness^{9,19,24}, demonstrating a functional role for the AQP1 ion channel.

AQP1 channels are not the only pathway for Li^+ transport across cell membranes. Li^+ also is conducted through voltage-gated Na^+ channels²⁵⁻²⁷ and the Na^+ -proton exchanger²⁸. Some of the Li^+ signal described here could involve additional channels or transporters. However, the alternative hypothesis that the lithium signal observed in HT29 cancer cells is due entirely to mechanisms unrelated to AQP1 seems unlikely for several reasons. First, results here showed that pharmacological inhibition with the AQP1 ion channel blocker, AqB011, significantly diminished the Li^+ signal to a level similar to the response observed in cells imaged in saline with TEA^+ (which does not bind to SHL). Other AQP modulators in the library of bumetanide derivatives that include AqB011 have been shown to be selective for specific AQP classes without off-target effects on other signaling and transport mechanisms^{29,30}. Second, the punctate Li^+ signal pattern was not evident in SW620 cells that have low levels of AQP1 expression but otherwise express various channels and transporters required for basic cellular function and low-level motility. Third, the cells used for studies here would not be expected to have appreciable levels of voltage-gated Na^+ channel expression. Lastly, the co-localization of AQP1 expression and Li^+ signals showed a robust correlation which was consistent with other work indicating that AQP1 is localized at the leading edges in subtypes of migrating cells. Evidence that AQP1 is not just a water channel but also works as a monovalent cation channel is contributing to our understanding of the diverse mechanisms that govern cell migration. Looking ahead to translational applications, we propose that the lithium sensor will be useful for investigating cation channel function in many types of living cells, including sensory cells, immune cells, cancer cells and more. The AQP1 ion channel itself is an attractive candidate for development of new therapeutics, and

the Li⁺ sensor SHL could be a powerful tool in high-throughput screening for new pharmacological agents that might ultimately help manage metastasis in aggressive AQP1-dependent cancers.

Acknowledgements

The study was funded by the Australian Research Council (ARC) DP160104641. Sensor development was supported by the Centre for Nanoscale BioPhotonics, with funding from ARC CE140100 003. This work was performed in part at the OptoFab node of the Australian National Fabrication Facility utilizing Commonwealth and South Australian State Government Funding. The authors acknowledge Dr. Xiaozhou Zhang for useful discussions.

Author Contributions

JVP and SH contributed equally to this work. JVP, SH, GS, MK performed the experiments and analyzed the data. JVP, SH and AJY designed the research and wrote the paper. SH and AA designed and developed SHL. All authors discussed the results and conclusions and commented on the manuscript.

References

1. Petrie, R.J., Doyle, A.D. & Yamada, K.M. Random versus directionally persistent cell migration. *Nat Rev Mol Cell Biol* **10**, 538-49 (2009).
2. Krummel, M.F., Bartumeus, F. & Gerard, A. T cell migration, search strategies and mechanisms. *Nat Rev Immunol* **16**, 193-201 (2016).
3. Papadopoulos, M.C., Saadoun, S. & Verkman, A.S. Aquaporins and cell migration. *Pflugers Arch* **456**, 693-700 (2008).
4. Olson, M.F. & Sahai, E. The actin cytoskeleton in cancer cell motility. *Clinical & experimental metastasis* **26**, 273 (2009).
5. Friedl, P. & Wolf, K. Tumour-cell invasion and migration: diversity and escape mechanisms. *Nat Rev Cancer* **3**, 362-374 (2003).
6. Agre, P. et al. Aquaporin CHIP: the archetypal molecular water channel. *Am J Physiol* **265**, F463-76 (1993).
7. King, L.S., Kozono, D. & Agre, P. From structure to disease: the evolving tale of aquaporin biology. *Nat Rev Mol Cell Biol* **5**, 687-98 (2004).
8. Pei, J.V., Burton, J.L., Kourghi, M., De Ieso, M.L. & Yool, A.J. Drug discovery and therapeutic targets for pharmacological modulators of aquaporin channels. in *Aquaporins in Health and Disease: New Molecular Targets For Drug Discovery* (eds. Soveral, G., Casinin, A. & Nielsen, S.) 275-297. (CRC Press, Oxfordshire, UK, 2016).
9. Hu, J. & Verkman, A.S. Increased migration and metastatic potential of tumor cells expressing aquaporin water channels. *FASEB J* **20**, 1892-4 (2006).
10. McCoy, E. & Sontheimer, H. Expression and function of water channels (aquaporins) in migrating malignant astrocytes. *Glia* **55**, 1034-43 (2007).

11. Anthony, T.L. et al. Cloned human aquaporin-1 is a cyclic GMP-gated ion channel. *Molecular Pharmacology* **57**, 576-588 (2000).
12. Boassa, D. & Yool, A.J. Single amino acids in the carboxyl terminal domain of aquaporin-1 contribute to cGMP-dependent ion channel activation. *BMC physiology* **3**, 12-12 (2003).
13. Rivera-Fuentes, P. et al. A Far-Red Emitting Probe for Unambiguous Detection of Mobile Zinc in Acidic Vesicles and Deep Tissue. *Chem Sci* **6**, 1944-1948 (2015).
14. Kolmakov, K. et al. Red-emitting rhodamine dyes for fluorescence microscopy and nanoscopy. *Chemistry* **16**, 158-66 (2010).
15. Klajn, R. Spiropyran-based dynamic materials. *Chemical Society reviews* **43**, 148-84 (2014).
16. Heng, S. et al. Photoswitchable calcium sensor: 'On'-'Off' sensing in cells or with microstructured optical fibers. *Sensors and Actuators B: Chemical* **252**, 965-972 (2017).
17. Heng, S., Nguyen, M., Kosteki, R., Monroe, T.M. & Abell, A.D. Nanoliter-scale, regenerable ion sensor: sensing with a surface functionalized microstructured optical fiber. *RSC Advances* **3**, 8308-8317 (2013).
18. Stubing, D.B., Heng, S. & Abell, A.D. Crowned spiropyran fluoroionophores with a carboxyl moiety for the selective detection of lithium ions. *Organic & biomolecular chemistry* **14**, 3752-7 (2016).
19. Pei, J.V. et al. Differential Inhibition of Water and Ion Channel Activities of Mammalian Aquaporin-1 by Two Structurally Related Bacopaside Compounds Derived from the Medicinal Plant *Bacopa monnieri*. *Mol Pharmacol* **90**, 496-507 (2016).
20. Fogh, J., Fogh, J.M. & Orfeo, T. One hundred and twenty-seven cultured human tumor cell lines producing tumors in nude mice. *J Natl Cancer Inst* **59**, 221-6 (1977).
21. Yool, A.J., Stamer, W.D. & Regan, J.W. Forskolin stimulation of water and cation permeability in aquaporin 1 water channels. *Science* **273**, 1216-8 (1996).
22. Campbell, E.M., Birdsell, D.N. & Yool, A.J. The Activity of Human Aquaporin 1 as a cGMP-Gated Cation Channel Is Regulated by Tyrosine Phosphorylation in the Carboxyl-Terminal Domain. *Molecular Pharmacology* **81**, 97-105 (2012).
23. Saparov, S.M., Kozono, D., Rothe, U., Agre, P. & Pohl, P. Water and ion permeation of aquaporin-1 in planar lipid bilayers. Major differences in structural determinants and stoichiometry. *J Biol Chem* **276**, 31515-20 (2001).
24. Kourghi, M., Pei, J.V., De Ieso, M.L., Flynn, G. & Yool, A.J. Bumetanide Derivatives AqB007 and AqB011 Selectively Block the Aquaporin-1 Ion Channel Conductance and Slow Cancer Cell Migration. *Mol Pharmacol* **89**, 133-40 (2016).
25. Hille, B. The permeability of the sodium channel to metal cations in myelinated nerve. *J Gen Physiol* **59**, 637-58 (1972).
26. Richelson, E. Lithium ion entry through the sodium channel of cultured mouse neuroblastoma cells: a biochemical study. *Science* **196**, 1001-2 (1977).
27. Timmer, R.T. & Sands, J.M. Lithium intoxication. *J Am Soc Nephrol* **10**, 666-74 (1999).
28. Lenox, R.H., McNamara, R.K., Papke, R.L. & Manji, H.K. Neurobiology of lithium: an update. *J Clin Psychiatry* **59 Suppl 6**, 37-47 (1998).
29. Migliati, E. et al. Inhibition of aquaporin-1 and aquaporin-4 water permeability by a derivative of the loop diuretic bumetanide acting at an internal pore-occluding binding site. *Mol Pharmacol* **76**, 105-12 (2009).
30. Yool, A.J. et al. AqF026 is a pharmacologic agonist of the water channel aquaporin-1. *J Am Soc Nephrol* **24**, 1045-52 (2013).

Methods

Electrophysiology

Two-electrode voltage clamp recordings were used to determine the ability of Li^+ to carry current in AQP1-expressing oocytes. Recordings were performed at room temperature in standard isotonic Na^+ saline and in Li^+ -substituted isotonic saline containing 100 mM NaCl or 100mM LiCl respectively, and 2 mM KCl, 4.5 mM MgCl_2 , and 5 mM HEPES, pH 7.3. Capillary glass electrodes (1–3 M Ω ; 1 M KCl) were used for recordings. cGMP was applied to the bath saline at a final concentration of 10-20 μM using the membrane-permeable cGMP analog [Rp]-8-[para-chlorophenylthio]-cGMP (Sigma-Aldrich, Castle Hill NSW Australia). Ion conductances were determined by linear fits of current amplitudes as a function of voltage, applied by a step protocol from +60 to -110 mV from a holding potential of -40 mV^{19,24}. Ionic conductance values were monitored over 25 minutes after the bath application of cGMP to allow sufficient time to achieve maximal response. Recordings were done using a GeneClamp amplifier and pClamp 9.0 software (Molecular Devices, Sunnyvale CA USA).

Cancer cell cultures and imaging

HT29 and SW620 colorectal cancer cell lines (American Type Culture Collection ATCC, Manassas, VA USA) were cultured in complete DMEM, consisting of Dulbecco's Modified Eagles Medium supplemented with 10% fetal bovine serum (V/V), penicillin and streptomycin (100 U/ml each) and 1 x glutaMAX™ (Life Technologies, Scoresby, VIC, Australia). Cultures were maintained in 5% CO_2 at 37°C. Cells were seeded on an 8-well uncoated Ibidi μ -Slides (Ibidi, Munich, Germany) at a density of 1.0×10^5 cells/ml and allowed 24 hours to settle.

All confocal imaging experiments were performed in a darkroom. Prior to imaging, cells were incubated with 50 μM of sensor for 2 hours then washed twice with warm phosphate buffered saline. For the AqB011-treated group, cells were then incubated with 20 μM AqB011 for 2 hours, or with vehicle (0.1% dimethylsulfoxide; DMSO). All cells were stained with 0.5 mg/mL of Hoechst 33258 for 20 mins. Either Li^+ saline (137 mM LiCl, 3.5 mM KCl, 0.68 mM KH_2PO_4 , 5 mM HEPES, 10 mM glucose and 4.4 mM MgSO_4) or TEA^+ saline (with 137 mM TEA Cl substituted for NaCl; other components the same) was used for imaging. The μ -Slide was mounted on a Leica TCS SP5 laser scanning confocal microscope (Leica, Germany) with the 63x objective selected. To detect the signal emitted by the SHL sensor, the excitation/emission setting $\text{Ex}=513 \text{ nm}$ / $\text{Em}=550 \text{ nm}\sim 700 \text{ nm}$ was

used. For visualizing Hoechst 33258 staining, the setting Ex=405 nm /Em= 425 nm~ 500 nm was used.

Live cell imaging was performed using previously published methods¹⁹. In brief, HT29 cells were seeded at a density of 1.0×10^6 cells/ml on an 8-well uncoated Ibidi μ -Slide (Ibidi, Munich Germany). Cells were imaged in the presence of a mitotic inhibitor FUDR (100 ng/mL). Circular wounds were created in each well using published techniques¹⁹. Images were acquired with a Nikon TiE Live Cell Microscope (Nikon, Tokyo Japan) at 37 °C with 5% CO₂. Images were taken at 50 min intervals over 24 hours using Nikon NIS-Elements software (Nikon, Japan), and analyzed by Image J (National Institutes of Health, MD USA). Gaussian distributions were generated with GraphPad Prism software (CA USA).

siRNA transfection

HT29 cells were cultured in either a 6-well plate or an 8-well uncoated Ibidi μ -Slide in complete DMEM to reach 30% confluency prior to transfection. Transfection using Lipofectamine 2000 ([11668019](#), Life Technologies, Scoresby, VIC, Australia) was done with 50 nM of either Ambion Silencer Select AQP1 siRNA (4390824, Life Technologies, Scoresby, VIC, Australia) or Ambion Silencer Select Negative Control #1 siRNA (4390843, Life Technologies, Scoresby, VIC, Australia), together with 50 nM Dharmacon siGLO Green Transfection Indicator (D-001630-01-05, Millennium Science, Mulgrave, VIC, Australia). Cells were incubated in 5% CO₂ at 37°C condition for 48 hours prior to confocal imaging or real-time PCR analyses. For detecting the signal emitted by siGLO Green, the setting Ex=496 nm/ Em=506 nm~606 nm was used.

Quantitative Reverse-Transcription Polymerase Chain Reaction

At 48 hours post-transfection, cells were harvested from the 6-well plates and RNA was extracted using Invitrogen PureLink RNA Mini Kit (1876897, Life Technologies, Scoresby, VIC, Australia) according to the manufacturer's protocol. RNA was quantified with Take3 Micro-Volume Plates and the Synergy 2 plate reader (BioTek, Winooski, VT). The RNA (1 μ g) was reverse transcribed using QuantiNOVA Reverse Transcription Kit (205413, Qiagen, Chadstone Centre, VIC, Australia). Quantitative Reverse-Transcription Polymerase Chain Reactions of the reference sequence ribosomal protein S13 (RPS13) and AQP1 were performed using SYBR Select Master Mix (4472908, Life Technologies, Scoresby, VIC, Australia) in triplicate in the Rotorgene 6000 (Qiagen, Chadstone Centre, VIC, Australia). Primers used for AQP1 are as follows: Forward primer AGTCACTTCCCCAAGATCTGC, Reverse primer CAGGTGGGTCCCTTTCTTCA.

Immunohistochemistry

Cells were cultured in 8-well Ibidi μ -Slides (Ibidi, Munich, Germany) to achieve 50% confluency prior to the experiment. Cells were rinsed with phosphate-buffered saline (PBS), fixed in 4% paraformaldehyde for 20 minutes at room temperature (RT), and washed 4 times in PBS (5 min each, at RT) on a rocker. Cells were permeabilized with 0.1% PBS Tween for 5 minutes, washed three times with PBS (5 min each, at RT) on a rocker, and then blocked with 10% goat serum in PBS (GS/PBS) for 40 min at RT on a rocker. Incubation with the rabbit anti-AQP1 antibody (ab15080, Abcam, Victoria, Australia) in 0.1%GS/PBS was 2 hours at RT. The cells were then washed three times in PBS (7 min each; at RT) on a rocker and incubated with Alexa488-conjugated goat anti-rabbit antibody (ab150077, Abcam, Victoria, Australia) diluted in 0.1%GS/PBS (35 min; at RT in the dark). After washing three times in PBS (7 min each; at RT) on a rocker, cells were incubated with Hoescht 33258 (Sigma-Aldrich, Castle Hill, NSW Australia) for 5 min in the dark. The cells were rinsed with PBS twice and mounted using Hydromount mounting media (Sigma-Aldrich, Castle Hill, NSW Australia).

In cell photo switching experiment

Plates were mounted on microscope with UV lamp and overhanging table light. The first image was taken after the plate was transferred from incubator to microscope and been exposed under white light for 10 minutes (OFF1). Then the plate was exposed to UV (632nm) light for 10 minutes and the second image was taken (ON1). In the next 10 minutes, one image was taken every 2 minutes during white light exposure. The seventh image was labelled as OFF2. The last image was taken after the plate was incubated in total dark for 10 minutes (ON2). Fluorescence intensities were quantified using Image J software (National Institutes of Health, MD USA).

Figures and Legends

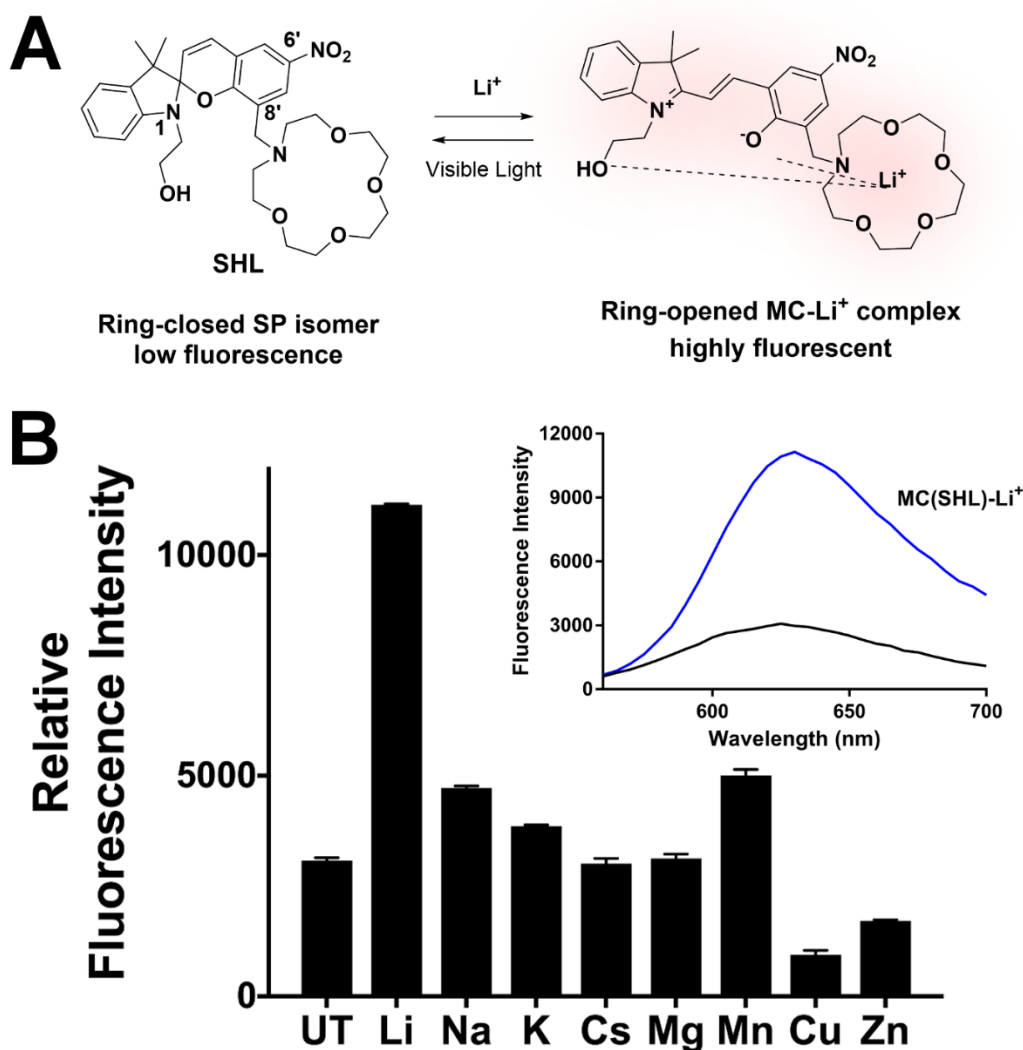


Figure 1. Properties of the lithium sensor SHL.

(A) Structures of the spiropyran (SP) and merocyanine-lithium complexes of the sensor SHL (MC(SHL)-Li⁺), and reversible binding of Li⁺. The ring-closed spiropyran has lower fluorescence than the open merocyanine. (B) Fluorescence intensities of SHL (50 μM) in the presence of Li⁺ or other biologically relevant metal ions. Excitation wavelength=532 nm; emission wavelength= 625 nm. (Inset) Fluorescence spectra of SHL in water (50 μM). Black spectrum: SHL with no added Li⁺. Blue spectrum: SHL with Li⁺ (100 μM).

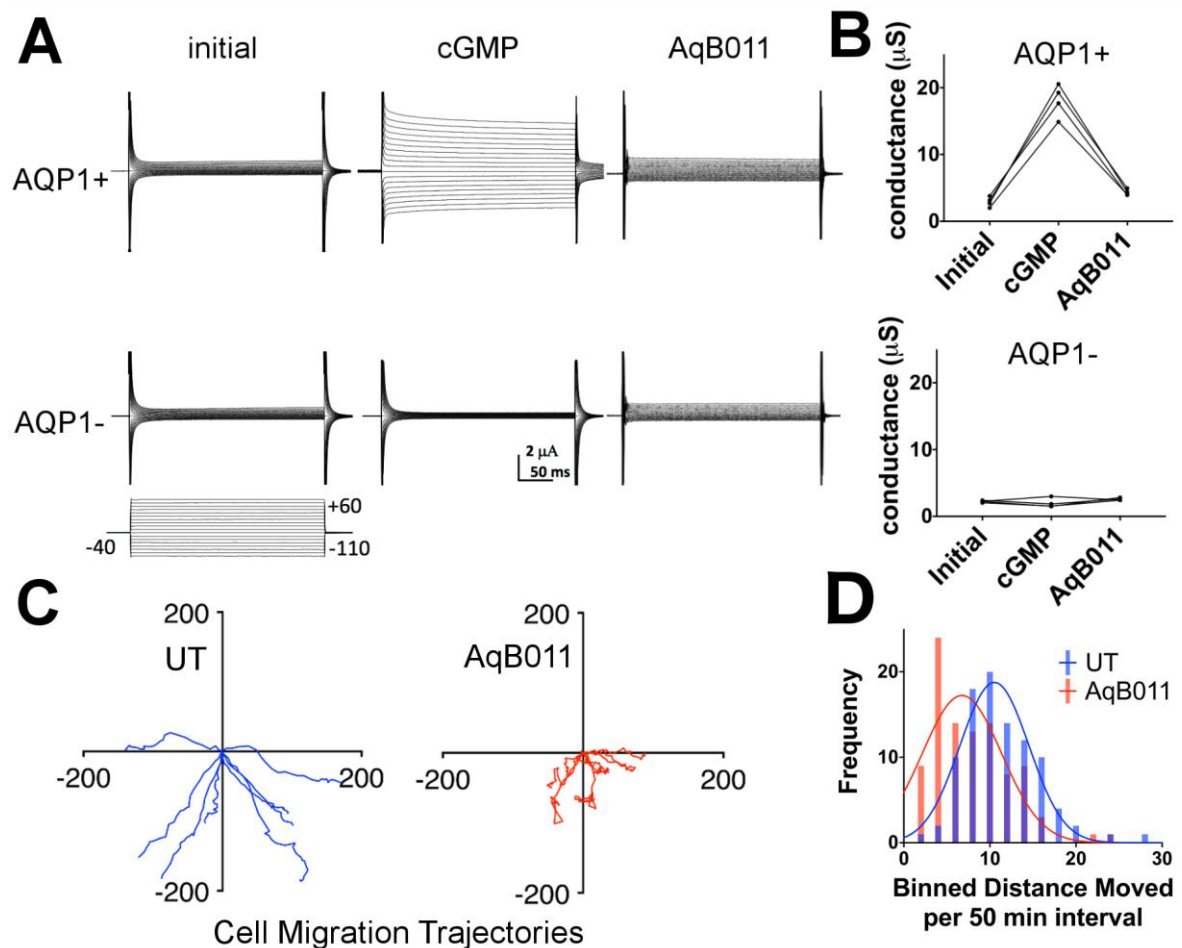


Figure 2. AQP1 ion channels are permeable to Li^+ and blocked by the pharmacological agent AqB011, which also impairs migration in an AQP1-expressing cancer cell line.

(A) Two-electrode voltage clamp recordings in Li^+ isotonic saline of human AQP1-expressing (AQP1+) and non-expressing control (AQP1-) *Xenopus* oocytes. After initial recordings (initial), ionic conductance responses were activated in AQP1+ but not AQP1- oocytes by 25 min after application of CPT-cGMP (cGMP). Post-incubation in AqB011 ($30 \mu\text{M}$; 2 h), the AQP1 conductance was unresponsive to the second application of cGMP (AqB011). (B) Trend plots illustrate responses for AQP+ oocytes measured before (initial), after the first application of CPT-cGMP (cGMP), and after the second application of CPT-cGMP following 2 hour incubation in saline with AqB011 (AqB011). Ion conductance responses were not observed in AQP1- control oocytes. (C) Migration trajectories for individual HT29 cells were monitored by live cell imaging at 50 min intervals over 24 h, with and without AqB011 ($80 \mu\text{M}$). $n = 8$ cells per treatment. (D) Compiled Gaussian distributions of individual cell distances moved per 50 min interval, and illustrating impaired rates of migration in the AqB011-treated HT29 cells (mean \pm SEM with AqB011 was $5.69 \pm 0.54 \mu\text{m/h}$, and without AqB011 was $8.83 \pm 0.22 \mu\text{m/h}$; $n = 8$ per treatment group).

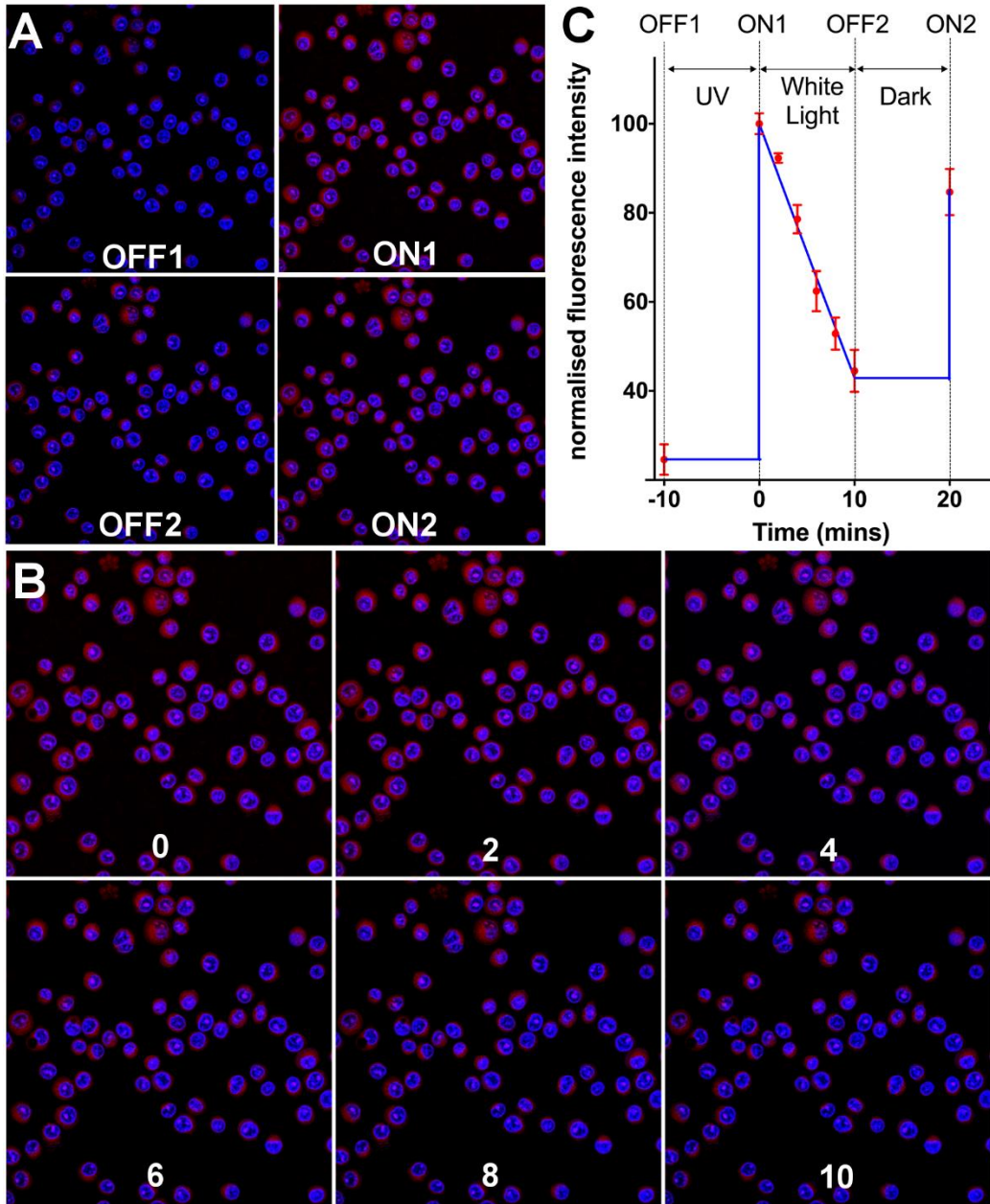


Figure 3. Confocal time series for SHL signals in HT29 cells.

(A) HT29 cells were incubated with 50 μM SHL for 2 h prior to imaging. Cell nuclei were labelled with Hoescht 33258 (blue). Four distinctive states of the sensor during the photoswitch cycles are illustrated. Cells were first illuminated under visible light radiation for 10 min to convert majority of the sensor back to non-fluorescent SP isomer (OFF1). Then, cells were illuminated under UV light for 10 min to convert SP isomer to fluorescent MC(SHL)-Li⁺ complex (ON1), followed by exposure under white light for 10 min with measurement taken every 2 min (OFF2). Finally, cells were incubated in the dark for 10 min to allow the formation of the MC isomer, and the binding of Li⁺ to form the MC(SHL)-Li⁺ complex (OFF2). (B) 10 min white light illumination was applied to cells after ON1 state; images were taken every 2 min as illustrated. Red SHL signals gradually faded with time. (C) Red fluorescent signals were measured for individual cells in the field of view and values were normalized to ON1 state. Data are mean \pm S.E.M.; the n value is 43. A single-phase decay function was fitted to values between ON1 (100 RFU) and OFF2 (44.51 RFU) state; the half-life was determined to be 4.13 minutes with a τ value estimated at 5.95 minutes. After 10 min incubation in the dark, sensors converted back to the MC isomer, and the normalized intensity increased from 44.51 RFU (OFF2) to 84.65 RFU (ON2).

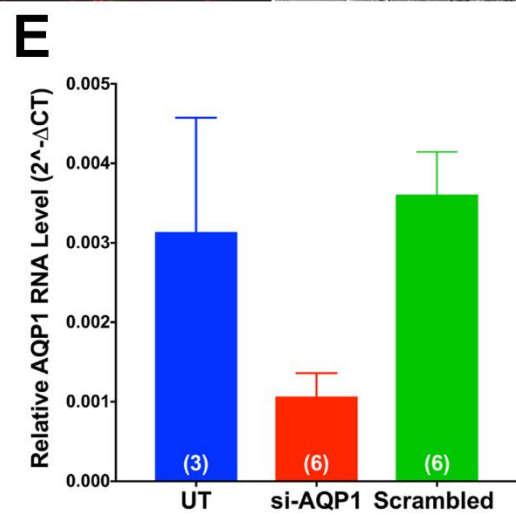
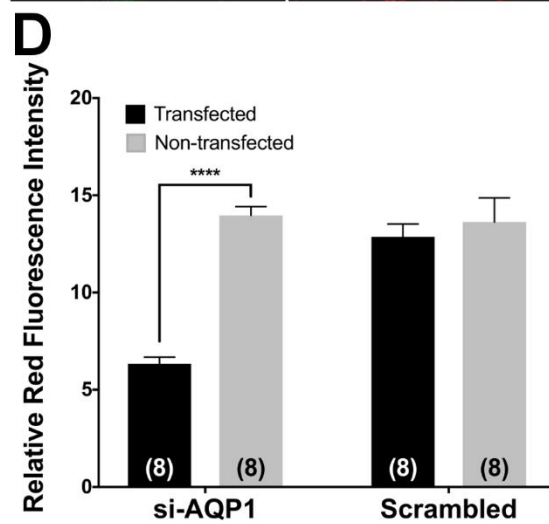
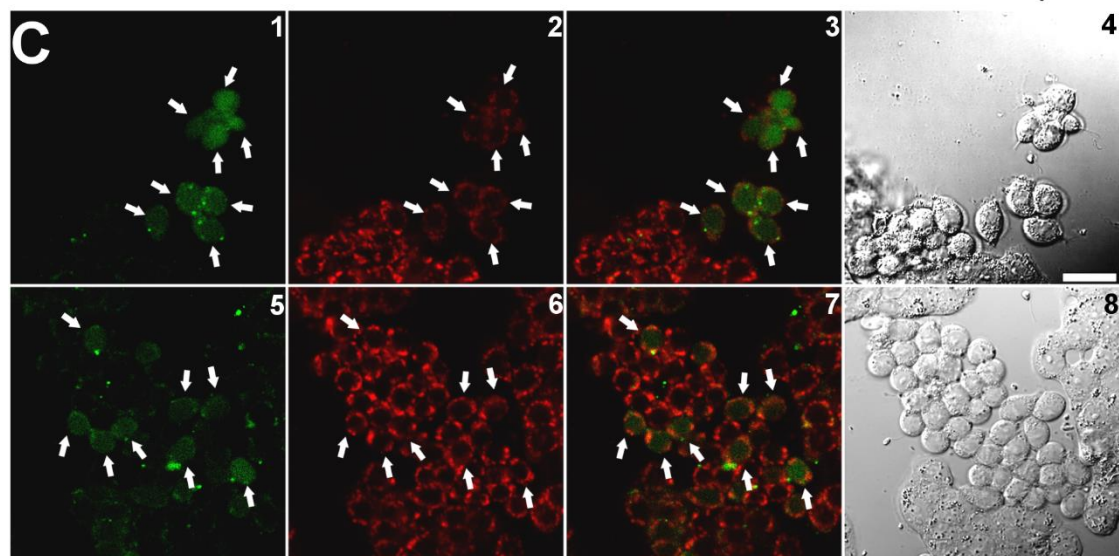
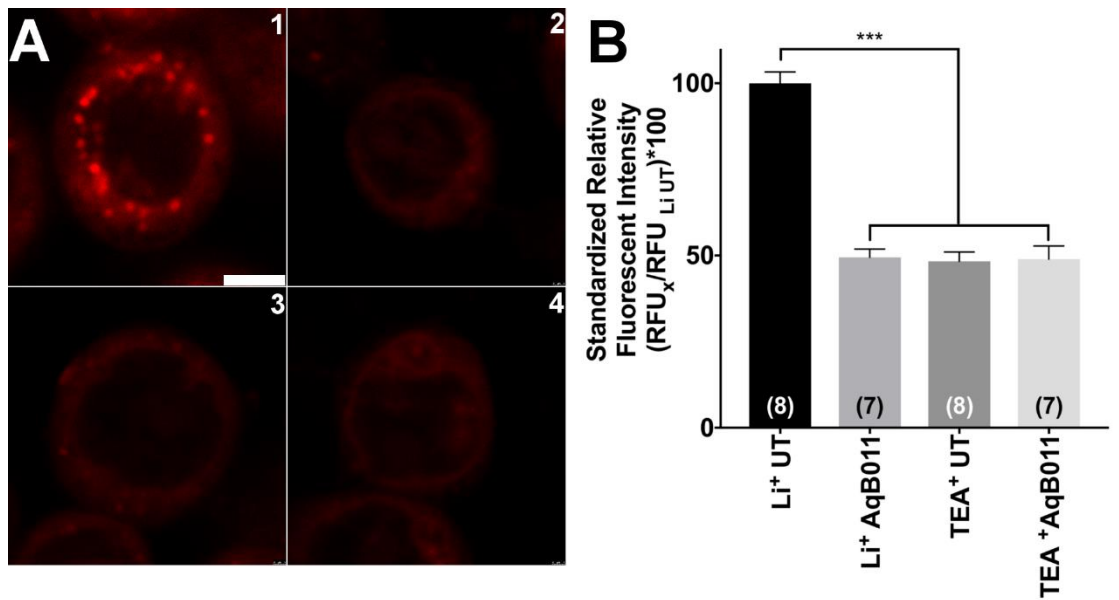


Figure 4. (A) Distinctive punctate Li^+ hot spots were observed in HT29 cells imaged in Li^+ substituted extracellular saline (1). In cells that were pre-treated with 20 μM AqB011 for 2 h, Li^+ hot spots were not observed (2). Similar losses of ‘hot spot’ events were observed after the removal of Li^+ from the extracellular saline by equimolar substitution of TEA^+ (3). Pre-treatment with 20 μM AqB011 (2 h) caused no further change in the signal in the absence of extracellular Li^+ (4). (B) Li^+ -selective fluorescent signals were quantified by measuring red fluorescent intensities of individual cells. Intensities were normalized to those of HT29 cells imaged in Li^+ saline. Li^+ entry was significantly compromised by pharmacological block (AqB011) or removal of Li^+ ion from the saline by equimolar replacement with other cations such as TEA^+ . (C) HT29 cells were transfected with either siRNA targeting AQP1 (si-AQP1, upper panels) or scrambled siRNA (Scrambled, lower panels) before confocal imaging. Cells were pre-incubation in transfection indicator siGLO Green (Green, 1 and 5) and SHL (Red, 2 and 6). Stacked images of both Green and Red channels were illustrated in 3 and 7 and bright field imaged were illustrated in 4 and 8. Li^+ signals were impaired in cells successfully transfected with AQP1 siRNA (cells with green nucleus, 3) but not in cells transfected with scrambled siRNA (cells with green nucleus, 7). (D) Li^+ -selective fluorescent signals were quantified by measuring red fluorescent intensities of individual cells that were either transfected (green nucleus signal) or non-transfected (no nucleus signal). Li^+ entry was significantly impaired in cells with AQP1 knockdown. (E) AQP1 RNA levels were quantified by using RT-PCR. AQP1 RNA levels were lowered in cells transfected with siRNA targeting AQP1 (si-AQP1) compared with either cells without transfection (UT) or cells with scrambled siRNA transfection (scrambled).

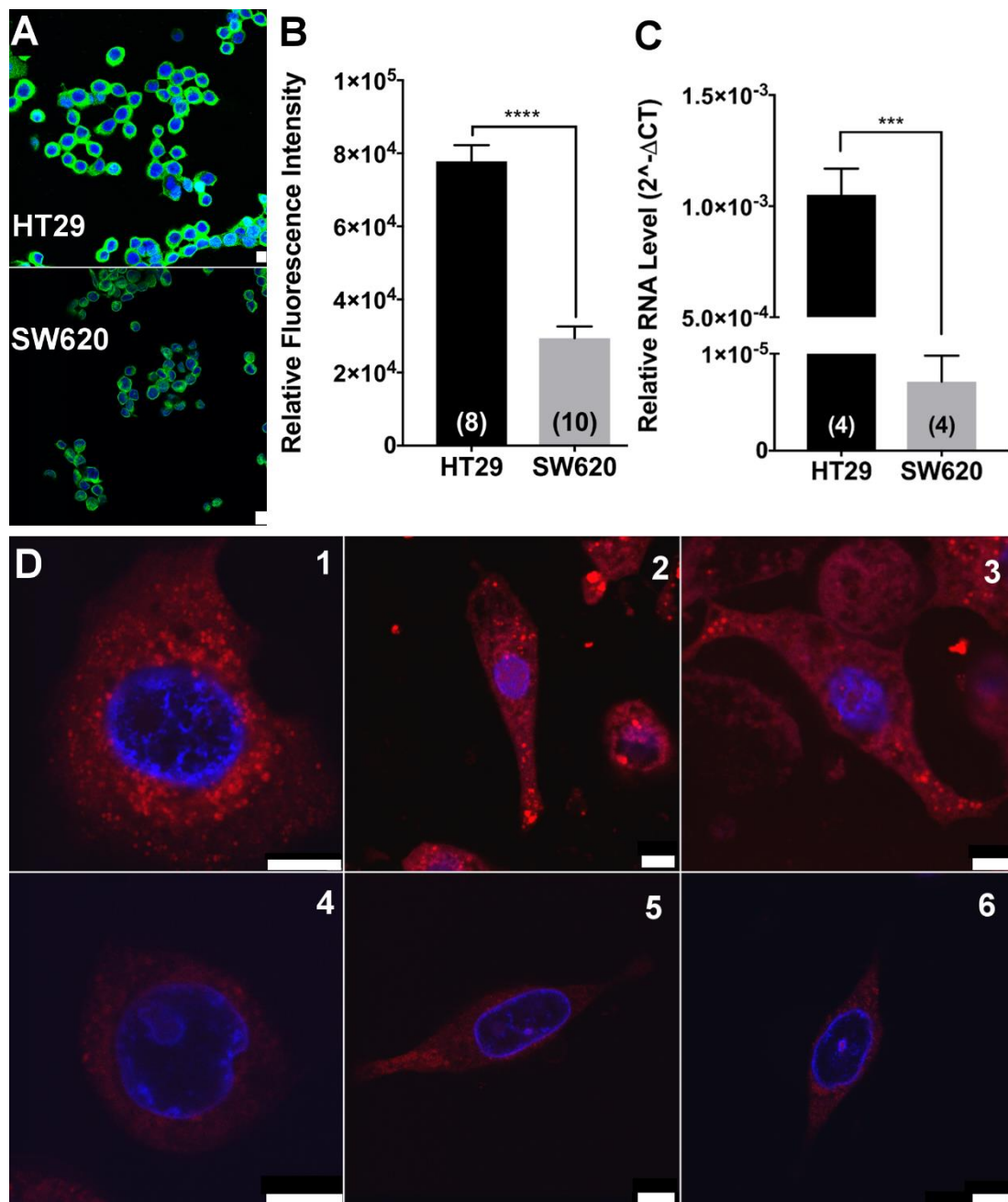


Figure 5. Characterization of lithium hot spots in AQP1-expressing and AQP1-deficient cells. (A) Cells were labeled with Hoescht nuclear stain (blue) and anti-AQP1 antibody (tagged with fluorescent secondary antibody; green). (B) Anti-AQP1 immunofluorescence intensities for HT29 cells were approximately 2.6-fold higher than in SW620 cells. (C) AQP1 RNA levels measured by reverse-transcription quantitative-PCR were more than 100 fold lower in SW620 cells as compared with HT29 cells. (D) HT29 and SW620 cells were loaded with SHL for 2 h prior to imaging. A strong Li⁺ signal was observed in all HT29 cells (1, 2, 3) as compared with the minimal Li⁺ signals observed in SW620 cells (4, 5, 6). In non-migrating HT29 cells, Li⁺ hot spots appeared as widely distributed across the cell (1). In migrating HT29 cells, Li⁺ hot spots were concentrated at leading edges of the cells (2, 3). White scale bars indicate 5 μm.

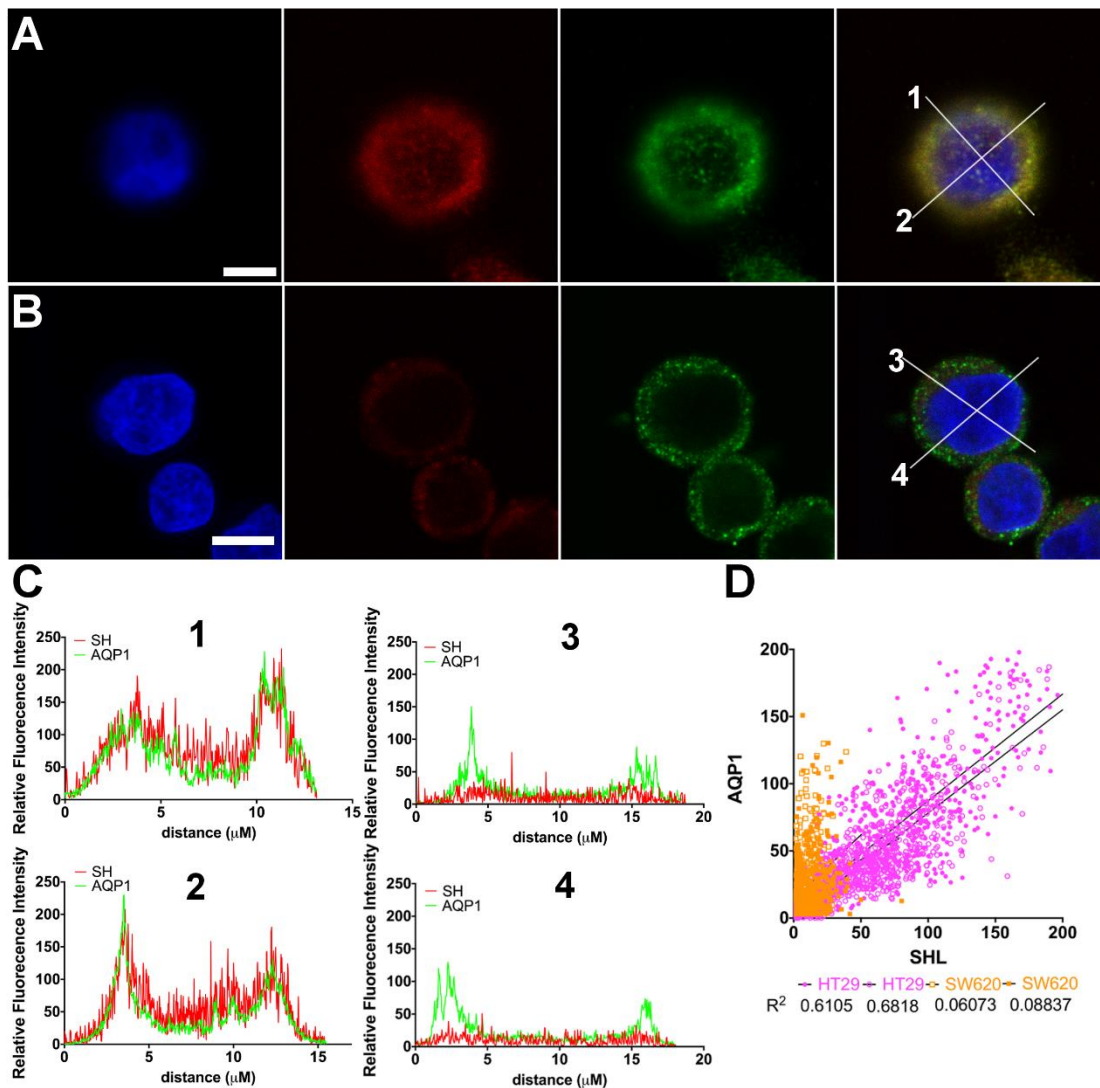


Figure 6. Quantitative confocal analyses of the co-localization of AQP1 and Li⁺ hot spots. HT29 cells (A) and SW620 cells (B) were pre-incubated with SHL (red) and then fixed and labelled with AQP1 primary antibody and AlexaFluro-488 conjugated secondary antibody (green). Nuclei were stained with Hoescht (blue). Both the Li⁺ and AQP1 signals were at higher intensities in HT29 cells than in SW620 cells. In the far-right panels, all three signal bandwidth images are combined, with co-localized red and green signals seen as yellow. Fluorescence signals from the MC(SHL)-Li⁺ complex and AQP1 were strongly co-localized in HT29 cells but not in SW620 cells. (C) Two cross-sections through cell centers were selected (labeled 1 and 2 for HT29; 3 and 4 for SW620). The red Li⁺ and green AQP1 signal intensities in the cross-sectional lines were plotted as a function of X-Y distance across the cell. HT29 cells showed robust levels and a strong correlation between Li⁺ and AQP1 signal intensities, not seen in SW620 cells. (D) Linear regression analyses quantified the correlation between Li⁺ signal and AQP1 signal intensities in HT29 cells (pink) and SW620 cells (orange), for data from panel C. R² values calculated using GraphPad Prism 7 were 0.61 and 0.68 for HT29 cell cross sections, and 0.06 and 0.09 for SW620 cells.

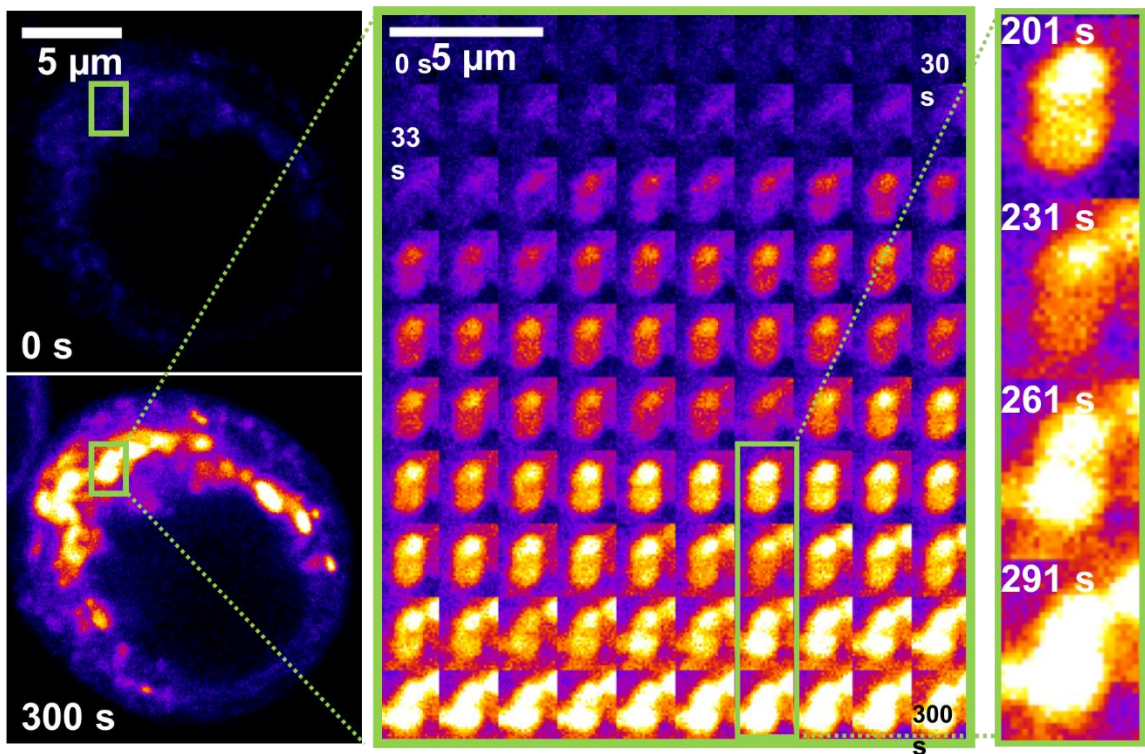


Figure 7. Dynamic properties of Li^+ hot spots illustrating ON/OFF SHL probe transitions in a living HT29 cell. HT29 cells pre-loaded with SHL were imaged for 100 frames at 3 s intervals. Extracellular saline was replaced with Li^+ saline at time 0. Multiple Li^+ hot spots were activated, as illustrated in the left panels at time 0 and 300s. Images were cropped to show higher magnification views of two discrete Li^+ hot-spots (middle panel) as a time-lapse montage, illustrating the independent ON/OFF/ON transitions of the hot spots (inset, right).

APPENDIX B

Engineering of Surface Chemistry for Enhanced Sensitivity in Nanoporous Interferometric Sensing Platforms

Cheryl Suwen Law,^{1,3} Georgina M. Sylvia,^{2,3,4} Madieh Nemati,¹ Jingxian Yu,^{2,3,4} Dusan Losic,¹ Andrew D. Abell,^{2,3,4} * and Abel Santos.^{1,2,3} *

¹School of Chemical Engineering, ²Department of Chemistry, ³Institute for Photonics and Advanced Sensing (IPAS), and ⁴ARC Centre of Excellence for Nanoscale BioPhotonics (CNBP), The University of Adelaide, Adelaide, SA 5005, Australia.

ACS Appl. Mater. Interfaces, **2017**, 9(10), 8929-8940; doi:10.1021/acsami.7b01116.

(Impact Factor 2016: 7.501, Ranking in Materials Science, Multidisciplinary: Q1.)

Engineering of Surface Chemistry for Enhanced Sensitivity in Nanoporous Interferometric Sensing Platforms

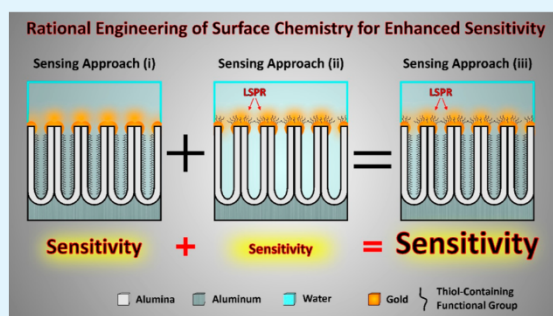
Cheryl Suwen Law,^{†,§} Georgina M. Sylvia,^{‡,§,||} Madieh Nemati,[†] Jingxian Yu,^{‡,§,||} Dusan Losic,^{†,||} Andrew D. Abell,^{*,‡,§,||} and Abel Santos^{*,†,‡,§,||}

[†]School of Chemical Engineering, [‡]Department of Chemistry, [§]Institute for Photonics and Advanced Sensing (IPAS), and ^{||}ARC Centre of Excellence for Nanoscale BioPhotonics (CNBP), The University of Adelaide, Adelaide, SA 5005, Australia

S Supporting Information

ABSTRACT: We explore new approaches to engineering the surface chemistry of interferometric sensing platforms based on nanoporous anodic alumina (NAA) and reflectometric interference spectroscopy (RIfS). Two surface engineering strategies are presented, namely (i) selective chemical functionalization of the inner surface of NAA pores with amine-terminated thiol molecules and (ii) selective chemical functionalization of the top surface of NAA with dithiol molecules. The strong molecular interaction of Au³⁺ ions with thiol-containing functional molecules of alkane chain or peptide character provides a model sensing system with which to assess the sensitivity of these NAA platforms by both molecular feature and surface engineering. Changes in the effective optical thickness of the functionalized NAA photonic films (i.e., sensing principle), in response to gold ions, are monitored in real-time by RIfS. 6-Amino-1-hexanethiol (inner surface) and 1,6-hexanedithiol (top surface), the most sensitive functional molecules from approaches i and ii, respectively, were combined into a third sensing strategy whereby the NAA platforms are functionalized on both the top and inner surfaces concurrently. Engineering of the surface according to this approach resulted in an additive enhancement in sensitivity of up to 5-fold compared to previously reported systems. This study advances the rational engineering of surface chemistry for interferometric sensing on nanoporous platforms with potential applications for real-time monitoring of multiple analytes in dynamic environments.

KEYWORDS: nanoporous anodic alumina, reflectometric interference spectroscopy, surface chemistry engineering, optical sensing, sensing performance



1. INTRODUCTION

Optical sensors are powerful analytical tools that play vital roles in biomedical research, environmental monitoring, homeland security, and other applications.¹ Advantages of optical sensing systems include immunity to electromagnetic interference, label-free and remote sensing capabilities, and identification of analytes of interest by characteristic spectroscopic signatures.^{2,3} Optical sensors collect analytical information through the interaction between light and matter using optical transduction techniques such as surface plasmon resonance (SPR), surface-enhanced Raman scattering (SERS), photoluminescence, and interferometry.^{4–7} Among these, interferometric sensors offer a versatile, label-free sensing approach for broad sensing applications.^{8–15} The underlying principle of reflectometric interference spectroscopy (RIfS) is based on white light interferometry on solid thin films, which results in the formation of a characteristic interference pattern by the Fabry–Pérot effect.^{8,9} Pioneering RIfS systems combined functional polymeric thin films deposited onto glass slides as sensing platforms for gas sensing,^{8,10} label-free immunosensing,¹⁰ and biomolecular interaction analysis (BIA).^{9,11} The use

of nanoporous thin films based on porous silicon as transducer elements opened new opportunities to develop advanced sensing systems for the detection of small organic molecules, DNA, and proteins.^{12–15} The nanoporous structure of porous silicon makes it an excellent platform for the development of photonic structures with precisely engineered optical properties such as well-resolved Fabry–Pérot fringes in the RIfS spectrum. Nevertheless, the relatively poor chemical stability in aqueous media of porous silicon leads to unstable optical signals, which is undesirable for practical sensing applications.^{16,17} Alternative nanoporous materials, such as nanoporous anodic alumina (NAA), demonstrate similar advantages to those of porous silicon while addressing chemical instability limitations due to the inert nature of alumina (aluminum oxide, Al₂O₃). Versatility of nanopore geometry and surface chemistry, chemical and mechanical stability, and optical properties make NAA an excellent platform for developing interferometric sensing

Received: January 22, 2017

Accepted: February 27, 2017

Published: February 27, 2017

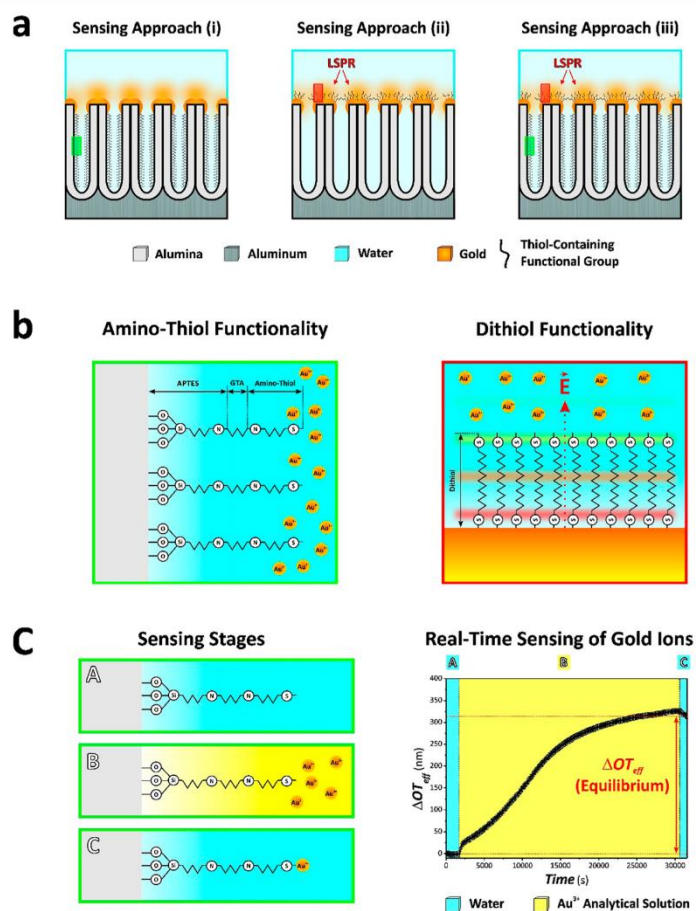


Figure 1. Sensing concepts and surface chemistries of NAA sensing platforms in combination with RIFs. (a) Sensing approaches used in our study: (i) selective functionalization with amino-thiol functional molecules inside the nanopores of NAA platforms, (ii) selective functionalization with dithiol functional molecules on the top surface of NAA platforms, and (iii) selective dual functionalization with amino-thiol and dithiol functional molecules inside the nanopores and on the top surface of NAA platforms, respectively. (b) Details of the surface chemistry structure for amino-thiol (left: magnified view of green rectangle shown in (a)) and dithiol (right: magnified view of red rectangle shown in (b)) functional molecules (note: for dithiol molecules, a localized surface plasmon resonance (LSPR) sensing approach was used, where the sensitivity of the system relies on the electromagnetic field generated in gold-coated NAA platforms, \vec{E}). (c) Stages of the sensing approach used in our study (left) and example of real-time sensing of gold ions in NAA platforms based on changes in the effective optical thickness measured by RIFs (note: real sensing for 8-amino-1-octanethiol for $[Au^{3+}] = 80 \mu M$).

devices.¹⁸ The combination of RIFs with NAA platforms has recently shown significant and promising potential for qualitative and quantitative detection of a broad range of analytes, such as gases, metal ions, biomolecules, and organic molecules.^{19–25}

The sensitivity of interferometric sensors based on NAA and analogous nanoporous materials relies on the magnitude of the interaction between the nanoporous matrix and analyte molecules.^{26,27} This interaction is translated into changes in the effective medium of the nanoporous film, the magnitude of which is established by five main factors, including (i) the optical properties of the analyte molecules, (ii) the size of the analyte molecules, (iii) the nature of the medium filling the nanopores (e.g., air or water), (iv) the chemical and physical interaction between the analyte molecules and the surface of the nanoporous matrix, and (v) the effective medium of the sensing platform.²⁵ The surface of NAA can be chemically

modified with different functional molecules in order to attain chemical selectivity toward analytes of interest.²⁵ This factor is of critical importance, not only to selectively capture targeted analyte molecules but also for the sensitivity of the system, as this is strongly dependent on how surface functional groups interact with analyte molecules. Therefore, a suitable chemical functionalization strategy can result in enhanced sensing performances, which is a critical aspect to consider in the development of optical sensing systems for real-time monitoring of analytes in dynamic environments.

Herein, we demonstrate that a rational engineering of the surface chemistry in NAA interferometric platforms can significantly enhance the overall sensing performance. In this study, the gold–thiol interaction in NAA interferometric platforms was chosen as a sensing binding model to discern the effect of different factors upon the overall sensitivity. NAA platforms were functionalized with different thiol-containing

B

DOI: 10.1021/acsami.7b01116
ACS Appl. Mater. Interfaces XXXX, XXX, XXX–XXX

Table 1. Summary of the Characteristics of the Different Functional Molecules Used in Our Study

Functional Molecule Name	Functional Molecule Structure	Molecular Parameter	Sensing Approach	Molecular Mass (g mol ⁻¹)	Contact Angle (°)
L-cysteine				121.16	36 ± 2
Cysteamine				113.61	39 ± 3
L-cysteine Methyl Ester		Functional Features	(i)	171.65	50 ± 2
AAC				263.42	59 ± 3
3-amino-1-propanethiol				127.64	34 ± 2
6-amino-1-hexanethiol		Molecular Length	(i)	169.72	51 ± 3
8-amino-1-octanethiol				197.77	65 ± 2
1,3-propanedithiol				108.23	105 ± 2
1,6-hexanedithiol		Molecular Length	(ii)	150.31	113 ± 1
1,9-nonanedithiol				192.39	120 ± 5

functional molecules. Three sensing approaches were used to establish the effect of these functional configurations on the sensing performance (Figure 1a). This involved (i) selective chemical functionalization of the inner surface of NAA with amino-thiol molecules of different molecular features and sizes, (ii) selective chemical functionalization of the top surface of NAA with dithiol molecules of different sizes, and (iii) selective chemical functionalization of both the top and inner surface of NAA with amino-thiol molecules and dithiol molecules. Changes in the effective optical thickness of NAA platforms after exposure to analytical solutions containing gold ions (Au³⁺) are used as the sensing principle (Figure 1b). This process is monitored in real time by RfS, enabling the real-time assessment of the interaction between thiol functional groups present in NAA platforms and Au³⁺ ions (Figure 1c).

2. EXPERIMENTAL SECTION

2.1. Materials. High purity (99.9997%) aluminum (Al) foils 0.32 mm thick were supplied by Goodfellow Cambridge Ltd. (UK). Oxalic acid (H₂C₂O₄), perchloric acid (HClO₄), chromium trioxide (CrO₃), 3-aminotrimethoxysilane (H₂N(CH₂)₃Si(OC₂H₅)₃, APTES), hydrogen peroxide (H₂O₂), glutaraldehyde (CH₂(CH₂CHO)₂, GTA), phosphate buffered saline (PBS), L-cysteine (C₃H₇NO₂S), cysteamine

hydrochloride (C₂H₇NS·HCl), 3-amino-1-propanethiol hydrochloride (C₃H₉NS·HCl), 6-amino-1-hexanethiol hydrochloride (C₆H₁₃NS·HCl), 8-amino-1-octanethiol hydrochloride (C₈H₁₉NS·HCl), 1,3-propanedithiol (C₃H₈S₂), 1,6-hexanedithiol (C₆H₁₄S₂), 1,9-nonanedithiol (C₉H₂₀S₂), and gold(III) chloride hydrate (HAuCl₄·H₂O) were purchased from Sigma-Aldrich (Australia) and used as received, without further purification. L-Cysteine methyl ester hydrochloride (C₄H₉NO₂S·HCl) was purchased from TCI Co., Ltd., and used as received, without further purification. AlaAlaCys (AAC) was synthesized by stepwise coupling of Fmoc-Cys (Trt) and Fmoc-Ala amino acids through a standard solid phase synthesis with N-fluorenylmethyloxycarbonyl/cysteine(trityl) (N-Fmoc/Cys(Trt)) protecting group strategy (see Supporting Information for further details about the synthesis of the tripeptide AAC). Ethanol (C₂H₅OH, EtOH) and phosphoric acid (H₃PO₄) were supplied by ChemSupply (Australia). Ultrapure water Option Q2-Purelabs (Australia) was used in the preparation of aqueous solutions for this study.

2.2. Fabrication of Nanoporous Anodic Alumina (NAA) Platforms. Al substrates were anodized through a two-step electrochemical anodization process reported elsewhere.^{28–31} In brief, square-like Al chips 1.5 × 1.5 cm² were sonicated in EtOH and ultrapure water for 15 min, respectively, and then dried under air stream. Before anodization, Al chips were electropolished in a mixture of EtOH and HClO₄ 4:1 (v:v) at 20 V and 5 °C for 3 min. The first anodization step was performed in an aqueous solution 0.3 M oxalic acid at 40 V and 6 °C for 20 h. The resulting NAA layer was subsequently removed by

C

DOI: 10.1021/acsami.7b01116
ACS Appl. Mater. Interfaces XXXX, XXX, XXX–XXX

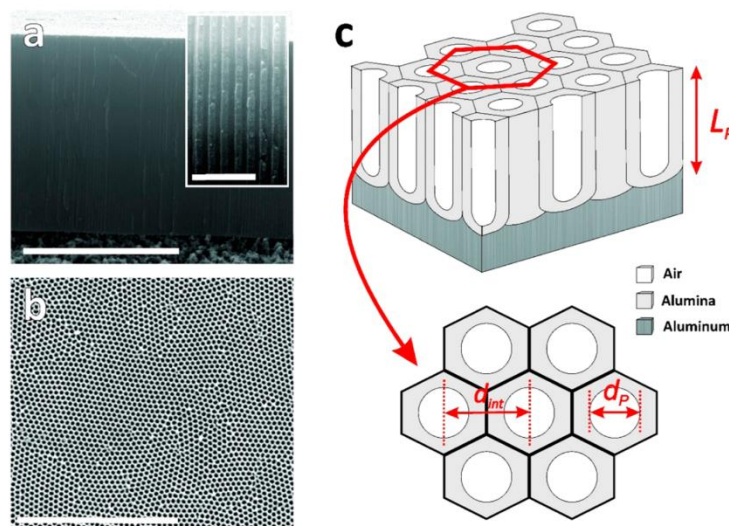


Figure 2. Structural characterization of NAA sensing platforms used in our study. (a) Cross-sectional SEM view of a NAA platform showing straight cylindrical nanopores from top to bottom (scale bar = 5 μm) and inset showing detail of the cylindrical nanopores (scale bar = 500 nm). (b) Top SEM view of a NAA platform featuring characteristic hexagonally arranged cylindrical nanopores across its surface as a result of a two-step anodization process (scale bar = 3 μm). (c) Schematic illustration providing a visual description of the geometric features of NAA platforms with details of the structural parameters (L_p = pore length, d_p = pore diameter, and d_{int} = interpore distance).

wet chemical etching in a mixture of 0.2 M chromic acid (H_2CrO_4) and 0.4 M H_3PO_4 at 70 $^\circ\text{C}$ for 3 h. The second anodization step was carried out under the same conditions (0.3 M $\text{H}_2\text{C}_2\text{O}_4$, 40 V and 6 $^\circ\text{C}$) for 2 h. Lastly, the nanoporous structure of these NAA platforms was widened by wet chemical etching in an aqueous solution of H_3PO_4 (5 wt %) at 35 $^\circ\text{C}$ for 15 min.

2.3. Surface Chemistry Modification Using Amino-Thiol Functional Molecules: Sensing Approach (i). The functionalization of the inner surface of NAA sensing platforms was carried out via silanization with APTES.^{32–35} The as-produced NAA sensing platforms were first hydroxylated by immersion in hydrogen peroxide (30 wt %) at 90 $^\circ\text{C}$ for 10 min and then dried under air stream. Next, hydroxylated NAA platforms were functionalized with 3-aminopropyltriethoxysilane by chemical vapor deposition at 110 $^\circ\text{C}$ for 3 h and then washed with ethanol and distilled water. To activate the amine terminal group ($-\text{NH}_2$) of APTES molecules immobilized onto the inner surface of NAA platforms, these were fully immersed in an aqueous solution of 2.5 vol % glutaraldehyde in PBS for 30 min. GTA-activated NAA sensing platforms were then ready for the immobilization of amino-thiol functional molecules, which was carried out by immersing these platforms into different amino-thiol solutions for 18–20 h. Table 1 summarizes all the thiol-containing functional molecules used in this study. Two parameters of the functional molecules were analyzed using sensing approach (i): namely, the molecular features of amino-thiol molecules and their size. To analyze the former parameter, GTA-activated APTES-functionalized NAA platforms were functionalized with 1 mg mL^{-1} in PBS solution (pH = 7.4) of L-cysteine, cysteamine hydrochloride, L-cysteine methyl ester hydrochloride, and AAC, following the above-mentioned process (*vide supra*). As far as the analysis on the molecular size is concerned, GTA-activated APTES-functionalized NAA platforms were functionalized with 1 mg mL^{-1} in PBS solution of 3-amino-1-propanethiol hydrochloride, 6-amino-1-hexanethiol hydrochloride, and 8-amino-1-octanethiol hydrochloride. Note that amino-thiol-functionalized NAA platforms were washed with ultrapure water and dried under air stream after functionalization. Finally, the amino-thiol-functionalized NAA sensing platforms were coated with an ultrathin layer of gold (i.e., 4–5 nm) using a sputter coater equipped with a film thickness monitor

(sputter coater 108auto, Cressington, USA) to enhance light interference.^{16,21}

2.4. Surface Chemistry Modification Using Dithiol Molecules: Sensing Approach (ii). The top surface of gold-coated NAA sensing platforms was selectively functionalized with a set of dithiol molecules (Table 1) by direct immersion in a solution of functionalizing molecules over 18–20 h to generate self-assembled monolayers of dithiol molecules onto gold sputtered onto the top surface of NAA platforms. The dithiol solutions used were 1 mg mL^{-1} of 1,3-propanedithiol, 1,6-hexanedithiol, and 1,9-nonanedithiol in EtOH. The dithiol-functionalized NAA platforms were then washed with EtOH and ultrapure water after functionalization to remove physisorbed molecules, dried under air stream, and stored under dry conditions until further use.

2.5. Surface Chemistry Modification Using Both Amino-Thiol and Dithiol Molecules: Sensing Approach (iii). After establishing the most sensitive thiol-containing functional molecules in approaches (i) and (ii) (i.e., amino-thiols and dithiols, respectively), a set of NAA platforms were selectively functionalized with both thiol-terminated molecules, sequentially. In this process, NAA platforms were first hydroxylated, silanized, and activated using the above-mentioned silanization protocol. The GTA-activated APTES-functionalized NAA platforms were then ready for the selective immobilization of amino-thiol molecules onto the inner surface of their nanopores, which was carried out under batch condition (i.e., immersion of NAA platforms in amino-thiol solution for 18–20 h). The amino-thiol-functionalized NAA platforms were then coated with a thin layer of gold, and their top surface was selectively functionalized with dithiol molecules under batch conditions for 18–20 h following the protocol used in approach (ii).

2.6. RfFS System and Detection of Gold Ions (Au^{3+}). Details of our RfFS setup have been reported elsewhere.^{20,22} In brief, white light from a tungsten source was directed onto the surface of thiol-functionalized NAA platforms with an illumination spot of 2 mm by a bifurcated optical probe. The collection fiber of the optical probe collected and transferred the reflected light from the illumination spot to a miniature spectrophotometer (USB 4000 + VIS-NIR-ES, Ocean Optics, USA). The optical spectra were obtained in the range 400–1000 nm and saved at intervals of 30 s with an integration time of 20 s, with 20 average measurements. The acquired RfFS spectra were

D

DOI: 10.1021/acsami.7b01116
ACS Appl. Mater. Interfaces XXXX, XXX, XXX–XXX

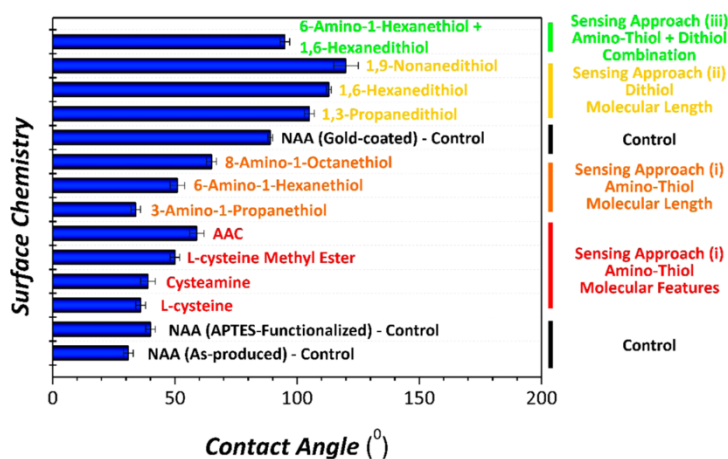


Figure 3. Contact angle characterization for the different surface chemistries assessed in our study.

processed by applying fast Fourier transform using Igor Pro library (Wavemetrics, USA) to estimate the effective optical thickness (OT_{eff}) of the NAA sensing platforms (eq 1):

$$OT_{\text{eff}} = 2n_{\text{eff}}L_p \cos \theta \quad (1)$$

where OT_{eff} is the effective optical thickness of the film, n_{eff} is the effective refractive index of the NAA platform, L_p is its physical thickness, and θ is the angle of incidence of light (i.e., $\theta = 0^\circ$ in this case).

The sensitivity of thiol-functionalized NAA platforms toward gold ions was assessed by RfS through changes in OT_{eff} as a function of the concentration of gold ions. This binding process was monitored in real time using a custom-designed flow cell. A stock solution of Au^{3+} ions (1 mM) was prepared by dissolving $\text{HAuCl}_4 \cdot \text{H}_2\text{O}$ in ultrapure water, and analytical solutions of Au^{3+} with concentrations ranging from 20 to 80 μM with an interval of 20 μM were obtained by dilution of the Au^{3+} stock solution. Thiol-functionalized NAA sensing platforms were packed in a custom-made flow cell based on transparent acrylic plastic and analytical solutions were flowed at a rate of 100 $\mu\text{L min}^{-1}$. This flow rate was maintained throughout the sensing experiments by a peristaltic pump (LongerPump BT100-2J) with an equivalent pumping angular rate of 1.4 rpm. The sensing experiments started with the establishment of stable baseline by flowing ultrapure water. Once a stable baseline was obtained, analytical solutions of Au^{3+} of different concentrations (20, 40, 60, and 80 μM) were introduced into the flow cell. The interaction between Au^{3+} ions present in the analytical solutions and thiol functional groups on the surface of functionalized NAA platforms induced sharp changes (i.e., increment = red-shift) in the OT_{eff} of NAA platforms. After OT_{eff} achieved a stable value, ultrapure water was flowed for 15 min to obtain the total change of OT_{eff} (ΔOT_{eff}) associated with the corresponding concentration of Au^{3+} ions. Note that fresh thiol-functionalized NAA platforms were used to establish the total effective optical thickness change for each analytical concentration of Au^{3+} .

2.7. Structural Characterization of NAA Sensing Platforms. Scanning electron microscopy (SEM) images of NAA sensing platforms were acquired using a field-emission gun scanning electron microscopy (FEG-SEM FEI Quanta 450). These images were used to establish the geometric features of NAA platforms by image analysis using ImageJ (public domain program developed at the RSB of the NIH).³⁶

2.8. Contact Angle Measurement in NAA Sensing Platforms. The contact angle for each NAA sensing platforms was measured by a tensiometer (Attension Theta optical tensiometer). The sensile drop technique was used in these experiments, where a water droplet was formed on the end of a syringe, which was descended until the water

droplet touched the surface of the sample stage, followed by the withdraw of the needle away from the stage. Image analysis was used to establish the contact angle on the surface of NAA platforms containing functional groups.

3. RESULTS AND DISCUSSION

3.1. Structural Characterization of NAA Sensing Platforms. SEM images of the NAA platforms reveal the characteristic geometric features of NAA produced by a two-step anodization approach (Figure 2). Cross-sectional SEM images of these platforms show vertically aligned straight cylindrical nanopores from top to bottom (Figure 2a). Top SEM images reveal that these nanoporous photonic films feature hexagonally arranged nanopores homogeneously distributed across their surface (Figure 2b) with an average pore diameter (d_p) of 66 \pm 6 nm, pore length (L_p) of 6.0 \pm 0.1 μm , and interpore distance (d_{int}) of 105 \pm 4 nm (Figure 2c).

3.2. Contact Angle Measurements of Functionalized NAA Sensing Platforms. The successful functionalization of NAA platforms with thiol-containing functional molecules using approaches (i) and (ii) was validated and analyzed by contact angle measurements (Figure 3). Note that the purpose of contact angle measurements was to establish the effect of the molecular interaction and conformation among the functionalizing molecules on the hydrophobic character of functionalized NAA platforms. As such, these NAA platforms for sensing approach (i) were not coated with a thin layer of gold to mimic the surface chemistry inside the nanopores. Two samples were used as control references for NAA platforms functionalized following approach (i) (i.e., selective functionalization of the inner surface of the nanopores with amino-thiol functional molecules), being the as-produced and APTES-functionalized NAA platforms. The contact angle of these NAA platforms was found to be 31 \pm 2° and 40 \pm 2°, respectively. Whereas as-produced NAA platforms have a hydrophilic character, the functionalization of their inner surface with APTES molecules induces a relatively weak hydrophobic character due to the presence of amine terminal groups ($-\text{NH}_2$) (Figure 3). As for the effect of the molecular features of cysteine-like molecules, Figure 3 shows that the hydrophobic character of the NAA increases in the following order: L-cysteine (36 \pm 2°) < cysteamine (39 \pm 3°) < L-cysteine methyl

E

DOI: 10.1021/acsami.7b01116
ACS Appl. Mater. Interfaces XXXX, XXX, XXX–XXX

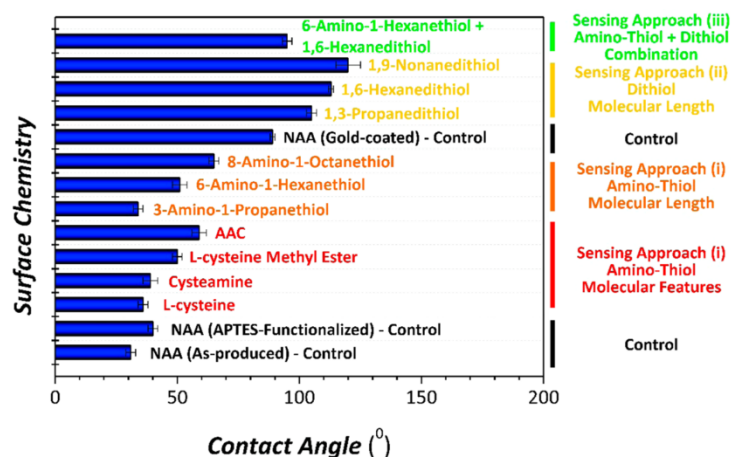


Figure 3. Contact angle characterization for the different surface chemistries assessed in our study.

processed by applying fast Fourier transform using Igor Pro library (Wavemetrics, USA) to estimate the effective optical thickness (OT_{eff}) of the NAA sensing platforms (eq 1):

$$OT_{\text{eff}} = 2n_{\text{eff}}L_p \cos \theta \quad (1)$$

where OT_{eff} is the effective optical thickness of the film, n_{eff} is the effective refractive index of the NAA platform, L_p is its physical thickness, and θ is the angle of incidence of light (i.e., $\theta = 0^\circ$ in this case).

The sensitivity of thiol-functionalized NAA platforms toward gold ions was assessed by RfS through changes in OT_{eff} as a function of the concentration of gold ions. This binding process was monitored in real time using a custom-designed flow cell. A stock solution of Au^{3+} ions (1 mM) was prepared by dissolving $\text{HAuCl}_4 \cdot \text{H}_2\text{O}$ in ultrapure water, and analytical solutions of Au^{3+} with concentrations ranging from 20 to 80 μM with an interval of 20 μM were obtained by dilution of the Au^{3+} stock solution. Thiol-functionalized NAA sensing platforms were packed in a custom-made flow cell based on transparent acrylic plastic and analytical solutions were flowed at a rate of 100 $\mu\text{L min}^{-1}$. This flow rate was maintained throughout the sensing experiments by a peristaltic pump (LongoPump BT100-2J) with an equivalent pumping angular rate of 1.4 rpm. The sensing experiments started with the establishment of stable baseline by flowing ultrapure water. Once a stable baseline was obtained, analytical solutions of Au^{3+} of different concentrations (20, 40, 60, and 80 μM) were introduced into the flow cell. The interaction between Au^{3+} ions present in the analytical solutions and thiol functional groups on the surface of functionalized NAA platforms induced sharp changes (i.e., increment = red-shift) in the OT_{eff} of NAA platforms. After OT_{eff} achieved a stable value, ultrapure water was flowed for 15 min to obtain the total change of OT_{eff} (ΔOT_{eff}) associated with the corresponding concentration of Au^{3+} ions. Note that fresh thiol-functionalized NAA platforms were used to establish the total effective optical thickness change for each analytical concentration of Au^{3+} .

2.7. Structural Characterization of NAA Sensing Platforms. Scanning electron microscopy (SEM) images of NAA sensing platforms were acquired using a field-emission gun scanning electron microscopy (FEG-SEM FEI Quanta 450). These images were used to establish the geometric features of NAA platforms by image analysis using ImageJ (public domain program developed at the RSB of the NIH).³⁶

2.8. Contact Angle Measurement in NAA Sensing Platforms. The contact angle for each NAA sensing platforms was measured by a tensiometer (Attension Theta optical tensiometer). The sessile drop technique was used in these experiments, where a water droplet was formed on the end of a syringe, which was descended until the water

droplet touched the surface of the sample stage, followed by the withdraw of the needle away from the stage. Image analysis was used to establish the contact angle on the surface of NAA platforms containing functional groups.

3. RESULTS AND DISCUSSION

3.1. Structural Characterization of NAA Sensing Platforms. SEM images of the NAA platforms reveal the characteristic geometric features of NAA produced by a two-step anodization approach (Figure 2). Cross-sectional SEM images of these platforms show vertically aligned straight cylindrical nanopores from top to bottom (Figure 2a). Top SEM images reveal that these nanoporous photonic films feature hexagonally arranged nanopores homogeneously distributed across their surface (Figure 2b) with an average pore diameter (d_p) of 66 ± 6 nm, pore length (L_p) of 6.0 ± 0.1 μm , and interpore distance (d_{int}) of 105 ± 4 nm (Figure 2c).

3.2. Contact Angle Measurements of Functionalized NAA Sensing Platforms. The successful functionalization of NAA platforms with thiol-containing functional molecules using approaches (i) and (ii) was validated and analyzed by contact angle measurements (Figure 3). Note that the purpose of contact angle measurements was to establish the effect of the molecular interaction and conformation among the functionalizing molecules on the hydrophobic character of functionalized NAA platforms. As such, these NAA platforms for sensing approach (i) were not coated with a thin layer of gold to mimic the surface chemistry inside the nanopores. Two samples were used as control references for NAA platforms functionalized following approach (i) (i.e., selective functionalization of the inner surface of the nanopores with amino-thiol functional molecules), being the as-produced and APTES-functionalized NAA platforms. The contact angle of these NAA platforms was found to be 31 ± 2° and 40 ± 2°, respectively. Whereas as-produced NAA platforms have a hydrophilic character, the functionalization of their inner surface with APTES molecules induces a relatively weak hydrophobic character due to the presence of amine terminal groups ($-\text{NH}_2$) (Figure 3). As for the effect of the molecular features of cysteine-like molecules, Figure 3 shows that the hydrophobic character of the NAA increases in the following order: L-cysteine (36 ± 2°) < cysteamine (39 ± 3°) < L-cysteine methyl

E

DOI: 10.1021/acsami.7b01116
ACS Appl. Mater. Interfaces XXXX, XXX, XXX–XXX

ester ($50 \pm 2^\circ$) < AAC ($59 \pm 3^\circ$). These results show that the presence of additional functional groups (e.g., carboxyl, ester, methyl, etc.) has a significant impact on the hydrophobic character of these photonic films (Table 1). For instance, AAC is a tripeptide and thus possesses two amide functional groups. As a result, AAC-functionalized NAA platforms have the strongest hydrophobic character among the cysteine-like functional molecules analyzed in our study. This property in turn determines the surface interaction between analyte molecules (i.e., Au^{3+}) in an aqueous matrix and the surface of the sensing platforms. Another important factor which plays a role in the overall hydrophobic character of functionalized NAA platforms is the length of the functional molecules. To discern the effect of this parameter, we analyzed the contact angle in a set of NAA platforms functionalized with amino-thiol molecules (Figure 3 and Table 1). Our results reveal that the hydrophobic character of NAA platforms increases with the length of the amino-thiol functional molecules in the following order: 3-amino-1-propanethiol ($34 \pm 2^\circ$) < 6-amino-1-hexanethiol ($51 \pm 3^\circ$) < 8-amino-1-octanethiol ($65 \pm 2^\circ$) (Figure 3 and Table 1). As such, the longer the amino-thiol backbone, the more hydrophobic the character of the functionalized surface. It is worthwhile noting that thiol groups ($-\text{SH}$) are hydrophobic. Therefore, the conformation of the functional layer immobilized onto the surface of NAA has a direct effect upon the overall hydrophobic character of these films. This result suggests that functional layers of 8-amino-1-octanethiol molecules immobilized onto the inner surface of GTA-activated APTES-functionalized NAA platforms have a more compact assembly as compared to other functional amino-thiol molecules of shorter backbone structure. As such, more thiol functional terminal groups would be exposed across the surface of NAA, increasing the hydrophobic character of NAA platforms functionalized with 8-amino-1-octanethiol.

Finally, we assessed the contact angle of NAA films functionalized with dithiol molecules following approach (ii). In this case, a gold-coated NAA platform was used as a control, the contact angle of which was found to be significantly more hydrophobic (i.e., $89 \pm 1^\circ$) than that of noncoated or amino-thiol-functionalized NAA platforms (Figure 3). The hydrophobic character of these NAA platforms was further increased after selective chemical functionalization with dithiol groups following sensing approach (ii) (Figure 1a). We also analyzed the effect of the length of dithiol molecules on the hydrophobic character of NAA platforms. Our results demonstrate that as per the amino-thiol molecules, longer molecules give a more hydrophobic character to the NAA platform in the following order: 1,3-propanedithiol ($105 \pm 2^\circ$) < 1,6-hexanedithiol ($112 \pm 1^\circ$) < 1,9-nonanedithiol ($119 \pm 5^\circ$). Therefore, this result verifies that longer molecules can provide more compact self-assembled monolayers of dithiol functional groups onto the surface of gold-coated NAA platforms.

3.3. Evaluation of Sensitivity in NAA Sensing Platforms Functionalized with Amino-Thiol Functional Molecules. A range of amino-thiol molecules containing a common cysteine-like backbone structure was used to modify the surface chemistry of NAA platforms and discern the effect of molecular functionalities and backbone length on the sensing performance of NAA interferometric sensors. Prior to immobilization, silanization and activation of amine terminal groups were performed. In this process, NAA platforms were pretreated with hydrogen peroxide for hydroxylation of the inner surface of nanopores (i.e., generation of hydroxyl groups).

Silanization of these NAA platforms was carried out by chemical vapor deposition of APTES molecules to endow as-produced NAA platforms with amine functionality through the silane layer, inside the nanopores.³⁷ The amine functional groups of APTES molecules were then activated by GTA molecules, which provides aldehyde functionality, through the immersion of NAA platforms in GTA solution. The immobilization of amino-thiol molecules on the GTA-activated NAA platforms occurred through the amine binding formed between the aldehyde functionality of GTA molecules and the amine group of amino-thiol molecules.³⁷ A schematic illustration of the immobilization and binding of these molecules onto the inner surface of GTA-activated APTES-functionalized NAA platforms is shown in Figure 1c. Both the inner and top surfaces of the NAA were functionalized with APTES, GTA, and amino-thiol molecules. Note that these amino-thiol-functionalized NAA platforms were coated with a thin layer of gold before they were used as sensing platforms. This layer of gold covered the functional molecules attached onto the top surface of NAA platforms, preventing top surface functional groups from interacting with Au^{3+} ions. Thus, there was no occurrence of binding events on the top surface of NAA platforms, and only amino-thiol molecules functionalized on the inner surface of nanopores were exposed to Au^{3+} ions for binding.

3.3.1. Effect of Molecular Features in Amino-Thiol Functional Molecules. The cysteine-like molecules immobilized onto the inner surface of NAA platforms have similar backbone structure, where they have both amine and thiol groups, but they differ in their functional groups along the molecule (e.g., carboxyl, ester, etc.), as shown in Table 1. These amino-thiol functionalized NAA sensing platforms were combined with RfS and their sensitivity assessed by measuring changes in the effective optical thickness of the film ($\Delta\text{OT}_{\text{eff}}$) in response to the binding of Au^{3+} ions present in analytical solutions of different concentration (20, 40, 60, and 80 μM) using sensing approach (i) (Figure 1a). Figure 4a displays representative graphs showing $\Delta\text{OT}_{\text{eff}}$ as a function of time for NAA platforms functionalized with L-cysteine, cysteamine, L-cysteine methyl ester, and AAC. Note that a stable baseline was first obtained in ultrapure water before injection of the analyte solution containing Au^{3+} ions. An increase in OT_{eff} was observed as the Au^{3+} solution was flowed through the system, which indicates the binding between Au^{3+} ions and thiol functional groups immobilized onto the inner surface of these NAA platforms. This observation is true for all cases (i.e., L-cysteine, cysteamine, and AAC) except for L-cysteine methyl ester, where there was a decrease in OT_{eff} at the initial stage of the flowing of Au^{3+} solution. The decrease in OT_{eff} observed might be due to conformational changes upon the interaction between Au^{3+} and L-cysteine methyl ester. Ultrapure water was flowed again through the system for 15 min once the binding between gold ions and thiol groups reached the equilibrium, which was characterized by a plateau in the spectra. In this process, $\Delta\text{OT}_{\text{eff}}$ was found to decrease slightly due to the removal of physisorbed gold ions, which is in good agreement with previous studies using a similar sensing approach.²² The correlation between $\Delta\text{OT}_{\text{eff}}$ and the concentration of Au^{3+} for cysteine-like molecules with different molecular features is shown in Figure 4b. This analysis reveals a linear dependence of $\Delta\text{OT}_{\text{eff}}$ with $[\text{Au}^{3+}]$ for all the cysteine-like molecules within the range of concentrations studied. As the concentration of gold ions in the analytical solution increases, more Au^{3+} ions

F

DOI: 10.1021/acsami.7b01116
ACS Appl. Mater. Interfaces XXXX, XXX, XXX–XXX

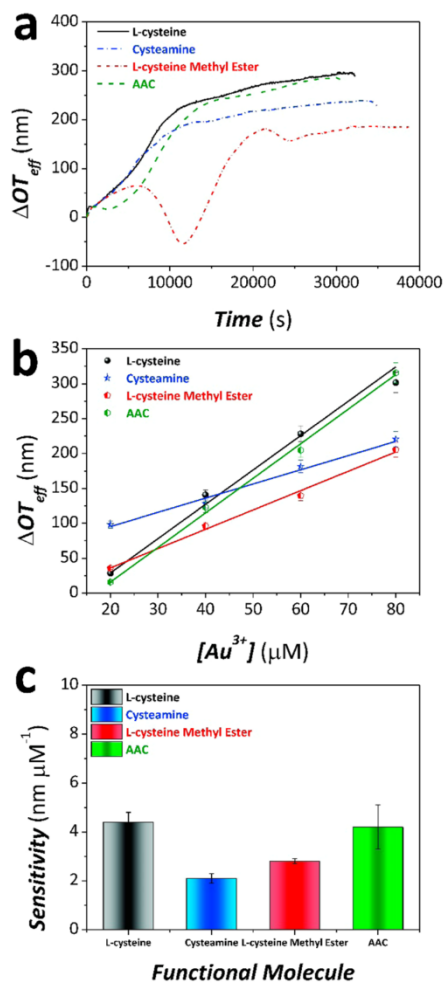


Figure 4. Assessment of optical sensitivity for amino-thiol functional molecules with different molecular features in NAA sensing platforms through the detection of different concentrations of gold ions using sensing approach (i). (a) Representative graph showing the effective optical thickness change in NAA sensing platforms functionalized with L-cysteine, cysteamine, L-cysteine methyl ester, and AAC for a concentration 80 μM of Au^{3+} measured in real time by RIFS. (b) Linear fitting lines for NAA sensing platforms modified with L-cysteine, cysteamine, L-cysteine methyl ester, and AAC used to establish the linear correlation between $\Delta\text{OT}_{\text{eff}}$ and $[\text{Au}^{3+}]$ for the range of concentrations 20, 40, 60, and 80 μM . (c) Bar chart summarizing the sensitivities (i.e., slope of linear fittings shown in (b)) for NAA sensing platforms modified with L-cysteine, cysteamine, L-cysteine methyl ester, and AAC.

are available to be bound by thiol functional groups present in the inner surface of NAA platforms, which in turn is translated into greater changes in the effective optical thickness. The slope of these linear fittings corresponds to the sensitivity of the system, expressed in terms of effective optical thickness change per concentration unit (i.e., $\text{nm } \mu\text{M}^{-1}$) (Figure 4c). Our results indicate that L-cysteine and AAC provide approximately the same level of sensitivity to Au^{3+} ions (4.4 \pm 0.4 and 4.2 \pm 0.6 $\text{nm } \mu\text{M}^{-1}$, respectively), whereas NAA platforms functionalized

with L-cysteine methyl ester and cysteamine show the least sensitivity (i.e., 2.8 \pm 0.1 and 2.1 \pm 0.2 $\text{nm } \mu\text{M}^{-1}$, respectively). Unlike the other amino-thiol molecules, the only site for cysteamine molecules to interact with Au^{3+} ions is via the thiol terminal group. Thus, the amount of gold ions immobilized onto the inner surface of NAA platforms is approximately equivalent to the number of cysteamine molecules available inside the surface of NAA nanopores. As a result, the low sensitivity achieved by cysteamine-functionalized NAA platforms when detecting gold ions (2.1 \pm 0.2 $\text{nm } \mu\text{M}^{-1}$) could be associated with the lack of other functionalities along its backbone structure, which might provide further sites for binding interactions. Although L-cysteine methyl ester possesses a terminal-ester functional group, the presence of this additional functional group compared to L-cysteine only slightly improves the sensitivity of the NAA platforms toward Au^{3+} ions (2.8 \pm 0.1 $\text{nm } \mu\text{M}^{-1}$), as revealed by the results shown in Figure 4c. In contrast to cysteamine and L-cysteine methyl ester, the carboxylic acid groups of L-cysteine and AAC might be able to interact with gold ions through van der Waals forces, increasing the occurrence of gold ion capturing events inside the nanopores and thus enhancing the overall sensitivity of the system as a result (i.e., 4.4 \pm 0.4 and 4.2 \pm 0.6 $\text{nm } \mu\text{M}^{-1}$, respectively). Carboxylic acid is known as one of the common building blocks for the formation of molecular self-assembled layers on metal surfaces through chemisorption.³⁸ Therefore, we suggest that L-cysteine and AAC molecules immobilized onto the inner surface of NAA nanopores could also bind to areas that are free of APTES linkage molecules through the direct chemisorption of carboxylic acid on APTES-free aluminum oxide.³⁹ This would result in an increment in the number of thiol-terminated molecules present on the inner surface of NAA nanopores, which in turn would be translated into a significant enhancement of the sensitivity of the NAA platforms toward Au^{3+} ions. As mentioned before, the size and the refractive index of the functional molecules immobilized onto the inner surface of NAA platforms could also have an impact on the overall sensitivity of the system.²⁵ It can be observed that whereas cysteamine has the smallest chemical structure among the functional molecules analyzed in this section of our study, the functional molecule AAC has the biggest molecular size, which could contribute to a more sensitive system due to the bigger magnitude of the $\Delta\text{OT}_{\text{eff}}$ in NAA platforms when interacting with Au^{3+} ions.

3.3.2. Effect of Molecular Length in Amino-Thiol Functional Molecules. NAA sensing platforms were functionalized with amino-thiol molecules featuring different backbone lengths by APTES silanization and subsequent immobilization by GTA activation and functionalization of amino-thiol molecules. These NAA platforms were then gold coated before being used as sensing platforms. The amino-thiol molecules used in our study to assess the effect of the molecular length by sensing approach (i) were 3-amino-1-propanethiol, 6-amino-1-hexanethiol, and 8-amino-1-octanethiol. As depicted in Table 1, these molecules possess a terminal amine group ($-\text{NH}_2$), which is responsible for attachment to the GTA-activated APTES molecules immobilized onto the inner surface of NAA nanopores. Additionally, a terminal thiol group ($-\text{SH}$) is responsible for Au^{3+} ions capture, and the sole variation between these amino-thiol molecules is the length of the carbon chain between the terminal functional groups. Assessment of the sensitivity of these amino-thiol-functionalized NAA platforms was carried out using the protocol outlined

G

DOI: 10.1021/acsami.7b01116
ACS Appl. Mater. Interfaces XXXX, XXX, XXX–XXX

previously based on sensing approach (i) (Figure 1a). Figure 5a shows an example of real-time sensing in these NAA-

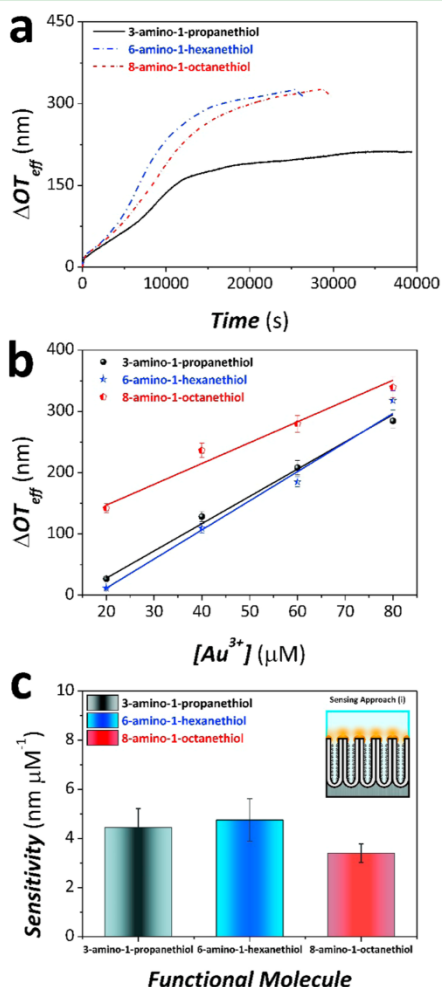


Figure 5. Assessment of optical sensitivity for amino-thiol functional molecules with different molecular lengths in NAA sensing platforms through the detection of different concentrations of gold ions using sensing approach (i). (a) Representative graph showing the effective optical thickness change in NAA sensing platforms functionalized with 3-amino-1-propanethiol, 6-amino-1-hexanethiol, and 8-amino-1-octanethiol for a concentration 80 μM of Au^{3+} measured in real time by RIFS. (b) Linear fitting lines for NAA sensing platforms modified with 3-amino-1-propanethiol, 6-amino-1-hexanethiol, and 8-amino-1-octanethiol used to establish the linear correlation between ΔOT_{eff} and $[\text{Au}^{3+}]$ for the range of concentrations 20, 40, 60, and 80 μM . (c) Bar chart summarizing the sensitivities (i.e., slope of linear fittings shown in (b)) for NAA sensing platforms modified with 3-amino-1-propanethiol, 6-amino-1-hexanethiol, and 8-amino-1-octanethiol.

functionalized platforms, while Figure 5b depicts the correlation between Au^{3+} ions concentration and ΔOT_{eff} establishing the linear dependency of ΔOT_{eff} for amino-thiol-functionalized NAA platforms with $[\text{Au}^{3+}]$. It is apparent that the higher the concentration of gold ions in the analyte solution, the more Au^{3+} ions available to interact with amino-thiol molecules

immobilized onto the inner surface of NAA nanopores. As such, ΔOT_{eff} increases with the concentration of gold ions, linearly, within the range of analyte concentrations used in our study. The sensitivity provided by these amino-thiol molecules of different molecule length was estimated by the slope of the fitting lines for the respective amino-thiol molecules shown in Figure 5b. An overview of the sensitivity of these amino-thiol molecules is presented in the bar chart of Figure 5c. Our analysis reveals that NAA platforms functionalized with 6-amino-1-hexanethiol have the greatest sensitivity (4.8 \pm 0.9 nm μM^{-1}) followed by 3-amino-1-propanethiol (4.4 \pm 0.8 nm μM^{-1}). Interestingly, 8-amino-1-octanethiol-functionalized NAA platforms showed the least sensitivity toward Au^{3+} ions (3.4 \pm 0.4 nm μM^{-1}). Previous studies indicated that functional molecules of bigger molecular size immobilized onto the inner surface of nanoporous materials can provide more significant changes in the effective optical thickness of the sensing platforms, resulting in a higher sensitivity toward targeted analytes.^{26,27} Nevertheless, we found this to be partly true for NAA platforms functionalized with 3-amino-1-propanethiol and 6-amino-1-hexanethiol, where the latter (i.e., 6C) is slightly more sensitive toward Au^{3+} ions as compared to the former (i.e., 3C). However, 8-amino-1-octanethiol was the least sensitive molecule, despite being the longest (i.e., 8C) of those investigated. This might be due to the molecular orientation and conformation of 8-amino-1-octanethiol immobilized onto the inner surface of NAA nanopores. The longer carbon chain length of 8-amino-1-octanethiol might lead to molecules becoming folded or crumpled up inside the nanopores, shielding the thiol functional groups from interacting with Au^{3+} ions. In contrast, the shorter lengths of 3-amino-1-propanethiol and 6-amino-1-hexanethiol molecules could facilitate the orientation and alignment in such a way that the amount of sensing molecules and available thiol functional groups inside the nanopores is higher than that of 8-amino-1-octanethiol molecules. Based on these observations, we postulate that there is an optimal size in terms of overall sensitivity of the system for the functionalizing molecules to be immobilized onto the inner surface of NAA nanopores.

3.4. Evaluation of Sensitivity of NAA Sensing Platforms Functionalized with Dithiols of Different Molecular Sizes toward Au^{3+} Ions. Sensing approach (ii) corresponds to a localized surface plasmon resonance (LSPR) sensing configuration (Figure 1b). It is known that a LSPR approach in NAA sensing platforms can provide high sensitivity and low limit of detection performances due to the disturbance and interaction between the electromagnetic field generated around nanometric metallic structures and analyte molecules.^{40,41} In our study, NAA sensing platforms were coated with a thin layer of gold before functionalization with dithiol molecules of different molecular length (i.e., carbon chain). The dithiol molecules used in this study feature different backbone lengths, 1,3-propanedithiol (3C), 1,6-hexanedithiol (6C), and 1,9-nonanedithiol (9C). The chemical structures of the dithiol molecules possess a terminal thiol group at each end of the molecule as shown in Table 1. Unlike the previous sensing approach where the amino-thiol molecules were selectively immobilized inside the NAA nanopores, these dithiol molecules were selectively attached on the top surface of gold-coated NAA nanopore through the well-known affinity interaction between gold on the surface of NAA and one of the thiol groups of the dithiol molecules. The other thiol group remains free to detect Au^{3+} ions during the flow of analyte solutions.

H

DOI: 10.1021/acsami.7b01116
ACS Appl. Mater. Interfaces XXXX, XXX, XXX–XXX

The attachment of dithiol molecules on the gold-coated surface of NAA is illustrated in Figure 1b. An example of real-time sensing and the resulting linear correlation between the concentration of Au^{3+} ions and $\Delta\text{OT}_{\text{eff}}$ for each dithiol molecule is presented in Figure 6a,b. These results indicate that $\Delta\text{OT}_{\text{eff}}$ increases linearly with the concentration of gold ions present in the analyte solutions. As the concentration of Au^{3+} increases, there are more gold ions available to be

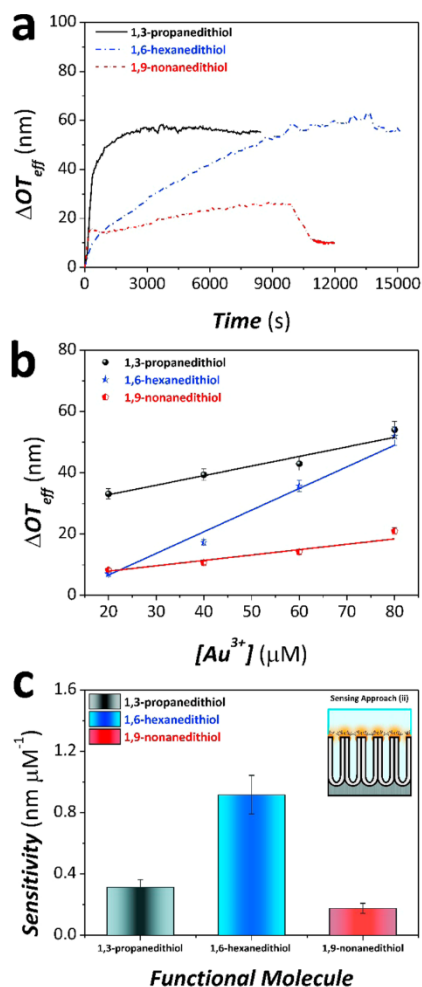


Figure 6. Assessment of optical sensitivity for dithiol functional molecules with different molecular lengths in NAA sensing platforms through the detection of different concentrations of gold ions using sensing approach (ii). (a) Representative graph showing the effective optical thickness change in NAA sensing platforms functionalized with 1,3-propanedithiol, 1,6-hexanedithiol, and 1,9-nonanedithiol for a concentration $80 \mu\text{M}$ of Au^{3+} measured in real time by RfS. (b) Linear fitting lines for NAA sensing platforms modified with 1,3-propanedithiol, 1,6-hexanedithiol, and 1,9-nonanedithiol used to establish the linear correlation between $\Delta\text{OT}_{\text{eff}}$ and $[\text{Au}^{3+}]$ for the range of concentrations 20, 40, 60, and $80 \mu\text{M}$. (c) Bar chart summarizing the sensitivities (i.e., slope of linear fittings shown in (b)) for NAA sensing platforms modified with 1,3-propanedithiol, 1,6-hexanedithiol, and 1,9-nonanedithiol.

captured by dithiol molecules attached on the surface of NAA. As a result, the occurrence of gold–thiol binding events on the gold-coated surface of NAA increases, producing a greater $\Delta\text{OT}_{\text{eff}}$ of the film. Figure 6b shows the linear fittings corresponding to the different NAA sensing platforms functionalized with the dithiol molecules used in our study. These fittings were used to assess the sensitivity of these dithiol molecules toward gold ions using sensing approach (ii). As indicated by the bar chart in Figure 6c, NAA platforms functionalized with 1,6-hexanedithiol are the most sensitive platforms toward Au^{3+} ions, with a sensitivity of $0.9 \pm 0.1 \text{ nm } \mu\text{M}^{-1}$, whereas 1,3-propanedithiol and 1,9-nonanedithiol have significantly poorer sensitivity of 0.3 ± 0.1 and $0.2 \pm 0.1 \text{ nm } \mu\text{M}^{-1}$, respectively. In the LSPR approach used in our study, the gold–thiol binding events taking place on the gold-coated surface of NAA platforms induce a change in the local refractive index environment, which is measured through changes in effective optical thickness of the film by RfS. It is worth noting that the electromagnetic fields near the metal surface are greatly enhanced; however, the electromagnetic strength decreases rapidly with the distance from the metallic structure (Figure 1b). Therefore, it is expected that the sensitivity of NAA sensing platforms using sensing approach (ii) will increase if they are functionalized with dithiol molecules of smaller molecular size. Duyn and co-workers demonstrated the reduction of LSPR sensitivity with distance from the surface of metallic structures using self-assembled monolayers of increasing length.^{42–44} Dithiols of shorter chain length present the thiol terminal group inside the strongest part of the electromagnetic field generated on the gold-coated surface of NAA (Figure 1b). Therefore, gold–thiol binding events occurring within that part of the localized electromagnetic field can significantly change the overall effective optical thickness of the platform. NAA platforms functionalized with 1,9-nonanedithiol exhibit low sensitivity, and this might be due to the fact that the thiol group responsible for the interaction with Au^{3+} ions is located far from the active zone of the local electromagnetic field, where its strength is poor. Thus, changes in the local refractive index environment due to gold–thiol interaction are not optimal to be translated into changes in the effective optical thickness of the film, as indicated by the low sensitivity achieved in these NAA platforms. In contrast, NAA platforms functionalized with 1,6-hexanedithiol exhibited the highest sensitivity, indicating that the binding between thiol and Au^{3+} ions occurs at a distance where the electromagnetic field presents the highest strength. NAA platforms functionalized with 1,3-propanedithiol had a low sensitivity probably due to the decay in the strength of the electromagnetic field.

It is noteworthy that sensitivities of NAA sensing platforms modified with dithiol molecules using sensing approach (ii) were significantly lower than that of amino-thiol molecules using sensing approach (i). Our results also indicate that the required time for the binding of Au^{3+} ions to dithiol molecules immobilized on the gold-coated surface of NAA platforms to reach equilibrium was shorter than that of amino-thiol molecules selectively immobilized inside the nanopores. This might be associated with the presence of more thiol functional groups on the surface of NAA platforms. The top surface area used in sensing approach (ii) with dithiol molecules is much smaller than that of the inner surface of NAA nanopores used in sensing approach (i) for the immobilization of amino-thiol molecules. As a result, less gold–thiol binding events occur on the gold-coated dithiol-functionalized surface of NAA plat-

I

DOI: 10.1021/acsami.7b01116
ACS Appl. Mater. Interfaces XXXX, XXX, XXX–XXX

forms, and thus changes in the effective optical thickness of these NAA platforms are smaller, resulting in lower sensitivities.

3.5. Evaluation of Sensitivity of NAA Sensing Platforms with Dual Functionalization. We performed a pioneering set of experiments in order to discern whether the implementation of sensing approaches (i) and (ii) into the same NAA platform results in an additive enhancement of the overall sensitivity of the system. To this end, NAA sensing platforms were functionalized on both the inner surface of NAA nanopores as well as the gold-coated surface of NAA platforms (sensing approach (iii) as illustrated in Figure 1a) using the most sensitive molecules identified from sensing approaches (i) and (ii). 6-Amino-1-hexanethiol (inner surface) and 1,6-hexanedithiol (top surface), with individual sensitivities of 4.8

0.9 and 0.9 $0.1 \text{ nm } \mu\text{M}^{-1}$, respectively, were used as sensing molecules for sensing approach (iii). Following hydroxylation and silanization, NAA sensing platforms were functionalized with 6-amino-1-hexanethiol. The amino-thiol modified NAA platforms were then coated with gold before selective functionalization of their top surface with 1,6-hexanedithiol molecules. The dual-functionalized NAA platforms were then used in the detection of gold ions by RfS. The obtained results presented in Figure 7a,b show that $\Delta\text{OT}_{\text{eff}}$ increases with increasing Au^{3+} in the analyte solution, following a linear relationship between these two parameters. Note that the binding of Au^{3+} to the dual-functionalized NAA platforms took a longer time to reach the equilibrium, which might be due to the presence of functionalizing molecules on the top surface of NAA and their interaction with Au^{3+} might act as a hindrance barrier to the flow of Au^{3+} into the nanopores, delaying the occurrence of Au^{3+} –amino-thiol interaction inside the nanopores, thus taking longer time to reach the equilibrium. The sensitivity of NAA platforms using sensing approach (iii) was found to be $5.6 \pm 1.0 \text{ nm } \mu\text{M}^{-1}$. Significantly, the combined functionalization of both the inner and top surfaces of NAA platforms provides an almost additive enhancement of the sensitivity compared to that of NAA platforms functionalized with either 6-amino-1-hexanethiol or 1,6-hexanedithiol alone, using sensing approaches (i) and (ii) individually. The sensitivities of these three NAA platforms are compared in Figure 7c. These results indicate that the sensitivity enhancement is approximately additive due to the combined effect of amino-thiol and dithiol molecules selectively immobilized onto NAA platforms. Functionalization of both the inner and top surfaces of NAA nanopores results in more thiol functional groups on the surface of NAA platforms, which are then exposed to gold ions present in the analyte solution. As a result, greater changes in the effective optical thickness of these NAA platforms occur, increasing the overall sensitivity of the system. These results demonstrate that the sensitivity of NAA sensing platforms can be improved by a rational engineering of the surface chemistry. In our case, we found that this rational engineering can make it possible to achieve a 6-fold greater sensitivity than that obtained in previous studies.²¹

4. CONCLUSIONS

We have demonstrated for the first time a rationale toward enhancing sensitivity in thiol-modified NAA sensing platforms by surface chemistry engineering. The surface chemistries of NAA sensing platforms were selectively modified using thiol-containing molecules (i.e., amino-thiol and dithiol molecules) with a range of molecular features and backbone sizes and using

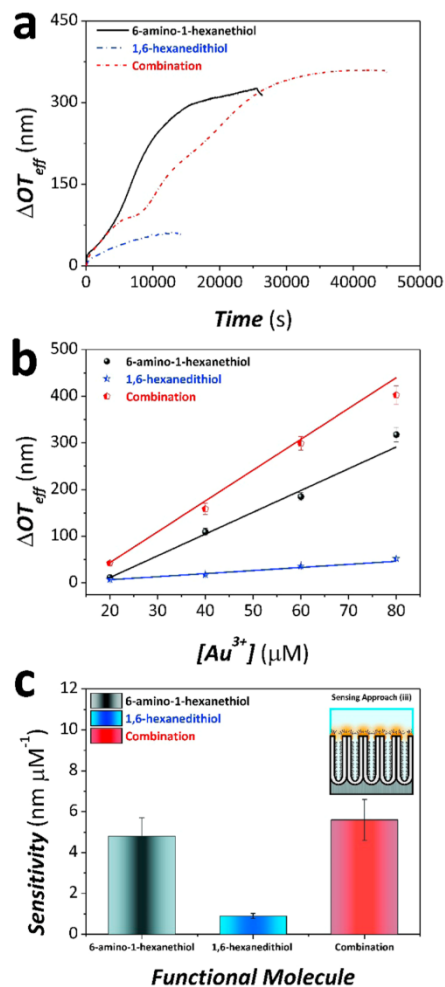


Figure 7. Assessment of optical sensitivity for combined functional molecules in NAA sensing platforms through the detection of different concentrations of gold ions using sensing approach (iii). (a) Representative graph showing the effective optical thickness change in NAA sensing platforms functionalized with 6-amino-1-hexanethiol, 1,6-hexanedithiol, and the combination of both for a concentration $80 \mu\text{M}$ of Au^{3+} measured in real time by RfS. (b) Linear fitting lines for NAA sensing platforms modified with 6-amino-1-hexanethiol, 1,6-hexanedithiol, and the combination of both used to establish the linear correlation between $\Delta\text{OT}_{\text{eff}}$ and $[\text{Au}^{3+}]$ for the range of concentrations 20, 40, 60, and $80 \mu\text{M}$. (c) Bar chart summarizing the sensitivities (i.e., slope of linear fittings shown in (b)) for NAA sensing platforms modified with 6-amino-1-hexanethiol, 1,6-hexanedithiol, and the combination of both.

two different sensing approaches. A series of experiments based on the detection of gold ions were carried out to assess the effect of these functional molecules and the sensing approach on the sensitivity of the system. Changes in the effective optical thickness of these NAA platforms were used as the sensing parameter for the establishment of the overall sensitivity of the system. Our experiments revealed that 6-amino-1-hexanethiol molecules provide the best sensing performance of the amino-thiol modified NAA platforms using sensing approach (i), with

J

DOI: 10.1021/acsami.7b01116
ACS Appl. Mater. Interfaces XXXX, XXX, XXX–XXX

a sensitivity of $4.8 \pm 0.9 \text{ nm } \mu\text{M}^{-1}$. NAA sensing platforms modified with 1,6-hexanedithiol were the most sensitive platform ($0.9 \pm 0.1 \text{ nm } \mu\text{M}^{-1}$) for dithiol-functionalized NAA platforms using approach (ii). To further enhance the overall sensitivity of the system, NAA sensing platforms were modified using a dual functionalization approach with 6-amino-1-hexanethiol and 1,6-hexanedithiol, as these two molecules offered the best individual sensitivities as compared to other amino-thiol and dithiol molecules. Our results indicated that the sensing performance of the resulting NAA platforms has an additive enhancement of sensitivity ($5.6 \pm 1.0 \text{ nm } \mu\text{M}^{-1}$) as a result of the combined Au^{3+} ion binding capacity of 6-amino-1-hexanethiol (inner surface) and 1,6-hexanedithiol (top surface).

We have established that the performance of a sensor is dependent on the molecular makeup and backbone length of the functional molecule employed as well as the sensing approach utilized. The sensitivity of a sensing system can be enhanced through a rational engineering of the surface chemistry on the sensing platform, where these interferometric sensing platforms can be functionalized with analyte-specific molecules that respond to the same targeted analytes but may differ in their backbone structures or molecular sizes. Different functional groups or molecular sizes can endow a sensing platform with more sensitivity. In conclusion, our study provides a better understanding and deeper insight into potential optimization pathways through surface chemistry engineering and opens up new opportunities for the development of ultrasensitive sensors, with potential applicability in a broad range of fields and disciplines.

■ ASSOCIATED CONTENT

Supporting Information

The Supporting Information is available free of charge on the ACS Publications website at DOI: 10.1021/acsami.7b01116.

Synthesis process used to produce the cysteine-like compound AAC (PDF)

■ AUTHOR INFORMATION

Corresponding Authors

*(A.D.A.) Phone + 61 8 8313 5652; e-mail Andrew.abell@adelaide.edu.au.

*(A.S.) Phone +61 8 8313 1535; e-mail abel.santos@adelaide.edu.au.

ORCID

Dusan Losic: 0000-0002-1930-072X

Andrew D. Abell: 0000-0002-0604-2629

Abel Santos: 0000-0002-5081-5684

Notes

The authors declare no competing financial interest.

■ ACKNOWLEDGMENTS

Authors thank the support provided by the Australian Research Council (ARC) through the grants DE140100549, CE140100003, DP120101680, and FT110100711 and the School of Chemical Engineering (UoA). Authors thank the Adelaide Microscopy (AM) Centre for FEG-SEM characterization.

■ REFERENCES

- (1) Fan, X.; White, I. M.; Shopova, S. I.; Zhu, H.; Suter, J. D.; Sun, Y. Sensitive Optical Biosensors for Unlabeled Targets: A review. *Anal. Chim. Acta* **2008**, *620*, 8–26.
- (2) Jeffrey, W. C.; Daniel, M. R. Label-Free Biosensors for Biomedical Applications. In *Optical, Acoustic, Magnetic, and Mechanical Sensor Technologies*; CRC Press: 2012; pp 45–78.
- (3) Gauglitz, G.; Moore, D. S. *Handbook of Spectroscopy*; John Wiley & Sons, Inc.: Weinheim, 2010.
- (4) McDonagh, C.; Burke, C. S.; MacCraith, B. D. Optical Chemical Sensors. *Chem. Rev.* **2008**, *108*, 400–422.
- (5) Borisov, S. M.; Wolfbeis, O. S. Optical Biosensors. *Chem. Rev.* **2008**, *108*, 423–461.
- (6) Eggins, B. R. *Chemical Sensors and Biosensors*; John Wiley & Sons: West Sussex, 2008; Vol. 28.
- (7) Santos, A.; Kumeria, T.; Losic, D. Nanoporous Anodic Alumina: A Versatile Platform for Optical Biosensors. *Materials* **2014**, *7*, 4297–4320.
- (8) Belge, G.; Beyerlein, D.; Betsch, C.; Eichhorn, K.-J.; Gauglitz, G.; Grundke, K.; Voit, B. Suitability of Hyperbranched Polyester for Sensoric Applications—Investigation with Reflectometric Interference Spectroscopy. *Anal. Bioanal. Chem.* **2002**, *374*, 403–411.
- (9) Birkert, O.; Tünnemann, R.; Jung, G.; Gauglitz, G. Label-Free Parallel Screening of Combinatorial Triazine Libraries using Reflectometric Interference Spectroscopy. *Anal. Chem.* **2002**, *74*, 834–840.
- (10) Gauglitz, G.; Brecht, A.; Kraus, G.; Mahm, W. Chemical and Biochemical Sensors Based on Interferometry at Thin (Multi-) Layers. *Sens. Actuators, B* **1993**, *11*, 21–27.
- (11) Schmitt, H.-M.; Brecht, A.; Piehler, J.; Gauglitz, G. An Integrated System for Optical Biomolecular Interaction Analysis. *Biosens. Bioelectron.* **1997**, *12*, 809–816.
- (12) Lin, V. S.-Y.; Motesharei, K.; Dancil, K.-P. S.; Sailor, M. J.; Ghadiri, M. R. A Porous Silicon-Based Optical Interferometric Biosensor. *Science* **1997**, *278*, 840–843.
- (13) Dancil, K.-P. S.; Greiner, D. P.; Sailor, M. J. A Porous Silicon Optical Biosensor: Detection of Reversible Binding of IgG to a Protein A-Modified Surface. *J. Am. Chem. Soc.* **1999**, *121*, 7925–7930.
- (14) Janshoff, A.; Dancil, K.-P. S.; Steinem, C.; Greiner, D. P.; Lin, V. S.-Y.; Gurtner, C.; Motesharei, K.; Sailor, M. J.; Ghadiri, M. R. Macroporous p-Type Silicon Fabry-Perot Layers. Fabrication, Characterization, and Applications in Biosensing. *J. Am. Chem. Soc.* **1998**, *120*, 12108–12116.
- (15) Schwartz, M. P.; Alvarez, S. D.; Sailor, M. J. Porous SiO_2 Interferometric Biosensor for Quantitative Determination of Protein Interactions: Binding of Protein A to Immunoglobulins Derived from Different Species. *Anal. Chem.* **2007**, *79*, 327–334.
- (16) Santos, A.; Balderrama, V. S.; Alba, M.; Formentín, P.; Ferré-Borrull, J.; Pallarès, J.; Marsal, L. F. Nanoporous Anodic Alumina Barcodes: Toward Smart Optical Biosensors. *Adv. Mater.* **2012**, *24*, 1050–1054.
- (17) Salonen, J.; Laine, E.; Niinisto, L. Thermal Carbonization of Porous Silicon Surface by Acetylene. *J. Appl. Phys.* **2002**, *91*, 456–461.
- (18) Chen, Y.; Santos, A.; Wang, Y.; Kumeria, T.; Wang, C.; Li, J.; Losic, D. Interferometric Nanoporous Anodic Alumina Photonic Coatings for Optical Sensing. *Nanoscale* **2015**, *7*, 7770–7779.
- (19) Pan, S.; Rothberg, L. J. Interferometric Sensing of Biomolecular Binding using Nanoporous Aluminum Oxide Templates. *Nano Lett.* **2003**, *3*, 811–814.
- (20) Alvarez, S. D.; Li, C.-P.; Chiang, C. E.; Schuller, I. K.; Sailor, M. J. A Label-Free Porous Alumina Interferometric Immunosensor. *ACS Nano* **2009**, *3*, 3301–3307.
- (21) Kumeria, T.; Santos, A.; Losic, D. Ultrasensitive Nanoporous Interferometric Sensor for Label-Free Detection of Gold (III) Ions. *ACS Appl. Mater. Interfaces* **2013**, *5*, 11783–11790.
- (22) Dronov, R.; Jane, A.; Shapter, J. G.; Hodges, A.; Voelcker, N. H. Nanoporous Alumina-Based Interferometric Transducers Ennobled. *Nanoscale* **2011**, *3*, 3109–3114.

K

DOI: 10.1021/acsami.7b01116
ACS Appl. Mater. Interfaces XXXX, XXX, XXX–XXX

- (23) Nemati, M.; Santos, A.; Kumeria, T.; Losic, D. Label-Free Real-Time Quantification of Enzyme Levels by Interferometric Spectroscopy Combined with Gelatin-Modified Nanoporous Anodic Alumina Photonic Films. *Anal. Chem.* **2015**, *87*, 9016–9024.
- (24) Law, C. S.; Santos, A.; Nemati, M.; Losic, D. Rational Engineering of Nanoporous Anodic Alumina Photonic Crystals by Sawtooth-Like Pulse Anodization. *ACS Appl. Mater. Interfaces* **2016**, *8*, 13542–13554.
- (25) Santos, A.; Kumeria, T.; Losic, D. Optically Optimized Photoluminescent and Interferometric Biosensors Based on Nanoporous Anodic Alumina: A Comparison. *Anal. Chem.* **2013**, *85*, 7904–7911.
- (26) Pacholski, C.; Sartor, M.; Sailor, M. J.; Cunin, F.; Miskelly, G. M. Biosensing Using Porous Silicon Double-Layer Interferometers: Reflective Interferometric Fourier Transform Spectroscopy. *J. Am. Chem. Soc.* **2005**, *127*, 11636–11645.
- (27) Pacholski, C.; Yu, C.; Miskelly, G. M.; Godin, D.; Sailor, M. J. Reflective Interferometric Fourier Transform Spectroscopy: A Self-Compensating Label-Free Immunosensor Using Double-Layers of Porous SiO₂. *J. Am. Chem. Soc.* **2006**, *128*, 4250–4252.
- (28) Masuda, H.; Fukuda, K. Ordered Metal Nanohole Arrays Made by a Two-Step Replication of Honeycomb Structures of Anodic Alumina. *Science* **1995**, *268*, 1466–1468.
- (29) Masuda, H.; Yada, K.; Osaka, A. Self-Ordering of Cell Configuration of Anodic Porous Alumina with Large-Size Pores in Phosphoric Acid Solution. *Jpn. J. Appl. Phys.* **1998**, *37*, L1340–L1342.
- (30) Masuda, H.; Hasegawa, F.; Ono, S. Self-Ordering of Cell Arrangement of Anodic Porous Alumina Formed in Sulfuric Acid Solution. *J. Electrochem. Soc.* **1997**, *144*, L127–L130.
- (31) Nielsch, K.; Choi, J.; Schwirn, K.; Wehrspohn, R. B.; Gösele, U. Self-Ordering Regimes of Porous Alumina: The 10 Porosity Rule. *Nano Lett.* **2002**, *2*, 677–680.
- (32) Santos, A.; Macias, G.; Ferré-Borrull, J.; Pallarès, J.; Marsal, L. F. Photoluminescent Enzymatic Sensor Based on Nanoporous Anodic Alumina. *ACS Appl. Mater. Interfaces* **2012**, *4*, 3584–3588.
- (33) DeLouise, L. A.; Miller, B. L. Enzyme Immobilization in Porous Silicon: Quantitative Analysis of The Kinetic Parameters for Glutathione-S-Transferases. *Anal. Chem.* **2005**, *77*, 1950–1956.
- (34) DeLouise, L. A.; Kou, P. M.; Miller, B. L. Cross-Correlation of Optical Microcavity Biosensor Response with Immobilized Enzyme Activity. Insights into Biosensor Sensitivity. *Anal. Chem.* **2005**, *77*, 3222–3230.
- (35) Jani, A. M. M.; Kempson, I. M.; Losic, D.; Voelcker, N. H. Dressing in Layers: Layering Surface Functionalities in Nanoporous Aluminum Oxide Membranes. *Angew. Chem., Int. Ed.* **2010**, *49*, 7933–7937.
- (36) Abràmoff, M. D.; Magalhães, P. J.; Ram, S. J. Image Processing with ImageJ. *Biophotonics Int.* **2004**, *11*, 36–42.
- (37) Gunda, N. S. K.; Singh, M.; Norman, L.; Kaur, K.; Mitra, S. K. Optimization and Characterization of Biomolecule Immobilization on Silicon Substrates using (3-aminopropyl) triethoxysilane (APTES) and Glutaraldehyde Linker. *Appl. Surf. Sci.* **2014**, *305*, 522–530.
- (38) Jadhav, S. A. Self-Assembled Monolayers (SAMs) of Carboxylic Acids: An Overview. *Cent. Eur. J. Chem.* **2011**, *9*, 369–378.
- (39) Bandyopadhyay, K.; Patil, V.; Vijayamohan, K.; Sastry, M. Adsorption of Silver Colloidal Particles through Covalent Linkage to Self-Assembled Monolayers. *Langmuir* **1997**, *13*, 5244–5248.
- (40) Santos, A.; Kumeria, T.; Losic, D. Nanoporous Anodic Aluminum Oxide for Chemical Sensing and Biosensors. *TrAC, Trends Anal. Chem.* **2013**, *44*, 25–38.
- (41) Anker, J. N.; Hall, W. P.; Lyandres, O.; Shah, N. C.; Zhao, J.; Van Duyne, R. P. Biosensing with Plasmonic Nanosensors. *Nat. Mater.* **2008**, *7*, 442–453.
- (42) Mayer, K. M.; Hafner, J. H. Localized Surface Plasmon Resonance Sensors. *Chem. Rev.* **2011**, *111*, 3828–3857.
- (43) Malinsky, M. D.; Kelly, K. L.; Schatz, G. C.; Van Duyne, R. P. Chain Length Dependence and Sensing Capabilities of the Localized Surface Plasmon Resonance of Silver Nanoparticles Chemically Modified with Alkanethiol Self-Assembled Monolayers. *J. Am. Chem. Soc.* **2001**, *123*, 1471–1482.
- (44) Haes, A. J.; Zou, S.; Schatz, G. C.; Van Duyne, R. P. Nanoscale Optical Biosensor: Short Range Distance Dependence of The Localized Surface Plasmon Resonance of Noble Metal Nanoparticles. *J. Phys. Chem. B* **2004**, *108*, 6961–6968.

L

DOI: 10.1021/acsami.7b01116
ACS Appl. Mater. Interfaces XXXX, XXX, XXX–XXX